Università degli Studi di Cagliari

Dipartimento di Fisica

PhD DEGREE

DarkSide-20k sensitivity, directional dark matter detection and the role of coherent elastic neutrino-nucleus scattering background

Cycle: XXX

Scientific Disciplinary Sectors	FIS/01 and FIS/02
PhD Student	Matteo Cadeddu
Coordinator of the PhD Programme	Prof. Alessandro De Falco
Supervisors	Dr. Alessandro Cardini and Dr. Marcello Lissia

Final exam. Academic Year 2016-2017. Thesis defence: February-March 2018 Session

Cycle: XXX

DarkSide-20k sensitivity, directional dark matter detection and the role of coherent elastic neutrino-nucleus scattering background

PhD DEGREE, Final exam. Academic Year 2016-2017. Thesis defence: February-March 2018 Session

Reviewers: Prof. Giuliana Fiorillo and Dr. Francesco Vissani

Supervisors: Dr. Alessandro Cardini and Dr. Marcello Lissia

Università degli Studi di Cagliari

Istituto Nazionale di Fisica Nucleare

Dipartimento di Fisica

Via Università 33

09124 Cagliari

Contents

1 Introduction 1

2 Theoretical overview of dark matter 7
2.1 Evidence for dark matter . . . 10
2.1.1 Velocity dispersion of spiral galaxies . . . 11
2.1.2 Gravitational lensing . . . 11
2.1.3 Cosmological evidence . . . 14
2.1.4 N-body simulations of Universe evolution . . . 17
2.2 Properties of dark matter . . . 20
2.2.1 Big Bang Nucleosynthesis and charged dark matter particles 21
2.3 Particle dark matter candidates . . . 22
2.3.1 Weakly Interacting Massive Particles . . . 23
2.3.2 Sterile neutrinos . . . 25
2.3.3 Axions . . . 26
2.4 Detection of dark matter . . . 28
2.4.1 Collider production . . . 28
2.4.2 Indirect detection . . . 29
2.4.3 Direct detection . . . 32
2.5 Alternatives to dark matter . . . 32

3 Direct detection of dark matter 35
3.1 Direct detection formalism . . . 36
3.1.1 Spin-independent cross section . . . 39
3.1.2 Spin Dependent cross section . . . 41
3.1.3 The final event rate . . . 42
3.1.4 Nuclear form factor . . . 44
3.2 Distribution of DM in our galaxy . . . 50
3.3 Dark matter speed distribution . . . 53
3.3.1 Annual modulation of DM rate . . . 60
3.3.2 Daily and directional variation of DM rate . . . 62
3.4 Final SI WIMP differential rate for different nuclei . . . 63

3.5 DM differential event rate uncertainties . . . 65
3.5.1 Nuclear physics uncertainties . . . 68
3.5.2 Particle physics uncertainties . . . 69
3.5.3 Astrophysical uncertainties . . . 70
3.6 Direct detection experiments current limits and anomalies . . . 73
3.6.1 Current limits and results . . . 77
3.6.2 Future experiments . . . 82
3.7 Conclusions . . . 83

4 DarkSide-20k **85**
4.1 Overview and goals of DarkSide-20k . . . 86
4.1.1 Nuclear recoils . . . 89
4.1.2 Electron recoils . . . 90
4.1.3 Surface recoils and Cherenkov backgrounds . . . 92
4.2 Experimental design of DarkSide-20k . . . 93
4.2.1 The LAr TPC . . . 93
4.2.2 The active vetoes: Water Cherenkov Veto and Liquid Scintillator Veto . . . 95
4.3 Procurement and purification of the underground argon target . . . 98
4.3.1 The Aria project . . . 99
4.4 Physics reach . . . 100
4.4.1 Simulation of backgrounds in DarkSide-20k . . . 104
4.4.2 DarkSide-20k energy acceptance . . . 110

5 WIMP Sensitivity of DarkSide-20k and future detectors **115**
5.1 The background impact on the WIMP sensitivity . . . 116
5.1.1 Likelihood for upper limits . . . 117
5.1.2 Likelihood for discovery . . . 120
5.2 CEnNS background contribution . . . 122
5.3 Neutrino-nucleus cross section . . . 123
5.4 Neutrino Fluxes . . . 126
5.4.1 Solar neutrinos . . . 127
5.4.2 Atmospheric neutrinos . . . 128
5.4.3 Diffuse supernova neutrinos . . . 129
5.5 Event rate for argon and xenon . . . 129
5.5.1 One neutrino isoevent curve for argon and xenon . . . 131
5.6 Kinematic differences in WIMP and neutrino reconstruction . . . 141
5.6.1 DarkSide-20k and Argo/GADMC detector sensitivity . . . 150
5.6.2 ARIA impact on sensitivity curves . . . 154

5.7 Argon-xenon comparison in view of standard electroweak interactions on electrons . . . 156

6 Directional dark matter detection 163
6.1 Directional detectors and columnar recombination . . . 164
6.2 Cross section and differential rates . . . 167
6.2.1 Recoil rate in Galactic angular coordinates . . . 170
6.3 Recoil directional signals at LNGS . . . 173
6.3.1 Differential rates as functions of the polar angle . . . 174
6.3.2 Vertical and horizontal event categories . . . 175
6.4 Seasonal effects . . . 176
6.5 Statistical analysis for a directional signal . . . 180
6.6 Conclusions . . . 188

7 Experimental constraint of coherent neutrino scattering 191
7.1 The COHERENT experiment . . . 193
7.2 CEnNS cross section with the inclusion of the neutron form factor 197
7.2.1 The PREX measurement and its implications . . . 199
7.3 Parametrization of the neutron and proton form factors . . . 200
7.4 Fitting procedure of the COHERENT data . . . 203
7.4.1 Future sensitivity of R_n . . . 208
7.5 Implications of COHERENT results for dark matter searches . . . 210

8 Conclusions 213

A Derivation of the SM coherent ν-nucleus cross sections 217

Bibliography 219

1 Introduction

The existence of dark matter (DM) in the Universe is one of the most fascinating problems that modern physics needs to solve. Since its proposal by Jan Oort and Fritz Zwicky in the 1930s, it has nowadays been accepted by the physics community in order to explain many otherwise puzzling astrophysical and cosmological anomalies. Dark matter properties can be inferred from the observation of several phenomena and it is commonly believed that roughly 25% of the mass-energy content of the universe is in some non-baryonic form that does not interact electromagnetically nor via the strong force. Possible alternative explanations, such as theories proposing modifications to Einstein's theory of gravity, have failed so far to explain these observations across all scales. The most promising candidate for dark matter and the most relevant one for this thesis is a yet to be discovered *weakly interacting massive particle* (WIMP). Those particles, that cannot be found within the Standard Model (SM), must interact weakly enough to survive a myriad of bounds set by precision astrophysical and cosmological tests and heavy enough to have been in non-relativistic motion when they decoupled from the hot particle plasma in the early stages of the expansion of the Universe. Many theories that predict the existence of phenomena not included in the SM provide a valuable WIMP candidate that could be experimentally observed thanks to its possible interactions with SM particles.

Despite the worldwide efforts to answer to such an urgent question, at the moment of writing, no clear direct indication that such particles exist has been found at particle accelerators or elsewhere. Hence, the nature of the dark matter is still a mystery that involves thousands of scientists from different fields that have developed several methods in order to *capture* these elusive particles.

Models in which the dark matter particles can annihilate suggest the possibility to indirectly search for dark matter by the observation of annihilation final state products, among which neutrinos, antiprotons and positrons can be found. Indirect astrophysical searches have the advantage of associating any SM particle excess with a dark matter over-density region. However, the search of such

an excess in astrophysical observations is difficult and it is affected by large uncertainties.

The *golden method* to observe dark matter is represented by direct searches that aim to spot effects of a possible interaction between a dark matter candidate with the target material of the detector. Different technologies are currently exploited to diversify direct dark matter searches. A non exhaustive list comprises bubble chambers, cryogenic bolometers with ionization or scintillation detection, point contact germanium and sodium/caesium iodide scintillation detectors, and finally experiments using liquid xenon (LZ, LUX, XENON1T and PandaX-II among others) and, more recently, liquid argon (ArDM, DEAP-3600, MiniCLEAN, WArP and DarkSide-50 among others). At the moment of writing, two of the dual-phase liquid xenon experiments, namely XENON1T and PandaX-II, possess the most stringent limits on WIMP-nucleon cross section in the WIMP mass range from about 10 GeV to 10 TeV.

Due to the lack of a clear observation of dark matter, the motivation for direct WIMP searches remains extremely strong, driving the efforts to construct a new generation of experiments. In order to explore lower cross sections and improve current sensitivity levels by a few orders of magnitude, it now becomes mandatory to build detectors with tens of tonnes of active target mass. However, at this stage the control of backgrounds coming from neutrino-electron scattering would be of utmost importance for a possible discovery of dark matter. In this context, argon detectors outperform other technologies with their outstanding β/γ background rejection. For this reason, a two-phase liquid argon time projection chamber of 20 tonne active mass, capable of collecting an exposure of 100 tonne year, has been proposed by the DarkSide Collaboration. This detector, to be located at Laboratori Nazionali del Gran Sasso, is called DarkSide-20k and it is expected to operate in a so-called background free regime, so that a positive claim can be made with as few events as possible. This means that for the nominal exposure the number of instrumental background interactions will be kept to less than 0.1 events, apart from background events induced by Coherent Elastic neutrino-Nucleus Scattering (CEnNS).

Nuclear recoils from CEnNS are indistinguishable from WIMP-induced nuclear recoils and thus represent an irreducible source of background. The proposal to quantitatively estimate the impact of this background and the detailed calculation of the number of CEnNS events attended in DarkSide-20k has been carried out

for the first time during this thesis project. It has been found that, with the nuclear recoil energy thresholds needed to achieve the excellent electron recoil rejection in argon, only atmospheric neutrinos and the diffuse supernova neutrino background are energetic enough to produce nuclear recoils in the WIMP region of interest. As a result of this study, it has been discovered that this background cannot be neglected. On the contrary, it will represent the main background source for DarkSide-20k and it must be accounted for in the derivation of the WIMP-nucleon sensitivity curve. The latter has been determined as well in this thesis and represents the official outcome of the DarkSide-20k experiment.

It is a recent news that the four world-leading liquid argon dark matter collaborations (ArDM at LSC, DarkSide-50 at LNGS, DEAP-3600 and MiniCLEAN at SNOLAB) have agreed to continue the collaboration beyond DarkSide-20k to build an even larger experiment, with a fiducial mass of a few hundreds of tonnes, capable of collecting an exposure between 1000-3000 tonne year. Similarly to DarkSide-20k, this detector will be able to remove all backgrounds except the CEnNS component. However, at these exposures, the latter contribution will be significant, reaching the "ultimate limit" of dark matter searches in absence of directional sensitivity. This ultimate limit is usually referred to as the *neutrino floor*, the knowledge of which has been deepened as a part of this thesis project.

Being the number of CEnNS events at this exposure so large that the WIMP-nucleon sensitivity will start to saturate, a breakthrough will be represented by the development of directional detectors, able to provide information on the incoming WIMP or neutrino direction. During this thesis project, the feasibility studies for an argon dark matter detector able to discriminate the recoil direction of a nucleus after a dark matter interaction have been developed. Several prototypes of directional detectors exist but they are usually limited in mass, thus being capable of collecting limited exposures. A promising technique for a very large-mass detector with directional DM capability would be to exploit the phenomenon called *Columnar Recombination* (CR). As a part of this PhD project, the author has collaborated to the development of a more realistic extension of the original CR model. All these studies corroborated the motivation for the construction of a small prototype dual-phase TPC called RED, which is part of the DarkSide program and currently in his commissioning phase, that aims to prove the directional sensitivity using a beam of neutrons.

Due to the fact that the coherent elastic scattering of neutrinos off nuclei has eluded detection for about four decades since its prediction, as a part of this thesis project, the study of possible physics effects beyond the SM modifying CEnNS predictions has been developed. This study is relevant due to the importance of this background for DarkSide-20k. Unexpectedly, this process has been detected for the first time in August 2017 by the COHERENT Collaboration, and it turned out to be 77 ± 16 per cent of the SM value. This deficit has been interpreted by the author of this thesis including in the SM predictions the contribution of the neutron form factor, which has usually been neglected until now. As a by-product of this analysis, it was possible to experimentally determine for the first time the average radius of the caesium iodine (CsI) nuclei. This result provides a better understanding of the neutrino background for future direct dark matter experiments but has also implications in many fields, including neutron stars phenomenology, stellar collapse processes and obviously nuclear physics models. Finally, the author of this thesis has also worked on the interaction between dark matter and argon nuclei within an effective field theory framework, re-analysing the last DarkSide-50 experimental results in terms of limits on non-relativistic effective operators from non standard interactions. However, since this study refers to DarkSide-50, it will not be discussed here.

This thesis is organised as follows. The second and third chapter familiarises the reader to all the necessary knowledge to understand the topics presented. In particular, the second chapter gives an introduction to dark matter and reviews the evidences in support of the DM paradigm, while the third chapter focuses on the discussion of direct detection techniques and contains a short review of the current state of art and exclusion limits. The DarkSide-20k experiment is presented in the fourth chapter. In the fifth chapter the statistical tools used to obtain upper limits on the WIMP-nucleon cross section are initially presented, followed by the derivation of the predicted number of neutrino background events in DarkSide-20k. Finally, the calculation of the 90% Confidence Level (C.L.) WIMP-nucleon cross section sensitivity of the DarkSide-20k experiment and of a future detector capable of achieving an exposure between 1000-3000 tonne year will be reported. In the sixth chapter the potential of a DM detector able to discriminate the recoil nucleus direction will be examined and finally, in the seventh chapter, the method used to obtain the first measurement of the average CsI neutron density radius fitting the COHERENT data will be illustrated. To conclude, in the eighth chapter, the results obtained are summarised and commented upon.

Most of the work contained in this thesis has been published in a series of papers listed here

- M. Cadeddu, C. Giunti, Y. F. Li and Y. Y. Zhang, "Average CsI neutron density distribution from COHERENT data", Phys. Rev. Lett. 120, 072501, 2018 [1]

- M. Cadeddu and E. Picciau, "Impact of neutrino background prediction for next generation dark matter xenon detector", J. Phys. Conf. Ser. 956, 2018 [2]

- C. E. Aalseth et al., "DarkSide-20k: A 20 Tonne Two-Phase LAr TPC for Direct Dark Matter Detection at LNGS", Arxiv:1707.08145 (Accepted by European Physical Journal Plus), 2018 [3]

- V. Cataudella, A. de Candia, G. D. Filippis, S. Catalanotti, M. Cadeddu, M. Lissia, B. Rossi, C. Galbiati, and G. Fiorillo, "Directional modulation of electron-ion pairs recombination in liquid argon", JINST, vol. 12, no. 12, p. P12002, 2017 [4]

- M. Cadeddu et al., "Recoil Directionality Studies in Two-Phase Liquid Argon TPC Detectors", EPJ Web Conf., vol. 164, no. 07036, 2017 [5]

- M. Cadeddu et al., "Potential for an argon directional dark matter detector", Arxiv:1704.03741 (to be submitted to JHEP), 2017. [6]

- G. Fiorillo and M. Cadeddu, "Directionality in Dark Matter search", PoS, vol. NOW2016, p. 091, 2017 [7]

- M. Cadeddu, "Dark Matter search with directional sensitivity", Nuovo Cim., vol. C40, no. 1, p. 66, 2017 [8]

- M. Cadeddu, "A directional Dark Matter argon detector at LNGS", J. Phys. Conf. Ser., vol. 689, no. 1, p. 012015, 2016 [9]

The author's name appears also in other papers published together with the DarkSide Collaboration, see Refs. [10, 11, 12, 13, 14, 15, 16].

2 Theoretical overview of dark matter

Contents

2.1 Evidence for dark matter 10
2.2 Properties of dark matter 20
2.3 Particle dark matter candidates 22
2.4 Detection of dark matter 28
2.5 Alternatives to dark matter 32

In the last two centuries, significant progresses have been made towards a rational understanding of the Universe and more and more complex experiments have been built to gather information on a plethora of natural phenomena. The Standard Model (SM) of particle physics is the theory that describes, to the best of today's knowledge, the fundamental particles and the forces through which particles interact, namely the electromagnetic, the strong and the weak interactions. Over the last decades, the SM has been extensively scrutinized and its predictions have been confirmed by innumerable experimental results. In the recent years, a big success of the SM has been the discovery of the so-called Higgs boson, thanks to the ATLAS and CMS experiments. It is a massive spin-0 particle predicted by the Higgs mechanism, which is responsible for the mass of bosons and fermions in the SM. However, despite the many successes, some big questions are still unanswered and there is a general consensus that the SM must be an effective theory whose validity breaks down at some higher energy scale, larger than few hundred GeV according to most recent experimental constraints. For example, the most familiar force in our everyday lives, gravity, is not included or contributions from physics beyond the SM are needed in order to explain the large matter-antimatter asymmetry that resulted in the matter dominated universe we observe today.

Among these, one of the most intriguing question in physics which needs to be answered is the origin of the so-called Dark Matter (DM), which existence and

properties are inferred from its gravitational effects. In particular, its existence is needed to explain a number of otherwise puzzling astronomical observations, as it will be explained in this chapter, and it cannot be constituted by SM particles. The answer to this big problem involves thousands of scientists from different fields, ranging from astronomy to particle physics passing by cosmology. Despite these world-wide efforts to answer to such an important and urgent question, it still represents one of the most demanding challenge of particle physics. Indeed, the interaction of DM particles must be very weak in order to survive a myriad of bounds set by precision astrophysical and cosmological tests. Thus, the failure to observe dark matter particles so far tells us that their interactions must be even weaker.

The detection of DM using terrestrial detectors would give strong clues about the nature and possibly the identity of DM. As it will be explained in this chapter, the most intriguing candidate for DM is a so called Weakly Interactive Massive Particle (WIMP), that broadly speaking is a new, yet undiscovered, big-bang relic particle that interact via gravity and any other force, possibly also not included in the SM, which is as weak or weaker than the weak nuclear SM force. WIMPs could in principle be detected through their collisions with ordinary nuclei in an instrumented target, producing low-energy ($<$200 keV) nuclear recoils. So far, the analysis of these so-called *Direct Detection* (DD) experiments has given no positive results or clues in the last decades. Very low interaction rates are expected for such particles, based on the model for their production and existing limits. Since the discovery limit is a function of the exposure, the product between the active mass of the detector and its live-time, one could expect that the discovery of DM is only a matter of time. However, since the interaction between DM and ordinary matter is very weak, possible background contaminations of the signal assume a crucial role and have to be taken into account. Current direct detection experiments have demonstrated to be able to reduce the background content to a level for which a discovery should still be possible if the interaction is not too weak. However, there are two important issues to take into account. One is related to the reliability of the possible discovery when measuring only the recoil energy of the target nuclei. Indeed, accumulating statistics during several years the recoil rate is expected to modulate with a year-periodicity due to the WIMPs relative velocity change caused by the Earth orbital motion. However, many backgrounds, like particles originating from cosmic rays, are known to modulate with a similar year periodicity. Thus, in presence of background contaminations

it is difficult to be fully convinced that the measured modulation is only due to DM interactions, mining the reliability of the result. The second problem of this detection technique is connected with the fact that near future DM experiments will be sensitive to Coherent Elastic neutrino-Nucleus Scattering (CEnNS), which produce an experimental indistinguishable signal with respect to that induced by a DM particle, representing an irreducible source of background.

A common partial solution for these two problems will be to develop so-called *directional DM detectors*. This kind of detectors would be able to provide information not only on the nuclear recoil energy induced by a DM scattering on nucleus but also on the incident direction of the DM particle. The latter is useful since, exploiting the Earth rotation around its own axis, a sizeable diurnal modulation rate is expected. Since there are not known backgrounds that can reproduce a similar behaviour, this technique can help in disentangling the signal and background hypotheses in a stronger way than using only the energy spectrum information. Since the incident DM direction is correlated with the direction of motion of the solar system through the galaxy towards the Cygnus constellation, this preferential direction is the ultimate tool to reduce any other isotropic background, like CEnNS from atmospheric and diffuse supernova neutrinos, or even better to distinguish backgrounds with a definite but different incident direction, like for example solar neutrinos. Such efforts are advancing rapidly thanks to the simultaneous technological developments and new results are expected in the next decade.

At the moment of writing, a clear evidence for DM interactions in terrestrial laboratories is still lacking. Without a detection of a possible particle candidate, the only answer to the origin of DM question can be developed reviewing the current evidence for its existence. Evidences for DM are found on scales from the Milky Way up to the cosmological horizon, with a range of observations which cannot be adequately explained with the observed constituents of the Universe. Dark matter is an invisible component introduced to reconcile these observations with the known laws of physics - most importantly, General Relativity (GR). Beyond this general definition, there is a wide range of particle physics candidates which may play the role of dark matter. These new particle candidates are usually provided by theories of physics beyond the SM, meaning that the study of the properties of dark matter can shed light on theories of high energy physics. Many

of these proposed dark matter candidates have weak but non-zero interactions with particles of the SM, giving hope that DM could be discovered also through non gravitational-only effects.

In this chapter, the evidences in support of the DM paradigm, including constraints from precision cosmology will be summarised. Some of the features which DM particles must satisfy will be discussed, as well as describing a few specific candidates in more detail. Finally, current progresses and constraints from direct and indirect searches for particle DM will be reviewed.

2.1 Evidence for dark matter

In 1933, Zwicky measured the velocity dispersion of eight galaxies in the Coma cluster [17], 99 Mpc away from the Milky Way, finding an unexpectedly large velocity dispersion, $\sigma = 1019 \pm 360\,\mathrm{km\,s^{-1}}$. By applying the Virial Theorem, that relates the velocity of orbiting objects to the amount of gravitational force acting on them, he concluded from these observations that the mean density of the Coma cluster would have had to be 400 times greater than that which was derived from luminous matter, calling this exceeding non-luminous mass *dark matter*. Despite the fact that this estimate was too large due to an old value for the Hubble parameter H_0 used in the calculation, and despite the fact that it is now known that some of this mass is in the form of hot ($\sim$1 million K) X-ray emitting intracluster gas [18], a large discrepancy remains. Current estimates of the mass-to-light ratio of the Coma cluster give a value of roughly 150 times that of the Sun [19, 20]. This discovery turned out to be one of the most profound scientific revolutions of the 20th century. Despite the initial scepticism, further studies revealed that the Coma cluster was not unusual.

In this section, the evidences that lead physicists to believe in the existence of DM will be briefly summarised. After this section it will be clear that evidence for dark matter appears over a wide range of distance scales. Dark matter is required to explain the formation and growth of large scale structure, the dynamics of both galaxies and galaxy clusters and the anisotropic temperature distribution of the CMB among others. In spite of this, there remain several problems and unanswered questions with the dark matter paradigm that will be reviewed in Sec. 2.1.4.

2.1.1 Velocity dispersion of spiral galaxies

The measurement of the rotation curves of many galaxies, namely the velocity versus the radial distance for stars and gas in spiral galaxies, gives strong indications of the existence of dark matter. A spiral galaxy like our own has most of the luminous material concentrated in a central hub at small radii, plus a thin disc. This suggests that the velocity, v, should increase at small distances, r, from the galaxy center and fall off at large distances, namely $v \approx r^{-1/2}$. On the contrary, the observed rotation curves are flat at large r, at least to values of r comparable with the disc radius, implying a total mass growing linearly with radius [21, 22]. In fact, observations of hydrogen 21 cm emission indicate that the constancy of the circular velocity extends well beyond the optical edge of galaxies [23, 24]. However, the inclusion of an approximately spherically symmetric, non-luminous dark matter halo can reconcile this expectation with the observed flat rotation curves, as schematically shown in Fig. 2.1. As it can be seen analysing the different components in this figure, the visible and gaseous components alone cannot explain the flatness of the curves at large radii. Instead, one has to assume the existence of a dark halo or a modified theory of gravity (MOND), see Sec. 2.5, to explain the shapes of these curves. The density profiles $\rho(r)$ required to provide a good fit to rotation curve data may be consistent with those obtained from N-body simulations, such as the Navarro-Frenk-White profile [25]

$$\rho(r) = \frac{\rho_0}{r/R_s(1 + r/R_s)^2}\,, \tag{2.1}$$

which is described by a characteristic density ρ_0 and scale radius R_s. N-body simulations and evidences for DM coming from them will be explained in Sec. 2.1.4. The rotation curve of the Milky Way itself has also been studied [26, 27, 28] and found to be almost flat. Using a variety of techniques, it is also possible to measure a non-zero DM density near the Sun's position. An understanding of this density has significant implications for the study of dark matter direct detection.

2.1.2 Gravitational lensing

Gravitational lensing is an effect of Einstein's theory of GR. The gravitational field of a massive object causes light rays passing close to that object, and thus through its gravitational field, to be bent. The more massive the object, the stronger its gravitational field and hence the greater the bending of light rays. Thus, by

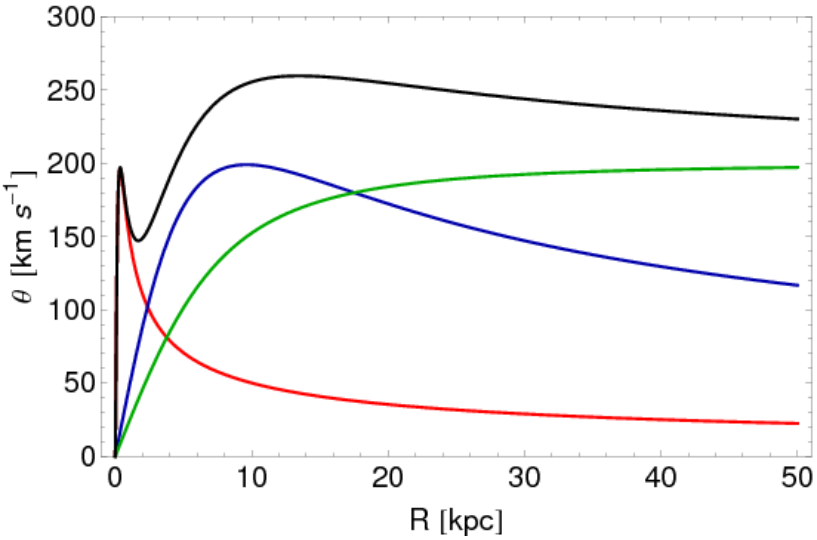

Fig. 2.1.: Schematic illustration of galaxy rotation curves (circular velocity as a function of galactocentric distance). The different components contributions are separately shown. The total circular velocity (black) and also the contributions from the spherical nucleus (red), the disk (blue) and that of the dark matter halo (green) are separately plotted. Figure form Ref. [29].

looking at the gravitational lensing distortions, the mass profile of galaxy centers or galaxy clusters can be measured. Lensing can also act like a magnifying glass, allowing us to see images of galaxies that would otherwise be too faint to see. Two different regimes of gravitational lensing can be defined, so called strong and weak lensing. Strong lensing happens when the light from a bright source has to go through a massive object, like a cluster of galaxies, before to reach us and it is thus deflected by large angles. In this case, it is easy to see and measure the effects of lensing. In particular, the strength of the deflection is proportional to the square root of object mass. However, there are not that many clusters in the sky that are so big that they cause such a large lensing effect. So even if strong lensing is indeed very useful it is also pretty rare. In fact, most galaxies visible from Earth are lensed such that their shapes are altered by only $\sim 1\%$, an effect that is called weak gravitational lensing. In this case the gravitational lensing angle is quite small to be measured and it is only possible to study the average lensing effect on a set of galaxies. By making some assumptions, like that all galaxies are roughly elliptical in overall shape, and that they are orientated randomly on the sky, in the presence of a lensing effect, one would expect that the galaxies in a patch of sky would appear to align themselves together slightly on the sky, as lensing stretches all their images in the same direction. In this way, any deviation from a random distribution of galaxy shape orientations is a direct

measure of the lensing signal in that patch of sky. Weak lensing can thus be used to measure the gravitational lensing signal on any part of the sky. The result of many studies of gravitational lensing is that the baryonic matter is not enough to account for the lensing effects that are observed.

Several experiments based on gravitational lensing have also tried to use this effect to search for relatively compact objects, non-luminous and with a mass as low as 10^{-7} solar masses. Lensing effects on this scale are known as micro-lensing. These bodies are commonly referred to as Massive Compact Halo Objects (MaCHOs), and many dozens of such microlensing events have been observed in recent years. Present data indicate that these non-luminous stellar objects, undoubtedly of baryonic matter like normal stars, have a small potential contribution to the total dark matter content, being the current upper limit equal to 1.7×10^{-7}.

Lensing has also been used to study the properties dark matter itself, meaning that it cannot be accounted for by ordinary baryonic matter. This can be achieved observing the so-called Bullet Cluster, a system of two galaxy clusters that recently (on cosmological time-scale) collided. An X-ray and optical (visible) light picture of such an event is shown in Fig. 2.2. The majority of the light coming from the Bullet Cluster comes from hot X-ray emitting gas. It has been overlaid onto the visible-light image in pink. Superimposed in blue it is possible to see the location of the dark matter in the cluster, determined from measuring the lensing signal from the visible-light images of the galaxies. During the collision, the baryonic X-ray gas particles, the 'normal' matter, will interact with each other through both gravity and electrostatic forces, slowing and shocking one another. The dark matter particles, however, only interact through gravity and can pass through each other unimpeded by electrostatic interactions. This means that the X-ray gas lags behind the dark matter as the two clusters escape the collision, causing the observed offset. Thus, even if most of the visible matter is in the centre of the image, gravitational lensing proves that most of the mass lies further out. This offset is then a very strong indication for the presence of a far more weakly interacting form of matter than baryonic matter, with a total mass that by far exceeds the baryonic mass.

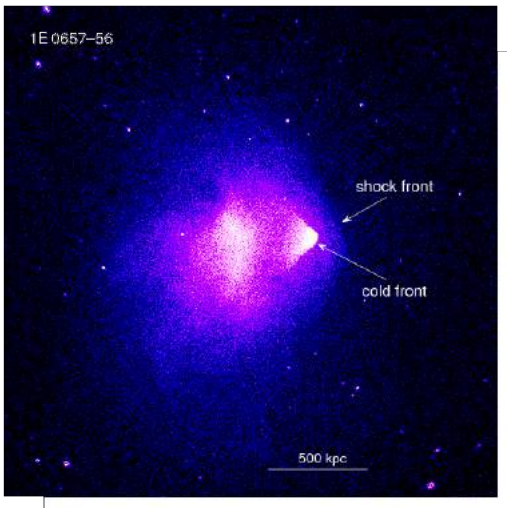

Fig. 2.2.: Chandra X-ray image of A 3667 (MV07) with superimposed the optical (visible) light. Credit: NASA/Chandra X-ray Observatory.

2.1.3 Cosmological evidence

Dark matter evidences are such that, the most recognized model that summarizes our understanding about the origin of the Universe, includes Dark Matter as a key component. For this reason it is called the Lambda Cold Dark Matter (ΛCDM) model of modern cosmology. Developed in the late 1990s, this model is the simplest parametrization of the Big Bang cosmological model that is broadly consistent with several observations, namely the existence and properties of the cosmic microwave background, the large-scale structure in the distribution of galaxies, the abundances of hydrogen (including deuterium) and helium and the accelerating expansion of the universe observed in the light from distant galaxies and supernovae. The name of the model indicates its two principal ingredients: Λ refers to a Cosmological constant, i.e. the energy density or Dark Energy of the vacuum, and CDM stands for Cold Dark Matter, slowly moving particles that account for a wide variety of cosmological observations that seem to imply the presence of *missing mass*.

In this framework, the total energy density of the Universe receives three contributions, namely the radiation density ρ_r, the dark energy density ρ_Λ and the matter density ρ_m. The latter can be further subdivided into baryonic ρ_b, and cold dark matter component ρ_{CDM}. Those quantities are usually given in terms of fraction of total density, $\Omega_i = \rho_i/\rho_c$, being ρ_c the critical density required for the universe to be flat and homogeneous. Up to today knowledges, the energy density

of the Universe today is dominated by the constant and uniform contribution of the vacuum, Λ. This constant term was originally introduced by Einstein before the advent of the Big Bang scenario in order to avoid spontaneous collapse of the Universe. Nowadays, this contribution is needed to exert a negative pressure and to drive the accelerating expansion of the Universe, whose discovery was rewarded in 2011 with a Nobel Prize in Physics [30, 31]. According to this model, the structures that emerged in the early Universe are caused by the clustering of a non-interacting, slow moving and yet undetected matter component [32], usually referred to as Cold Dark Matter. The fact that DM is non-interacting (or at least, interacts only very weakly) means that it begins to collapse gravitationally earlier in cosmic time than baryonic matter. After decoupling, baryons then fall into the gravitational wells produced by the infalling DM structures. Without DM, the baryonic matter in the Universe could not have had enough time to collapse to form the range of gravitationally bound structures we see today [33, 32].

Cosmological experiments sensitive to the expansion and structure formation history of the Universe, like e.g. Planck [34] WMAP [35], BOSS [36] and CFHTLenS [37, 38], allow to precisely determine the contributions of the various different components to the energy density of the Universe, constraining cosmological parameters. In this framework, a lot of information has been gathered by measuring Baryon Acoustic Oscillations (BAOs) [39]. BAOs are regular, periodic fluctuations in the density of the visible baryonic matter (normal matter) of the universe, basically a feature imprinted on the distribution of matter in the Universe by acoustic waves prior to recombination. They can be measured by using galaxy redshift surveys, such as SDSS [40], to map out the large scale structure of the Universe. In the same way that supernovae provide a “standard candle” which can be used to measure luminosity distances in the Universe, the identification and the fit of the acoustic peak provide a “standard ruler” for measuring cosmological distances. Thus, redshift surveys of type-Ia supernovae [41] for which we know the luminosity allow to reconstruct these distance scales over cosmic time. This information allows to constrain the expansion history of the Universe and therefore the various contributions to the density of the Universe.

A particularly sensitive probe for determining the dark matter contribution to the energy budget of the Universe is the measurement of the temperature anisotropies of Cosmic Microwave Background (CMB) photons. The CMB is the electromagnetic radiation left over from an early stage of the universe in Big Bang cosmology. Indeed, at the end of the so-called epoch of recombination, in which neutral

atoms were formed, the universe became transparent to electromagnetic radiation, and photons were able to freely travel ever since and can still be observed today with a temperature of $2.726 \pm 0.010\,\mathrm{K}$. The recent Planck experiment [34]

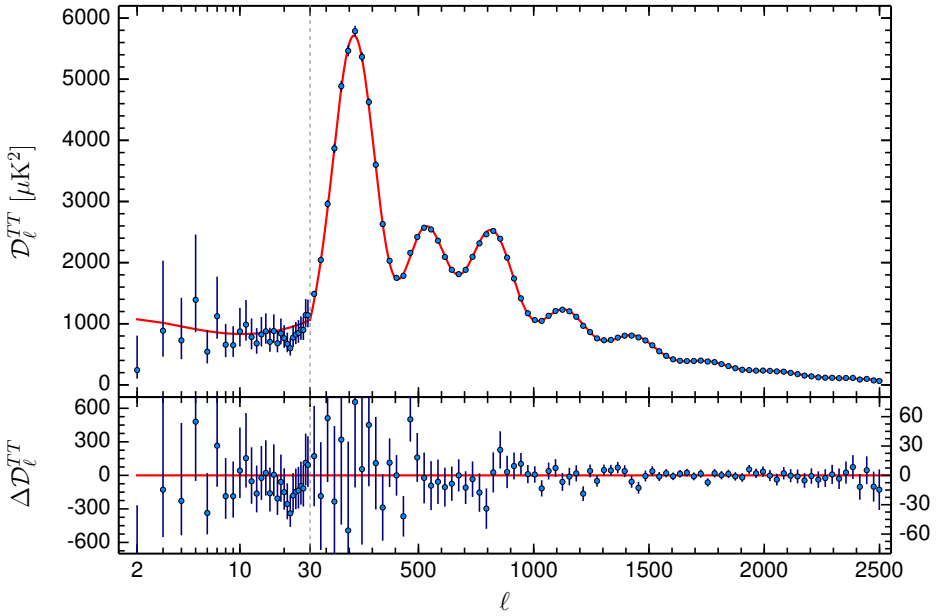

Fig. 2.3.: Angular power spectrum of CMB temperature anisotropies as measured by the Planck satellite. Data are shown as blue points with the best fit ΛCDM cosmological model shown as a red line. Figure from Ref. [34].

measured the angular power spectrum of these CMB temperature anisotropies. The power spectrum is simply a measurement of the amount each point in the universe deviates from the mean temperature, decomposed into spherical harmonics. Indeed, while the CMB is mostly isotropic, showing that the universe is largely homogeneous, small anisotropies are present due almost entirely to the temperature fluctuations in the early universe that were caused by the under- and over-densities in different regions as particles began to freeze out at different times. The intensity and size of these fluctuations depend entirely on the different components and species present at the time, making the CMB sensitive to the amount of dark matter present in the early universe. Figure 2.3 shows the results of these measurements, as well as the best fit using the six parameters ΛCDM model. The amplitude of the power spectrum at various values of l, the angular size (π/l) of a given spherical harmonic, gives a quantitative measurement of the anisotropies in the CMB, which allows us to determine the abundance of different kinds of particles in the universe after the freeze out, as well as many

Parameter	68% limits
Ω_Λ	0.685 ± 0.013
$\Omega_m h^2$	0.1426 ± 0.0020
$\Omega_b h^2$	0.02222 ± 0.00023
$\Omega_{CDM} h^2$	0.1197 ± 0.0022
H_0	67.31 ± 0.96

Tab. 2.1.: Density parameter Ω (defined in the text) of the cosmological constant (Λ), total matter (m), and separate baryonic (b) and cold dark matter (CDM) components, as obtained by the Planck Collaboration [34]. The reduced Hubble constant is defined as $h = H_0/(100\,\text{km s}^{-1}\text{Mpc}^{-1})$.

other properties. The contributions of the cosmological constant, the total matter component, and the separate baryonic and dark matter components to the total energy density of the Universe are shown in Table 2.1. These are given in terms of the density parameter $\Omega_i = 8\pi G\rho_i/3H_0^2$, where G is Newton's constant, H_0 is the Hubble parameter and ρ_i is the energy density of component i. These results, constrained with an accuracy of less than 2%, point to the conclusion that ~84% of the matter content of the Universe is in fact dark.

2.1.4 N-body simulations of Universe evolution

The success of the ΛCDM paradigm is also due to the results coming from so-called N-body simulations. An N-body simulation is a computer simulation that involves a large number of particles interacting according to basic physical laws. N-body simulations are used to track the evolution of structure in the Universe. In such a simulation, millions of particles are configured according to an initial density distribution and are allowed to interact following the laws of gravity. The computer calculates how the particles will move under the influence of gravity in a small time step, and uses the resulting distribution of particles as the starting point for a new calculation. By calculating many time steps, the simulation can track the growth of structures in the model system. Depending on the initial density distribution and cosmological parameters selected, different structures appear at different stages of evolution.

In 1973, the astronomers Jeremiah Ostriker and James Peebles used for the first time N-body simulations to study how galaxies evolve. They programmed 300 mass points into their computer to represent groups of stars in a galaxy rotating

about a central point. Their simulated galaxy resulted in more mass points, or stars, toward the center and fewer toward the edge. For a galaxy of the size of the Milky Way, we know that a star (a mass point in a N-body simulation) about halfway out the edge moves at about 200 kilometers per second and orbits the center in about 50 million years. Ostriker and Peebles found that in a time less than an orbital period, most of the mass points would collapse to a bar-shaped, dense concentration close to the center of the galaxy with only a few mass points at larger radii. This looked nothing like the elegant spiral or elliptical shapes that exists in our Universe. However, adding a static, uniform distribution of mass from 3 to 10 times the size of the total mass of the mass points, they found that a more recognizable structure would emerge. For the first time there were numerical evidence that dark matter was necessary to form the types of galaxies we observe in our Universe.

Most of N-body simulations currently used are DM-only, simulating only the gravitational dynamics of collisionless particles. However, an increasing number are incorporating baryonic physics such as gas dynamics, as well as stellar evolution, chemical enrichment and a variety of interaction processes (see e.g. [42, 43]). As it can be easily understood, these simulations are resource intensive because the number of interactions the computer must calculate at each time step is proportional to the number of particles squared. A sophisticated N-body simulation can require tens of thousands of supercomputer hours. In particular, appropriately accounting for baryonic physics is extremely complex and in some cases the strength of these processes is unknown and must be tuned in the simulations to match observations [44].

In spite of this, a consistent picture has emerged from several N-body simulations. The distribution of galaxies observed in large scale structure surveys matches that predicted by N-body simulations over a range of distance scales [45]. In addition, simulations have begun to accurately reproduce the observed populations of elliptical and spiral galaxies [43], as well as obtaining Milky Way-like simulated galaxies [42]. This ability of simulations containing DM to reproduce structures observed in the Universe is a further strong evidence in support of the DM paradigm.

Problems with dark matter in N-body simulations

There have emerged several issues with the dark matter dominated model of structure formation as studied with N-body simulations. For example, DM-only simulations predict the existence of a large number of massive subhalos around Milky Way-size galaxies [46]. Using semi-analytical models of galaxy formation Kauffmann et al. [47] predicted that a Milky Way-size halo should host over 100 subhalos massive enough to support observable satellite galaxies. However, the known population of dwarf spheroidal (dSph) satellite galaxies for the Milky Way is on the order of 20 [48], although more ultra-faint satellites are still being discovered (e.g. see Ref. [49]). This discrepancy between the predicted and observed amount of substructure in CDM structure formation is often referred to as the "missing satellite problem" [50]. However, a recent work [51] suggests that it is possible to obtain a match between the observed satellite counts and the number of luminous satellites predicted by CDM. This match can be obtained including in the simulations the phenomena of feedback that keeps cold gas from forming stars, which could be caused by ionizing photons that heat up colder gas, supernovae explosions that eject colder gas outside the galaxy, stellar winds, etc. This paper attempts to demonstrates that once the above described effects are taken into account, missing satellite problem ceases to exist.

A related issue is the so-called "too big to fail" problem, which concerns the density of dark matter subhalos. In particular, it is found that the most massive DM subhalos found in N-body simulations are too massive compared to the visible matter contained in the Milky Way's dSph satellites [52]. On the contrary, if the observed dSph galaxies are hosted instead by less massive subhalos, this leaves a large number of more massive DM halos which have not yet been observed [53].

Finally, there is also a discrepancy between observed and simulated density profiles of galaxies. This is the so-called "Core-Cusp" problem (for a review, see Ref. [54]). N-body simulations indicate that the DM density should be sharply peaked near the centres of DM halos [55, 25]. In contrast, observations of the rotation curves of a large number of galaxies (in particular low surface brightness and dSph galaxies) suggests the presence of a core - a flat dark matter density profile near the centre [56, 57]. While these results are still under debate (for example, Ref. [58] find rotation curves consistent with *cuspy* density profiles),

they may indicate a discrepancy between the process of structure formation in the Universe and that implied by ΛCDM.

A number of possible solutions to these issues have been suggested. Baryonic effects such as dynamical friction and stellar and supernova feedback (see for example Refs. [59, 60, 61]) can lead to the expulsion of DM from the centres of halos, reducing the total halo mass and leading to a flatter central density profile. Others have suggested that a *warm* dark matter model may be a better fit to the data [62, 63, 64], reducing the amount of structure on small scales, as we will discuss in Sec. 2.2. Whatever the ultimate resolution of these problems, it is clear that dark matter dominated structures such as dSph galaxies are a testing ground for an even more precise understanding of structure formation in the DM paradigm.

2.2 Properties of dark matter

Beyond its gravitational contribution to the Universe, at the moment still very little is known about the nature of particle dark matter. However, the success of the ΛCDM model and the lack of a confirmed detection so far means that some hints on properties of any potential candidate can be derived.

For example, it is now clear that DM cannot have an electromagnetic charge, otherwise it would have been seen in a range of searches that will be quickly summarised here. Namely, the possibility that CHArged Massive Particles (CHAMPs) may account for dark matter was proposed by De Rujula et al. [65]. Such particles can be free and stable or may instead bind with electrons or positrons to form heavy neutral hydrogen-like objects. However, null searches for anomalous hydrogen in sea water [66] and anomalous heavy elements [67], as well as searches for CHAMPs in cosmic ray experiments [68] indicate that CHAMPs must be present in negligible densities in the Milky Way for masses in the range $10 - 10^8$ GeV. Millicharged DM is also strongly constrained. Searches for neutrino magnetic moments in reactor experiments exclude DM with charge greater than $10^{-5}e$ for keV-scale masses and below [69]. Searches for distortions in the CMB caused by the interactions of millicharged particles limit the DM charge to be less than $10^{-7}e$ for masses of 1 eV and below [70]. It is also known that DM candidates cannot carry a bare colour charge. In this case, DM particles would interact strongly with particles of the SM, causing problems to galaxy formation [71] and the formation

of the CMB [72] due to scattering off baryons. We are left with the conclusion that DM particles must carry no (or almost no) conventional electromagnetic or strong charge. This rules out most of SM particles as accounting for DM, hinting strongly that these particles must derive from theories of physics beyond the Standard Model.

Any particle candidate must also be stable or long-lived otherwise it cannot play the role of dark matter today. For models in which DM is not indefinitely stable, this allows us to place stringent limits on the lifetime of the DM particle, simply speaking its lifetime must be larger than the age of universe [73, 74]. Moreover the self-interaction as well as the ordinary matter interaction cross sections must be very weak. A good DM candidate must furthermore be produced with sufficient abundance to match the currently observed value of the cold dark matter energy density, $\Omega_{CDM}h^2 = 0.1197 \pm 0.0022$, as shown in Table 2.1. If it is produced with a smaller abundance, the candidate cannot account for the entirety of the Universe's dark matter. It could still contribute, but only along with other candidates, as in Ref. [75]. If, on the other hand, it is produced with too abundantly, it could exceed the DM density constraint set by recent observations.

Finally, it must be compatible with primordial nucleosynthesis. This last point deserve a better explanation and will be discussed in more detail in the next section.

2.2.1 Big Bang Nucleosynthesis and charged dark matter particles

Primordial nucleosynthesis (or Big Bang Nucleosynthesis, BBN) describes the production of light nuclei in the first few minutes after the Big Bang. By solving a set of coupled Boltzmann equations describing the nuclear reactions of protons, neutrons and light nuclei, we can obtain the primordial abundances of these light nuclei and compare it with the found values [76]. Significantly, these abundances depend strongly on the baryon to photon ratio η and therefore the total baryon density. Fits to data lead to the result $\Omega_b h^2 = 0.017 - 0.024$ [77], independent of the value obtained from CMB measurements (Table 2.1). Thus, the baryonic matter can make up only a fraction of the total matter density of the Universe. This provides further evidence that particle dark matter must consist of some non-baryonic particle.

The results of BBN are also very sensitive to light new species, which can alter the number of relativistic degrees of freedom in the early Universe and therefore affect the expansion rate. These include, for example, gravitinos [78] and right-handed neutrinos [79]. BBN therefore provides strong constraints on models in which these particles play the role of DM. In addition, the decay of dark matter particles into electromagnetic or hadronic showers during nucleosynthesis can drastically change the primordial abundances of the light elements. BBN can therefore be used to constrain models in which dark matter decays promptly (or in which dark matter is produced by the decays of heavier particles) [80].

2.3 Particle dark matter candidates

As it has been explained in Sec. 2.2, valid DM candidates need to satisfy several conditions and constraints. In this section, possible candidates that can be derived from existing physics models will be analysed. There are in fact a number of possible extensions of the SM that could provide dark matter candidates. These models differ from each other since they predict different masses and interactions of DM candidates with SM particles. Exploiting these differences and using the results coming from various direct and indirect searches it is possible to put constraints on the different models. Two main categories of DM candidates can be identified, namely so-called *hot* (relativistic), *warm* and *cold* (non-relativistic) dark matter candidates. As already anticipated, in order to reproduce the formation of galactic structure in the early universe, it is known that the majority of the DM in the universe cannot be hot. This means that DM must have been travelling non-relativistically when it was produced in the early universe. The typical speed of DM particles in the early universe defines the so-called *free-streaming length*. Below this length-scale, density perturbations are suppressed due to Landau damping [81]. For non-relativistic species produced by thermal freeze-out, this free-streaming length scales as $M_\chi^{-1/2}$ for thermal relics of mass M_χ [82]. For particle candidates which are too light, and which therefore travel too quickly after decoupling, small scale structures cannot form and cannot match the distribution of structures we see today. Light particles which are produced via a mechanism other than thermal freeze-out may still account for DM (see e.g. Ref. [83]), though this alternative mechanism must still ensure that it is not produced with relativistic speeds. In practice, constraints on the free-streaming length imply that thermally-produced DM cannot have a mass greater than around 1 keV [84]. It is typically assumed that dark matter is significantly heavier than this, decoupling ultra-

non-relativistically in the early Universe, rendering it cold. Warm dark matter candidates with keV-scale masses have been suggested to explain the subhalo structures at the scale of dSph galaxies, as discussed in Sec. 2.1.4. However, hot dark matter, which decouples at relativistic speeds, is strongly-constrained and cannot make up more than around 1% of the total dark matter component [85, 86].

In this section the most motivated candidates that are also consistent with observations will be illustrated, namely so-called Weakly Interacting Massive Particles, neutrinos and axions. Some further examples include WIMPless dark matter [87], primordial black holes [88], mirror dark matter [89] and little Higgs dark matter [90], as well as minimal approaches to DM [91], but they will not be discussed in detail in this thesis.

2.3.1 Weakly Interacting Massive Particles

Perhaps the most likely dark matter candidates, and the ones that has searched most by experimentalists, are the stable, weakly interacting massive particles, χ, that decoupled when they were non-relativistic, and thus constitute cold dark matter, with practically no radiation pressure. In fact, WIMP candidates can be found in a wide range of models of particle physics beyond the standard model. Such a WIMP candidate may be provided by the Lightest Supersymmetric Particle (LSP) in supersymmetric theories [92]. In supersymmetry (SUSY), each of the known SM particles has a supersymmetric partner (or "spartner"), with bosons having fermionic partners and vice versa. The symmetry must be broken, otherwise SM particles and their partners would have the same mass. This additional symmetry is often invoked to help alleviate the hierarchy problem, i.e. understanding why the mass of the Higgs boson is so smaller than the Planck mass [93]. In models which possess R-parity, which may be required to protect the proton from decay, particles carry R-parity 1 while supersymmetric particles ("sparticles") carry R-parity -1. The conservation of this number means that the lightest sparticle cannot decay into SM particles and it is therefore stable, making it a promising DM candidate.

These particles would have been produced like other particles in thermal equilibrium in the Big Bang, and their abundance today would be determined by their annihilation cross-section to SM quark and lepton pairs, e.g. $\chi\overline{\chi} \to q\bar{q}$. The

standard scenario for the production of dark matter is referred to as thermal freeze-out [32]. In this scenario, DM particles remain in kinetic and chemical equilibrium with SM particles in the very early Universe through scattering and annihilation processes. Their number density n follows a Maxwell-Boltzmann distribution

$$n \propto \exp(-M_\chi/T)\,, \tag{2.2}$$

for a particle mass M_χ and temperature T. As the Universe expands, however, the particles become diluted, reducing the interaction rate until eventually the DM particles become decoupled from the SM particles and are "frozen-out". They are then left with the abundance they had when they decoupled, which is further diluted by the expansion of the Universe to become the abundance we see today. The exact relic abundance depends on $\langle\sigma_{\rm ann}v\rangle$, the average annihilation cross section of the DM particles weighted by the DM speed. If this is small, DM will decouple early when the temperature of the Universe is still high, leading to a large relic abundance. If the annihilation cross section is large, DM will remain in equilibrium for longer, even as the particles become more and more diluted. The DM then freezes out later, with a lower temperature and lower relic abundance. The resulting relic abundance for GeV-scale DM is given approximately by [32]:

$$\Omega_{CDM}h^2 \approx \frac{3\times10^{-27}\ \text{cm}^3\ \text{s}^{-1}}{\langle\sigma_{\rm ann}v\rangle}\,. \tag{2.3}$$

This leads to a canonical value of around $\langle\sigma_{\rm ann}v\rangle \approx 3\times10^{-26}$ cm^3 s^{-1} for the annihilation cross section, which corresponds to the measured abundance of CDM. This coincides well with the value expected for particles with SM weak-scale interactions, called for this reason WIMPs, leading some to refer to this argument as the *WIMP miracle*. A Big Bang relic population of weakly interacting particles, with mass in the 10 GeV-TeV range, would naturally have the correct present density and they could also helps in solving the hierarchy problem. In reality, the full differential equations describing the DM number density must be solved [94], accounting for co-annihilations [95], which may boost the total cross section. However, the simplicity of this scenario makes such thermal relics an attractive candidate for DM.

Depending on the parameters of the supersymmetric theory, there are many possibilities for which sparticles can be the LSP. One popular and well-studied possibility is the lightest neutralino χ [96], which is a linear combination of the wino, the bino and the CP-even higgsino, the neutral supersymmetric partners of the W, the B, the U(1) gauge field corresponding to weak hypercharge, and

the Higgs boson, respectively. The properties of the lightest neutralino can vary dramatically depending on the mixing between these different components and the underlying supersymmetric parameters [97]. According to the Minimal Supersymmetric Standard Model (MSSM), a theory with ∼100 free parameters, the neutralino is a stable Majorana particle, with no electric or color charge, with a mass in the range GeV$< M_\chi <$TeV. In some more constrained theories, with a smaller number of parameters, it is also possible to make more precise quantitative predictions for the properties of the neutralino. Two examples are the cMSSM (constrained MSSM) and the pMSSM (phenomenological MSSM). The first model, the simplest one, with only 5 free parameters, has become disfavoured after the recent experimental evidence at the LHC. The pMSSM model is instead based on some experimentally motivated assumptions (as the R-parity conservation and the absence of new CP violations) and it allows to reduce the number of free parameters number down to 19. In other cases, the LSP may be the sneutrino [98], a partner of the standard model neutrino. Another alternative is the gravitino, which provides a good cold DM candidate for masses above around 100 keV [99].

WIMPs also arise in theories of universal extra dimensions, in which the additional dimensions are compactified, leading to a tower of excited states of the standard model particles [100]. These "Kaluza-Klein" (KK) particles also possess a KK-parity, which means that the lightest KK particle (LKP) is stable [101]. One possibility for the LKP is the first excitation of the B weak hypercharge boson, $B^{(1)}$. In this case, the WIMP would be a spin-1 particle with a mass of around 1 TeV (in order to be produced thermally with the correct relic abundance) [102]. It has also been shown that the first KK excitations of the photon and neutrino are viable DM candidates if they also have masses at the TeV scale [103]. In contrast to the LSP, the LKP is described by a relatively small parameter space and may be more easily constrained by upcoming experiments [104].

WIMPs can in principle be detected in different ways, as it will be explained in Sec. 2.4.

2.3.2 Sterile neutrinos

In the SM there are three species of neutrinos, namely ν_e, ν_μ and ν_τ, with a not-vanishing but small mass. Measurements done by Planck indicate an upper bound

on their total mass of $\sim$0.72 eV (0.17 eV) using Planck TT+LowP (Planck TT, TE, EE+lowP+BAO) data [34]. In addition to photons, positrons and electrons, ν_e, ν_μ and ν_τ neutrinos would have been produced in the early universe, all with comparable densities. These relic neutrinos are possible dark matter candidates and have the great advantage that they are known to exist. However, the problem with SM neutrinos is that they are hot dark matter. They were relativistic when they decoupled and relativistic when the large-scale structures in the universe were forming. As a consequence they will stream rapidly under gravity and tend to iron out any primordial density fluctuations, which are needed to seed such structures. The conclusion is that neutrinos may constitute some of the dark matter, but cannot account for a large fraction.

However, a possible expansion of the SM which allows to describe in a natural way the smallness of the neutrino mass, through the so-called See-Saw mechanism, consists in adding one or three generations of sterile massive neutrinos. A sterile neutrino could be either an additional flavour of neutrino that does not couple to any other known leptons, except possibly indirectly by oscillating into another flavour, or a right-handed neutrino (or left-handed anti-neutrino) that is invisible due to its failure to couple with leptons like its left-handed counterpart. Sterile neutrinos would also be a natural candidate for warm dark matter. They would be detectable through their tiny mixing with active neutrinos. No theory can predict their exact mass scale but high enough masses such that they are not-relativistic are not excluded by Planck measurements, that refer only to relativistic species. Moreover, astrophysical observations [105, 106] currently limit the mass of warm sterile neutrinos [107], by looking at the level of small-scale structure formation observed in the universe, to be larger than 10 keV. If sterile neutrinos are near this lower mass bound, there must be at least one other form of dark matter; however, sufficiently massive sterile neutrinos may explain the modern dark matter density without violating small-scale structure observations.

2.3.3 Axions

One of the most fundamental principle in physics is that of symmetry. A symmetry operation leaves (at least conceptually) a system invariant. In particle physics, the discrete symmetries with a significant relevance are

- *Charge conjugation, C*: It changes the sign of all internal quantum charges, like the sign of the electric charge of a particle.

- *Parity, P*: It is a reflection operator that changes the sign of all three spatial coordinates. For example, under this operation the momentum, $\overrightarrow{p}$, of a particle changes its sign, $-\overrightarrow{p}$.

- *Time reversal, T*: It reverses the time coordinate (t $\rightarrow$ -t).

Each of these three discrete symmetries and also partial combinations, like CP, is broken in weak interactions. According to quantum chromodynamics (QCD) there could be a violation of CP symmetry also in strong interactions. However, CP seems to be a valid symmetry for QCD according to many experimental results, among all the search for an anomalous neutron electric dipole moment. This problem is often referred to as the *strong CP problem*.

Axions are hypothetical light neutral pseudoscalar particles originally introduced by Peccei and Quinn [108] to solve the strong CP problem. The problem can in fact be solved by invoking a new spontaneously broken symmetry, leading in turn to the prediction of the axion, which (if it exists) would certainly have been produced in great abundance as a sort of condensate in the early universe [109]. Being produced out of equilibrium, with the so-called Misalignment Mechanism, axions could constitute "cold" dark matter, and, for masses in the range $10^{-5}-10^{-3}$ eV, can account for the observed cosmological dark matter [110]. Masses of the order of μeV are excluded by the constraint on the relic density from the ΛCDM cosmological paradigm. Masses larger than 1 eV are instead disfavoured by other observations.

Axions might in principle be detected using a microwave cavity in a strong magnetic field; they would be converted to microwave photons in the field. Many experiments are currently being designed and operated to explore the meV mass range. Currently underway experiments are ADMX [111] and CAST [112], aiming to detect the conversion of axions to photons in a magnetic field.
Also of interest are axion-like particles, which emerge naturally in string theory and are expected to span many orders of magnitude in mass and coupling strength [113].

2.4 Detection of dark matter

As it has been explained in the previous sections, many theories beyond the SM provides DM candidates that can interact, even if very weakly, with SM particles. This allows these models to be tested. Of course, it could still be possible that DM interacts only gravitationally. In this section, the different strategies that can be pursued to probe the various models of particle DM will be listed and analysed.

A diagrammatic way to summarize interactions between DM and SM particles is represented in Fig. 2.4. Production, annihilation and scattering processes between DM and SM particles can be used as a window to detect particle DM. Each of these processes leads to a distinct detection strategy, referred to as collider, indirect and direction detection.

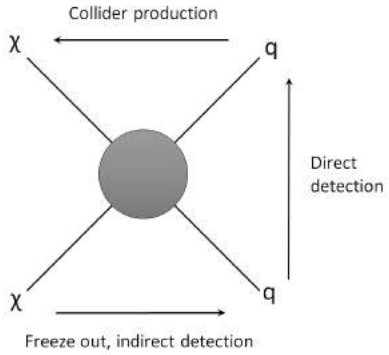

Fig. 2.4.: Schematic diagram of different strategies to detect a dark matter particle χ. From righ to left: production at colliders; from bottom to top: direct detection via elastic scattering on nuclei; from left to right: indirect detection through DM annihilation and identification of decay products.

2.4.1 Collider production

Searches for DM at particle colliders such as the LHC rely on the process depicted from right to left in Fig. 2.4, namely the fact that SM particles interact to produce dark matter particles. However, the weak interactions of the DM means that once produced, it will escape the detector around the interaction point without being observed. Thus, collider searches for DM must look for signatures of it different from directly observing it.

One approach is to look for signatures which are predicted by a particular theory. For example, looking for evidence of KK states [114, 115], or searching for particle

signatures from decay chains which are expected from SUSY [116, 117]. While this allows constraints to be placed on specific models, the range of models may be large, meaning that each must be constrained separately.

A different approach is to look for deviations from SM expectations and use these to put limits on the operators of a generic Effective Field Theory (EFT), see e.g. Ref. [118]. One possibility is to look for the pair production of DM particles, with initial state radiation of a SM particle, which may be observed as a single jet or a single boson or lepton, depending on which particle was radiated, accompanied by missing energy, which is carried away by the DM. By combining all possible particles radiated at the initial state, one can place limits on the effective operators which describe SM-DM interactions [119]. Using this kind of approach one can exclude DM with a standard thermal freeze-out cross section for masses $M_\chi < 15\,(75)$ GeV in the case of vector (axial-vector) couplings to quarks [120].

A great advantage of this second approach is that it is possible to translate these limits into bounds on signals at direct and indirect experiments, giving the possibility for collider results to be incorporated with other experimental searches in a complementary fashion [121]. However, attention must be put in applying the EFT approach at the LHC in a naive way as well as in translating this to other search channels [122, 123].

So far, despite the numerous searches that are currently pursued at the LHC, there has been no evidence observed [124]. The non-observation of supersymmetric particles at the LHC has also begun to place some stringent constraints on SUSY models, and the simplest DM candidates are now in tension with experimental limits [125], though they are not yet excluded [126]. The second run of LHC (2015-2018) and future upgrades (from 2021 on) should be able to explore more of the possible dark matter parameter space.

2.4.2 Indirect detection

If DM can annihilate into SM particles, as described from left to right in Fig. 2.4, then it may be detected indirectly, by searching for these excess annihilation products and subsequent related decay products. The Fermi-LAT collaboration have published limits on searches for unexpected spectral lines and new contributions

to the diffuse background of gamma rays [127, 128, 129, 130]. Cosmic ray experiments such as PAMELA [131] have aimed to measure the $p^{\pm}$ and $e^{\pm}$ abundances in cosmic rays. Few years ago, the AMS experiment [132] has confirmed a rise in the cosmic ray positron fraction at energies above 10 GeV, which was previously observed by PAMELA [133] and Fermi-LAT [134]. This feature has been interpreted as tentative evidence for dark matter annihilations (see e.g. Ref. [135, 136]). Recently, the DArk Matter Particle Explorer (DAMPE) experiment detected, during its first 530 days of scientific observation, a tantalizing hint [137] of a peak at about 1.4 TeV in the Cosmic Ray Electrons plus positrons (CREs) spectrum, see Fig. 2.5, that could be due to dark matter. Moreover, the direct detection of a spectral break at E∼0.9 TeV confirms the evidence found by HESS, clarifying the behaviour of the CRE spectrum at energies above 1 TeV.

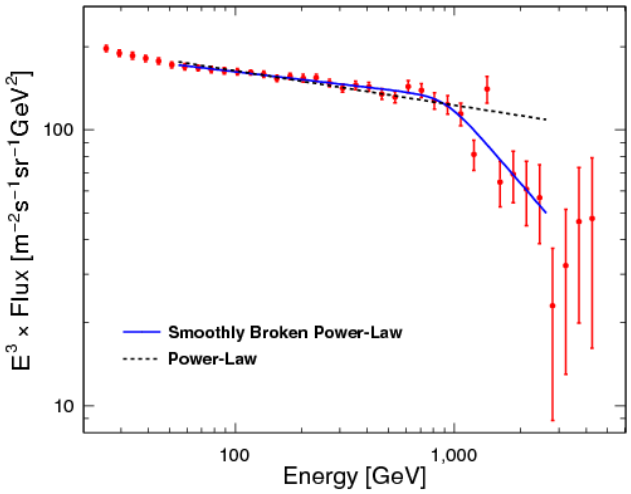

Fig. 2.5.: Comparison of two spectral models for the DAMPE Cosmic Ray Electrons plus positrons spectrum. The dashed and solid line show the best fit results of the single power-law and smoothly broken power-law models, respectively. Figure from Ref. [137].

Due to the presence of astrophysical magnets, the trajectory of charged cosmic rays is deflected, making it impossible to resolve individual sources [138]. On the other hand, photons are not deflected, allowing specific locations to be targeted. Since the signal rate along the line of sight is proportional to the DM annihilation rate, any potential signal should scale as the square of the dark matter density. Thus, in order to maximize the signal rate one has to point into areas where the DM density is expected to be high [139], like for example dSph galaxies, which are dark matter dominated objects. The Fermi-LAT telescope [140] has so far found no significant gamma ray excess after a survey of about 25 Milky Way

satellite galaxies. Depending on the WIMP mass and annihilation channel, upper limits coming from these searches on the annihilation cross section are getting close to the thermal freeze-out value of $\langle \sigma_{\rm ann} v \rangle \approx 3 \times 10^{-26}$ cm^3 s^{-1}. In 2012 the presence of a bump in the gamma ray spectrum of Fermi-LAT data around 130 GeV [141] has been suggested by Weniger. However, subsequent analysis has found that this feature may be a systematic effect in the detector [142] and that it is difficult to reconcile it with conventional models for dark matter [143, 144].

The sensitivity of gamma ray searches can be extended up to TeV-scale masses thanks to ground-based Imaging Atmospheric Cherenkov Telescopes (IACTs). These experiments rely on the Cherenkov radiation produced from charged particles produced when very high energy gamma rays hit the atmosphere. The current generation of IACTs experiments, like HESS [145], MAGIC [146] and VERITAS [147], are used to conduct searches for line-like gamma ray spectra as well as searches for signals from dwarf galaxies. However, these limits are typically around two orders of magnitude above the thermal cross section. The Cherenkov Telescope Array (CTA) will be the next generation ground-based observatory for gamma-ray astronomy at very-high energies. With more than 100 telescopes located in the northern and southern hemispheres, CTA will be the world's largest and most sensitive high-energy gamma-ray observatory. It may be able to probe down to this thermal cross section for high WIMP masses [148].

DM particles may scatter with nuclei of the Sun and the Earth, losing energy and eventually becoming captured. This would result in a local over-density of DM, making the Sun and the Earth potentially rich source of DM annihilation processes. The only annihilation products which can escape are neutrinos. They can then be detected at neutrino telescopes such as ANTARES [149] and IceCube [150]. Because the neutrino flux depends on the scattering rate of DM with nuclei, such signals can probe similar parameter spaces to direct detection experiments. In almost 3 years of data taking the IceCube Collaboration [151] found no significant excess of neutrinos over the background, measuring neutrinos produced in atmospheric air showers from cosmic ray interactions. This results in the most stringent limit on a neutrino signal from dark matter with mass between 10 GeV and 100 GeV, with a limit of $\langle \sigma v \rangle = 1.18 \times 10^{-23}$ cm^3 s^{-1} for 100 GeV DM particles self-annihilating via $\tau^+\tau^-$ to neutrinos.

2.4.3 Direct detection

Processes described from bottom to top in the diagram in Fig. 2.4 lead to the possibility of scattering between DM and SM particles. The principle of direct detection is to look for nuclear recoils due to this scattering in a dedicated detector [152, 153]. WIMPs with GeV-scale masses and speeds $v \sim 10^{-3}\, c$ are expected to produce keV-scale nuclear recoils, which are difficult to detect. In addition, due to the expected low cross section for such interactions, the predicted rate is very small. Thus, this kind of DM detection is very challenging and implies the usage of large (ton-scale) detectors and also sophisticated methods for discriminating signal from background. This method of detection of dark matter is the one exploited in this thesis and it will be explained in more details in Chap. 3.

2.5 Alternatives to dark matter

In this chapter, I have discussed a wide range of evidences that suggest the existence of DM, as well as some unresolved problems with the ΛCDM paradigm. In this last section, the possibility that these observations can be explained not by invoking a new matter species but by a modified law of gravity is considered. Milgrom [154, 155, 156] proposed the idea of Modified Newtonian Dynamics (MOND). According to this theory, for small accelerations, namely smaller than some characteristic value a_0, the usual Newtonian dynamics no longer holds. More in detail, the acceleration $\mathbf{a}$ of a particle in a gravitational field Φ_N is governed by

$$\tilde{f}(|\mathbf{a}|/a_0)\mathbf{a} = -\nabla\Phi_N\,. \tag{2.4}$$

The interpolation function $\tilde{f}$ tends to unity for large values (the Newtonian limit) but tends to $|\mathbf{a}|/a_0$ for values $|\mathbf{a}| \ll a_0$ (the MOND limit). At large distances from the centres of galaxies, the acceleration will drop below a_0 and Eq. 2.4 reduces to $a = v_c^2(r)/r = \sqrt{a_0 \nabla\Phi_N}$, where v_c is the circular velocity. Assuming that there is no DM content, the mass M enclosed within a radius r becomes constant and one obtains $|\nabla\Phi_N| \approx GM/r^2$. Combining these results, it is possible to see that

$$v_c^4(r) \approx GMa_o\,, \tag{2.5}$$

which is independent of radius. The key point of MOND is that a flat rotation curve is obtained without the need to invoke DM. Moreover, Eq. 2.5 is the baryonic

Tully-Fisher law, which relates the baryonic mass of a galaxy with the asymptotic rotation velocity, and which does not have an obvious origin in DM-based models [157]. The value for the characteristic acceleration obtained from fits to over 100 galaxies is $a_0 = 1.2 \times 10^{-10}$ m s^{-2} [21], which also reproduces the measured proportionality constant in the Tully-Fisher law [158].

The phenomenological approach of MOND can be written into a fully covariant theory of modified gravity, which is known as tensor-vector-scalar (TeVeS) gravity [159]. This theory contains new dynamical vector and scalar degrees of freedom and contains a free function, analogous to the interpolation function $\tilde{f}$. The formalism for both lensing [160] and cosmological perturbations [161] have both been studied in TeVeS, with perturbations in the new scalar and vector fields allowing structure to form without the need for DM.

This kind of models has been severely ruled out [162] after the joint detection of gravitational waves (GW) observed by the LIGO and VIRGO interferometers [163] and the optical counterpart [164] from the coalescence of binary neutron stars. This simultaneous detection of GW and electromagnetic signals rules out a class of modified gravity theories known as "Dark matter emulators", including TeVeS.

Phenomenologically, MOND is able to explain the rotation curves of galaxies surprisingly well. More recently, Verlinde [165] has given an original but controversial derivation of the MOND formula. He has proposed that the dark matter phenomena can be attributed to an elastic response of the dark energy medium. One common problem of this approach is the difficulty to obtain a "metric-covariant" theory. In fact, such theories are usually formulated in the weak-field regime, whereas it is known that gravity requires a metric-covariant description given by GR, at least at solar system scales. In a recent work [166], some authors proposed that the additional component of the acceleration, commonly attributed to DM, can be explained as a radial pressure generated by the reaction of the dark energy fluid to the presence of baryonic matter. With this approach they are able to correctly reproduce the leading features of a MOND-like potential at galactic scales obtaining a covariant theory.

To summarize, MOND can generally give good fits to galaxy rotation curves [21, 167, 168] and can do so with fewer free parameters than DM halo models. Moreover, MOND can also reduce the tension between the visible mass in clusters

and the dynamical or lensing masses [169, 170], but typically only to within a factor two, still requiring some collisionless matter to fit the data [171]. However, the biggest problem is that relativistic extensions of MOND still do not reproduce the features of large scale structure, CMB and more importantly the Bullet Cluster behaviour with the same success as ΛCDM [172, 173].

3 Direct detection of dark matter

Contents

3.1 Direct detection formalism 36
3.2 Distribution of DM in our galaxy 50
3.3 Dark matter speed distribution 53
3.4 Final SI WIMP differential rate for different nuclei 63
3.5 DM differential event rate uncertainties 65
3.6 Direct detection experiments current limits and anomalies . . 73
3.7 Conclusions 83

If a terrestrial dark matter detector is exposed to a DM flux, the dark matter could scatter off the nucleus of the detector material, as a result of which the detector nucleus will suffer a recoil. The idea that particle DM may be observed in terrestrial detectors was first proposed by Goodman and Witten in 1985 [152] and by Drukier, Freese and Spergel in 1986 [153]. If DM can interact with particles of the SM, the flux and the interaction cross section of DM from the halo of the Milky Way may be large enough to cause measurable scattering from nuclei. If the subsequent recoils can be detected and their energy spectrum measured, it should be possible to infer some properties of the DM particles. In the simplest scenario, the scattering is considered to be elastic, and since the WIMPs kinetic energy in the Earth rest frame is mostly determined by the solar system velocity, the recoil energy of the nucleus will be very low. A dark matter direct detection experiment looks for the signature of this low recoil energy ($\sim$keV) of the nucleus due to the possible impact of dark matter.

However, the expected event rate for keV-scale recoils at such a detector would be of the order of 10^{-5} events per kg of detector material per day per keV recoil energy [174]. With such a low event rate, it is mandatory to reduce the background content as much as possible. Such detectors therefore should be installed in a very low background environment in order to detect this rare and very low recoil energy signal. In addition, detectors should be as large as

possible and sensitive to a wide range of recoil energies, in order to maximise the total number of events observed. Thus, specialised detectors are required to shield the active detector material from backgrounds and to discriminate between these backgrounds and signal events. The energy lost by the recoiling nucleus is detected by the effect it may produce in the detector. These can be scintillation light, ionization, bolometric current, phonon excitation, etc.

There exist at present a wide range of detectors using a variety of different sophisticated techniques for detecting such a weak signal against unavoidable backgrounds, each probing a slightly different range of DM parameter space.
The calculations of direct detection rates involve broadly two aspects. One involves both particle physics and nuclear physics, which are required to calculate the elastic scattering cross-sections, and the other is the astrophysics aspect that deals with inputs like galactic and solar dynamics results, the local dark matter density, the dark matter velocity distribution in galactic halo, etc. Knowledge of dark matter density is an essential ingredient in the computation of direct detection rates.

There remain a number of uncertainties in the direct detection of dark matter. These come from a variety of sources and can be approximately partitioned into experimental, nuclear, particle and astrophysical uncertainties. Understanding these uncertainties is important in order to interpreter the results of direct detection experiments in a proper way. I also helps in understanding whether a coherent picture can emerge from a number of different experimental results.

In this chapter, I will review the formalism for direct detection. I will then briefly discuss the most used experimental techniques to achieve the required sensitivity for DM searches. Eventually I will summarise current experimental results and constraints. A particular focus will be put on the role of the nuclear form factor and directional dark matter detection, that is a technique that could help to distinguish if a hypothetical signal seen by a future detector is a genuine signal or if it is due to other backgrounds which modulate with a year periodicity.

3.1 Direct detection formalism

In this section I will explain how to obtain the rate of nuclear recoils per unit detector mass due to elastic, non-relativistic scattering from a fermionic weakly

interacting massive particle. Dark matter is typically assumed to be spin-1/2, though the analysis here can be generalised to particles of arbitrary spin [175]. The differential event rate can be written straightforwardly as

$$\frac{\mathrm{d}R}{\mathrm{d}E_R} = N_T \, \Phi_\chi \frac{\mathrm{d}\sigma}{\mathrm{d}E_R} \,, \tag{3.1}$$

for recoils of energy E_R, N_T target particles, a DM flux Φ_χ and a differential scattering cross section $\mathrm{d}\sigma/\mathrm{d}E_R$. Per unit detector mass, the number of target particles is simply $N_T = 1/m_N$, for nuclei of mass m_N. The DM flux for particles with speed in the range $v \to v + \mathrm{d}v$ in the laboratory frame is $\Phi_\chi = n_\chi v f_1(v) \, \mathrm{d}v$. Here, n_χ is the number density of dark matter particles χ and $f_1(v)$ is the speed distribution for the dark matter. The orbit of the Earth means that its velocity is time-varying, producing an annual modulation in $f_1(v)$ and therefore in the direct detection event rate [176]. However, this modulation is expected to be a percent-level effect and we consider here only the time averaged distribution.

Denoting the local dark matter density by ρ_0, we can obtain the number density from the mass density dividing by the DM particle mass M_χ as $n_\chi = \rho_0/M_\chi$. By integrating over all DM speeds, we therefore obtain

$$\frac{\mathrm{d}R}{\mathrm{d}E_R} = \frac{\rho_0}{m_N M_\chi} \int_{v_\mathrm{min}}^{\infty} v f_1(v) \frac{\mathrm{d}\sigma}{\mathrm{d}E_R} \, \mathrm{d}v \,, \tag{3.2}$$

where v_min is the minimum velocity required to scatter a nucleus with recoil energy E_R

$$v_\mathrm{min} = \sqrt{\frac{m_N E_R}{2\mu_{\chi N}^2}} \,. \tag{3.3}$$

Here, we have written the reduced mass of the WIMP-nucleus system as $\mu_{\chi N} = M_\chi m_N/(M_\chi + m_N)$.

The differential scattering cross section per solid angle in the zero-momentum frame (ZMF), known also as center-of-momentum frame, Ω^*, is given by

$$\frac{\mathrm{d}\sigma}{\mathrm{d}\Omega^*} = \frac{1}{64\pi^2 s} \frac{p_f^*}{p_i^*} |\mathcal{M}|^2 \,, \tag{3.4}$$

where $\mathcal{M}$ is the scattering amplitude obtained from the Lagrangian. For elastic scattering, the final and initial momenta in the ZMF are equal $p_f^* = p_i^*$. The centre-of-mass energy squared, s, can be written as $s \approx (M_\chi + m_N)^2$, where we

have used the non-relativistic approximation. The recoil energy can be written in terms of the ZMF scattering angle θ^* as [174]

$$E_R = \frac{\mu_{\chi N}^2 v^2}{m_N}(1 - \cos\theta^*)\,. \tag{3.5}$$

Noting that $\mathrm{d}\Omega^* = \mathrm{d}\cos\theta^*\mathrm{d}\phi$, we can write

$$\frac{\mathrm{d}E_R}{\mathrm{d}\Omega^*} = \frac{\mu_{\chi N}^2 v^2}{2\pi m_N}\,, \tag{3.6}$$

and therefore

$$\frac{\mathrm{d}\sigma}{\mathrm{d}E_R} = \frac{1}{32\pi m_N M_\chi^2 v^2}|\mathcal{M}|^2\,. \tag{3.7}$$

The matrix element $\mathcal{M}$ is obtained from interaction terms in the Lagrangian between the DM particle and quarks. This will depend on the particular DM model under consideration and the full form of these interaction terms is not known. It is typically assumed that these terms can be adequately described by a contact interaction, meaning that the particles mediating the interaction are much more massive than the momentum transferred [177]. The momentum transfer in direct detection experiments is typically less than ~ 200 MeV, suggesting that this assumption is somehow reasonable.

Because the WIMPs have speeds of order $10^{-3}c$, the scattering occurs in the non-relativistic limit, allowing some important simplifications. In this limit, the axial-vector interaction simply couples the spins of the WIMP and quark. The scalar interaction induces a coupling of the WIMP to the number of nucleons in the nucleus, with the vector[1] and tensor interactions assuming the same form as the scalar in the non-relativistic limit [92]. All other interactions are typically suppressed by powers of v/c and so will be subdominant. Generically, then, the cross section is written in terms of spin-independent (SI) and spin-dependent (SD) interactions [152] as

$$\frac{\mathrm{d}\sigma_{\mathrm{TOT}}}{\mathrm{d}E_R} = \frac{\mathrm{d}\sigma_{SI}}{\mathrm{d}E_R} + \frac{\mathrm{d}\sigma_{SD}}{\mathrm{d}E_R}\,. \tag{3.8}$$

The theoretical calculation for the elastic scattering cross-section of a cold dark matter particle off a target nucleus requires three steps.

[1] For the case of a Majorana fermion, the vector current vanishes and we do not need to consider it.

1. The interaction at the fundamental level is guided by the coupling of the WIMP with quarks (and gluons) inside the nucleon. This coupling is dependent on the particle candidate of CDM for a chosen particle physics model and hence it is model dependent. The interaction at the fundamental level is guided by the coupling of the WIMP with quarks (and gluons) inside the nucleon.

2. Since it is the nucleus whose recoil energy or momentum transfer is important (WIMP-nucleus scattering), the second step is to translate this interaction from fundamental particle level to nucleonic level using proper hadronic matrix elements. Also needed is the distribution of quarks in nucleons.

3. The final step is to take into account the proper nuclear matrix elements that are obtained by evaluating the matrix elements of nucleon operator in the nuclear state.

As already said, the WIMP-nucleus scattering cross section derived following this prescription is constituted by two parts, the SI and SD one. In the next section I will explain in more detail each of them.

3.1.1 Spin-independent cross section

Spin-independent interactions are generated predominantly by scalar terms in a four-Fermi effective Lagrangian of the type

$$\mathcal{L} \supset \alpha_S^q \bar{\chi}\chi\bar{q}q\,, \tag{3.9}$$

which describes interactions with a quark species q with coupling α_S^q and χ represents the particle dark matter field. The operator $\bar{q}q$ is simply the quark number operator, which couples to the quark density. However, we should recall that the quarks are in nucleon bound states. We consider first the contributions from neutrons $|n\rangle$, so we should evaluate $\langle n|\bar{q}q|n\rangle$, adding coherently the contributions from both valence and sea quarks. These matrix elements are obtained from chiral perturbation theory [178] or Lattice QCD [179] and can be parametrised in terms of their contribution to the nucleon mass in the form:

$$m_n f_{Tq}^n \equiv \langle n|m_q\bar{q}q|n\rangle\,. \tag{3.10}$$

Adding the contributions of the light quarks q, as well as the heavy quarks Q and gluons g (which contribute through the chiral anomaly [180]), we can obtain the following expression

$$\langle n|\sum_{q,Q,g}\bar{q}q|n\rangle = \left(\sum_{q=u,d,s}\frac{m_n}{m_q}f_{Tq}^n\alpha_S^q + \frac{2}{27}f_{TQ}^n\sum_{Q=c,b,t}\frac{m_n}{m_q}\alpha_S^Q\right) \equiv f^n\,. \tag{3.11}$$

The parameters describing the contributions of the different quarks to the nucleon mass must be determined experimentally.

We now consider the matrix elements of the nucleon operators within a nuclear state, $|\Psi_N\rangle$: $\langle\Psi_N|f^n\bar{n}n|\Psi_N\rangle$. These operators now simply count the number of nucleons in the nucleus N_n, along with a momentum-dependent form factor, $F(q)$. This depends on the momentum transfer q and corresponds to the Fourier transform of the nucleon density. This takes into account the loss of coherence for nuclear scattering due to the fact that the nucleus is not point-like. We therefore obtain:

$$\langle\Psi_N|f^n\bar{n}n|\Psi_N\rangle = \langle\Psi_N|\Psi_N\rangle f^n N_n F_n(q) = 2m_N f^n N_n F_n(q)\,, \tag{3.12}$$

where we note that we require the wave functions to be normalised to $2E \approx 2m_N$ for a nucleus of mass m_N. We now add the contribution from protons to the matrix element, assuming[2] that $F_n \approx F_p = F$

$$\langle\Psi_N|f^n\bar{n}n + f^p\bar{p}p|\Psi_N\rangle = 2m_N(f^n N_n + f^p N_p)F(q)\,, \tag{3.13}$$

where now N_n and N_p are the neutron and proton numbers of the nucleus respectively.

The corresponding matrix element for the scalar WIMP operator $\bar{\chi}\chi$ is simple in the non-relativistic limit, which gives $2M_\chi$ [92, 181]. Combining these, we obtain the scalar matrix element

$$|\mathcal{M}_S|^2 = 16M_\chi^2 m_N^2\left|f^p Z + f^n(A-Z)\right|^2|F(q)|^2\,, \tag{3.14}$$

and the SI cross section

$$\frac{\mathrm{d}\sigma_{SI}}{\mathrm{d}E_R} = \frac{m_N}{2\pi v^2}\left|f^p Z + f^n(A-Z)\right|^2|F(q)|^2\,, \tag{3.15}$$

[2] This assumption is not always valid as we will see in Sec. 3.1.4

where we have used the atomic number Z and mass number A to describe the composition of the nucleus. It is conventional to write this in terms of the WIMP-proton SI cross section, which does not depend on the particular (A, Z) of the target nucleus and thus allows easy comparison between experiments. This cross section is given by

$$\sigma_{SI}^{p} = \frac{\mu_{\chi p}^{2}}{\pi}(f^{p})^{2}\,, \tag{3.16}$$

and so the WIMP-proton differential cross section is

$$\frac{\mathrm{d}\sigma_{SI}}{\mathrm{d}E_R} = \frac{m_N \sigma_{\mathrm{SI}}^{\mathrm{p}}}{2\mu_{\chi p}^{2} v^{2}} \left|Z + (f^{n}/f^{p})(A-Z)\right|^{2} \left|F(E_R)\right|^{2}\,. \tag{3.17}$$

For equal coupling between WIMP-proton and WIMP-neutron, which means $f^{p} = f^{n}$, the differential cross section becomes

$$\frac{\mathrm{d}\sigma_{SI}}{\mathrm{d}E_R} = \frac{m_N \sigma_{\mathrm{SI}}^{\mathrm{p}}}{2\mu_{\chi p}^{2} v^{2}} A^{2} \left|F(E_R)\right|^{2}\,, \tag{3.18}$$

in which we recognize the usual A^2 proportionality. This is telling us that for WIMP detection is preferable to use a heavy nuclei but since the form factor $|F(E_R)|^2$ decreases faster for bigger nuclei, as we will see in next sections, the optimal choice of the target nuclei depends on the WIMP mass range that we are interested in exploring. I will examine in depth this trade-off effect later.

3.1.2 Spin Dependent cross section

The spin-dependent interaction originates from axial-vector currents of the form

$$\mathcal{L} \supset \alpha_{AV}^{q}(\bar{\chi}\gamma^{\mu}\gamma_5\chi)(\bar{q}\gamma_{\mu}\gamma_5 q)\,. \tag{3.19}$$

These result in a coupling of the spins of the WIMP and nucleus. In analogy with the SI case, we can write the neutron quark matrix elements in the form [182, 183, 184]

$$\langle n|\bar{q}\gamma_{\mu}\gamma_5 q|n\rangle = 2 s_{\mu}^{n}\Delta_{q}^{n}\,, \tag{3.20}$$

where s_μ is the spin 4-vector and Δ_q parametrises the contribution of quark q to this total spin. Adding the contributions of the different quarks, we can define

$$a_{p,n} = \sum_{q=u,d,s} \frac{\alpha_{AV}^{q}}{\sqrt{2}G_F}\Delta_{q}^{p,n}\,, \tag{3.21}$$

which are the effective proton and neutron spin couplings.

Including the contribution from the WIMP axial-vector current, the nuclear matrix element can then be written as

$$\begin{aligned}&\langle\Psi_N|\sum_{q=u,d,s} a_{AV}^q(\bar{\chi}\gamma^\mu\gamma_5\chi)(\bar{q}\gamma_\mu\gamma_5 q)|\Psi_N\rangle \\ &\quad= 8\sqrt{2}G_F M_\chi\langle\Psi_N|a_p S_\mu^p + a_n S_\mu^n|\Psi_N\rangle s_\chi^\mu\left|F_{SD}(q)\right|^2 ,\end{aligned} \tag{3.22}$$

where s_χ^μ is the WIMP spin, $S^{p,n}$ are the total proton and neutron spin in the nucleus and $F_{SD}(q)$ is a form factor, as in the SI case, which is determined by the internal spin structure of the nucleus. From this, the full SD cross section is [174]

$$\frac{\mathrm{d}\sigma_{SD}}{\mathrm{d}E_R} = \frac{16m_N}{\pi v^2}G_F^2\frac{J+1}{J}\left|a_p\langle S_p\rangle + a_n\langle S_n\rangle\right|^2\left|F_{SD}(E_R)\right|^2 , \tag{3.23}$$

where J is the total nuclear spin and $\langle S_{p,n}\rangle$ are the expectation values for the proton and neutron spin in the nucleus.

Again, as in the SI case, it is convenient to rewrite this expression in terms of the proton cross section σ_{SD}^p, which is given by

$$\sigma_{SD}^p = \frac{24G_F^2}{\pi}\mu_{\chi p}^2(a_p)^2 . \tag{3.24}$$

This leads to the final expression for the SD cross section

$$\frac{\mathrm{d}\sigma_{SD}}{\mathrm{d}E_R} = \frac{2m_N\sigma_{SD}^p}{3\mu_{\chi p}^2 v^2}\frac{J+1}{J}\left|\langle S_p\rangle + (a_n/a_p)\langle S_n\rangle\right|^2\left|F_{SD}(E_R)\right|^2 . \tag{3.25}$$

3.1.3 The final event rate

It is helpful to collect these various results together to form a coherent picture of the event rate. Combining the SI and SD rates together, we can write

$$\frac{\mathrm{d}\sigma_{\mathrm{TOT}}}{\mathrm{d}E_R} = \frac{m_N}{2\mu_{\chi p}^2 v^2}\left(\sigma_{SI}^p\mathcal{C}_{SI}|F(E_R)|^2 + \sigma_{SD}^p\mathcal{C}_{SD}|F_{SD}(E_R)|^2\right) , \tag{3.26}$$

where the proton cross sections $\sigma^p_{SI,SD}$ were defined in the previous section, the form factors $F^2_{(SD)}$ will be discussed in more detail in Sec. 3.5.1 and we have defined the enhancement factors as

$$\mathcal{C}_{SI} = |Z + (f^n/f^p)(A - Z)|^2 \tag{3.27}$$

$$\mathcal{C}_{SD} = \frac{4}{3}\frac{J+1}{J}\left|\langle S_p\rangle + (a_n/a_p)\langle S_n\rangle\right|^2 . \tag{3.28}$$

We can now incorporate these into the full event rate

$$\frac{\mathrm{d}R}{\mathrm{d}E_R} = \frac{\rho_0}{2\mu^2_{\chi p} M_\chi}\left(\sigma^p_{SI}\mathcal{C}_{SI}|F(E_R)|^2 + \sigma^p_{SD}\mathcal{C}_{SD}|F_{SD}(E_R)|^2\right)\int_{v_{\min}}^{\infty}\frac{f_1(v)}{v}\,\mathrm{d}v\,. \tag{3.29}$$

Since in this thesis we are mainly interested to argon as a target material I will present only the SI event rate since ^{40}Ar is a spinless nucleus and the SD contribution vanishes.

The SI differential rate for equal coupling between WIMP and proton and WIMP and neutron is

$$\frac{\mathrm{d}R}{\mathrm{d}E_R} = \frac{\rho_0}{2\mu^2_{\chi p} M_\chi}\left(\sigma^p_{SI}A^2|F(E_R)|^2\right)\int_{v_{\min}}^{\infty}\frac{f_1(v)}{v}\,\mathrm{d}v\,, \tag{3.30}$$

where $\sigma^p_{SI} = \sigma^n_{SI} \equiv \sigma_{SI}$ will be referred to as the WIMP-nucleon cross section.

In a direct dark matter experiment, the coherence of elastic scattering is important as the target becomes insensitive to the energy deposition if the coherence is lost. One can make an estimation of the recoil energy for which such coherence will be lost for a target nucleus of mass number A. The WIMP-nucleus scattering interaction loses its coherence when the de Broglie wavelength λ (corresponding to the momentum transfer) becomes greater than the nuclear size $R \sim A^{1/3}$ fm. In natural units ($\hbar = c = 1$, 200 MeV fm$\simeq$1), the condition for coherent scattering can be written as

$$\lambda \lesssim A^{1/3}\,. \tag{3.31}$$

With the momentum transfer $|\mathbf{q}| = \sqrt{2m_N E_R}$ the condition in Eq. 3.31 takes the form

$$\lambda = \frac{1}{|\mathbf{q}|} = \frac{1}{\sqrt{2m_N[\mathrm{GeV}]\,E_R[\mathrm{keV}]}} \lesssim \frac{A^{1/3}}{200}\mathrm{MeV}^{-1}\,. \tag{3.32}$$

With the approximation $m_n = m_p \simeq 1\,\text{GeV}$ (m_n, m_p are the masses of proton and neutron, respectively), the nuclear mass is $m_N \simeq A\,\text{GeV}$. Thus from the condition in Eq. 3.32, the coherence is lost when

$$E_R \gtrsim \frac{2 \times 10^4}{A^{5/3}}\,\text{keV}\,. \tag{3.33}$$

Therefore, although the choice of heavier nuclei in principle gives enhanced scattering cross-section (see Eq. 3.18 and Eq. 3.30), care should be taken when designing a direct dark matter detection experiment in order to not loose the coherence. For example, for argon (A=40) the coherence is lost approximately for E_R greater than 43 keV, while for xenon (A=131) it happens for recoil energies greater than 6 keV. This point will be quantitatively studied in the next section in connection with the form factor which takes into account more properly the loss of coherence.

The shape of the differential event rate in Eq. 3.30 depends on a number of factors: the DM and target nuclear masses which determine the kinematics of the process (like the minimum WIMP velocity), the recoiling energy and the WIMP flux. A less trivial dependence is embedded in the nuclear form factor and in the shape of the DM speed distribution $f_1(v)$. I will analyse these two last ingredients in the following sections.

3.1.4 Nuclear form factor

Nuclear physics enters into the calculation of form factors, describing the internal nucleon and spin structures of the nuclei. For the SI case, the form factor is obtained from the Fourier transform of a spherically symmetric ground state mass distribution normalized so that $F(0) = 1$:

$$F(q) = \frac{1}{m_N}\int \rho_{\text{mass}}(r) e^{-i\mathbf{q}\cdot\mathbf{r}} d^3r = \frac{1}{m_N}\int_0^\infty \rho_{\text{mass}}(r)\,\frac{\sin qr}{qr}\,4\pi r^2 dr. \tag{3.34}$$

Since the mass distribution in the nucleus is difficult to probe, it is generally assumed that mass and charge densities are proportional

$$\rho_{\text{mass}}(r) = \frac{m_N}{Ze}\rho_{\text{charge}}(r), \tag{3.35}$$

so that charge densities, determined through elastic electron scattering, can be utilized instead. Because of the normalization at $q = 0$, the proportionality assumption amounts to

$$F_{\text{mass}}(q) = F_{\text{charge}}(q). \tag{3.36}$$

It is of course convenient to have an analytic expression for the form factor. Up to now, this expression has been provided by the Helm form factor F_{H} [185]. The latter is defined as the product of two fairly simple form factors: one associated with a uniform (box) density F_{B} and the other one accounting for a Gaussian falloff F_{G}

$$F_{\text{H}}(q) = F_{\text{B}}(q) F_{\text{G}}(q) = 3\,\frac{j_1(qR_0)}{qR_0} e^{-q^2\,s^2/2}\,, \tag{3.37}$$

where

$$F_{\text{B}}(q) = \int e^{-i\mathbf{q}\cdot\mathbf{r}} \rho_{\text{B}}(r) d^3r = \int e^{-i\mathbf{q}\cdot\mathbf{r}} \left(\frac{3\Theta(R_0 - r)}{4\pi R_0^3}\right) d^3r = 3\,\frac{j_1(qR_0)}{qR_0}\,, \tag{3.38a}$$

$$F_{\text{G}}(q) = \int e^{-i\mathbf{q}\cdot\mathbf{r}} \rho_{\text{G}}(r) d^3r = \int e^{-i\mathbf{q}\cdot\mathbf{r}} \left(\frac{e^{-r^2/(2\,s^2)}}{(2\pi\,s^2)^{3/2}}\right) d^3r = e^{-q^2\,s^2/2}\,. \tag{3.38b}$$

Here, Θ is the Heaviside function and $j_1(x)$ is the spherical Bessel function of order one

$$j_1(x) = \frac{\sin(x)}{x^2} - \frac{\cos(x)}{x}\,. \tag{3.39}$$

A great advantage of the Helm form factor is that it is defined in terms of a form factor that encodes the uniform interior density and another one that characterizes the nuclear surface. As a consequence, the Helm form factor is defined entirely in terms of two constants the box (or "diffraction") radius R_0 and the surface thickness s, parameters that need to be fit separately for each nucleus. A closed-form expression for the Helm density exists and it is given by,

$$\begin{aligned}\rho_{\text{H}}(r) = {} & \frac{1}{2}\rho_0 \left[\text{erf}\left(\frac{r + R_0}{\sqrt{2}\,s}\right) - \text{erf}\left(\frac{r - R_0}{\sqrt{2}\,s}\right)\right] \\ & + \frac{1}{\sqrt{2\pi}}\left(\frac{s}{r}\right)\rho_0 \left[\exp\left(-\frac{(r + R_0)^2}{2\,s^2}\right) - \exp\left(-\frac{(r - R_0)^2}{2\,s^2}\right)\right]\,,\end{aligned} \tag{3.40}$$

where $\rho_0 \equiv \frac{3}{4\pi R_0^3}$ and $\text{erf}(x)$ is the error function

$$\text{erf}(x) = \frac{2}{\sqrt{\pi}} \int_0^x e^{-z^2} dz. \tag{3.41}$$

The first three moments of the Helm distribution are given by the following simple expressions

$$R^2 \equiv \langle r^2 \rangle = \frac{3}{5} R_0^2 + 3s^2 \,, \tag{3.42a}$$

$$R^4 \equiv \langle r^4 \rangle = \frac{3}{7} R_0^4 + 6R_0^2 s^2 + 15s^4 \,, \tag{3.42b}$$

$$R^6 \equiv \langle r^6 \rangle = \frac{1}{3} R_0^6 + 9R_0^4 s^2 + 63R_0^2 s^4 + 105s^6 \,. \tag{3.42c}$$

The parameters R_0 and s are usually chosen to match numerical integration of Two-Parameter Fermi (Woods-Saxon) model or other parametric models of nuclear density. For example, Lewin and Smith [186] demonstrated a method for fitting parameters in the Helm form factor to muon spectroscopy data in the Fricke et al. compilation [187]. They performed a two-parameter least squares fit to the muonic spectroscopy data, finding the values of R_0 and s for the Helm form factor which best reproduce the numerical Fourier transform of a Two-Parameter Fermi distribution. Explicitly they set

$$R_0(A) = \sqrt{c(A)^2 + \frac{7}{3}\pi^2 a^2 - 5s^2} \tag{3.43}$$

and take $s \simeq 0.9$ fm, $a \simeq 0.52$ fm (as Fricke et al. in their table IIIA), and

$$c(A) \simeq 1.23 A^{1/3} - 0.60 \text{ fm} \tag{3.44}$$

which is a least squares fit to the same table in Fricke et al..
This procedure, however, should be approached with caution due to the fact that the results depend on the nuclear density model (in this case the Two-Parameter Fermi) which was used in the original fit to the data. Moreover, in the Fricke et al. compilation in their table IIIA, the value of the skin thickness was fixed, resulting in a one parameter fit. Hence the fit to the form factor generated from the muon spectroscopy data is in essence a fit to a fit. The advantage here is that a more accurate Helm form factor is generated which is analytic and eliminates the need for numerical integration. In Fig. 3.1 I show the square of the Helm form factor as in Eq. 3.37 using the Lewin-Smith [186] prescription for R_0 in Eq. 3.43 for three different nuclei, xenon (blue solid line), argon (red dashed line) and germanium (green dot-dashed line) as a function of recoil energy E_R in keV (top panel), the momentum transfer q in fm^{-1} (middle panel) and q in MeV (bottom panel).

It is important to note that the use of the Helm form factor has been adopted in all the WIMP rate calculations performed by all the direct detection collaborations

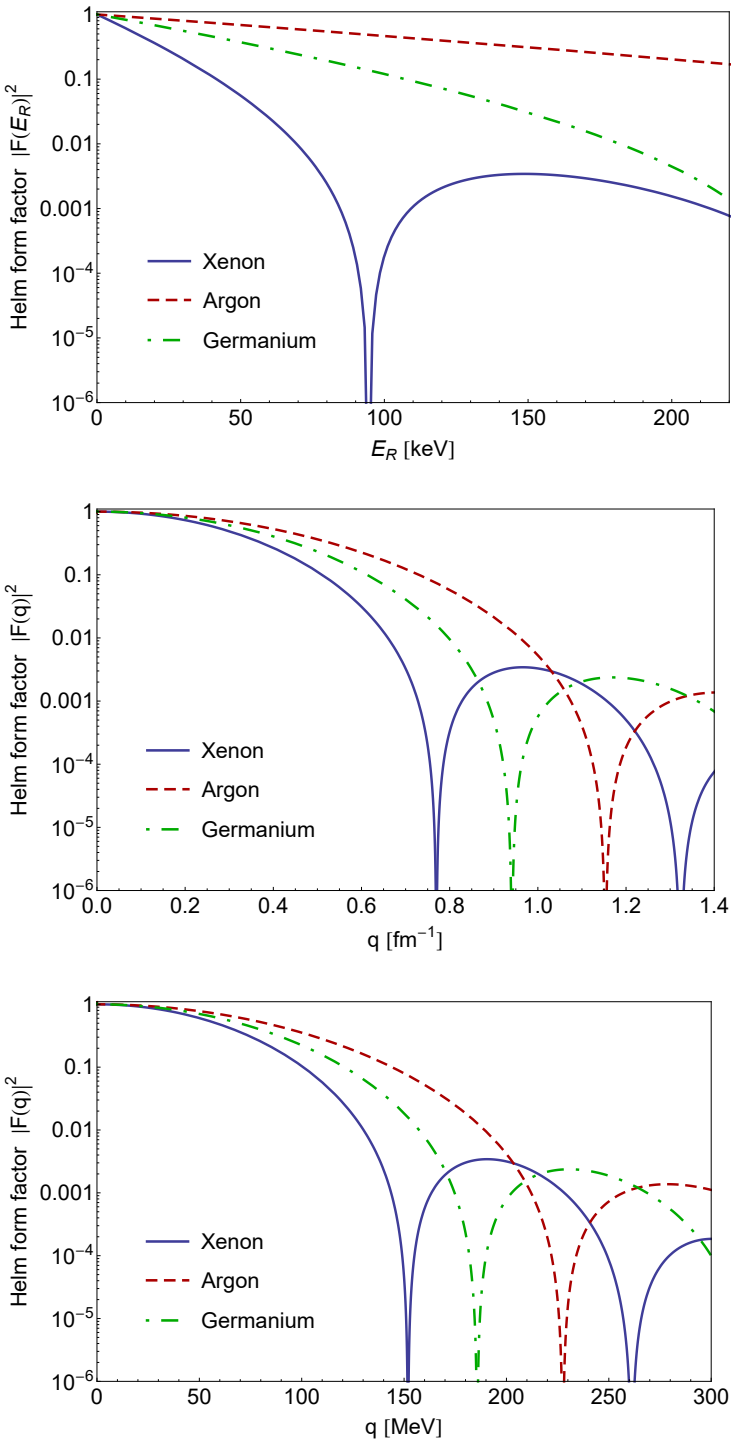

Fig. 3.1.: Square of the Helm form factor as in Eq. 3.37 using the Lewin-Smith [186] prescription for R_0 in Eq. 3.43 for three different nuclei, xenon (blue solid line), argon (red dashed line) and germanium (green dot-dashed line) as a function of recoil energy E_R in keV (top panel), the momentum transfer q in fm^{-1} (middle panel) and the momentum transfer in MeV (bottom panel).

when obtaining their results (i.e. the exclusion or sensitivity curves). The reason is twofold. One is that the Helm form factor with the Lewin and Smith prescription provides an analytical way to obtain straightforwardly the form factor for all the interested nuclei with only one free parameter, namely the atomic number A. The second reason concerns the need to uniform all the experimental results in order to make the comparison between the different exclusion curves in a simply way.

However, I want to remind here that the WIMP event rate formula in Eq. 3.30 is effected by two main approximations. The first is that the form factor of the proton distribution is equal to that of the neutron, namely $F_n \approx F_p = F$ which as we will see in the discussion in Chap. 7, it is not necessarily true and moreover it is very relevant. The second is that the Helm form factor, $F = F_H$ does not represent the distribution of all the nucleons in the nucleus but rather the proton distribution since it has been obtained through the electron scattering data which probe only the charged distribution.
Relaxing all these hypotheses, the WIMP event rate, for equal couplings $f_p = f_n$, should read as

$$\frac{\mathrm{d}R}{\mathrm{d}E_R} = \frac{\rho_0 \sigma_{SI}^p}{2\mu_{\chi p}^2 M_\chi} \left(|Z F_p(E_R) + (A-Z) F_n(E_R)|^2 \right) \int_{v_{\min}}^{\infty} \frac{f_1(v)}{v} \, \mathrm{d}v \,, \tag{3.45}$$

where $F_n(E_R)$ and $F_p(E_R)$ are, respectively, the nuclear neutron and proton form factors. The neutron distribution is basically not known because it is more difficult to obtain experimentally than the information on the proton nuclear form factor, that can be obtained with elastic electron-nucleus scattering and other electromagnetic processes. Probably for this reason, in the dark matter community the approximation that $F_n \approx F_p = F_H$ has been extensively used and it is at present the most used prescription despite its limitation.

I will examine this problem in Chap. 7 and I will propose a possible extension in view of the possibility to extract some information of the neutron form factor using the coherent elastic neutrino nucleus scattering data [1] from the COHERENT experiment [188].

In the SD case, however, the situation is even more complicated. In order to calculate the SD cross section, we need to know the proton and neutron spin content $\langle S_{p,n} \rangle$ as well as the form factor $|F_{SD}|^2$. The form factor can be written in the form

$$|F_{SD}(E_R)|^2 = S(E_R)/S(0) \,, \tag{3.46}$$

in terms of the response function $S(E_R)$. This response function can in turn be decomposed into three spin-dependent structure functions (SDSFs)

$$S(E_R) = a_0^2 S_{00}(E_R) + a_0 a_1 S_{01}(E_R) + a_1^2 S_{11}(E_R)\,, \tag{3.47}$$

where $a_0 = a_p + a_n$ is the isoscalar coupling and $a_1 = a_p - a_n$ is the isovector coupling. The zero momentum transfer value $S(0)$ is related to the proton and neutron spin expectation values by [189]

$$S(0) = \frac{2J+1}{\pi}\frac{J+1}{J}\left|a_p\langle S_p\rangle + a_n\langle S_n\rangle\right|^2 . \tag{3.48}$$

We can therefore write the SD cross section of Eq. 3.25 as

$$\frac{\mathrm{d}\sigma_{SD}}{\mathrm{d}E_R} = \frac{2\pi}{3}\frac{m_N\sigma_{SD}^p}{\mu_{\chi p}^2 v^2}\frac{1}{2J+1}\frac{S(E_R)}{(a_p)^2} . \tag{3.49}$$

The nuclear physics is now encapsulated in a single response function $S(E_R)$ (or equivalently two SDSFs S_{00} and S_{11}). The functional form for S_{ij} can be calculated from shell models of the nucleus [190]. However, there are a number of competing models in the market, for example the Independent Single Particle Shell Model [191], the Odd Group Model [192] and the Interacting Boson Fermion Model [193] just to cite some of them. Different methods to account for forces between quarks are used by this models which result in different forms for the SDSFs. This is a clear sign of a big uncertainty associated to the SD cross section. This problem was studied and partially solved by Cerdeño et al. [194]. He proposed a parametrisation for the spin structure functions in terms of $u = (qb)^2/2$, where $b = \sqrt{41.467/(45.0A^{-1/3} - 25.0A^{-2/3})}$ is the oscillator size parameter. It was shown that the Cerdeño parametrisation was able reduce the uncertainties in the SD cross section.

3.2 Distribution of DM in our galaxy

In order to understand the distribution of dark matter in the Milky Way and the correlated speed distribution of the DM, one may broadly consider three important zones, namely the galactic center, the solar neighbourhood, and the DM halo that extends much beyond the visible Milky Way disk and that surrounds the disk and bulge of the Milky Way. The galactic center is difficult to probe from the position of the solar system as the visible light is mostly obscured by the interstellar medium on the line of sight. However, it is known that there is a bulge in the central region of the galaxy but it is difficult to estimate the mass of it since its evolution cannot be treated without considering the evolution of the galactic disk. However, the stars in the bulge contribute dominantly to the luminosity of it up to about 1 kpc from the galactic center. Near the galactic center, there is a star cluster which is a mixture of old and new stars. This cluster has a central cusp that follows a power law $\sim r^{-1.2}$ up to about 0.22 pc and afterwards it appears to follow a broken power law with $\sim r^{-1.7}$ for larger distances from the center.
Many such observational results may be used to determine some properties of dark matter in the galaxies such as the local DM density, the mass of the halo, etc. But one also needs to know, for example, the velocity distribution of DM, the DM substructure, and also the profile of the halo. In cases such as these where the observational results are not sufficient, one has to depend on theoretical models and N-body numerical simulations. Some of these theoretical models rely on numerical simulation and consider that there is a perturbation called a seed perturbation and that the materials accrete around this seed perturbation in a self-similar manner. However, it is realized that the formation of a DM halo cannot be represented by this simplistic model. The dark matter halo formation can have a very different history. For example, some halos might have experienced the violent merger of smaller mass halos. Therefore the simplistic model of self-similar accretion should be considered with this kind of chaotic and violent picture for the formation of DM halos. It is perhaps also becoming increasingly apparent that the DM halo is not just a smooth distribution of DM. The halo perhaps has lots of substructures with an average smooth nature. These substructures in fact may store important information of the particle nature of the DM.

The numerical simulation for halo formation is generally based on the spherical accretion of mass and the merger of lower mass halos. But the halos formed by such clustering may not be that spherical. In fact, the more massive a halo is, the more it tends to deviate from its spherical nature. With the increase of mass, the

shape of the halo tends to be more and more prolate while the major axis tracks the large-scale structure distribution. In simulation, a uniform grid of particles is first considered for the unperturbed Universe and a linear density perturbation is introduced. The growth around the perturbation is then simulated. The overdense region breaks away from the Universe's expansion. The gravitating (self-bound) dark matter halo formation is then studied. These simulations predicts a density profile steeper than $\rho \propto r^{-2}$ (for the spherical symmetric case) [195]. In order to construct a universal halo density profile, the spherically averaged profiles are considered. The simulation indicates that the slope at the central inner region is asymptotically $\rho \propto r^{-1}$ [196] and at the outer region, the density profile suffers a steeper nature ($\rho \propto r^{-3}$), indicating a double power law profile. One of these, the Navarro-Frenk-White (NFW) profile, is nearly universal for wide range of halo masses. Recent results from Aquarius simulations suggest that at the central region of the halo, the profile tends to be progressively more shallow rather than acquiring an asymptotic slope [197]. This behaviour favours more the Einasto profile given by $\rho(r) = \rho^{-2} \exp[-((r/r_{-2})^{\alpha} - 1)]$, where ρ^{-2} is the density at r_{-2}, the radius at which the log slope is -2 for the Milky Way, α=0.17.

The local dark matter density in the solar neighbourhood is important for various DM calculations. Firstly, the experimental bounds on DM direct detection cross sections for different DM masses are becoming more and more stringent as we will see in Sec. 3.6. Indirect detection experiments are coming up with new results in detecting the excess gamma rays, positron excess, etc as we have briefly seen in Sec. 2.4.2. The theoretical calculations for these excesses on the basis of dark matter annihilations also require the knowledge of local DM density. To complicate the situation, there is the idea of the presence of a DM disk which is distinct from the DM halo. The theoretical probe for the existence of such a disk demands understanding of the distribution of DM in our neighbourhood. The calculation of the local density depends on the potential which is calculated from the stellar distribution function. The stellar distribution function f is defined such that the total number of stars in an elementary phase space volume $d^3\boldsymbol{x}\, d^3\boldsymbol{v}$ is $f(\boldsymbol{x}, \boldsymbol{v})\, d^3\boldsymbol{x}\, d^3\boldsymbol{v}$ where $d^3\boldsymbol{v}$ denotes an elementary volume in velocity space around the velocity $\boldsymbol{v}$. From this, the density of stars perpendicular to the disk plane, $\rho_s(z)$, is estimated from the gravitational potential $\phi(z)$ perpendicular to the disk. Now, this potential is due to both stars and DM. With a model for $\phi(z)$, the total density (dark matter + stellar), ρ_T is formulated. The resulting equations are then solved iteratively to obtain solutions for ρ_T and $\rho_s(z)$ from which the local dark matter density is estimated. Computer-based studies of the models of

galaxy formation and their comparison with relevant observational results, lead to obtaining the density profile of the galactic halo. Some simulations seem to suggest a central density cusp and self-similar halo, whereas the observations are indicative of a flat density profile. For the simulations, one generally considers that the dominant component of DM is nonbaryonic cold DM that is nonrelativistic, collisionless, and interacts with baryons only gravitationally. These simulations however do not support the possibility of a baryonic component of DM in the formation of a flat halo. If the galactic gas and stars at the outer region of the galaxy move with a constant circular velocity, the density profile of the dark matter halo should go as ρ^{-2}, for appropriate r. This profile is similar to the case of a system of particles that is self-gravitating and isothermal, having constant velocity dispersion. Thus, the approximated isothermal density profile is given by

$$\rho\left(r\right) = \frac{\rho_{\text{cen}}}{1 + \frac{r^2}{r_{\text{core}}^2}}\,, \tag{3.50}$$

where ρ_{cen} is the density at the center and r_{core} is the core radius. In the zone where $r < r_{\text{core}}$, this isothermal density profile becomes almost constant, suggesting a finite central density. But some other simulations claim to have obtained a cuspy nature of central dark matter density whereby ρ diverges as r^{-1} in the central region. In other words, ρ tends to infinity at the center (this is the "Core-Cusp" problem introduced in Sec. 2.1.4). But this nature of the halo profile at the central region is difficult to verify for the case of spiral galaxies as the baryons dominate gravitationally in the inner region of a normal galaxy. The other suitable alternatives are to investigate the dark-matter-rich spiral dwarf galaxies. Studies of rotation curves of such galaxies indicate that the halo density is not infinite at the center and appears to support a shallow isothermal type profile as shown in Eq. 3.50. However there are other halo profiles that are in vogue such us the Moore profile [198] and different kind of parametric form of the Einasto halo profile [199].

The other important aspect is the velocity distribution of dark matter in the DM halo. Knowledge of it is important for both direct and indirect detection calculations. For the case of direct detection, the high-energy tail of the velocity distribution is more relevant. Since the scattering process of dark matter off the target nucleus is driven by the kinematics of the process, it is more sensitive to the high-velocity end of the profile. On the other hand, the indirect detection of DM through,for example, the high-energy solar neutrinos produced by the annihilation of DM captured by the gravity of solar core, is more sensitive to the

lowest velocity of the profile. From the knowledge of the motion of collisionless stars in galaxies and considering the influence of other constituents of the galaxy leads one to apply the central limit theorem that brings to a Maxwell-Boltzmann distribution for velocities. The latter distribution for the DM velocities is given by

$$f(\mathbf{v}) = \frac{1}{\sqrt{(2\pi\sigma_v^2)^3}} \exp\left[-\frac{1}{2}\left(\frac{\mathbf{v}}{\sigma_v}\right)^2\right], \tag{3.51}$$

where σ_v is the velocity dispersion. It should be noted that this distribution depends only on the velocity. This is thus an isotropic distribution and may perhaps be derived from a simple isothermal profile. However, as already said, the formation of the Milky Way via merger events may lead to significant structure in both the spatial and velocity distribution of the dark matter halo, including dark matter streams and tidal debris [200, 201, 202].

In the following section I will examine in more detail the velocity distribution of dark matter particles in the Galactic halo which affects the signal in dark matter detectors.

3.3 Dark matter speed distribution

The WIMP speed distribution is typically assumed to have a simple form in the so-called Standard Halo Model (SHM) [203, 204], in which WIMPs are considered to be an isothermal sphere with an isotropic, Maxwellian velocity distribution, truncated at the Galactic escape speed $v_{\rm esc} \approx 544\,{\rm km\ s^{-1}}$ [205, 206], and rms velocity dispersion σ_v. We define $\widetilde{f}(\mathbf{v})$ as the distribution in the rest frame of the dark matter population (*i.e.* the frame in which the bulk motion of the dark matter particles is zero); in the case of the (essentially) non-rotating smooth halo background, that frame is the Galactic rest frame. The lab frame distribution is obtained through a Galilean transformation as described later. The SHM velocity distribution is written as

$$\widetilde{f}(\mathbf{v}) = \begin{cases} \frac{1}{N_{\rm esc}}\left(\frac{3}{2\pi\sigma_v^2}\right)^{3/2} e^{-3\mathbf{v}^2/2\sigma_v^2}, & \text{for } |\mathbf{v}| < v_{\rm esc} \\ 0, & \text{otherwise.} \end{cases} \tag{3.52}$$

Here, the factor $N_{\rm esc}$ is required to satisfy the normalization condition:

$$\int \widetilde{f}(\mathbf{v})\, {\rm d}^3\mathbf{v} = 1\,, \tag{3.53}$$

which gives

$$N_{\rm esc} = \mathrm{erf}(z) - \frac{2}{\sqrt{\pi}} z e^{-z^2} \,, \tag{3.54}$$

with $z \equiv v_{\rm esc}/v_0$ and $v_0 = \sqrt{2/3}\,\sigma_v$[3] is the most probable speed, with an approximate value of 235 km/s [207, 208, 209, 210].

By integrating over all directions we obtain $f(v)$ and the speed distribution is then given by

$$f_1(v) = f(v)\, v^2 = \int \widetilde{f}(\mathbf{v})\, v^2 \, \mathrm{d}\Omega_v \,. \tag{3.55}$$

The Maxwellian distribution is truncated at the escape velocity $v_{\rm esc}$ to account for the fact that WIMPs with sufficiently high velocities escape the Galaxy's potential well and, thus, the high-velocity tail of the distribution is depleted. The DM escape velocity in the Milky Way is estimated from that of high-velocity stars.

For obtaining the DM direct detection rates at Earth, the velocity in the galactic rest frame $v_{\rm gal}$ should be transformed into the Earth rest frame, which can be realized by the transformation

$$\boldsymbol{v}_r = \boldsymbol{v}_{\rm gal} - \boldsymbol{v}_{\rm E} \,, \tag{3.56}$$

where v_E is the velocity of the Earth with respect to the galactic rest frame. The Earth moves with the solar system through the Galaxy with the same velocity $v_{\rm sol}$ and it has a periodic orbital velocity $v_{\rm orb}$ around the sun. Thus, the expression for v_E is

$$v_{\rm E} = v_{\rm sol} + v_{\rm orb} \cos\gamma \left(\frac{2\pi\,(t - t_0)}{T} \right) \,. \tag{3.57}$$

In the above equation γ denotes the angle subtended by the Earth's orbital plane (ecliptic) at the galactic plane ($\gamma \simeq 60°$), $v_{\rm orb}$ is about 30 km/s, T(= 1 year) is the time period of Earth's revolution around the sun and t_0 is a reference time in a year. The velocity $v_{\rm sol}$ of the solar system in the galactic rest frame is given by

$$v_{\rm sol} = v_0 + v_{\rm pec} \,, \tag{3.58}$$

where v_0 is the speed of the local system around the galactic center at the position of solar system, $v_{\rm pec}$ is the peculiar velocity, about 12 km/s, which is the velocity

[3] Note that if we write the speed distribution function as in Eq. 3.51 the relation between the dispersion and the velocity becomes $v_0 = \sqrt{2}\,\sigma_v$.

of solar system with respect to the local system and for v_0 a value of 220 km/s can be adopted[4].

With this variable change we can obtain the relevant one-variable DM velocity distribution in the Earth reference frame for direct detection experiment. Ignoring for the moment the seasonal motion of the Earth around the Sun[5], we manipulate Eq. 3.52

$$\widetilde{f}(\boldsymbol{v})d^3\boldsymbol{v} = \frac{1}{N_{\rm esc}(v_0\sqrt{\pi})^3}e^{-v^2/v_0^2}d^3\boldsymbol{v}\,, \tag{3.59}$$

to obtain the one-variable velocity distribution

$$f_1(v)dv = \frac{4v^2N}{v_0^3\sqrt{\pi}}e^{-v^2/v_0^2}dv\,. \tag{3.60}$$

With the variable change in Eq. 3.56, we have

$$f(\boldsymbol{v}_r)d^3\boldsymbol{v}_r = f(\boldsymbol{v})d^3\boldsymbol{v} = f(\boldsymbol{v}_r+\boldsymbol{v}_E)d^3\boldsymbol{v}_r \quad \text{because } d^3\boldsymbol{v} = d^3\boldsymbol{v}_r\,. \tag{3.61}$$

For a fixed v_r, we integrate the polar angle between $\boldsymbol{v}_r$ and $\boldsymbol{v}_E$ to obtain the final result

$$f_1(v_r)dv_r = N\frac{v_r dv_r}{v_E v_0\sqrt{\pi}}\left(e^{-(\min(v_r-v_E,v_{\rm esc}))^2/v_0^2} - e^{-(\min(v_r+v_E,v_{\rm esc}))^2/v_0^2}\right)\,. \tag{3.62}$$

Note that if $v_r > v_{\rm esc}+v_E$, then $f_1(v_r)=0$.

The one-variable DM velocity distribution in the Earth reference frame enters into the direct detection rate, see Eq. 3.30, through the integral[6]

$$\eta(v_{\rm min}) \equiv \int_{v_{\rm min}}^{\infty}\frac{f_1(v)}{v}\,{\rm d}v\,, \tag{3.63}$$

which is referred to as the "velocity integral" or the "mean inverse speed".

[4] The canonical value for the disk rotation speed has typically been assumed to be 220 km/s [207], but more recent estimates tend to place it 5–15% higher [208, 209, 210]. A value of 235 km/s is more centrally located within current estimates and is more frequently being used as a fiducial value, though 220 km/s remains viable.

[5] This will be the topic of Sec. 3.3.1.

[6] Since all the calculations in the following will be done in the Earth reference frame, I will for simplicity use $v_r \equiv v$.

For the SHM, the mean inverse speed η can be analytically solved [211, 212] resulting in

$$\eta(v_{\rm min}) = \begin{cases} \dfrac{1}{v_{\rm obs}} & \text{for } z < y,\ x < |y-z|\,, \\ \dfrac{1}{2N_{\rm esc}v_{\rm obs}}\left[\mathrm{erf}(x+y) - \mathrm{erf}(x-y) - \frac{4}{\sqrt{\pi}} y e^{-z^2}\right] & \text{for } z > y,\ x < |y-z|\,, \\ \dfrac{1}{2N_{\rm esc}v_{\rm obs}}\left[\mathrm{erf}(z) - \mathrm{erf}(x-y) - \frac{2}{\sqrt{\pi}}\,(y+z-x)\, e^{-z^2}\right] & \text{for } |y-z| < x < y+z\,, \\ 0 & \text{for } y+z < x \end{cases} \tag{3.64}$$

where x and y are defined as $x \equiv v_{\rm min}/v_0$ and $y \equiv v_E/v_0$.

In Fig. 3.2 I show the DM velocity distribution $f(v)$ evaluated at the Earth reference frame (top panel) and the corresponding one-variable distribution $f_1(v)$ (bottom panel) in the Standard Halo Model. It is possible to see that the first vanishes at $v = v_E + v_{\rm esc} = 232 + 544$ km/s $= 776$ km/s which is the maximum speed that a DM particle can have in the SHM as seen by a detector at Earth. The one-variable speed $f_1(v)$ presents a maximum at $v = v_{\rm esc} - v_E = 544 - 232$ km/s $=$ 312 km/s. In Fig. 3.3 I show the mean inverse speed in Eq. 3.64 for different WIMP masses, namely $M_\chi = (20,\ 50,\ 200$ and $1000)$ GeV, for an argon nuclei (top panel) and for a xenon nuclei (bottom panel). The mean inverse speed shows a maximum value for $E_R = 0$ keV and it decreases monotonically as the recoil energy increase and the drop is smaller as the WIMP mass increase. For a WIMP mass of $M_\chi = 20$ GeV in argon the reduction of $\eta(v_{\rm min})$ starts to be become important for $E_R \gtrsim 40$ keV and it reaches a null value for $E_R \simeq 61$ keV. For xenon the reduction is even more important and it starts at $E_R \gtrsim 21$ keV and it reaches a null value for $E_R \simeq 33$ keV. This determines the behaviour of the sensitivity to WIMPs for small values of the WIMP mass, as we will see later. To better understand this point, it is instructive to study the behaviour of $\eta(v_{\rm min})$ as a function of the WIMP mass for different recoil energies, as in Fig. 3.4. For argon we note that for a recoil energy of 2 keV the mean inverse speed is different from zero for WIMP masses greater than ~ 2.5 GeV, for $E_R = (5,\ 10,\ 15,\ 20,$ and $25)$ keV the same happens for $\sim 4.1,\ 6.1,\ 7.8,\ 9.3,$ and 10.7 GeV, respectively. For xenon we have that the mean inverse speed goes more quickly to zero at fixed WIMP mass. Indeed, for $E_R = 2$ keV the minimum WIMP mass for which η is different from zero is 4.4 GeV (to be compared with 2.5 GeV for argon) and for the other recoil energies this value is

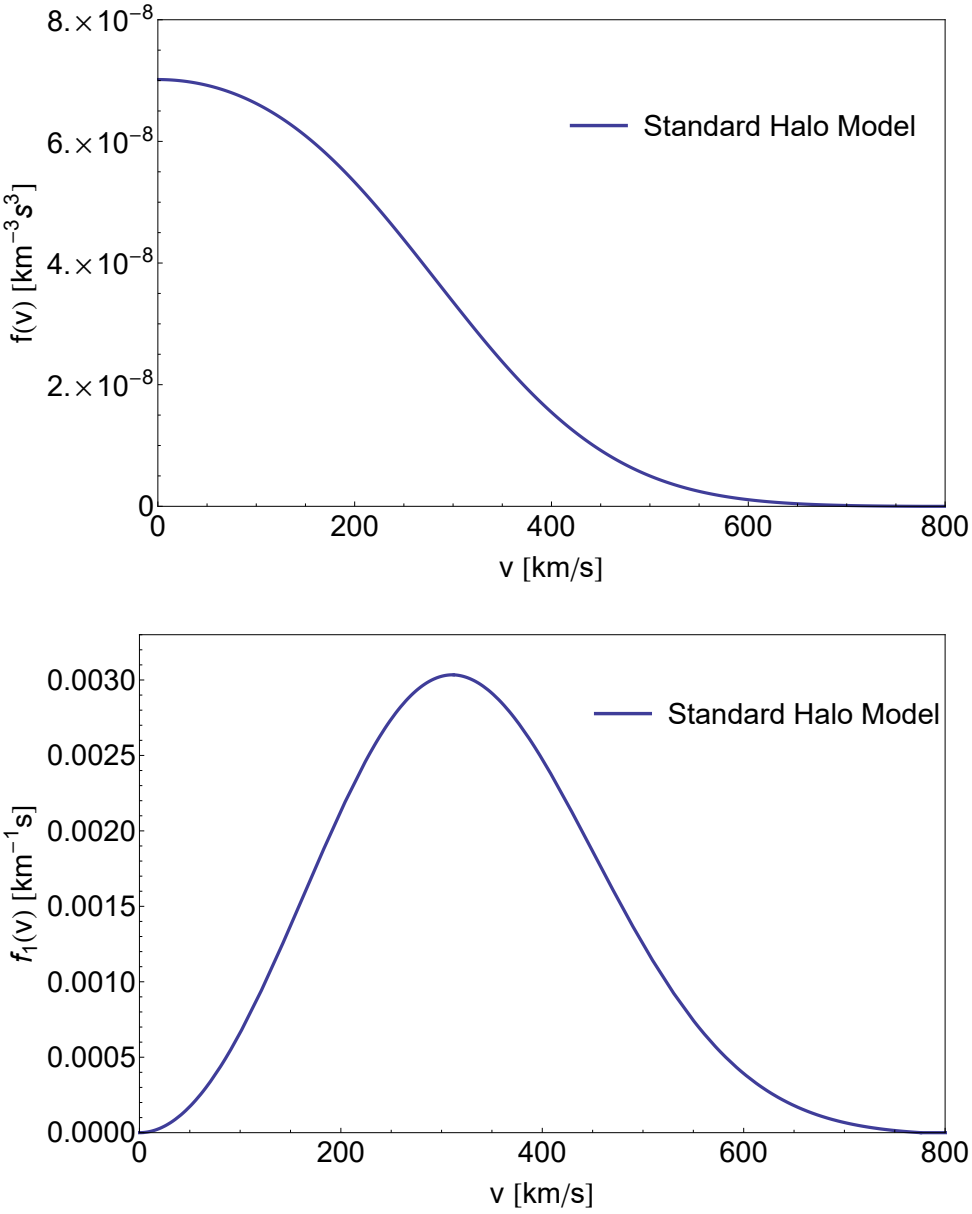

Fig. 3.2.: Dark matter velocity distribution $f(v)$ evaluated at the Earth reference frame (top panel) and the corresponding one-variable distribution $f_1(v)$ (bottom panel) in the Standard Halo Model.

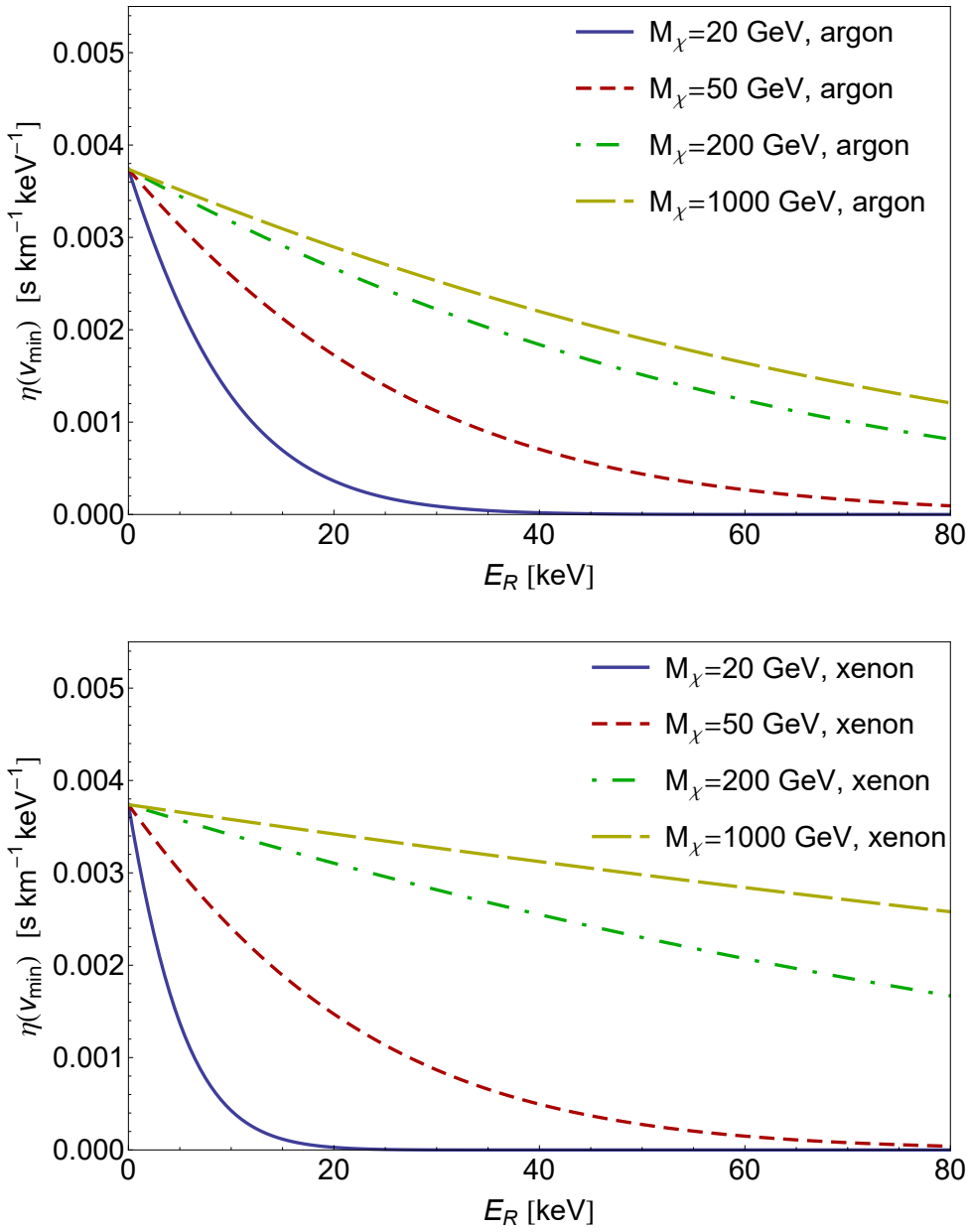

Fig. 3.3.: Mean inverse speed $\eta(v_{\rm min})$ in Eq. 3.64 for argon (top panel) and for xenon (bottom panel) as a function of the recoil energy E_R in keV for four different WIMP masses $M_\chi = (20,\ 50,\ 200 \text{ and } 1000)$ GeV.

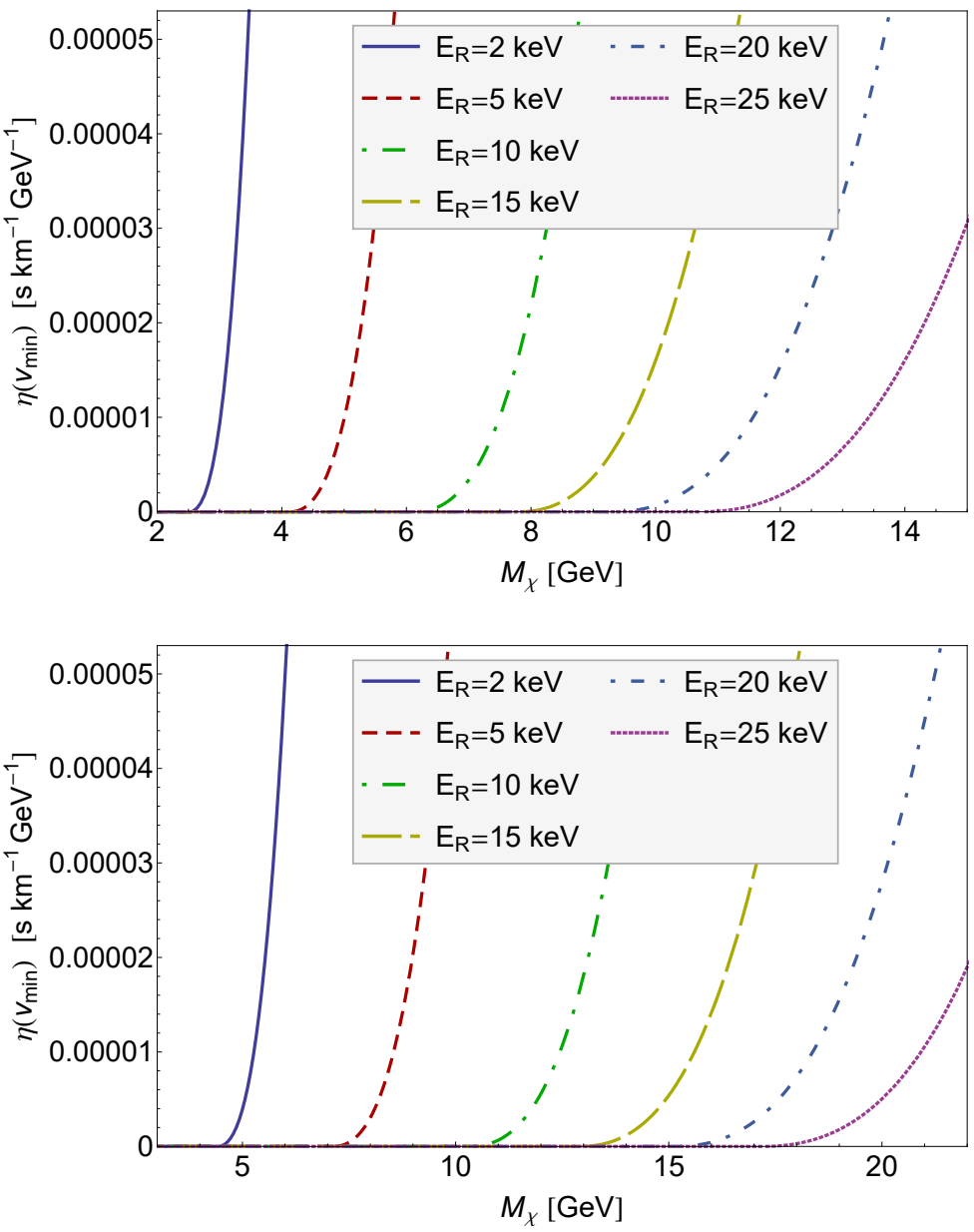

Fig. 3.4.: Mean inverse speed $\eta(v_{\min})$ in Eq. 3.64 for argon (top panel) and for xenon (bottom panel) as a function of the WIMP mass M_χ in GeV for six different recoil energies $E_R = (2,\ 5,\ 10,\ 15,\ 20,\ \text{and}\ 25)$ keV.

systematically greater than for the argon case. From this observation we note that argon is a better target to explore low WIMP masses. However, for large WIMP masses the trend is inverted as visible from top panel of Fig. 3.5. As highlighted for the WIMP mass of 200 GeV, the mean inverse speed is bigger for xenon than for argon. The value of the WIMP mass for which we have approximatively the same distribution for η in xenon and argon as a function of the recoil energy is about 67.5 GeV. The ratio between the mean inverse speed for argon and xenon, $\frac{\eta_{\mathrm{Ar}}(v_{\mathrm{min}})}{\eta_{\mathrm{Xe}}(v_{\mathrm{min}})}$, for different WIMP masses is show in the bottom panel of Fig. 3.5. As visible for masses below about 67.5 GeV the $\eta_{\mathrm{Ar}}(v_{\mathrm{min}})$ can be significantly larger then the xenon one. Above 67.5 GeV $\eta_{\mathrm{Xe}}(v_{\mathrm{min}})$ becomes larger showing however a smaller dependency on the mass.

This is somehow counterintuitive because in the dark matter community often it is reported that xenon is better than argon to explore low WIMP masses and vice versa for high masses. However, until now we have considered only the contribution of the DM velocity distribution on the WIMP differential rate. As we have seen in Eq. 3.30 the latter receives contribution also from the form factor, atomic number, and other kinematic variables. In particular, including the contribution of the form factor the curves shown in Fig. 3.5 become as those shown in Fig. 3.6. The effect of the form factor is that also for high WIMP masses the argon is above xenon. This advantage is however partially lost (especially at low WIMP masses) when considering the impact of the coherence term A^2 as I will show in Sec. 3.4.

3.3.1 Annual modulation of DM rate

Before to move to the final WIMP differential rate I want to discuss a consequence of including the Earth's motion during the year.

The annual periodicity of Earth's motion around the sun, v_{E} in Eq. 3.57, imparts a periodic variation of the detection rate. This is usually referred to as annual modulation of the DM rate that should be observable by DD experiments. This annual variation in the rate of dark matter signal can be understood from Fig. 3.7.

According to the SHM, the sun (along with the Earth) moves through the "static" dark matter halo of the Milky Way in the direction of the Cygnus constellation. As

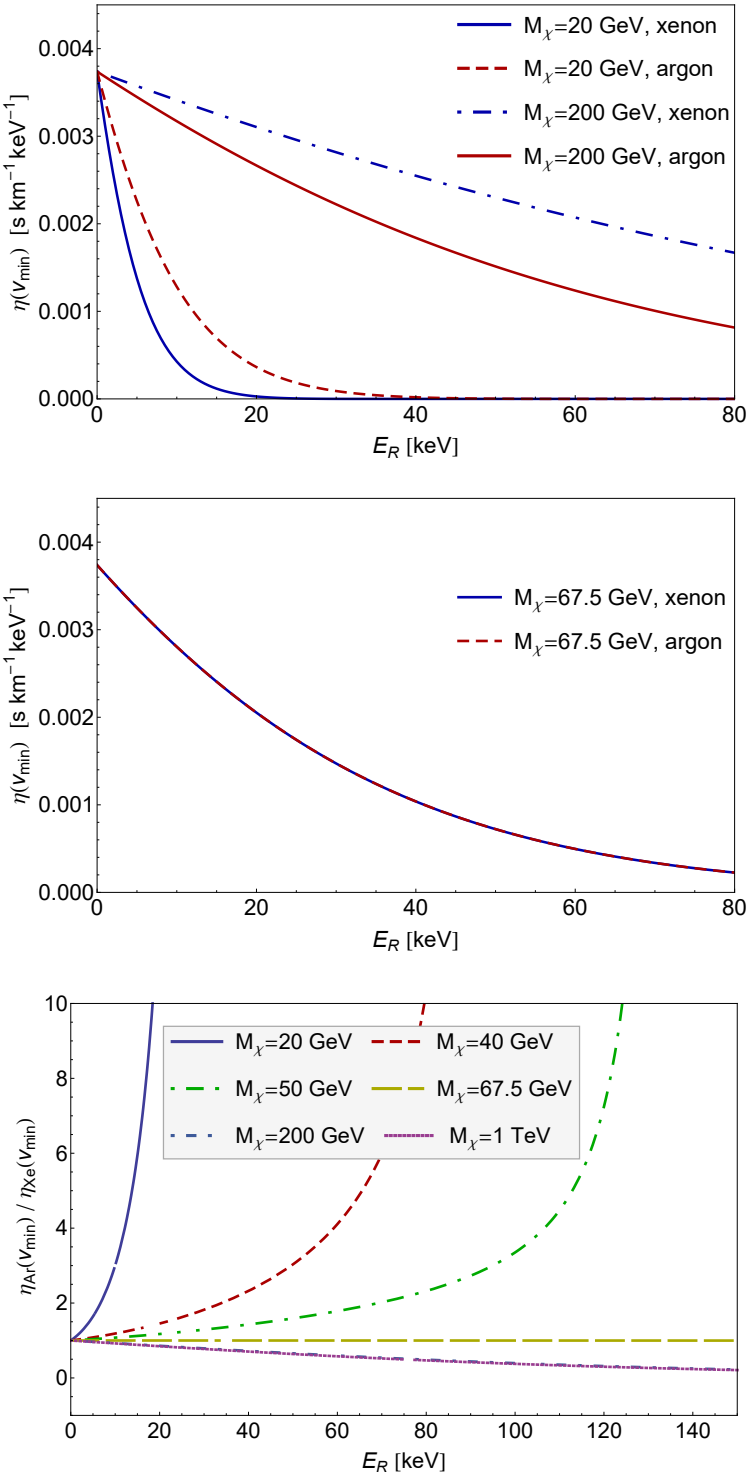

Fig. 3.5.: Mean inverse speed $\eta(v_{\rm min})$ in Eq. 3.64 as a function of the recoil energy E_R in keV for WIMP masses $M_\chi = (20,$ and $200)$GeV for argon (red lines) and xenon (blue lines)(top panel) and for the value of the WIMP mass, ∼67.5 GeV, which allows to have approximatively the same distribution of η for argon and xenon nuclei (middle panel). In the bottom panel it is shown the ratio $\dfrac{\eta_{\rm Ar}(v_{\rm min})}{\eta_{\rm Xe}(v_{\rm min})}$ for different values of WIMP masses.

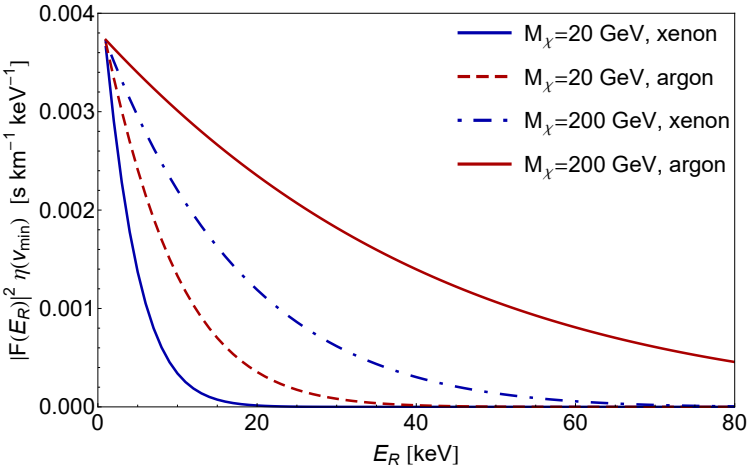

Fig. 3.6.: The curves show the quantity $|F(E_R)|^2\,\eta(v_{\rm min})$ as a function of the recoil energy E_R in keV for WIMP masses $M_\chi = (20,\text{ and }200)$GeV for argon (red lines) and xenon (blue lines).

a result, the Earth will encounter an apparent DM wind coming from the direction opposite to the direction of motion of the sun or solar system (see Fig. 3.7). At any position of the Earth on its orbit, its velocity can be decomposed into two perpendicular components. For the position of the Earth when one of its velocity components, v_p is parallel to the direction of motion of the solar system, the Earth will be encountered by the maximum amount of dark matter since the direction of the velocity component at this position is opposite in direction (antiparallel) to the flow of the apparent DM wind. The situation is just reversed (after 6 months from the former position) when the direction of v_p is the same as that of the apparent DM wind. In this situation the DM flux encountered by the Earth will be minimum. Thus, there is a modulation of the DM flux encountered by the Earth from a maximum to a minimum over a year. Therefore, the dark matter detection rate in a terrestrial direct detection experiment will also undergo similar modulation.

3.3.2 Daily and directional variation of DM rate

Along with the orbital motion, the Earth also has a rotational motion about its own axis with a time period of $\simeq$ 24 hours or a sidereal day. As a result of this rotation, the apparent WIMP wind will experience a directional anisotropy as the Earth goes around its own axis. This can be understood from the fact that an orthogonal system of axes (e.g., Cartesian coordinates x-y-z) attached

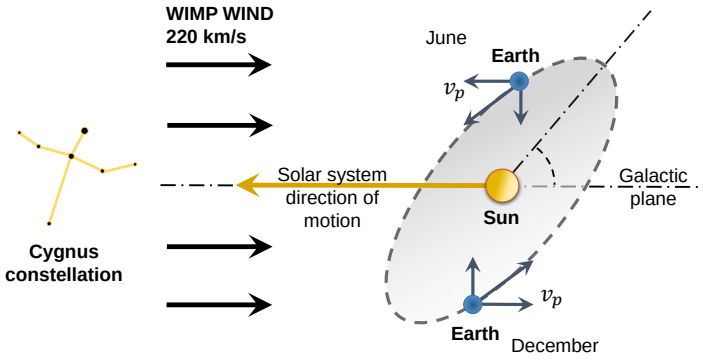

Fig. 3.7.: Schematic diagram to explain the annual modulation of dark matter direct detection signal.

to the laboratory situated at a certain latitude will also suffer a rotation with the rotational motion of the Earth. As a result of this, the positive direction, for example, of an axis x or y or z will continually change its directionality before the system of axes comes back to its original configuration after one rotation time period of the Earth (one sidereal day). Hence, the directional measurement of dark matter will accordingly show a variation in the detected yield. This is illustrated in Fig. 3.8. Since the Earth also has an orbital motion around the sun and a motion around the galaxy (as a part of the solar system that goes around the galactic center), the variation in dark matter detection rates due to diurnal motion of the Earth will also be affected by these motions.

I will examine more in detail the implications of such a modulation when I will explore the potentialities of a directional dark matter detector located at Laboratori Nazionali del Gran Sasso (LNGS) in Chap. 6.

3.4 Final SI WIMP differential rate for different nuclei

Finally, in this section I will derive and show the spin-independent WIMP differential rate in Eq. 3.30 for different nuclei, namely xenon, argon, silicon and germanium.

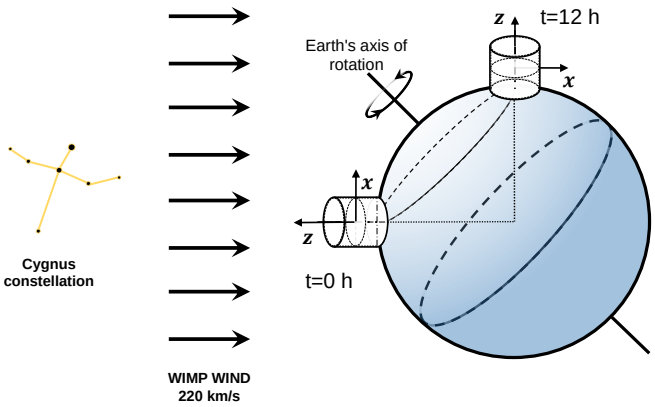

Fig. 3.8.: Schematic diagram that shows the change in orientation of the coordinate axes attached to a terrestrial dark matter detection laboratory due to the rotation of Earth around its own axis.

In Figs. 3.9 and 3.10 this rate for argon (solid blue), xenon (dashed red), germanium (dot-dashed green) and silicon (dashed yellow) targets and several WIMP masses is shown.

As we increase the mass of the target nucleus, we see an increase in the low energy event rate. This is a consequence of the A^2 enhancement for SI interactions, resulting in the xenon ($A \approx 131$)[7] spectrum being a factor of around 10 higher than the argon ($A = 40$) spectrum at low energies. When considering higher energies, however, we observe that the spectrum for heavier targets decays more quickly. This is due to a more sharply falling form factor; the larger size of the nucleus results in a more rapid loss of coherence as the recoil energy increases. The drop of the xenon event rate at around 100 keV recoil energy visible in Fig. 3.10 reflects a feature of the xenon Helm form factor.

Moreover, as the WIMP mass increases the recoil spectrum becomes flatter. This is primarily due to the dependence of $v_{\min}$ on M_χ (shown in Eq. 3.3). As we increase M_χ, the reduced mass $\mu_{\chi N}$ increases, meaning that $v_{\min}$ varies more slowly with energy. This means that the integral over the speed distribution also varies more slowly with energy (see top panel of Fig. 3.5). Physically, low mass WIMPs require a larger speed to impart the same recoil energy and as we increase the recoil energy this required speed grows quickly. The rapid cut-off in the spectrum observed in the $M_\chi = 20$ GeV case, especially for xenon (top panel

[7] Note that A is given as an approximated number because of the presence of different xenon isotopes.

of Fig. 3.9) occurs when there are no more WIMPs below the Galactic escape speed which have sufficient speed to produce recoils of the desired energy. Since in this thesis I will focus mainly on argon as a target material, in Fig. 3.11 the SI differential event rate for argon is shown for five different WIMP masses, namely $M_\chi = (20,\ 50,\ 100,\ 200 \text{ and } 1000)$ GeV.

Considering a real experiment, the detector will be only sensitive to recoil energies within a given range, namely between a minimum energy E_{min} (often called threshold E_{th}) to a maximum energy E_{max} (often called E_{up}). This energy range depends on the particular nuclei used as a target due to different technologies used and problems related to the specific background content. The total number of the expected events is then obtained by integrating over this range of recoil energies and the exposure, which is the product of the livetime T and the detector mass M (Exp $\equiv M\,T$). In a real experiment there will be also a nuclear recoil acceptance function, $A(E_R)$, which takes into account all the backgrounds cuts, the WIMP signal selection efficiency and the experimental resolution. These experimental details will be discussed in the description of the DarkSide-20k experiment (see Chap. 4) which is a next generation argon DM detector and object of this thesis.

The predicted number of WIMP events is then given by

$$N_\chi = M\,T \int_{E_{\text{th}}}^{E_{\text{up}}} A(E_R) \frac{\mathrm{d}R}{\mathrm{d}E_R}\,\mathrm{d}E_R\,. \tag{3.65}$$

3.5 DM differential event rate uncertainties

The calculation of the DM differential event rate $\mathrm{d}R/\mathrm{d}E_R$ and, in turn, the calculation of the predicted number of WIMP events requires not only a knowledge of the DM parameters M_χ and SI/SD cross sections but also a number of other factors which enter into the calculation. It is important to understand how uncertainties in these different factors and parameters propagate into the event rate in order to ensure that the conclusions we draw from direct detection experiments are reliable [184]. These uncertainties are divided into three separate classes: nuclear physics, particle physics and astrophysics.

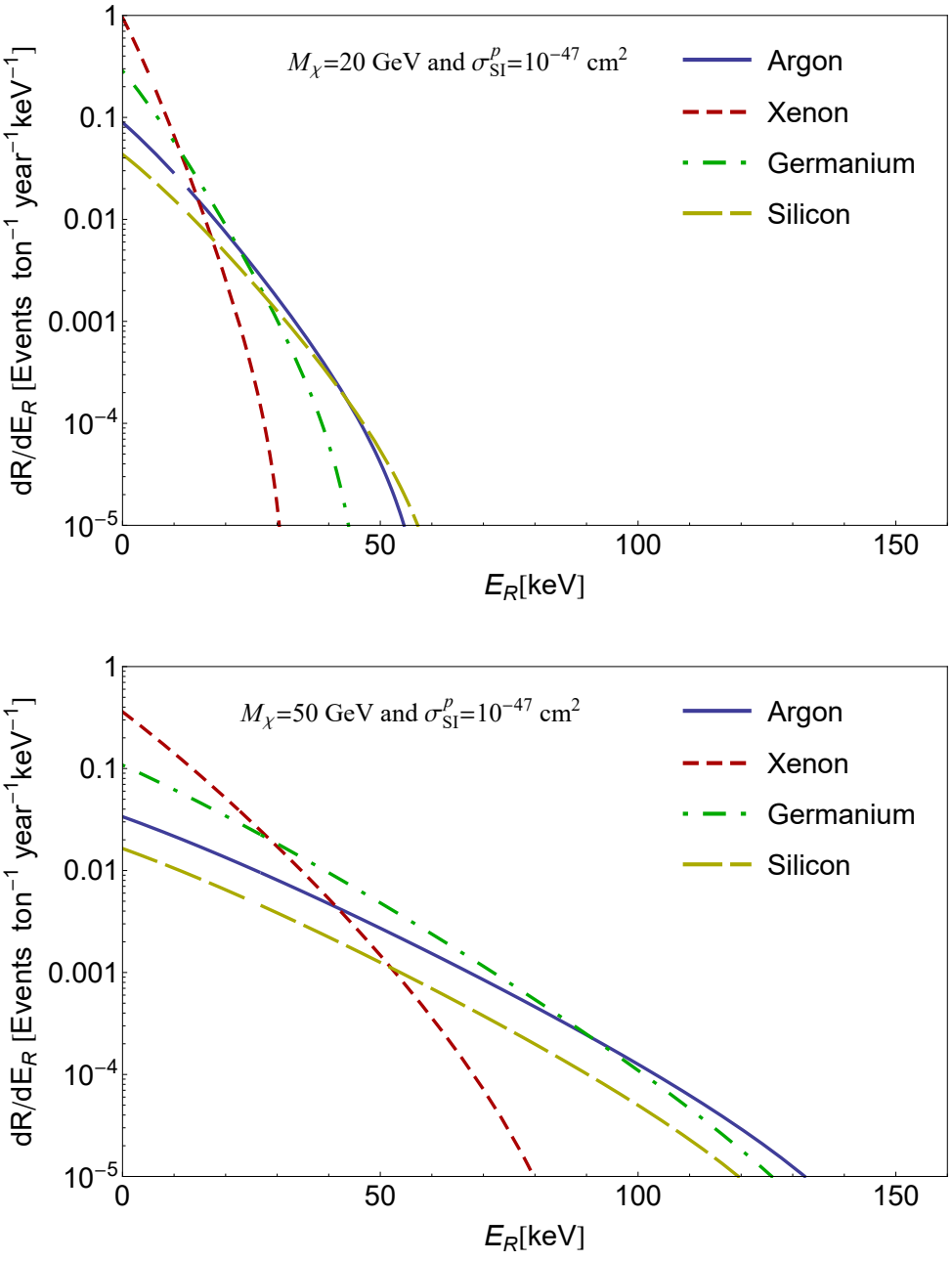

Fig. 3.9.: Spin-independent differential event rates predicted for the nuclear targets Argon (solid blue), Xenon (dashed red), Germanium (dot-dashed green) and Silicon (dashed yellow) and for $M_\chi = (20 \text{ and } 50)$ GeV, assuming $f_p = f_n$. We assume a Standard Halo Model speed distribution, $\rho_0 = 0.3$ GeV cm^{-3} and a spin-independent cross section $\sigma^{\rm p}_{\rm SI} = 10^{-47}$ cm^2. The Helm form factor [185] is assumed (see Sec. 3.5.1).

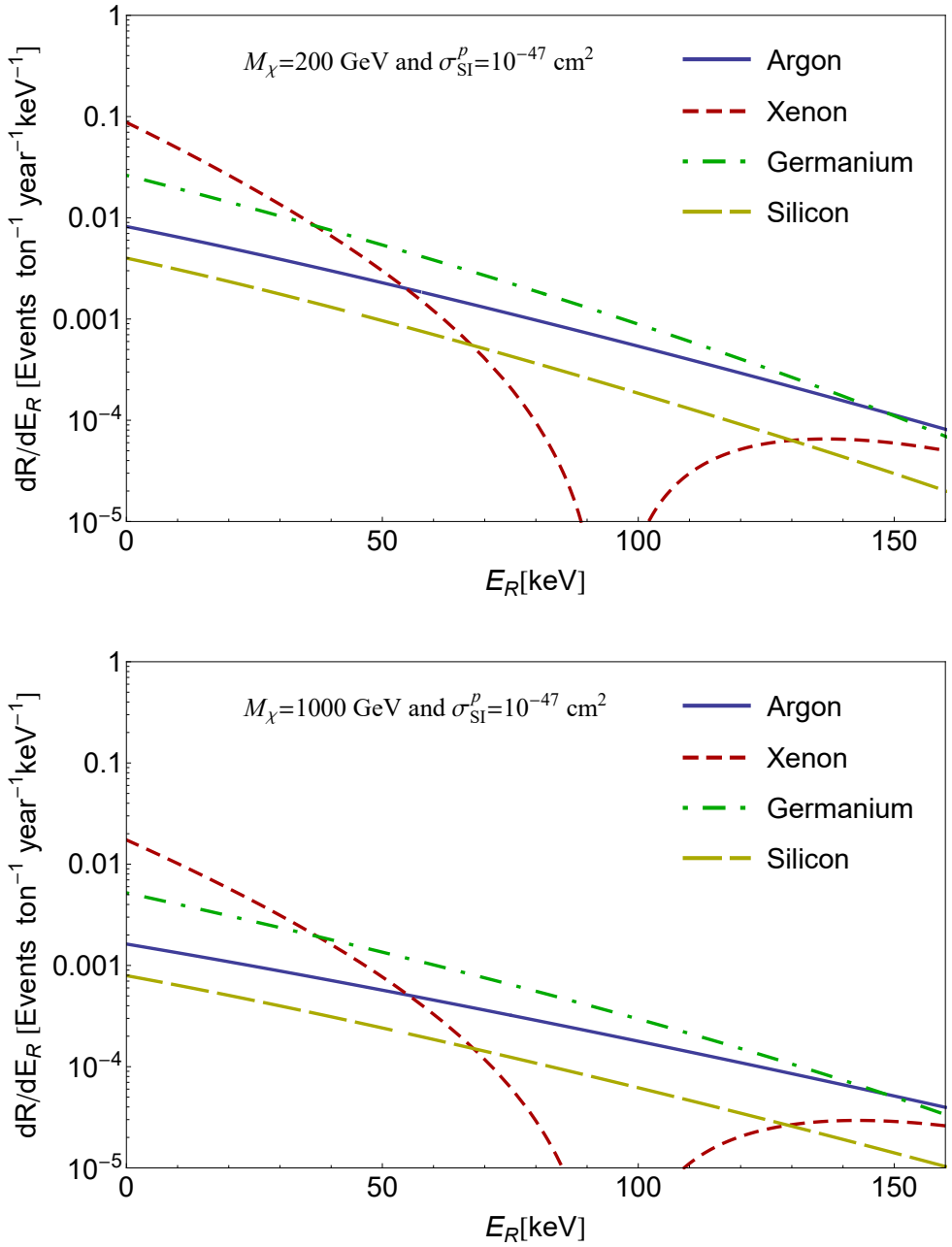

Fig. 3.10.: Spin-independent differential event rates predicted for the nuclear targets Argon (solid blue), Xenon (dashed red), Germanium (dot-dashed green) and Silicon (dashed yellow) and for $M_\chi = (200\,\text{and}\,1000)$ GeV, assuming $f_p = f_n$. We assume a Standard Halo Model speed distribution, $\rho_0 = 0.3$ GeV cm^{-3} and a spin-independent cross section $\sigma^{\rm p}_{\rm SI} = 10^{-47}$ cm^2. The Helm form factor [185] is assumed (see Sec. 3.5.1).

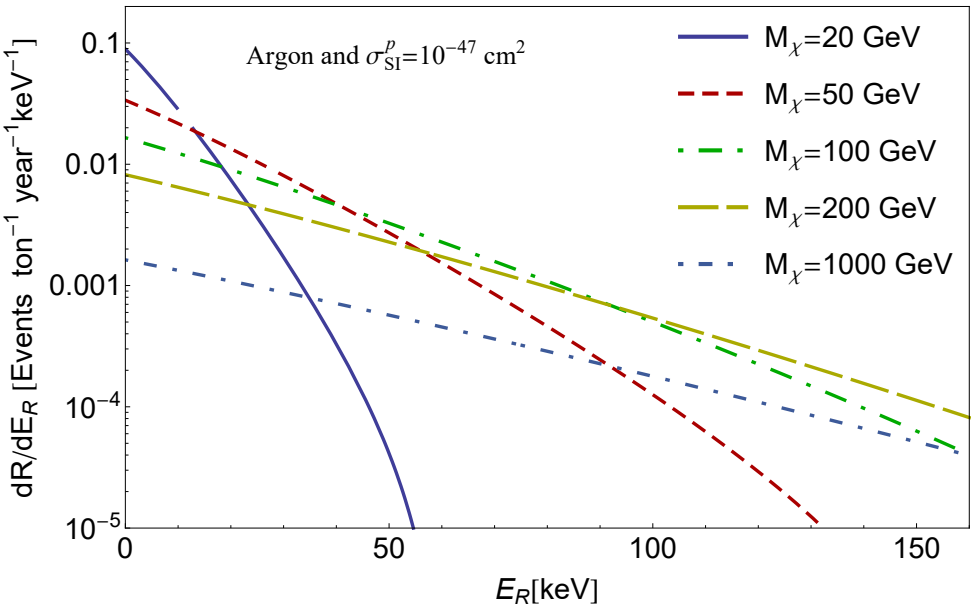

Fig. 3.11.: Spin-independent differential event rates predicted for argon and for different WIMP masses $M_\chi = (20,\ 50,\ 100,\ 200$ and $1000)$ GeV, assuming $f_p = f_n$. We assume a Standard Halo Model speed distribution, $\rho_0 = 0.3$ GeV cm^{-3} and a spin-independent cross section $\sigma^{\rm p}_{\rm SI} = 10^{-47}$ cm^2. The Helm form factor [185] is assumed (see Sec. 3.5.1).

3.5.1 Nuclear physics uncertainties

If one considers the nucleon-level effective operators (and equivalently the WIMP-nucleon cross sections) the main uncertainty related to nuclear physics which affects the WIMP rate calculation is that concerning the coherent nature of the interaction. Indeed, the predictions rely on the assumption that proton and neutron form factor are the same. Moreover due to the lack of knowledge of the neutron distribution inside the nucleus, it is generally assumed that the proton form factor could provide a good description also for the neutron part. The key parameter that is assumed to be the same is the radius of both proton and neutron distributions, that in turn determine the form factor shape. This assumption is relatively well motivated, since theoretical models point out to a difference between neutron and proton radius in the range 0.1-0.2 fm. However, there are very few experimental indications that this difference could be larger [213] leading to a sizeable effect in the predicted number of WIMP events. This issue will be scrutinized in Chap. 7.

If one, instead, wishes to deal directly with quark-level couplings, he has to consider nucleon matrix elements. As we have already seen, nuclear physics enters into the calculation of the nucleon matrix elements $m_n f^n_{Tq} \equiv \langle n|m_q \bar{q} q|n\rangle$ in Eq. 3.10. The factors f^n_{Tq} must be determined experimentally, and have values

$$f^p_{Tu} = 0.020 \pm 0.004,\ f^p_{Td} = 0.026 \pm 0.005,\ f^p_{Ts} = 0.118 \pm 0.062\,, \tag{3.66}$$

with $f^p_{Tu} = f^n_{Td}$, $f^p_{Td} = f^n_{Tu}$ and $f^p_{Ts} = f^n_{Ts}$. The main uncertainties come from the determination of the π-nucleon sigma term, determined either experimentally from low energy pion-nucleon scattering [214, 215, 178] or from Lattice QCD calculations [179, 216]. Similarly, the spin contributions Δ_q to the nucleus values must be obtained experimentally [217, 218, 183, 219] and they are

$$\Delta^p_u = 0.77 \pm 0.08;\ \Delta^p_d = -0.38 \pm 0.08;\ \Delta^p_s = -0.09 \pm 0.08\,, \tag{3.67}$$

although efforts are being made to obtain these values directly via calculation [220, 221].

3.5.2 Particle physics uncertainties

Like the WIMP mass M_χ and SI/SD cross sections also the ratio of proton to neutron couplings must be determined experimentally. In the case of SI scattering, the dominant contribution comes from the coupling to strange quarks f_{Ts}, which is equal for protons and neutrons. It is therefore typically assumed that $f^p = f^n$, even though one can consider also isospin violating dark matter models [222, 223, 224]. Similarly, for the SD interaction, a specific relation is typically assumed between the proton and neutron couplings, such as $a_p/a_n = \pm 1$. While specific models often predict such a relation [92], it should be noted that this ratio is a model dependent quantity.

Further uncertainty is derived from the form of the interaction terms themselves. Here, we have considered the dominant contributions to scattering in the case of non-relativistic contact interactions. Extensions including mediator particles have been considered [225, 226], as well as models in which DM can interact electromagnetically with nuclei [227, 228]. There has also been significant effort towards developing a general non-relativistic field theory for the interaction of WIMPs with nuclei [175, 229, 181, 177]. Current limits can be translated into limits on the couplings associated with a range of effective operators. While this

approach significantly widens the parameter space of dark matter direct detection, it is more general and does not rely on assumptions about DM interactions.

3.5.3 Astrophysical uncertainties

Astrophysical uncertainties enter into the direct detection event rate through the local dark matter density ρ_0 and the speed distribution $f_1(v)$.

DM density, ρ_0

The DM mass density sets the overall scale of the scattering rate, meaning that an accurate determination is important. However, being a scale factor it does not affect the outcome of the comparison between different experiments that assume the same DM density.
A possible method to obtain the value of ρ_0 is by mass modelling of the Milky Way. To do so it is necessary to build a model for the Galaxy incorporating various sources of mass, including first of all the DM halo, the stellar bulge, disc and also dust [230]. Fitting the velocities of some selected tracers, the total Milky Way mass, the local surface mass density and other similar data it is possible to derive the parameters of the model and extract ρ_0. Estimates using this method have generally a big uncertainty, typically lying in the range $0.2 - 0.4$ GeV cm^{-3} (see e.g. Ref. [230]). A recent determination combining different data sets obtains a value of $\rho_0 = 0.47^{+0.05}_{-0.06}$ GeV cm^{-3} [231].

An alternative method is to use local stellar kinematic data to constrain the gravitational potential near the Sun and thus obtain an estimate of ρ_0. Using kinematic data from roughly 2000 K-dwarfs, Garbari et al. [232] obtain the value $\rho_0 = 0.85^{+0.57}_{-0.50}$ GeV cm^{-3} while Zhang et al., using a larger sample of 9000 K-dwarfs, obtain 0.28 ± 0.08 GeV cm^{-3}. Including microlensing data, the range of allowed values at 1σ is $\rho_0 = 0.20 - 0.56$ GeV cm^{-3} [233]. A further model independent method was proposed by [234]. The advantage of such approaches is that one does not need to assume a particular form for the DM halo density profile.

In spite of the large number of determinations, no consistent value appears to be emerging, with values ranging from $0.2 - 0.6$ GeV cm^{-3}. There also remain a

number of uncertainties in these determinations, including the shape of the DM halo.

In order to have a common value the DM community agreed to adopt a standard value for the analysis of direct detection experiments of 0.3 GeV cm^{-3}. The same value will be assumed through this thesis.

DM speed distribution

As we have seen, the SHM distribution is obtained assuming a spherical, isothermal DM halo with density profile $\rho \sim r^{-2}$ that results in the relation $\sigma_v = v_0/\sqrt{2}$.

In this section, I want to highlight the main source of uncertainties that affect the parameters that enter into $f_1(v)$.

In particular, we have seen that the parameter v_0 is given by the local circular speed $v_c = 220 \pm 10\,\text{km s}^{-1}$ [235] plus a contribution from the peculiar motion of the Sun and the Earth's orbital motion. In the SHM, this speed is typically assumed to be close to the local circular speed, though more recent determinations of the solar velocity point towards higher values [236, 237], of about $240 - 250\,\text{km s}^{-1}$. Also σ_v is affected by some uncertainties. The relation $\sigma_v = v_0/\sqrt{2}$ is obtained from solving the Jeans equation assuming $\rho \sim r^{-2}$ [238]. Relaxing this assumption means that this relation no longer holds and that σ_v is no longer as well constrained. Finally, the Galactic escape speed can be estimated from the radial velocities of Milky Way stars. The RAdial Velocity Experiment (RAVE) survey, that covered 20000 square degrees of the sky, obtained the range for the radial velocity $v_{\text{esc}} = 544^{+64}_{-46}\,\text{km s}^{-1}$ at 90% confidence level [239].

Even taking into account these uncertainties, there are some reasons to believe that the SHM is unlikely to be an accurate representation of the DM halo. Among others, observations and N-body simulations that indicate that the halo should deviate from a $1/r^2$ profile and may not be spherically symmetric. To take these effects into account, alternative models have been proposed, like speed distributions associated with triaxial halos [240] or with more realistic density profiles [241], as well as analytic parametrisations which should provide more realistic behaviour at low and high speeds [242]. It is also possible to extract the speed

distribution from N-body simulations. Such distribution functions tend to peak at lower speeds than the SHM and have a more populated high speed tail [243, 244, 245].
It should be noted that N-body simulations do not probe down to the sub-milliparsec scales which are probed by direct detection experiments. There may be a concern then that the local dark matter distribution could be dominated by localised subhalos or streams which are not captured by these simulations and which may affect the interpretation of direct detection experiments. However, an analysis of N-body simulations has found that no individual subhalos should dominate the local distribution [246].
Another result obtained from simulations that is not included in the SHM is the possibility of a dark disk (dd). When baryons are included in simulations of galaxy formation, this can result in DM subhalos being preferentially dragged into the disk plane [247, 248]. The resulting dark disk co-rotates with approximately the same speed as the baryonic matter, though with a smaller velocity dispersion $\sigma_v^{dd} \sim 50\,\mathrm{km\ s^{-1}}$. Recent ERIS results [249] suggest that this dark disk should contribute to just 10% of the density of the halo.

The impact of all these uncertainties to the WIMP speed distribution has been studied in several works (see e.g. Refs. [250, 251, 252]). It has been shown that poor assumptions about the speed distribution may result in biased reconstructions of the DM mass and cross sections from future direct detection data. Even when including some uncertainties in the shape of the MB speed distribution, these works suggest that there could be still a bias in the reconstructed WIMP parameters. If the MB speed distribution cannot reproduce the shape of the event spectrum closely, the WIMP mass and cross section move to different values to compensate and improve the fit. Not only a bias is introduced, but the resulting contours are also smaller, leading to the erroneous believe that one could reconstruct the WIMP parameters with a higher precision.

However, despite these limitations of the SHM, as in the case of the Helm form factor it still represents the most used prescription by the DM community to describe the DM speed in the Milky Way.

We now turn our attention to the discussion of real experiments and the current state of dark matter direct searches.

3.6 Direct detection experiments current limits and anomalies

In order to measure the event spectrum, a range of obstacles must be overcome. A number of backgrounds can cause nuclear recoils and therefore mimic a WIMP signal. Furthermore, electron recoils can also deposit energy in the detector and must be distinguished from nuclear recoils caused by WIMP interactions. I will now summarise some of these backgrounds and how they can be mitigated. I will then discuss some of the different technologies which are used to discriminate electron from nuclear recoils and to measure the recoil energy itself.

One possible source of background is constituted by high energy cosmic rays. For this reason, direct detection experiments are typically operated underground, such as at the Laboratori Nazionali del Gran Sasso (LNGS) in Italy or the SNOLAB laboratory in Canada, in order to reduce the penetration of these cosmic rays. However, cosmogenic muons and neutrons can still penetrate the experiments, leading to the need for active shields which can detect these particles and provide a veto for any nuclear recoils they produce. It is also possible to veto events which produce multiple-scatters in the detector as WIMPs are expected to scatter only once. Passive shielding also reduces the neutron flux from surrounding rock and other sources.

Radioactive decays due to naturally occurring isotopes may cause keV energy nuclear recoils in the detector, meaning that care must be taken to reduce their impact. The radiopurity of the target material is therefore of utmost importance, as well as the radiopurity of the detector equipment itself. In some cases, the naturally occurring target material is contaminated with a particular radioisotope, such as ^{39}Ar contamination in argon. In these cases, special sources of the material must be found [253], or the amount of contamination must be carefully reduced [3].

Scatterings of DM particles off nuclei can be detected via subsequently produced light (scintillation photons from excitation and later de-excitation of nuclei), charge (ionization of atoms in a target material) or heat (phonons in crystal detectors) see Fig. 3.12 for a summary scheme. Using one or a combination of two such discrimination techniques is now often employed to disentangle a potential WIMP signal from nuclear recoils and background electron recoils. This

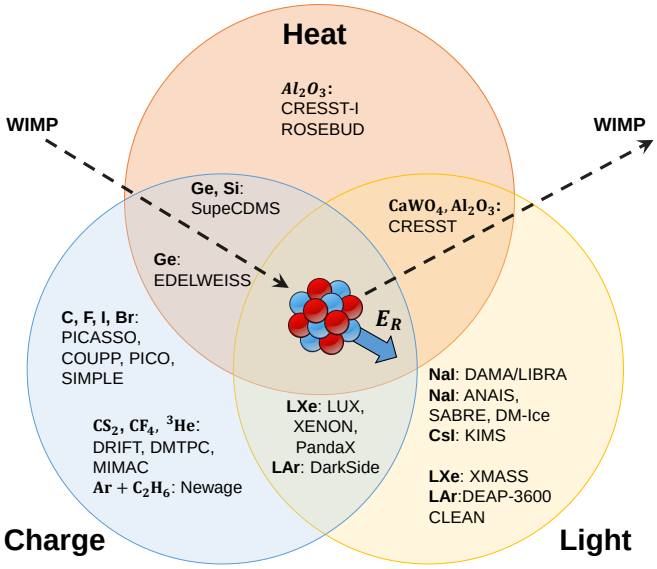

Fig. 3.12.: Direct dark matter detection experiments organised by energy deposition channel(s) used.

is possible due to different quenching factors that describe the difference between the recorded signal and the actually measured recoil energy. The electron recoils constitute the background of the experiment and can come from, e.g., γ-radiation from natural radioactivity or β-decays that take place in the detector surrounding materials, on its surface or even inside the detector. Other sources of background, e.g., neutrons or α-decays, can be associated with nuclear recoils that can mimic the WIMP signal. Therefore they need to be either screened out or rejected at the level of signal analysis. A particularly challenging type of such a background that will be very important for future detectors, especially for DM mass below 10 GeV, comes from coherent elastic neutrino-nucleus scatterings [254] and cause the existence of the so-called coherent neutrino background [255, 256]. This issue will be the main topic of Chap. 5.

Depending on the choice of signal detection technique a variety of target materials can be employed in DD searches. Light signal from DM-nucleus scattering can be collected, e.g., by using scintillating crystals.[8]

Crystal scintillator experiments such as DAMA/LIBRA [258, 259] use crystals of Thallium-doped Sodium Iodide, NaI(Tl), while KIMS [260] uses Thallium-doped Cesium Iodide, CsI(Tl), as the detector material. When a nuclear recoil

[8] Signal in single-phase liquid noble gas detectors also comes entirely from scintillation light emitted by ionized or excited dimers (for a review see [257]).

occurs with the nuclei in the crystal, scintillation occurs. The light is collected by photomultiplier tubes, with the total recoil energy being related to the amount of scintillation light produced. In the case of DAMA/LIBRA, electron-nuclear recoil discrimination is not employed. The experiment aims to observe the annual modulation of the signal which is expected due to the periodic motion of the Earth through the WIMP halo, as explained in Sec. 3.3.1. In other cases, such as NAIAD [261], pulse shape discrimination has been used to distinguish nuclear and electron recoils.

Phonon signal coming from DM-nuclei scattering in crystals can provide another important experimental signature in DM DD searches. This technique is particularly useful when looking for low mass DM due to a very low energy threshold. Moreover, one typically further improves the treatment of the background in such experiments by using cryogenic bolometers with additional charge or scintillation light readouts.

Cryogenic experiments, such as CDMS [262], CRESST [263], CoGeNT [264, 265] and EDELWEISS [266], use cryogenic crystals of materials such as germanium or silicon as target materials. When a WIMP recoils from a target nucleus, phonons are generated in the crystal along with an ionization signal. By summing the energy collected in these two channels (and accounting for any which may be incompletely collected), the total energy of the nuclear recoil can be obtained. The ratio of the total nuclear recoil energy and the ionization signal is referred to as the "ionisation yield" and can be used to discriminate electron from nuclear recoils. Indeed, electron recoils deposit more energy into ionisation. However, care must be taken to identify so-called "surface events", events occurring close to the detector surface which result in an incomplete collection of ionisation signal and can thus mimic a WIMP signal.

Noble liquid experiments use liquid (or two-phase) noble elements such as xenon and argon as target materials. Completed or operational xenon detectors include XENON1T [267], LUX [268] and PandaX-II [269]. In these detectors, xenon recoils produce a scintillation signal (S1) which can be observed directly using photomultiplier tubes. Ionisation electrons are also produced, which drift in an applied electric field, producing an electroluminescence signal (S2) in the gas phase. The sum of these signals can be used to reconstruct the total recoil energy, while the ratio S2/S1 is used to discriminate electron from nuclear recoils. The two signals can also be used to localise the event within the detector. A fiducial

volume is then defined within the detector, only events inside this volume are considered in data analysis. This allows liquid noble detectors to be self-shielding; the fiducial volume is in fact shielded by the remaining detector volume. The xenon technology has been used earlier in comparing to that of argon. The pioneer experiment utilising argon has been the WARP experiment [270]. The DarkSide-50 experiment, at LNGS, is currently operating as a dual-phase liquid argon TPC using timing of the scintillation signal (pulse shape discrimination) as a discriminant.

DM-nuclei scatterings also can be detected via heat signal in experiments based on superheated fluids used as a target material. DM particle passing through a detector can then be visualized thanks to an initiated process of bubble creation. Superheated liquid detectors such as COUPP [271], SIMPLE [272] and PICASSO [273] use a detector volume filled with droplets of superheated liquid such as C_4F_{10}. The deposition of kinetic energy by a WIMP will induce the nucleation of a bubble producing an acoustic signal which is detected by piezoelectric transducers. Energy deposition by other particles, such as muons, γ- and β-radiation, typically occurs over longer length scales and thus does not produce a signal. The temperature and pressure of the detector can be tuned to specify the threshold energy, the minimum energy which must be deposited before nucleation occurs. As such, superheated liquid detectors cannot measure the energy of specific events but rather the total event rate above the energy threshold. However, by increasing the latter, the recoil spectrum can effectively be measured. Due to the light targets such as fluorine used by these experiments, they are typically more sensitive to light WIMPs with SD interactions.

A final class of direct detection experiments are known as “directional” direct detection experiments. These aim to measure not only the energy deposited by WIMP scattering events but also the direction of the nuclear recoils. It is hoped that a recoil spectrum peaked in the direction opposite to the Earth’s motion will provide strong evidence for a DM origin for the recoils. One possibility for this is the use of specialised gas TPCs, which allow measurable track lengths from which the recoil direction can be determined. Unfortunately, this kind of detectors are limited in mass. Another possibility is to exploit the so-called columnar recombination effect [274] in double-phase liquid noble TPC. The directional detection of dark matter will be the subject of Chap. 6.

3.6.1 Current limits and results

In this section, I will review some of the experimental results in the direct dark matter detection. The DAMA/LIBRA experiment [258] operating at the LNGS laboratory in Italy, for two decades has been reporting to see an annually modulated DM-like signal, which currently has a significance at the level of 9.3σ [259]. The estimated mass of the DM particles from this measurement would range between 10 to 15 GeV or between 60 to 100 GeV depending on the actual nucleus involved in the scattering process (sodium or iodine, respectively). However, the DM interpretation of these results is in strong tension with null results published by some other collaborations: the first XENON1T limit [275], the final LUX [276] and the PandaX-II [269] limits, as well as, in the low mass region, with the limits from CDMSlite [277] and XMASS [278], which excluded the annual modulation of DM interpretation of the effect claimed by DAMA/LIBRA. Alternative explanations were also considered, including unknown source of background, as well as possible errors in data collection and processing (for a review see Ref. [279]). In addition, other experiments employing similar detection strategy have been proposed to verify the DAMA/LIBRA results. In particular, the results of the KIMS-CsI experiment [260] disfavour the interpretation of DAMA/LIBRA signal in which the DM particles scatter off iodine nuclei. This could be circumvented in specific scenarios, e.g., for Magnetic Inelastic DM (see, however, the recent XENON1T limit [280]), in models with dominant WIMP inelastic spin-dependent coupling to protons if different quenching factors are assumed in both experiments [281, 282] (for an detailed discussion see also Ref. [283] and for recent limits see Ref. [284]) or leptonically interacting DM particles that induce electron recoils [285].

An annual modulation signal was also observed in the CoGeNT experiment [264, 286, 287]. In this case too, the period and phase are consistent with expectations, though, the amplitude of the annual modulation is approximately 5 times larger than expected. The CoGeNT experiment observed an exponentially rising excess of events at low energies, down to 0.5 keV$_{ee}$ (electron equivalent recoil energy). A maximum likelihood analysis [287] pointed towards a ~ 8GeV WIMP interpretation, with a cross section of around $\sigma^p_{SI} \sim 5 \times 10^{-41}$ cm^2, though the significance of the "signal" lies at only 2.8σ. This signal was not confirmed in later searches in the similar mass range. On the other hand, the observed excess of events may be fully explained when an improved background treatment is applied, as pointed out in Ref. [288, 289]. The DM interpretation of the CoGeNT

data has also been disfavoured by other germanium detectors, e.g., CDEX [290] and MALBEK [291]. A halo-independent analysis performed in Ref. [292] for light ($\sim 10\,\mathrm{GeV}$) WIMPs showed a strong tension between the DM interpretation of the annual modulation of DAMA/LIBRA and CoGeNT events when compared with the CDMS-II silicon data.

Another DM-like signal was found in the data obtained by the CRESST-II Collaboration [263] in 2011. An excess in the expected number of events was observed in two mass ranges around $10\,\mathrm{GeV}$ and $25\,\mathrm{GeV}$ with the significance at the level of 4.2σ and 4.7σ, respectively. However, as it was pointed out in Ref. [293] and confirmed in a later study by the collaboration [294], the excess was mainly due to a missing contribution to the background (see also Ref. [283] and [279] for an updated discussion).

Finally, a recent analysis of the Silicon detector data from CDMS-II (CDMS-Si) [295] found 3 events in the signal region. However, the very low expected background means that this small number of events may be significant. The probability of the known backgrounds producing these three events has been calculated at 5.4% and a likelihood analysis shows consistency with a WIMP with $M_\chi \approx 9$ GeV and $\sigma^p_{SI} \approx 2 \times 10^{-41}$ cm^2. However, these results were not confirmed by the germanium CDMS-II [296], SuperCDMS [297] and CDMSlite [277] detectors and there is no plausible DM halo function for which this tension could be alleviated unless one assumes, e.g., exothermic DM with Ge-phobic interactions as discussed in Ref. [298]. Moreover, these results are in tension with those found by the EDELWEISS-III collaboration [299].

An alternative explanation is that the claimed signals are due to a DM particle, but that its properties are not as simple as in the canonical case, explaining why it has not been observed in all experiments. One possibility is that the astrophysical distribution of DM does not match the standard assumptions. I discussed this astrophysical distribution shortly in Sec. 3.5.3. However, it appears that even with this additional freedom, the different results cannot be reconciled [300, 301, 302, 303]. A number of particle physics models have also been considered to explain the results, including spin-dependent interactions [304], isospin violating dark matter (for which $f^p \neq f^n$) [222], inelastic dark matter [305] and mirror dark matter [306]. However, a consistent picture which reconciles all experimental datasets remains elusive [307].

The most stringent current limit on $\sigma^{\mathrm{p}}_{\mathrm{SI}}$ for large DM mass comes from null results of DM searches in dual phase (liquid-gas) xenon detectors: XENON1T [275] and PandaX-II [269], both of which are the most recent (and currently the strongest) limits, and the final LUX result [276]. All these three limits improved the previous best limit set by the XENON100 collaboration [308], see Fig.3.13. Overlaid in the figure, there is also the WIMP search discovery limit @3σ when considering the presence of the coherent neutrino background [256]. This is the so-called neutrino floor and it would be extensively explained in Chap. 5. Moreover, in the same figure the representative minimal supersymmetric model contours @2σ are shown. They represents the allowed regions once taking into account the experimental constrains on SUSY models after Run 1 at the Large Hadron Collider [309].

Moving to the spin-dependent case, the strongest up-to-date exclusion limits for spin-dependent cross section, $\sigma^{\mathrm{p}}_{\mathrm{SD}}$, from DD experiments were published by the PICO collaboration [314, 315] (see also LUX [316] and XENON100 [308] results). However, $\sigma^{\mathrm{p}}_{\mathrm{SD}}$ can also be effectively constrained by neutrino telescopes. See Fig. 3.14 for a summary plot of $\sigma^{\mathrm{p}}_{\mathrm{SD}}$ limits and future projections.
Concerning future plans, the PICO bubble chamber detectors can be made very large, have extremely low backgrounds, and work with diverse target nuclei. Most important recent scientific impacts have come from $\mathrm{C_3F_8}$ targets, where the $^{19}\mathrm{F}$ nucleus gives unique sensitivity to spin-dependent WIMP couplings to the proton. Due to coherent enhancement of the background neutrino rate, the ultimate background from atmospheric and solar neutrinos is expected to be two orders of magnitude lower for $\mathrm{C_3F_8}$ than for xenon, when cast in terms of spin-dependent sensitivity. In addition to the $\mathrm{C_3F_8}$ program, the PICO Collaboration is investigating alternative targets for future searches in PICO-40L, PICO-500, or an array of PICO-500 detectors.

It is important to note that the limits presented in the WIMP mass and WIMP-nucleon cross section plane can vary depending on the underlying assumptions about relevant astrophysical quantities, e.g., the local DM density and the DM velocity distribution. The dependence on the velocity distribution is typically weak [327], but can become more important, e.g., if detector is sensitive only to the tail of the distribution [212]. Alternatively, the limits can be shown in a DM halo-independent way [328] (see also Ref. [329] and references therein) if a positive signal is measured by at least two different targets.

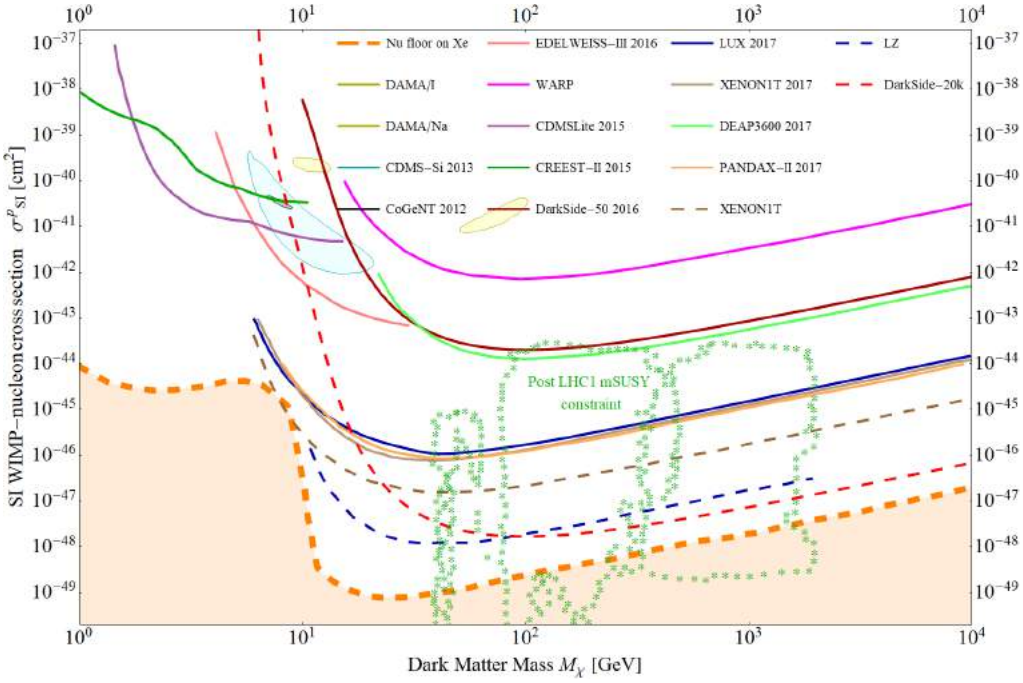

Fig. 3.13.: Current and future limits on DM direct detection spin-independent cross section, $\sigma_{\rm p}^{\rm SI}$ in cm^2, as a function of the WIMP mass, M_χ in GeV. The current limits are shown with solid orange (PandaX-II [269]), solid brown (XENON1T [275]), solid blue (LUX [276]), solid light green DEAP-3600 [310], solid dark red DarkSide-50 [10], solid light purple WARP [270], solid salmon pink EDELWEISS-III [299], solid dark green CRESST-II [311] and solid violet (CDMSlite-II [277]) lines. Future projections correspond to XENON1T [312] (dashed brown), LZ [313] (dashed blue) and DarkSide-20k [3], developed in this work (dashed red). Post-LHC-Run1 minimal-SUSY model allowed contours from ref. [309] are shown by green stars. The shaded areas on top of the plot correspond to the favoured regions for DM interpretations of anomalies reported in the literature by the CDMS-Si [295] (cyan), CoGeNT [264] (black-grey), CRESST-II [263] (light blue) and DAMA/LIBRA [258] (light yellow) collaborations. The shaded area below the dashed orange line on the bottom of the plot corresponds to the 3σ discovery limit for xenon in the presence of an irreducible neutrino background [256].

Implications for WIMP models Direct detection searches play a vital role in constraining various WIMP models. For instance, early negative results from the Heidelberg-Moscow experiment [330] led to an exclusion of the scenario in which the majority of DM was composed of the left-handed sneutrinos in the MSSM [331]. Since then, many other theoretical candidates have been constrained by null results of searches for the DM particles in DD experiments.

Limits from DD have also been derived on effective contact operators describing possible interactions between DM and the SM particles (see for example Refs. [332, 333]). One can then translate the usual DD limits shown in the $(M_\chi, \sigma_{\rm SI}^{\rm p})$ plane into the actual limits on the coefficients of the operators that contribute

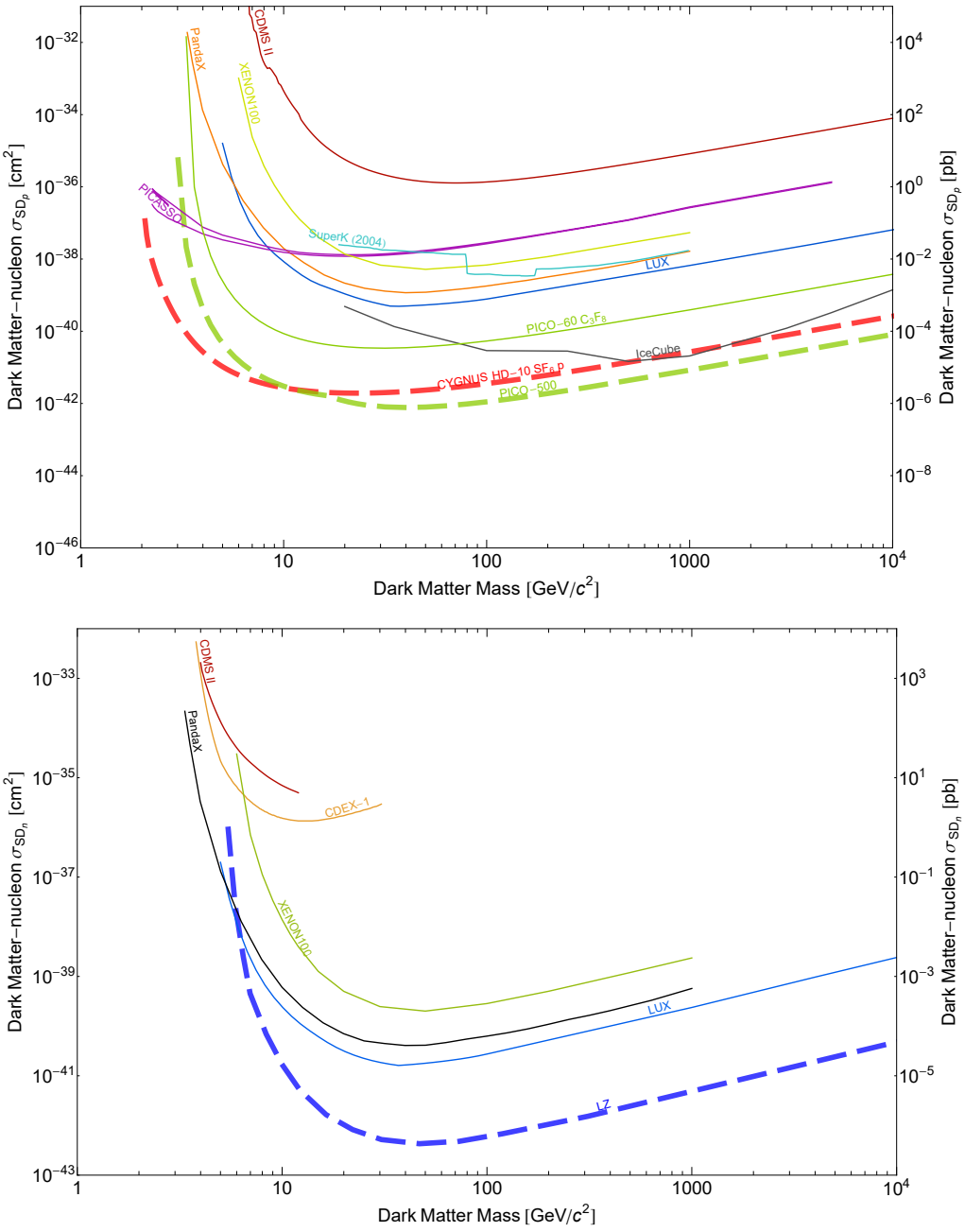

Fig. 3.14.: (Upper panel) Current and future limits on DM direct detection spin-dependent cross section on proton as a function of the dark matter mass. The current limits are shown with solid dark red (CDMS-II [317]), light yellow (XENON100 [308]), light blue Super-Kamiokande [318], purple PICASSO [319], orange PandaX [320], dark blue LUX [321], light green PICO-60 [322] and black IceCube[323] lines. Future projections correspond to CYGNUS HD-10 (red dashed) and PICO-500 [324] (green dashed). (Lower panel) Current and future limits on DM direct detection spin-dependent cross section on neutron as a function of the dark matter mass: (solid red) CDMS-II [325], (solid orange) CDEX-1 [326], (solid green) XENON100 [308], (solid black) PandaX-II [320], (solid blue) LUX [321] and the projected sensitivity for LZ (dashed blue).

to $\sigma_{\rm SI}^{\rm p}$, while the other coefficients remain free and can, e.g., help to achieve the proper value of the DM relic density. Stronger constraints can be obtained when both direct and indirect detection searches are taken into account (see for example Ref. [334]).

Another phenomenological approach consists in expanding the contact operator approach by introducing specific mediators ("portals") between the DM sector and the SM particles in a framework of so-called simplified models as suggested in Refs. [335, 336, 337, 338, 339]. It has been pointed out that gauge invariance and perturbative unitarity need to be carefully taken into account when constructing simplified models of DM interactions [340, 341]. For further discussion about the effective theory approach (EFT) and simplified models see Ref. [342] and references therein.

3.6.2 Future experiments

Experiments which are planned or under construction typically aim to scale up the size of current detectors and reduce unwanted backgrounds (in order to increase the sensitivity to lower cross sections) or decrease the energy threshold (which increases sensitivity to lower masses). In the low mass regime large part of the (M_χ, $\sigma_{\rm SI}^{\rm p}$) parameter space will be probed by the future germanium and silicon detectors in the SuperCDMS experiment operating at SNOLAB [343]. In the high mass region, there are a number of xenon ton scale detectors either in operation or planned for the near future, including the currently running XENON1T [267], and the future XENONnT [312] and LZ [313]. More far away in the future there is the project to build a 50 tonne (40 tonne active) detector called DARWIN [344]. Similarly, using argon as a target material, there is the currently running DEAP3600 [345], ArDM [346] and the future DarkSide-20k [3]. The argon dark matter community has recently coalesced into a Global Argon Dark Matter Collaboration (GADMC), with the goal of constructing and operating a 300 tonne argon detector allowing a kilotonne-year exposure for a dark matter search, which will follow the DarkSide-20k experiment at LNGS.

With this next generation of detectors, the aim is to achieve sensitivity to the SI WIMP-nucleon cross section down to $\sigma_{SI}^{p} = 10^{-48}$ cm^2. Below this value, irreducible backgrounds from solar and atmospheric neutrinos become important and the identification of a DM signal becomes more difficult [347].

There have also been a number of proposals for novel methods of directly detecting dark matter. These include using DNA-based detectors to provide high spatial resolution [348], using nano-scale explosives [349] or charged-coupled devices [350] to achieve very low energy thresholds and using proton-beam experiments as a source of dark matter for direct detection experiments [351]. It has also been suggested that the direct detection experiments could be used to search for DM interactions with electrons, rather than nuclei (see e.g. Refs. [352, 353]). Clearly, there are a range of approaches being pursued both in refining current technologies and developing new ones.

3.7 Conclusions

In this chapter, I have discussed the dark matter direct detection formalism, focusing on the contribution from scalar and axial-vector contact interactions. I have shown that the event rate can be divided into a spin-dependent and spin-independent contribution. After analysing all the different ingredients that enter the definition of the differential energy recoil spectrum, I have shown the final WIMP rate for different nuclei target and its dependence on the assumed WIMP mass. Finally, at the end of the chapter, I have discussed a number of sophisticated experiments that have been and continue to be developed which should allow the rare nuclear recoils produced by these interactions to be detected. The use of different channels such as scintillation, ionisation and phonons not only allows the energy of these events to be measured but also aids discrimination against electronic recoils which can act as a significant background.

Tentative hints of a signal from the DAMA/LIBRA, CRESST-II and CoGeNT experiments have been interpreted as evidence for a WIMP with mass $M_\chi \sim 10$ GeV and cross section $\sigma^p_{SI} \sim 10^{-41}$ cm^2. However, null results from XENON, CDMS, EDELWEISS-III and other experiments are in tension with this claimed signal. The origin of this discrepancy may lie in unidentified backgrounds or in an unconventional model for DM. Thus, corroboration from indirect and collider experiments is eagerly needed before such a signal can be confirmed.

As visible from Fig. 3.13, the post-LHC-Run1 minimal-SUSY model allowed contours show a preference for a WIMP mass between 50 GeV and 3 TeV and WIMP-nucleon cross section between $\sim 10^{-43}$cm^2 and $\sim 10^{-50}$cm^2. This preferred region has been further reduced by the recent results of XENON1T and PandaX-II

collaborations. The first has set the best limit on SI WIMP-nucleon cross section excluding the values down to $7.7 \times 10^{-47}\text{cm}^2$ for a 35 GeV WIMP mass while the second possesses the best limit for WIMP masses larger than about 100 GeV. In order to explore lower cross sections in this mass range it is necessary to build ton scale experiments. The most promising technology is represented by xenon and argon double-phase TPCs. These experiments are the future XENONnT, LZ, DARWIN with a xenon target and DarkSide-20k and GADMC for an argon target. They will explore the cross sections down to the $\sim 10^{-48}\text{cm}^2$ thanks to exposures of the order of tens (hundreds) of tonne year for xenon (argon).

At these exposures, the contribution of the coherent scattering of atmospheric and diffuse supernova neutrinos (and even from solar neutrinos for low threshold energies) starts to contribute becoming an irreducible source of background that needs to be carefully taken into account. The impact of this background on the sensitivity curves of DarkSide-20k, that will be described in Chap. 4, and future developments will be the topic of Chap. 5.

4 DarkSide-20k

Contents

4.1 Overview and goals of DarkSide-20k 86

4.2 Experimental design of DarkSide-20k 93

4.3 Procurement and purification of the underground argon target 98

4.4 Physics reach 100

I have shown in the previous chapter that, despite the worldwide efforts to search for dark matter the motivation for direct WIMP searches remains extremely strong, especially for high (above a few hundred GeV) masses that will be out of the LHC reach, and the region of low cross sections ($10^{-45}\,\mathrm{cm}^2$ to $10^{-48}\,\mathrm{cm}^2$) corresponding to Higgs-mediated scattering [354]. To discover the nature of dark matter particles, it is important for direct and indirect detection to reach new levels of sensitivity, improving them by a few orders of magnitude. For the direct detection searches, the ability to build experiments able to operate in a background-free mode will be crucial for a possible discovery of dark matter.

In this chapter I will focus in particular on an argon based DM detector called DarkSide-20k. The DarkSide-20k experiment has been proposed in 2015 and aims at a significant improvement in the sensitivity for the direct detection of WIMPs. It is proposed to achieve this goal with a liquid argon time projection chamber (LAr TPC) experiment with an active (fiducial) mass of 23 tonne (20 tonne), for a total exposure of 100 tonne year (t yr) to be accumulated in a run of 5 years. Thanks to its exceptionally low instrumental background, DarkSide-20k could extend its operation to a decade, increasing the exposure to 200 t yr.

The following chapter is based on Ref. [3], selecting the most relevant parts for this thesis.

4.1 Overview and goals of DarkSide-20k

Being dark matter interactions very rare, and the onset of ν-induced nuclear recoils for exposures of 100 tonne year and beyond, it is of utmost importance to contain the number of instrumental background interactions to <0.1 events , so that a positive claim can be made with as few events as possible. A discovery for dark matter could come at any exposure level, and even a low but non-zero instrumental background can hinder the task of discovering DM.

Among the variety of detector technologies, noble liquid TPCs, which detect both the scintillation light and the ionization electrons produced by recoiling nuclei, have significant advantages for direct dark matter searches. For liquid argon, the powerful discrimination against background using the time-development of the primary scintillation signal (pulse-shape discrimination or PSD), the precise determination of event positions in all three dimensions given by the TPC, and the effectiveness of chemical and cryogenic purification of the argon have all been demonstrated (see Refs. [355, 356] and references cited therein). The specific goal of searching for and discovering high-mass dark matter particles allows the search to be concentrated in the range of recoil energies from 30 keV to 200 keV (WIMP search region). In this region, argon detectors outperform other technologies with their outstanding β/γ background rejection, as verified by WArP [357] and DarkSide-50 [356].

The DarkSide Collaboration has published background-free WIMP search results (<0.1 events expected and no observed events in the search region) from an exposure of $(1422 \pm 67)\,\mathrm{kg}$ day with atmospheric argon (AAr) [356] and from a separate exposure of $(2616 \pm 43)\,\mathrm{kg}$ day with underground argon (UAr) [358]. The combined result of the AAr and UAr data analysis, leads to the expectation that a result free from instrumental background can also be obtained from a much larger exposure with a multi-tonne detector.

In addition to choosing a detector technology and target, the exact configuration of the target is an important choice. The light quenching in LAr introduced by the presence of a drift field was first discovered and then precisely measured by the SCENE experiment [359]. The precise measurements obtained with SCENE leads to the choice of a drift field of 200 V/cm, which minimally penalizes the light yield of nuclear recoils, containing its loss within 10%, and resulting in a barely noticeable loss of performance. Ultimately the reconstruction of energy of

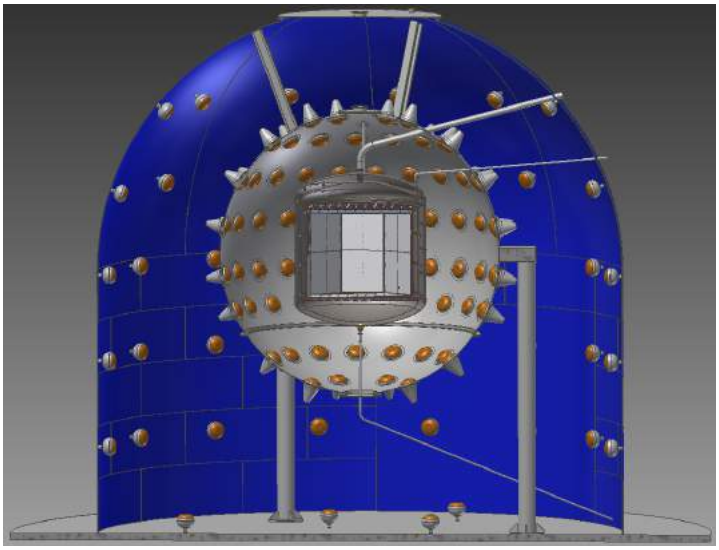

Fig. 4.1.: Cross sectional view of the DarkSide-20k experiment through its center plane, showing the water tank and the WCV detector, the stainless steel sphere and LSV detector, and the cryostat and LAr TPC.

the events is based on the consideration of both the scintillation signal, S1, and the ionization signal, S2, and so a very good resolution can be obtained.

The choice of using single- or dual-phase geometry is driven by the need to obtain the best performance in WIMP dark matter searches, and not a need for optimizing event reconstruction in terms of S1 and f_{90}, the fraction of S1 light detected in the first $90\,\mathrm{ns}$ of the pulse. The dual-phase LAr detector DarkSide-50 has demonstrated an impressive performance in background rejection by producing two independent background-free results, with AAr [356] and UAr [358]. The dual-phase xenon detectors have also achieved an impressive performance and lead the race for WIMP dark matter sensitivity.

On this basis, an enlarged DarkSide Collaboration proposed the construction of DarkSide-20k, a direct WIMP search detector using a LAr TPC with an active (fiducial) mass of $23\,\mathrm{t}$ ($20\,\mathrm{t}$) of UAr. As shown in Fig. 4.1, the DarkSide-20k TPC will be located underground at LNGS. DarkSide-20k will be a detector with ultra-low background levels and the ability to measure its backgrounds *in situ*. The projected sensitivity of DarkSide-20k which is one of the main topics of this thesis and that will be carefully illustrated in Chap. 5, is compared with other current and planned projects in Tab. 4.1.

Tab. 4.1.: Comparison of sensitivity for current dark matter experiments leading the search for high mass WIMPs and of future approved and proposed experiments. Also included are the calculated sensitivities for hypothetical xenon and argon-based experiments with an expectation of one coherent neutrino-nucleus scatter during their operation and with thresholds of 10 keV and 30 keV, respectively.

Experiment	Target	Exposure/[t yr]	$\sigma/[\mathrm{cm}^2]$ @1 TeV/c^2	$\sigma/[\mathrm{cm}^2]$ @10 TeV/c^2	Reference
DarkSide-50	Ar	0.011	9×10^{-44}	8×10^{-43}	[358]
XENON-100	Xe	0.021	2×10^{-44}	2×10^{-43}	[360]
LUX	Xe	0.092	1×10^{-45}	1×10^{-44}	[361]
ArDM	Ar	1.5	8×10^{-45}	7×10^{-44}	[362]
DEAP-3600	Ar	3.0	5×10^{-46}	5×10^{-45}	[363]
XENON1T	Xe	2	1×10^{-46}	1×10^{-45}	[312]
LZ	Xe	15	3×10^{-47}	3×10^{-46}	[313]
XENONnT	Xe	20	2×10^{-47}	2×10^{-46}	[312]
1 ν-induced	Xe	34	5.9×10^{-48}	5.8×10^{-47}	this thesis
nuclear recoil	Ar	52	1.6×10^{-47}	1.5×10^{-46}	
DarkSide-20k	UAr	100	1.2×10^{-47}	1.1×10^{-46}	this thesis
DarkSide-20k	DAr	200	7.4×10^{-48}	6.9×10^{-47}	this thesis
Argo	DAr	1000	2.7×10^{-48}	2.5×10^{-47}	this thesis

In the longer term, the aim of the DarkSide collaboration is to develop a path towards a dark matter detector to be built with a $300\,\mathrm{t}$ ($200\,\mathrm{t}$) active (fiducial) mass of depleted argon (DAr), UAr with an ^{39}Ar content further depleted by processing the UAr through a cryogenic distillation column. The details of this experiment are still under debate as well as its name. Indeed, it can be found in the literature both as Argoor GADMC. A successful DarkSide-20k experiment would represent a fundamental milestone toward the realization of Argo(GADMC). The latter is conceived to accumulate an exposure between 1000-3000 tonne year, free of background other than that induced by coherent scattering of neutrinos.

The low recoil energies and cross sections targeted with DarkSide-20k represent an enormous experimental challenge, especially in the face of daunting backgrounds from electron recoil interactions and from neutrons that mimic the nuclear recoil signature of WIMPs. To meet its challenge, DarkSide-20k will exploit the auxiliary facilities, including radon-free clean rooms, already built at LNGS as part of the DarkSide program. The cryostat will be placed inside a 8 m diameter stainless steel sphere filled with boron-loaded liquid scintillator, serving as an active neutron veto (LSV), which in turn will sit inside a newly constructed 15 m diameter 14.65 m tall stainless steel tank, filled with ultrapure water, functioning as an active muon veto (WCV). The LAr TPC will be instrumented with Silicon PhotoMultipliers (SiPMs) as photosensors. To provide the UAr target, the DarkSide Collaboration is already establishing, through the Urania and Aria

projects, the entire chain of extraction, purification, depletion, transport, and storage of low-radioactivity argon at the multi-tonne level.

In the next section the main sources of background for DarkSide-20k will be presented in detail.

4.1.1 Nuclear recoils

Neutrino-induced coherent nuclear scattering

With the nuclear recoil energy thresholds needed to achieve the excellent electron recoil rejection in LAr from pulse shape discrimination (PSD), only atmospheric neutrinos and the diffuse supernova neutrino background are energetic enough to produce nuclear recoils in the WIMP region of interest. Individual nuclear recoils from coherent scattering of neutrinos from the argon nuclei in the target are indistinguishable from WIMP-induced nuclear recoils. The exact calculation of the amount of this background that is expected for DarkSide-20k will be presented in Chap. 5.

Neutron scattering

Since individual elastic neutron scatters are essentially indistinguishable from elastic WIMP scatters, background from all sources of neutrons must be reduced well below the <0.1 events level. The main system that allows this is a highly efficient neutron veto system, similar to that used in DarkSide-50, which drew from the design of Borexino solar neutrino detector. Direct measurements of the cosmogenic backgrounds in Borexino and comparison with Monte Carlo simulations [364, 365] lead to the expectation that cosmogenic neutron backgrounds can be kept under control by using veto signals from the LSV and WCV, with no WIMP-like events expected for exposures much larger than that expected for DarkSide-20k.

Background due to radiogenic neutrons from (α,n) and fission decays in the construction materials of the LAr TPC must also be suppressed to below <0.1 events in the 100 t yr exposure. The rate of neutrons entering the detector will be reduced by using radiopure silicon-based photosensors and careful screening

and selection of construction materials. It is currently foreseen that the biggest contributor to this background will be the cryostat and the reflective panels of the LAr TPC, therefore, building the cryostat from either stainless steel or titanium will be investigated. Any residual neutron rate will be measured and efficiently rejected using the LSV. The sub-centimeter position resolution of the LAr TPC [356] also helps reducing background from radiogenic neutrons by fiducialization and rejecting events with multiple-sited energy deposition. With careful selection and screening of all construction materials and detector components, it is foreseen that the background due to radiogenic neutrons from (α,n) and fission decays can be kept below the <0.1 events level.

4.1.2 Electron recoils

For electron recoils, the successful strategy developed in DarkSide-50 was to reduce the raw rates by stringent materials screening and selection, then to suppress the remaining events by analysis cuts (fiducial volume, multiple-site energy deposition, etc.), and finally to apply PSD to identify residual electron recoil background events. The energy region of interest (ROI) for the WIMP search is 30 keV to 200 keV, roughly equivalent to $7\,\mathrm{keV}_{ee}$ to $50\,\mathrm{keV}_{ee}$. Given the effectiveness of self-shielding and fiducial cuts against external backgrounds for large detectors, the most important sources of electron recoil background for DarkSide-20k are those uniformly distributed throughout the fiducial volume and those which come from radioactive decays within the detector materials. These include decays of radioactive nuclides in the noble liquid target material itself, and electron scatters induced by solar neutrinos. Based on results from the DarkSide-50 experiment and Monte Carlo simulations, it has been demonstrated that these backgrounds can be held to below the required level (<0.1 events) in a 100 t yr exposure, if operated with a low-radioactivity argon target. The crucial sources of electron recoil background are:

Solar neutrino-induced electron recoils

Electron scatters from pp neutrinos within the energy ROI occur at a rate of 200 events /(t yr), giving $2.0 \times 10^4\,\mathrm{events}$ in the $100\,\mathrm{t\,yr}$ exposure. The β/γ rejection power demonstrated with DarkSide-50 in its AAr run [356] was better than one part in 1.5×10^7, more than sufficient to reject this pp neutrino background for

the entire planned exposure. This would also hold true for the 1000 (3000) t yr exposure planned for Argo (GADMC).

^{238}U, ^{232}Th, and daughters

The radioactive noble element radon may enter and dissolve in the LAr after being produced in the ^{238}U and ^{232}Th decay chains. The most important background contribution comes from β decays of the radon daughters whose spectra fall partly within the energy ROI. The ^{222}Rn specific activity in DarkSide-50 was measured to be below $2\,\mu\mathrm{Bq/kg}$. The ^{222}Rn concentration in DarkSide-20k is expected to be much lower than the upper limit obtained for DarkSide-50 due to the reduction in the surface-to-volume ratio. However, even if the ^{222}Rn contamination were at the DarkSide-50 upper limit, only $1000\,\mathrm{events/(t\,yr)}$ from ^{214}Pb β decays would be expected in the energy ROI, giving $1.0 \times 10^5\,\mathrm{events}$ in the total $100\,\mathrm{t\,yr}$ exposure. Once again the β/γ rejection power demonstrated with DarkSide-50 in its AAr run [356], better than one part in 1.5×10^7, is more than sufficient to exclude this source of background from the WIMP search region at the level required for an instrumental background free result.

The ^{39}Ar contamination

DarkSide-50 accumulated an exposure of $(1422 \pm 67)\,\mathrm{kg}$ day with AAr (^{39}Ar specific activity: $1\,\mathrm{Bq/kg}$), followed by an exposure of $(2616 \pm 43)\,\mathrm{kg}$ day with UAr (^{39}Ar specific activity: $(0.73 \pm 0.11)\,\mathrm{mBq/kg}$). Both campaigns provided background-free results, and with 1.5×10^7 events left in the energy ROI, but located in the electron recoil band, provided a limit on the suppression factor for electron recoil events $>1.5 \times 10^7$, provided by PSD alone. Argon extracted from the atmosphere is not an option for DarkSide-20k with its maximum drift time of $2.5\,\mathrm{ms}$, due to a constant pile-up of events that would exist, but using UAr with a much reduced ^{39}Ar component solves this constant pile-up problem. To better understand what ultimate electron recoil rejection factor can be achieved, the Geant4-based MC simulation package tuned using DarkSide-50 data was used to simulate large exposures of ^{39}Ar events inside the geometry of the DarkSide-20k detector. A suppression for ^{39}Ar events using only PSD is estimated to be $>3 \times 10^9$, more than sufficient to discriminate against the expected 1.8×10^8 remaining

^{39}Ar events coming from the UAr. This is further supported by the recent results from the DEAP-1 experiment, which show that a reduction fraction for electron recoils on the order of 10^{10} can be achieved in a LAr detector with a scintillation light yield of at least $8\,\mathrm{PE/keV_{ee}}$ [366].

The ^{85}Kr contamination

Recent data from DarkSide-50 show that the UAr contains ^{85}Kr at a specific activity of $(2.05 \pm 0.13)\,\mathrm{mBq/kg}$, a rate comparable to the ^{39}Ar activity just discussed. The ^{85}Kr in UAr comes either from atmospheric leaks during the collection and purification, or from deep underground natural fission processes. No attempt was made to remove Kr from the UAr for the DarkSide-50 target, simply because the presence of ^{85}Kr was not expected at the time of purification. For the LAr target, it is expected that the Urania UAr extraction plant will be able to reduce the ^{85}Kr to a level resulting in a specific activity much less than the residual ^{39}Ar. However, if for some reason the Urania plant is unable to reduce the ^{85}Kr to the desired level, Seruci-I at Aria will be capable of making the necessary chemical purification of the UAr. Kr in Xe has been reduced by a factor ∼1000 per pass by cryogenic distillation [367], which should be even better for Ar. Calculations show that the Aria cryogenic distillation column can reduce ^{85}Kr and other chemical impurities by a similar factor of more than 10^3 per pass, at a rate of O($1\,\mathrm{t/day}$), making this source of contamination negligible in DarkSide-20k.

4.1.3 Surface recoils and Cherenkov backgrounds

Surface recoils occur when a radioisotope decays on the interior surface of the detector. During the decay, it may eject an alpha particle toward the wall and recoil into the active argon volume, producing a nuclear recoil signal. In DarkSide-50, a surface recoil rate of $0.8\,\mathrm{mBq}$ was observed (across $0.75\,\mathrm{m^2}$ of surface area) and used to do a study of the alpha light yield in LAr. For the WIMP search all the surface events were rejected through the use of fiducial cuts, specifically a drift time cut. In the case that the surface backgrounds do not exactly scale when moving to DarkSide-20k, a radial fiducial volume cut, in addition to the drift time cut, is already envisioned and is taken into account when making the total exposure calculation. With the effectiveness of the drift-time cut seen

in DarkSide-50and the implementation of a radial fiducial volume cut surface backgrounds will contribute a negligible amount to the background budget.

Cherenkov background occurs when an electron recoil event is contaminated with Cherenkov light coming from a β/γ interaction in the surrounding detector materials either resulting from multiple Compton scattering of a single particle or a separate particle interacting in time-coincidence with the first. The Cherenkov light can overlap with the S1 signal from the LAr interaction producing an f_{90} value that a nuclear recoil would take. While the distribution of S1 light is a major factor in rejecting these types of events, the additional information given by the position reconstruction using the S2 signal allows for a more stringent cut to be placed, ensuring that no Cherenkov background event will survive the cut.

4.2 Experimental design of DarkSide-20k

This section gives a general overview of the project and introduces the features of the experiment. Fig. 4.1 shows the projected experimental arrangement, similar to an expanded version of the DarkSide-50 setup.

4.2.1 The LAr TPC

The DarkSide-20k LAr TPC is the dark matter detector and the central element of the experiment, with all auxiliary detectors and systems specified and designed in support of the LAr TPC. To achieve its stated physics goals, the LAr TPC must respond to a stringent set of requirements. The LAr TPC operates in a two-phase mode, utilizing both the liquid and gas phases of argon, as in DarkSide-50. Fig. 4.2 shows a 3D representation of the LAr TPC contained inside the cryostat. Energy deposits in the LAr target result in a characteristic production of excited and ionized argon atoms, according to the underlying process of a recoiling electron or nucleus. Excited argon atoms, which can also be produced by recombining ionization charge, lead to an efficient formation of argon excimers decaying via the emission of scintillation light containing two components with different time constants of emission. Both components combined together to yield an instant light signal S1. Due to the deep UV nature (around $128\,\mathrm{nm}$) of this scintillation light, which is absorbed by most materials, a thin layer of wavelength shifter must cover all exposed surfaces. Ionization electrons escaping recombination

Fig. 4.2.: 3D rendering of the DarkSide-20k LAr TPC and cryostat.

are drifted by an applied electric field to the top of the LAr, where a stronger applied field extracts the electrons into the gas pocket above the liquid. Here the strong field accelerates the electrons, enough for them to excite (but not ionize) the argon gas, producing a secondary scintillation signal S2, proportional to the ionization charge. For a simplified scheme of the S1 and S2 signal formation see Fig. 4.3.

Arrays of SiPMs, arranged in assemblies called photodetector modules (PDMs), are placed behind wavelength shifter coated windows at the top and bottom of the TPC, and read out both scintillation signals in each event. Substantial effort was put in the developments of this technology, since SiPMs promise a higher effective quantum efficiency, higher reliability at LAr temperature, and a much higher radiopurity than PMTs. S1 is used for energy determination, as well as for PSD, the latter is derived from the ratio of the prompt and delayed light fractions. S2 is used for energy and 3D position measurement of the event, the vertical coordinate from the drift time between S1 and S2, and the horizontal coordinates from the light pattern in the top photosensors.

All components of the detector, above all the inner components, like the LAr TPC, the cryostat, the SiPM arrays, and cables, must be made from materials of highest radiopurity to keep backgrounds as small as possible.

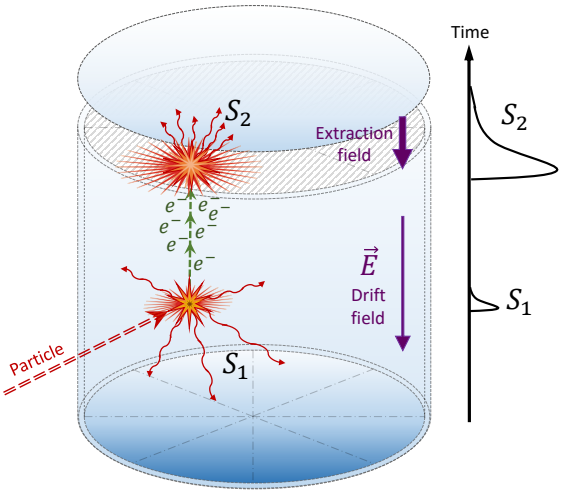

Fig. 4.3.: Schematic diagram of the functioning of dual-phase LAr TPC. WIMP scattering will induce nuclear recoils which in turn produce excitation and ionization. The recombination process results in a primary scintillation light called S1, which can be observed directly using silicon photomultipliers. Ionisation electrons drift in an applied electric field, producing an electroluminescence signal called S2 in the gas phase.

4.2.2 The active vetoes: Water Cherenkov Veto and Liquid Scintillator Veto

The veto system is crucial for the suppression of cosmogenic and radiogenic backgrounds originating from internal detector components, as well as from the surrounding environment. At the LNGS underground site, a depth of 3800 meter water equivalent (m.w.e.), the rate of cosmic rays is reduced to $1.1/(\mathrm{m}^2 \cdot \mathrm{hr})$. The outer veto, called Water Cherenkov Veto (WCV) provides general tagging of cosmic rays and shielding from radioactivity in the laboratory and the surrounding rock. The inner liquid-scintillator neutron veto (LSV) system targets events induced by internally- and externally-generated neutrons with high efficiency and is also effective to detect gamma-induced events in the LAr TPC. The requirement for the neutron detection efficiency is set as $>99\,\%$, a target that was achieved in DarkSide-50.

Nuclear recoils induced by single neutron scatters are indistinguishable from WIMP interactions. Even the large size of the LAr TPC does not allow a fiducial volume completely shielded from neutron-induced backgrounds. External passive

shielding provides protection against neutrons from outside the TPC (cosmogenic or radiogenic from Hall C), but not from neutrons from the components of the TPC itself. Neutron induced recoils will be suppressed using a LSV [368], a separate detector surrounding the TPC in which the neutrons from both internal and external sources are detected with very high efficiency, and the corresponding recoil events in the LAr TPC are identified and rejected. In addition to removing neutron backgrounds, the LSV also provides in situ measurements of the neutron backgrounds, allowing for reliable predictions of the number of neutron-induced recoils expected in the data sample to be made. It also has a substantial efficiency for detecting γ-rays from the TPC and cryostat.

To lower the background rate in the LSV in order to allow as low an energy threshold as possible for efficient neutron-detection, additional shielding is required surrounding the LSV. The LSV will be surrounded by a large tank of ultra-pure water, instrumented as a Cherenkov detector to veto cosmic rays, the WCV. This layered veto concept has been used very successfully in DarkSide-50 [356, 358, 369].

Neutrons that enter the LAr TPC come primarily from four sources:

- Radioactivity in the environment outside the detector;
- Cosmogenic interactions due to cosmic ray muons;
- Spontaneous fission reactions in the detector materials;
- (α,n) reactions in the detector materials.

Neutrons from the first two sources are suppressed by the shielding and signals generated by the veto detectors. Fission reactions that produce neutrons often generate multiple neutrons and high energy gamma-rays, significantly increasing the probability of multiple coincident interactions in either the LAr TPC or in the neutron veto. This leaves (α,n) neutrons as the most challenging type of neutron to veto, and much of the design is targeted around vetoing this class of neutrons with high efficiency.

(α,n) neutrons are produced by the alpha decays of radioisotopes in the detector materials, in particular by the ^{238}U,^{235}U, and ^{232}Th decay chains. Cross sections

for (α,n) reactions result in a neutron yield usually between 10^{-5} to 10^{-7} neutrons per equilibrium decay of the entire chain, with light elements giving the highest yields. (α,n) yield is strongly dependent on the α energy, making the lower sections of the ^{238}U and ^{232}Th decay chains particularly important.

It is planned to use a liquid scintillator doped with an isotope with a high cross section for thermal neutron capture. In DarkSide-50 this isotope was ^{10}B, accomplished by a solution of 1,2,4-TriMethylBenzene (PseudoCumene or PC) as solvent and 2,5-DiPhenylOxazole (PPO) as fluor mixed with TriMethylBorate (TMB) [356, 358, 369].

Neutrons can be detected by exploiting two signals, usually defined as prompt and delayed signals. The prompt signal is produced during the thermalization of the neutrons. Neutrons lose their energy by scattering off the nuclei of the scintillator, in particular hydrogen. Protons that are scattered by neutrons produce scintillation light. The scintillation light of the protons, although heavily quenched, can be detected by the PMTs. The thermalization of the neutrons is a fast process, usually contained in a narrow time window of a few hundred ns with respect to the scattering on argon, therefore a very low threshold can be used in a narrow prompt window.

The delayed signal is due to the neutron capture. The thermalized neutron can capture on various isotopes in the scintillator. ^{10}B, with a natural abundance of 20%, is one of the isotopes with the highest thermal neutron capture cross section, 3840 barn. The time scale and the relative probability of capture in boron, hydrogen, or carbon nuclei depends on the amount on boron in the scintillator, with ^{10}B dominant at all but the smallest concentrations. The capture on ^{10}B has two branches:

$$
\begin{aligned}
^{10}\mathrm{B} + n &\rightarrow {}^{7}\mathrm{Li} + \alpha\ (1775\,\mathrm{keV})\ [6.4\,\%] \\
^{10}\mathrm{B} + n &\rightarrow {}^{7}\mathrm{Li} + \alpha\ (1471\,\mathrm{keV})\ [93.6\,\%] \\
&\hookrightarrow {}^{7}\mathrm{Li} \rightarrow {}^{7}\mathrm{Li} + \gamma\ (478\,\mathrm{keV}).
\end{aligned}
$$

The advantage of the ^{10}B final products is that the alpha and ^{7}Li have very short range. Therefore if a neutron is captured on ^{10}B in the LSV, the reaction always produces some scintillation light. An important feature of this signal is that it is independent of the energy of the neutron, meaning that a neutron that has too low an energy to produce a detectable prompt signal may still produce a

detectable delayed signal. However, the light yield of alpha and ^{7}Li nuclei is highly suppressed due to ionization quenching, causing them to scintillate equivalent to a 50 to $60\,\mathrm{keV}$ electron. Detecting these reaction products therefore requires a high light collection efficiency. The time scale of the delayed signal depends on the TMB concentration. With a $50\,\%$ volume concentration, the neutron capture time is $2.2\,\mu\mathrm{s}$, and $\sim$99.2 % of neutron captures happens on ^{10}B (the rest of the captures happens mostly on H), while with a $5\,\%$ concentration, the neutron capture time is $22\,\mu\mathrm{s}$ and $\sim$92 % of neutron captures happens on ^{10}B.

4.3 Procurement and purification of the underground argon target

The collaboration has developed a broad strategy to increase the production of UAr to procure the target required for DarkSide-20k.
The Urania project will extract and purify the UAr from the CO_2 wells at the Kinder Morgan Doe Canyon Facility located in Cortez, CO at a production rate of 100 kg/day. The Urania project will extract at least $50\,\mathrm{t}$ of low-radioactivity UAr, providing the required $35\,\mathrm{t}$ of UAr to fill DarkSide-20k. It will be necessary to make a final chemical purification of the UAr before deployment into the LAr TPC (driven by the filtration capacity of the getter purification unit), bringing the chemical impurity levels to those shown in Table 4.2. Argon from active CO_2 wells in southwestern Colorado have been found to contain very low levels of the radioactive isotope ^{39}Ar, with the concentration shown to be a factor of $(1.4 \pm 0.2) \times 10^3$ below that of argon derived from the atmosphere [358].

Additionally, it would be beneficial to further deplete the UAr of ^{39}Ar, giving extended sensitivity to DarkSide-20k and a level of ^{39}Ar that is acceptable to be used in an experiment such as Argo. The Aria project will serve to chemically purify the UAr to better than the levels shown in Table 4.2 using a cryogenic distillation column called Seruci-I. Aria could also potentially further deplete the UAr of ^{39}Ar by a second, and larger cryogenic distillation column called Seruci-II. The ultimate goal of the Aria project is to process about $150\,\mathrm{kg/day}$ of argon through Seruci-II to achieve an additional depletion factor between 10 and 100 (in addition to the reduction of ^{39}Ar already seen in the UAr). However, the first objective of the Aria project is to chemically purify the UAr using Seruci-I.

Tab. 4.2.: Urania/Aria: Inlet purity required by the getter of DarkSide-20k.

Element	Inlet Purity Requirements (ppm)
CH_4	<0.25
CO	<0.1
CO_2	<0.1
H_2	<1
H_2O	<1
N_2	<1
O_2	<1

Therefore, the procurement of the UAr for DarkSide-20k is broken into two main operations, extraction of the UAr by Urania and then chemical purification by Aria using Seruci-I.

4.3.1 The Aria project

The aim of the Aria project is to perform chemical purification of the UAr extracted by Urania. Aria will also be the test bench to develop active depletion of ^{39}Ar from the UAr to possibly provide DAr targets for LAr detectors. Aria consists of two $350\,\mathrm{m}$ tall distillation columns of different processing diameters, Seruci-I and Seruci-II, capable of separating isotopes by means of cryogenic distillation, a process that exploits the tiny difference in volatility due to the difference in isotopic mass [370, 371, 372].

Aria is to be installed in underground vertical shafts of diameter $5\,\mathrm{m}$ and depth $350\,\mathrm{m}$, located at the Seruci mine campus of CarboSulcis, a mining company owned by the Regione Autonoma della Sardegna (RAS).

Algorithms developed by to calculate the relative volatility of argon isotopes [373], based on the extensive and detailed models available in the literature, predict that the volatility of ^{39}Ar relative to ^{40}Ar is 1.0015 ± 0.0001, and that it stays constant within theoretical uncertainties in the range of temperatures practical for the distillation of argon ($84\,\mathrm{K}$ to $100\,\mathrm{K}$). The small volatility difference can be used to achieve active isotopic separation by using a cryogenic distillation system with thousands of equilibrium stages [374, 375, 376, 377].

Calculations indicate that Seruci-I will be able to process UAr at a rate of O($1\,\mathrm{t/day}$), while removing all chemical impurities (including traces of N_2, CO_2, and Kr) with

separation power better than 10^3 per pass. Additionally, Seruci-I will be used to test the isotopic separation of the argon, in order to further reduce the ^{39}Ar content in the UAr. The same models which have been used to calculate the chemical purification rate, have also been used to show that Seruci-I would be able to isotopically separate the UAr at a rate of $10\,\mathrm{kg}$/day, while obtaining an ^{39}Ar depletion factor of 10 per pass. Scaling the model to the size required for Seruci-II predicts a processing rate of $150\,\mathrm{kg}$/day, while maintaining the same depletion factor.

4.4 Physics reach

The ability to identify, measure, and reject background will ultimately define the sensitivity of direct dark matter searches. DarkSide-20k is designed to perform a search for high mass (tens of GeV to hundreds of TeV) dark matter particles with an exposure of 100 t yr. DarkSide-20k will search for WIMPs in a broad energy range from 30 keV to 200 keV. Fig. 4.4 shows the nuclear recoil energy spectra for WIMPs interacting with argon nuclei, for various masses between 100 GeV and 10 TeV. The steeply falling rate with increasing recoil energy means that a lower energy threshold can greatly increases sensitivity for WIMP detection, as long as the detector still operates with a very low and well understood background. As will be detailed in this section, the operation of DarkSide-20k in an instrumental background-free mode is possible thanks to its outstanding rejection power for β/γ backgrounds using PSD, and rejection of neutron-induced nuclear recoils by the identification of multiple scatters thanks to the intrinsic spacial resolution of the LAr TPC and the system of two active vetoes.

DarkSide-20k's system of nested detectors is designed to efficiently reject the backgrounds described in Sec. 5.2: nuclear recoils induced by radiogenic and cosmogenic neutrons, electron recoils from gamma rays and radioactive contaminants in the LAr, and backgrounds from radon daughters deposited on detector surfaces. Detailed simulations projecting that DarkSide-20k will be operated in an instrumental background-free condition in the WIMP search region at the required exposure will be discussed in Sec. 4.4.1. These studies have been performed using G4DS, the Geant4-based Monte Carlo simulation tool developed by the DarkSide collaboration.

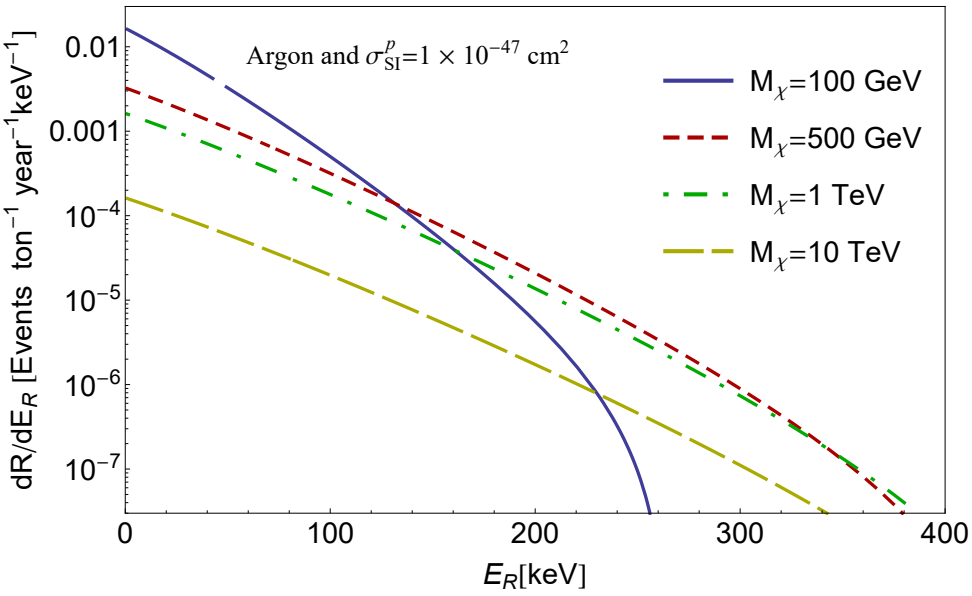

Fig. 4.4.: WIMP nuclear recoil spectra in argon as a function of the recoil energy in keV for different WIMP masses.

To provide unbiased results for the dark matter search at the limits of sensitivity offered by the detector, a blind analysis procedure will be implemented. The blind analysis employed by DarkSide-20k will build upon the procedure currently being developed by the DarkSide collaboration for DarkSide-50.

G4DS was designed with a modular architecture and describes the energy and time responses of each detector. It provides a rich set of particle generators, detailed geometry descriptions, finely-tuned physical processes, and a full optical propagation model for the photons produced by scintillation in liquid argon and liquid scintillator and by electroluminescence in gaseous argon.

For the LAr TPC, the main goal of G4DS is the accurate simulation of light production, propagation, and detection for background and signal events, in order to fully reproduce the responses of the detector in S1, S2, and time, the three primary variables on which the discrimination of β/γ background is based. This allows tuning of the analysis cuts and estimation of their efficiencies, as well as prediction of the β/γ and nuclear recoil backgrounds.

The light generation in LAr and GAr is handled using a custom Geant4 physical process, since details of atomic excitation, ionization, nuclear quenching, and

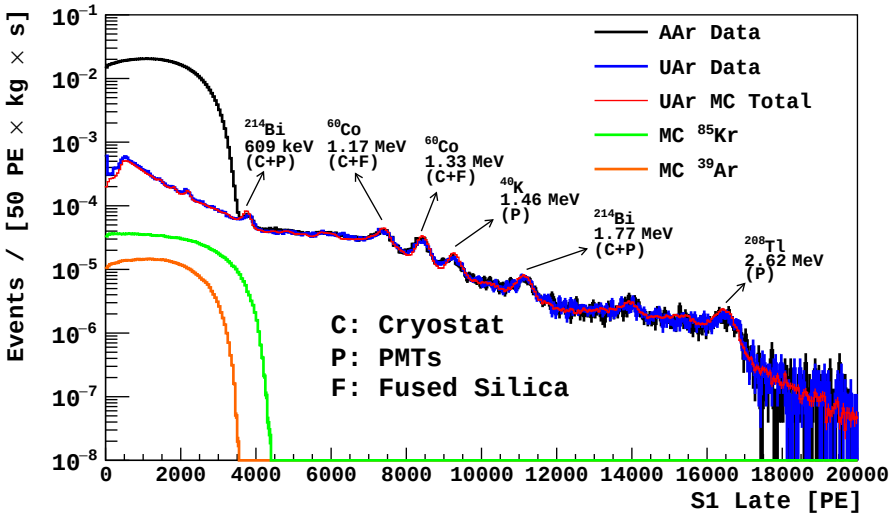

Fig. 4.5.: Comparison of measured field-off spectra for the UAr (blue) and AAr (black) targets, normalized to exposure. Also shown are the G4DS fit to the UAr data (red) and individual components from ^{85}Kr (green) and ^{39}Ar (orange) extracted from the fit. S1 Late is a modified S1 variable which begins waveform integration after the first 90 ns, to avoid channel saturation. [358]

electron-ion recombination effects are poorly known in argon, especially in presence of strong electric fields. A theoretical model based on an effective description of recombination was developed, which was tuned on calibration data and is able to accurately describe the light response of DarkSide-50 in both S1 and S2.

Another critical ingredient of G4DS is the tuning of optical properties of the materials through which light is propagated, and of the surfaces where light can be absorbed, reflected, or diffused. These parameters were again tuned by comparisons with selected data samples from the DarkSide-50 LAr TPC.

The DarkSide-50 electronics response was simulated in detail by generating arrival time and hit channel information for each photoelectron, and then convolving it with the typical single photo-electron time response and adding the simulated signals to actual PMT baseline responses to include noise.

The success of G4DS was validated by its ability to reproduce the background spectra in the latest analysis of the DarkSide-50 UAr data, as well as other specific distributions measured in the the DarkSide-50 LAr TPC. As one example, a strong validation of G4DS was made when it first detected the presence of ^{85}Kr in the

spectrum from the UAr target in DarkSide-50. The G4DS fit to the spectrum, shown in Fig. 4.5, would not converge in the region of the ^{39}Ar end point under the initial assumption of no other β component with a similar end point. The G4DS working group found that only by adding a significant ^{85}Kr component would the fit converge to the data. This hypothesis was confirmed by measuring the rate of coincidences due to the $0.43\,\%$ branching ratio of ^{85}Kr decaying to ^{85m}Rb. Not only did the G4DS analysis identify the missing spectral component, it also measured the absolute ^{85}Kr activity with great accuracy, as confirmed by the coincidence measurement. As Fig. 4.5 shows, G4DS is designed to reproduce with great accuracy the experimental features of the DarkSide-50 spectrum with a UAr target.

G4DS has been used to calculate the light yield of DarkSide-20k in its final configuration, obtaining the distribution shown in Fig. 4.6. This calculation used the optical parameters tuned on the DarkSide-50 data (plus an assumed self-absorption length of 300 m for the LAr scintillation light), the geometry of the detector as described in this thesis, and it assumed a 40% overall photon detection efficiency. G4DS estimates a light yield of 10 PE/keV, larger than that obtained in DarkSide-50, the result of many technical improvements of the DarkSide-20k design, larger geometrical coverage and increased photo detection efficiency for SiPMs, compared to PMTs.

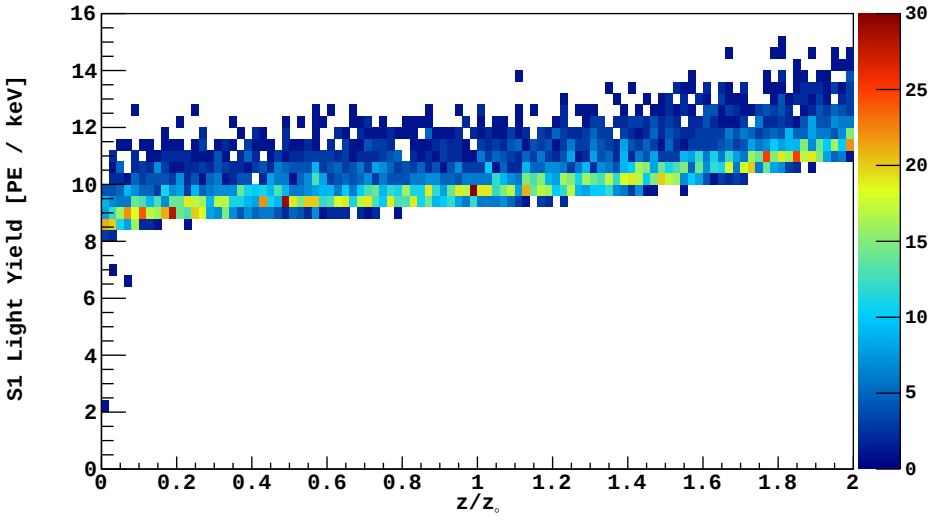

Fig. 4.6.: Light yield as a function of the vertical coordinate in DarkSide-20k for ^{39}Ar with an electric field of $200\,\mathrm{V/cm}$, as obtained with the G4DS simulation of the detector described in this thesis.

Tab. 4.3.: Expected β/γ and nuclear recoil (NR) backgrounds expected during the full DarkSide-20k exposure, based on current data and Monte Carlo simulations. The center column gives the total number of single-scatter events within the energy region of interest (ROI) before the application of the fiducial and veto cuts and the PSD. The right-most column is the total number of events surviving the veto cut, fiducial volume cut, and PSD. Internal β/γ background does not include the ^{39}Ar depletion expected from Aria. External backgrounds are shown for a stainless steel cryostat.

Background	Events in ROI $[100\,\mathrm{t\,yr}]^{-1}$	Background $[100\,\mathrm{t\,yr}]^{-1}$
Internal β/γ's	1.8×10^8	0.06
Internal NRs	negligible	negligible
e^--ν_{pp} scatters (This thesis)	2.0×10^4	negligible
External β/γ's	10^7	<0.05
External NRs	<81	<0.15
Cosmogenic β/γ's	3×10^5	$\ll 0.01$
Cosmogenic NRs	–	<0.1
ν-Induced NR(This thesis)	1.33±0.26	1.33±0.26

4.4.1 Simulation of backgrounds in DarkSide-20k

The background sources can be divided into three broad categories: 1) “Internal background", ionizing events due to radioactive contamination and neutrino interactions in the active argon itself; 2) “External background", ionizing events originating from radioactivity in the TPC and cryostat materials (radiogenic backgrounds from outside the cryostat are negligible due to the shielding provided by the veto) and 3) “Cosmogenic background", ionizing events originating from the residual cosmic ray flux in the laboratory.

A full background model of the detector has been built from the G4DS Monte Carlo simulation and is under continuous refinement. The current state of the background estimates for the proposed 100 t yr exposure of DarkSide-20k is summarized in Tab. 4.3 and discussed in detail in this section. Some of these numbers have been calculated as part of this thesis and their derivation will be explained in Chap. 5.

Internal background

^{39}Ar and ^{85}Kr: Recent data from DarkSide-50 running with low-radioactivity argon shows that the UAr contains ^{39}Ar and ^{85}Kr activity totaling slightly less than 3 mBq/kg. As stated previously, the DarkSide-50 run with AAr had an exposure of (1422±67) kg day and accumulated 1.5×10^7 ^{39}Ar events in the WIMP energy ROI after all standard analysis cuts except PSD. Every one of these events was eliminated when the PSD was applied, leaving the experiment free from this background and producing a lower limit for the reduction factor of ^{39}Ar of $>1.5 \times 10^7$.

A detector with similar PSD performance and filled with UAr would have to run for 5.5 t yr to accumulate the same number of ^{39}Ar events, and would also be expected to be free of ^{39}Ar background after PSD. Because the planned exposure is a factor 19 larger than this, assuming the DarkSide-50-measured lower limit for the reduction factor of the ^{39}Ar leads to a case in which the experiment would not remain background-free. Therefore the real rejection factor that can be expected must be estimated using alternative methods, such as Monte Carlo simulations and analytic modeling. This has been done for the case of DarkSide-20kand results are quoted in Tab. 4.3[1]. Additionally, assuming that two passes of the UAr through Seruci-II will reduce the ^{39}Ar by a factor of 100, there will be only about 1.8×10^6 residual decays of these isotopes in the DAr itself in the WIMP ROI during the full exposure of $100\,\mathrm{t\,yr}$. This would further extend the sensitivity of DarkSide-20k beyond that which has been estimated when using just the UAr, and would mark the beginning of the procurement of the target for a much larger detector, such as Argo.

Production of ^{39}Ar in the UAr by cosmic rays during collection, transportation, and storage of the UAr before its deployment into the DarkSide-20k detector have also been considered. Two codes that calculate the production and decay yields of isotopes from nuclear reactions induced by cosmic rays were used to calculate the production of ^{39}Ar in the UAr during a realistic altitude and exposure history covering its extraction and purification, shipment to the Aria site, processing there, and transportation to the underground laboratory. COSMO [378] and ACTIVIA [379] predicted ^{39}Ar specific activities of $1.5 \times 10^{-8}\,\mathrm{Bq/(kg\,day)}$ and $0.54 \times 10^{-8}\,\mathrm{Bq/(kg\,day)}$, respectively, much too small to be of concern.

[1] Note that the conservative assumption of the use of UAr with no further depletion of the ^{39}Ar has been made

Solar neutrino-induced electron scatters: The dominant solar neutrino interaction rate would be from neutrino-electron scattering by pp neutrinos. These occur at a rate of 200 events/(t yr) within the DarkSide-20k energy ROI, giving 2.0×10^4 events in the 100 t yr exposure. The β/γ rejection power demonstrated with DarkSide-50 in its AAr run [356] was better than one part in 1.5×10^7, more than sufficient to reject this pp neutrino background in the DarkSide-20k exposure. This would also hold true for the 1000 t yr exposure planned for Argo.

Neutrino-induced nuclear scatters: As discussed in Sec. 5.2, the coherent scattering of atmospheric neutrinos from argon nuclei is an irreducible physics background to WIMP searches. About 1.3 events are expected from this source in the 100 t yr exposure.

^{238}U, ^{232}Th, and daughters: The radioactive noble element radon may enter and diffuse in the LAr after being produced in the ^{238}U and ^{232}Th decay chains. The most important background contribution comes from β decays of the radon daughters whose spectra fall partly within the energy ROI. The ^{222}Rn specific activity in DarkSide-50 was measured and found to be below $2\,\mu\mathrm{Bq/kg}$. With its much smaller surface-to-volume ratio, the ^{222}Rn concentration in DarkSide-20k is expected to be much lower than in DarkSide-50, since radon will be coming from the detector surfaces and not the bulk. However, even if the ^{222}Rn contamination were at the DarkSide-50 level, only 1000 events/(t yr) from ^{214}Pb β decays would be expected in the energy ROI, giving 1.0×10^5 events in the total 100 t yr exposure. Once again the β/γ rejection power demonstrated with DarkSide-50 in its AAr run [356], better than one part in 1.5×10^7, is more than sufficient to eliminate this source of background from the WIMP search region at the level required for a DarkSide-20k result free from instrumental background.

External background

To ensure that external backgrounds are low enough to achieve the experiment goals, the DarkSide Collaboration will implement a careful program of background modeling, process and materials development, and materials radiopurity assay.

Radiogenic β/γ's: The energy spectrum resulting from the radioactive β/γ decays of the detector materials was measured quite precisely in DarkSide-50, for both the AAr and UAr data sets. The measured spectra were found to match very well, indicating that the target itself did not contribute to this background in a significant way, and also showed a sufficient amount of self shielding by the LAr. With this results in mind, and assuming the same level of activities as in DarkSide-50, DarkSide-20k will expect to see on the order of 10^7 electron recoils events within the WIMP ROI, coming from β/γ decays of the detector materials. Based on the discrimination power of the PSD technique to distinguish between electron recoil (ER) and nuclear recoil (NR) events that has been estimated, it is expected that this background will not cause any leakage events to appear in the WIMP search region, over the entire exposure of DarkSide-20k.

Radiogenic neutrons: Radiogenic neutrons are a potentially dangerous background since they cannot be removed by PSD. The very low levels of spontaneous fission occurring in the materials selected for DarkSide-20k also produce neutrons, but G4DS simulations with activity levels measured in DarkSide-50 or expected for DarkSide-20k show that these will be efficiently vetoed by the LSV, given the fission neutron multiplicity and the coincident fission γ-rays, leaving (α,n) as the chief background.

Early G4DS studies indicated that the (α,n) reactions in the Teflon (PTFE) reflector and the cryostat were likely to be the largest sources of neutrons, so further studies focused on these, testing several different configurations with 4×10^6 neutrons generated for each configuration. The resulting probability for mis-identifying a radiogenic NR as a WIMP candidate is then normalized to the known ^{238}U and ^{232}Th activities and the (α,n) yields in these materials, calculated with TALYS and SRIM simulation codes and reported in Tab. 4.4, to give the number of expected WIMP-like NRs appearing during the full 100 t yr of DarkSide-20k. The neutrons generated in the PTFE and steel have been simulated using (α,n) spectra from TALYS. The TMB concentration has been varied from $0\,\%$ to $50\,\%$ to find the most efficient LSV composition.

To use the simulation to evaluate LSV performance, a simulation of a typical TPC analysis, which would require a single, nuclear-recoil-like scatter in a chosen fiducial volume, is performed. These cuts are themselves quite effective in reducing neutron-induced background. The following is required:

Tab. 4.4.: Uranium and thorium decay chain (α,n) yields, per equilibrium decay of the entire chain, used in neutron background estimates. The yields were calculated with TALYS and SRIM. Equilibrium in the ^{238}U chain is often broken, and so it is divided in the simulations.

	^{238}U Upper	^{238}U Lower	^{232}Th
Steel	1.3×10^{-9}	5.4×10^{-7}	1.95×10^{-6}
Teflon (PTFE)	1.2×10^{-5}	8.9×10^{-5}	1.3×10^{-4}

Tab. 4.5.: Expected neutrons produced before the application of any cuts, fraction passing TPC cuts, fraction of events passing TPC cuts that also pass LSV cuts, and surviving neutron background events inside the WIMP search region for a DarkSide-20k exposure of $100\,\mathrm{t\,yr}$. Errors are statistical only.

Source	Neutrons produced in $5\,\mathrm{yr}$	Fraction passing TPC cuts	Fraction passing LSV cuts	Surviving n background in $100\,\mathrm{t\,yr}$
Teflon reflector panels	<1717	0.0072	0.0075	<0.093
Stainless steel cryostat	2384	0.0019	0.0133	0.060
Total				<0.153

- The event has a single resolved interaction in the TPC;
- The interaction is nuclear-recoil-like;
- The event is contained in the WIMP energy region;
- The event is inside the fiducial volume chosen, varied in these studies.

The simulations for neutrons originating in the Teflon reflector panels and stainless steel cryostat give the results shown in Table 4.5 for a TMB concentration of $20\,\%$ and a fiducial cut of $7\,\mathrm{cm}$. Fig. 4.7 shows the surviving neutron background as a function of both the TMB concentration and the fiducial cut.

Cosmogenic background

Nuclear interactions of cosmic ray muons with the rock surrounding the experimental halls produce neutrons and other particles that potentially give backgrounds in DarkSide-type detectors. Detailed simulation studies of these backgrounds were performed by members of the DarkSide Collaboration for Borexino, for DarkSide-50 with its veto system, and for a 3.3 t LAr TPC with the DarkSide-50 veto system, as described in Refs. [364, 365]. In these simulations, FLUKA was

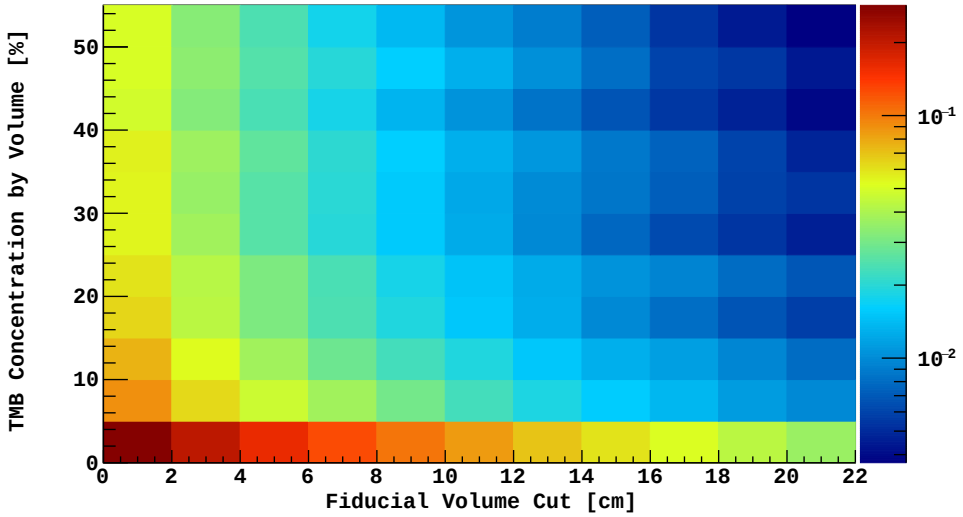

Fig. 4.7.: WIMP-like neutron recoils per year from both U and Th induced by (α,n) reactions in the stainless steel cryostat and in the PTFE panels.

used to predict the particle fluxes produced in the rock and incident on the experiments, starting from measured characteristics of the incident muon flux at LNGS.

The most dangerous class of background events for the WIMP search are neutron-induced nuclear recoils in the sensitive LAr volume resulting from events which deposit little or no energy in the vetoes. To study this category, Ref. [365] singled out all events for which at least one neutron (but <50 coincident particles) reached the active LAr region in their 3.3 t LAr TPC. A very conservative criterion ($dE_{LSV} > 1$ MeV) was defined to select events which should be considered detectable by the LSV. A portion of the Ref. [365] simulation was repeated for the proposed geometry using the Geant4-based simulation package. The most dangerous category of cosmogenic events was again singled out, *i.e.*, cosmogenic neutrons entering the water tank without accompanying charged particles (all other events are easily rejected by the WCV). DarkSide-20k is more efficient at rejecting such external cosmogenic neutrons because of the increased sizes of the WCV and LSV. The results for an exposure greater than 1000 t yr are compatible with no cosmogenic neutron reaching the LAr TPC and surviving application of the veto cuts.

The background estimate described above was based on cosmic ray muon-induced secondaries which are prompt and thus can be vetoed by the outer detector

systems. The cosmic ray showers can also produce radioisotopes with lifetimes of seconds to minutes (*i.e.*, sources of non-prompt background) in the detector and target materials. Production and decay of these isotopes were also simulated, and their decay products handed off to a Geant4-based Monte Carlo for simulation. Events that deposited a significant amount of energy in the veto detectors, interacted at more than one site inside the LAr TPC, or fell outside the energy ROI and the fiducial volume were removed. On the order of 3×10^5 events survive during a full exposure of 100 t yr all of which were β/γ events. This number is easily managed by the LAr PSD.

Based on current data and Monte Carlo simulations, the expected numbers of electron and nuclear recoil background events surviving analysis cuts, for the full 100 t yr exposure, is given in Tab. 4.3. Note that the table gives an estimated external NR background greater than 0.1 event. This rate is dominated by (α,n) production in the PTFE reflector panels. Actual measurements of the activity of the PTFE in DarkSide-50 produced only upper limits. The background estimate can thus be taken as an indication that more sensitive measurements of the PTFE must be made, and that the activity will be required to be at least a factor of ~ 2 below the achieved upper limits.

4.4.2 DarkSide-20k energy acceptance

The success of the experiment depends not only on background suppression, but also on a high detection efficiency for nuclear recoil events from WIMPs. The WIMP acceptance region is designed to have a leakage of electron recoils smaller than 0.005 events/(5-PE bin).

To determine the expected acceptance region for DarkSide-20k, 1.5×10^6 nuclear recoils in the range 1 keV to 200 keV were simulated. The simulation included the effect of the measured quenching factor for nuclear recoils in argon reported in Ref. [359], which matches the theoretical predictions. With this quenching factor, the above nuclear recoil ROI corresponds to the energy interval $<1\,\mathrm{keV}_{ee}$ to $50\,\mathrm{keV}_{ee}$ for β's. Additionally, 3.5×10^6 ^{39}Ar β-decays were simulated in the energy range of $7\,\mathrm{keV}_{ee}$ to $50\,\mathrm{keV}_{ee}$. The number of simulated electron recoils corresponds to $1\,\%$ the expected number of ^{39}Ar decays in the WIMP ROI for the 100 t yr exposure using UAr (assuming the ^{39}Ar reduction factor measured in DarkSide-50). The G4DS simulation was performed using the optical parameters,

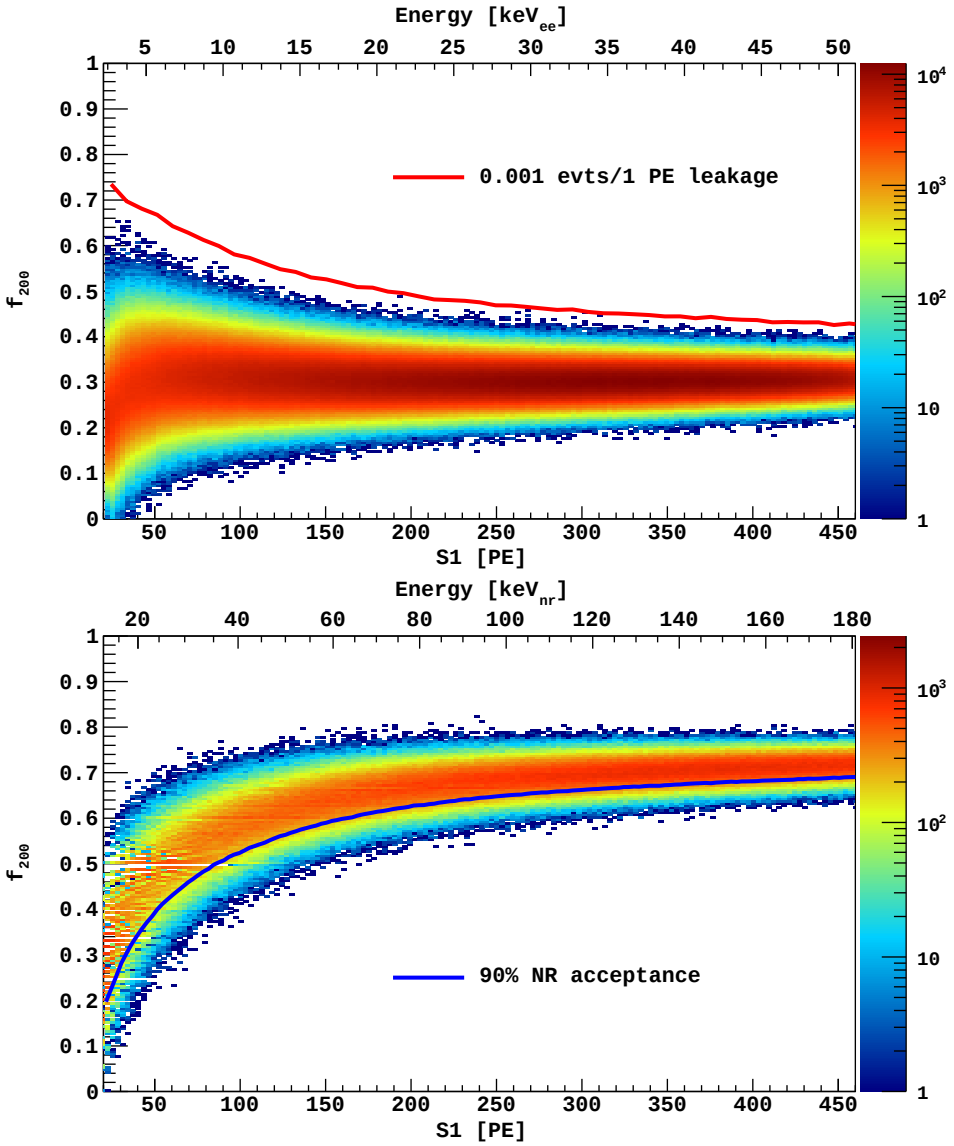

Fig. 4.8.: **Top:** Distribution of f_{200} as a function of S1 for ^{39}Ar β's. The red line on the left plot shows the leakage curve for β's generated from the requirement of $0.005\,\text{events}/(5\text{-PE bin})$. **Bottom:** Distribution of f_{200} as a function of S1 for NRs. The blue curve delimits the $90\,\%$ NR acceptance region. The WIMP search region is the region above both curves, red and blue. Note: for both plots, the energy scale atop the plots is only approximate.

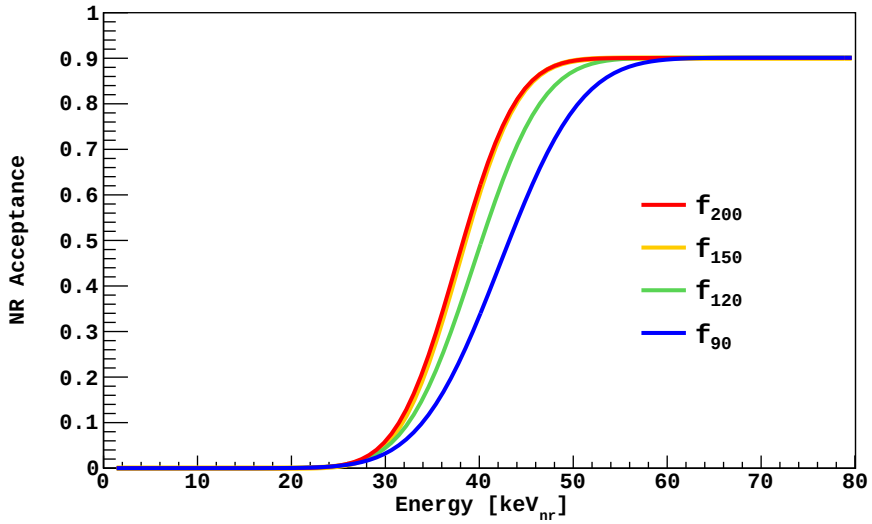

Fig. 4.9.: Comparison of nuclear recoil acceptance bands for f_{90}(blue), f_{120}(green), f_{150}(yellow), and f_{200}(red) as a function of the nuclear recoil energy in keV.

such as the index of refraction and the reflectivity of the different surfaces, that had been tuned with the DarkSide-50 data. The light yields of β's and nuclear recoils were corrected for the position within the LAr TPC, based on a light yield map obtained with ^{83m}Kr G4DS simulations. The average light yield predicted for DarkSide-20k in this study was 10 PE/keV for β/γ's at null field, corresponding to 9 PE/keV at a field of 200 V/cm.

The discrimination between β/γ and nuclear recoils was then determined using the PSD of LAr. In DarkSide-50, the discrimination parameter f_{90} was used, but due to the DarkSide-20k larger size and longer average distance the light has to travel before reaching the photosensors, f_{90} might not be the optimal distribution, thus the PSD performance of DarkSide-20k was simulated using four different parameters: f_{90}, f_{120}, f_{150}, and f_{200}, defined as the fraction of scintillation light collected in the first $90\,\mathrm{ns}$, $120\,\mathrm{ns}$, $150\,\mathrm{ns}$, and $200\,\mathrm{ns}$ respectively.

The large simulated sample of ER described above is still not sufficient to locate a PSD cut contour for the full exposure. To design the contour, an analytical model of the three PSD parameters was fit to the simulated sample and used to extrapolate to the required background rejection. For all three parameters, an NR acceptance region was defined by requiring that it contains a leakage of less than 0.005 events/(5-PE bin) ER events (total ER background then sums to <0.1 events in the WIMP search region), extrapolating to the full statistics

of ^{39}Ar events expected in DarkSide-20k. Note that in this study, the use of UAr was assumed, with the depletion factor measured in DarkSide-50 and *not* the additional depletion anticipated from Aria, we will relax this condition and its implication to WIMPs sensitivity in Sec. 5.6.2. The acceptance region was further bounded from below by the 90% NR detection-efficiency contour. As an example, the distribution of f_{200} as a function of S1 for β's and NRs is shown in Fig. 4.8. The lines on those plots correspond to the leakage curve for β/γ and to the 90% acceptance contour for NR.

For each of the four discrimination parameters considered, the NR acceptance band, as determined with the procedure detailed above, is converted into a function of energy and shown in Fig. 4.9. The comparison clearly favors f_{200}. There is no gain in further lengthening the window dedicated to the counting of the fast photoelectrons beyond the $200\,\mathrm{ns}$ of f_{200}. The resulting equivalent reduction factor for ^{39}Ar decays inside DarkSide-20k is found to be $>3 \times 10^9$, more than sufficient to maintain background-free operation for more than 200 t yr.

The acceptance band of Fig. 4.9 will be used to evaluate the sensitivity of DarkSide-20k to WIMP recoils. The other main ingredients to calculate the sensitivity are

- the statistical framework to calculate upper limits or discovery limits;
- the prediction for the irreducible coherent neutrino background;
- the impact of ARIA purification process on the background content of ^{39}Ar and its impact.

All these items will be described in the Chap. 5.

5 WIMP Sensitivity of DarkSide-20k and future detectors

Contents

5.1 The background impact on the WIMP sensitivity 116
5.2 CEnNS background contribution 122
5.3 Neutrino-nucleus cross section 123
5.4 Neutrino Fluxes 126
5.5 Event rate for argon and xenon 129
5.6 Kinematic differences in WIMP and neutrino reconstruction . . 141
5.7 Argon-xenon comparison in view of standard electroweak interactions on electrons 156

In this chapter I will present the calculation of the 90% Confidence Level (C.L.) WIMP-nucleon cross section sensitivity of the DarkSide-20k experiment and of a future detector capable of achieving an exposure between 1000-3000 tonne year. The final name and the experimental realization of this kind of detector is, at the time of writing, yet to be defined.

I have shown in Chap. 4 that DarkSide-20k will be able to contain the number of instrumental background interactions to < 0.1 events. The only irreducible background that is left comes from Coherent elastic neutrino-nucleus scattering (CEnNS) interactions. In this chapter I will present the prediction for the number of neutrino background events in DarkSide-20k. I will start presenting the statistical tools used to obtain upper limits on the WIMP-nucleon cross section (see Sec. 3.1.1) as a function of the WIMP mass. I will show that these upper limits and the discovery potential are drastically affected by the given number of background events.

5.1 The background impact on the WIMP sensitivity

Before going into the details of how backgrounds affect sensitivity, it is first important to make a firm distinction: it is statistically much easier to exclude a region of parameter space than it is to make a detection. Typical exclusion relies on a standard of $90\,\%$ likelihood, while a positive detection requires a $5\,\sigma$ standard: this is equivalent to saying that, once a reliable background model for the experiment has been built, the observed signal has a probability of 3×10^{-7} of being an artefact of statistical fluctuations in the background. A signal $3\,\sigma$ above the null hypothesis has a probability of 10^{-3}, and is generally referred to as "evidence", while a $1\,\sigma$ deviation, with a probability of 0.16, is "uninteresting".

Nowadays, experiments sensitive to weakly interacting dark matter particles are placing tight constraints on dark matter-nucleon cross sections. The most recent upper limits rule out a substantial chunk of parameter space for well-motivated theories (see Sec. 3.6.1). Even more exciting are the plans for future experiments which have excellent discovery potential. As these experiments get larger and more expensive, it becomes important for the community to agree on uniform standards for projecting the sensitivity of future experiments. Projections are often carried out simply by scaling exposures, defined as the product of fiducial detector mass M times integrated detector live time T. That is, the projected improvement in the upper limit (UL) on the cross section is taken to be

$$\frac{\sigma^{\mathrm{UL}}}{\sigma^{\mathrm{UL,curr}}} \to \frac{1}{\lambda} \equiv \frac{(MT)^{\mathrm{curr}}}{MT}. \tag{5.1}$$

Neglected in these projections is the effect of backgrounds. The purpose of this chapter is to provide a simple formalism that accounts for the degradation of a future experiment's reach due to backgrounds. A given experiment's projected constraint on the cross section should be multiplied by the *background penalty factor* introduced here to get a baseline estimate of that experiment's constraining power. This baseline estimate assumes that any future experiment will have the same background rate per volume as the current version of the experiment. Experimentalists could plausibly argue that they expect to reduce their background rates by some factor (here defined as r) and therefore they project a tighter constraint than the baseline estimate. The framework introduced here can also incorporate these arguments by computing the background penalty factor as a function of r.

5.1.1 Likelihood for upper limits

Let's consider a direct detection experiment with fiducial detector mass M operating for a time T. What is the likelihood that such an experiment will observe N events? We will assume that there are two sources of events: signal and background. The expected number of signal events is (see Eq. 3.65)

$$N_s(M_\chi) = M\,T \int_{E_{\rm min}}^{E_{\rm max}} A(E_R) \frac{{\rm d}R}{{\rm d}E_R}\,{\rm d}E_R \;= MTa(M_\chi)\sigma \tag{5.2}$$

where σ is the WIMP-nucleon cross section[1] that one wants to constrain and a is

$$a(M_\chi) = \frac{\rho_0}{2\mu_{\chi p}^2 M_\chi} A^2 F_{SI}^2(E_R) \int_{v_{\rm min}}^{\infty} \frac{f_1(v)}{v}\,{\rm d}v\,, \tag{5.3}$$

in which I have explicitly denoted the dependence on the WIMP mass, M_χ. All the quantities on the right of the formula have been already introduced in Chap. 3.

The expected number of background events is

$$N_b = rN_b^{\rm curr}\lambda \tag{5.4}$$

where $N_b^{\rm curr}$ denotes the number of background events observed in the current version of the experiment, λ has been introduced in Sec. 5.1 and r is the expected background rate normalized to its current value. If $r = 1$, the future version of this experiment will have the same background rate per volume as the current one. If $r < 1$ then the experiment projects to do better at background rejection than it is currently doing (even though there may be new sources of background at lower rates showing up in the new version).

The probability of seeing N events given σ is:

$$\mathcal{L}(N|N_s(\sigma)) = \frac{(N_s + N_b)^N e^{-[N_s+N_b]}}{N!}. \tag{5.5}$$

The Bayesian 90% C.L. upper limit on the cross section, $\sigma_{\rm UL}$, satisfies

$$\int_0^{N_s(\sigma_{\rm UL})} dN_s\,\mathcal{L}(N|N_s) = 0.90 \int_0^{\infty} dN_s\,\mathcal{L}(N|N_s). \tag{5.6}$$

[1] Note that it was indicated as $\sigma_{\rm SI}^p$ in Chap. 3.1.1

Since one wants to project the constraints for future experiments, the observed value of N is unknown. In principle, projecting future constraints requires the following steps:

- Generate a number of events N from the distribution in Eq. 5.5
- Compute the likelihood in Eq. 5.5 using this value of N as a function of N_s
- Use Eq. 5.6 to determine the 90% upper limit on N_s for this realization
- Repeat a large number of times and average all the upper limits

In practice, this is not necessary, since the averaged projected upper limit is within a few percent of that obtained by simply setting $N = N_b$ (we assume no signal and project upper limits). In this case, Eq. 5.6 determines $N_s(\sigma_{\rm UL})$ as a function of N_b. The lower curve in Fig. 5.1 shows this limit on N_s as a function of the number of background events in the case we have been considering so far, when the number of expected background events is known precisely. For example, an experiment which has zero expected background is projected to rule out $N_s > 2.3$. An experiment with one hundred expected background events (and no uncertainty on this background prediction) is projected to rule out all cross sections which predict $N_s > 17.8$.

However in real experiments, typically there will be a given uncertainty on the number of expected background events, so the probability of observing N events is actually an integral over the distribution of possible values of N_b. Let's assume that N_b follows a Gaussian distribution with mean $\bar{N}_b$ and variance σ_b^2. Then, Eq. 5.5 becomes

$$\begin{aligned}\mathcal{L}(N|\sigma) \quad \propto \quad & \int_0^\infty dN_b \, \exp\left\{\frac{-(N_b-\bar{N}_b)^2}{2\sigma_b^2}\right\} \\ & \times \frac{(N_s+N_b)^N e^{-[N_s+N_b]}}{N!}. \end{aligned} \tag{5.7}$$

We can again determine $N_s(\sigma_{\rm UL})$ from this likelihood function using Eq. 5.6. So for fixed $\bar{N}_b$ and σ_b, one can obtain a projected upper limit on the number of signal events. Clearly, this upper limit is a function of $\bar{N}_b$ and σ_b. Let's call this function $F(\bar{N}_b, \sigma_b)$. It monotonically increases as $\bar{N}_b$ increases and tends to 2.3 for small values of $\bar{N}_b$. For large values of $\bar{N}_b$, the uncertainty in the

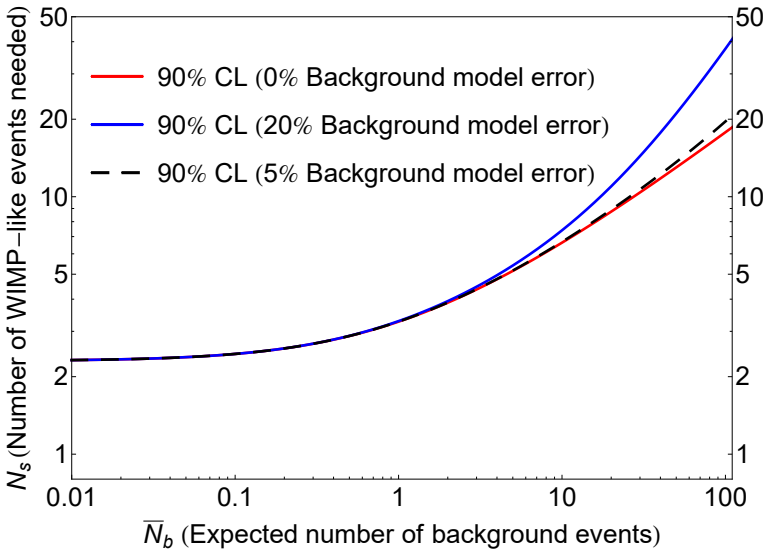

Fig. 5.1.: Maximum allowed number of signal events as a function of the number of background events in the experiment. For example, if there is one expected background event, then the expected upper limit on the number of signal events is 3.27. This means that all values of the cross-section which predict more than 3.27 events in the detector are ruled out. Lower (red) curve shows this limit when there is no uncertainty in the number of expected background events. Black-dashed (blue) curve show the effect of a 5% (20%) uncertainty in the number of background events.

background adds in quadrature with the Poisson uncertainty, so the uncertainty on the number of events is $\sqrt{\bar{N}_b + \sigma_b^2}$. Since the expected number of events is known within this uncertainty, it is possible to rule out a model which produces $N_s(\sigma_{\rm UL}) \geq 2\sqrt{\bar{N}_b + \sigma_b^2}$ at the 2-sigma level. This behaviour is shown by the $\sigma_b = 0.2\,\bar{N}_b$ curve (blue) in Fig. 5.1.

As indicated in Fig. 5.1, in the absence of backgrounds I have shown that an experiment can rule out models which predict $N_s > 2.3$. Given Eq. 5.2, this translates into an upper limit on the cross section of

$$\sigma_{\rm UL}(M_\chi) = \frac{2.3}{a(M_\chi)MT} \qquad \text{(Zero Background)}. \tag{5.8}$$

In Sec. 5.1 I have defined the ratio of the upper limit in a future experiment to the current one as: $\frac{\sigma_{\rm UL}}{\sigma_{\rm UL}^{\rm curr}} = \frac{1}{\lambda}$. Fig. 5.1 offers a way to flesh out this projection accounting for backgrounds. For example, consider an experiment which currently expects 10 background events, such that it is able to rule out all models which predict more than 10 events (from now on assuming $\sigma_b = 0.2\,\bar{N}_b$ and reading off from Fig. 5.1). If the background rate remains the same, then a future version of

this experiment with ten times the exposure will expect to see 100 background events. Reading off from Fig. 5.1 at $\bar{N}_b = 100$, we see that $N_s(\sigma_{\rm UL}) = 37.6$. Thus, the projected upper limit from the future experiment version is

$$a10MT\sigma_{\rm UL} = 37.6 \tag{5.9}$$

Dividing this by the current experiment upper limit with MT ten times smaller:

$$aMT\sigma_{\rm UL}^{\rm curr} = 10 \tag{5.10}$$

it is possible to see that the upper limit on the cross section projects to be tighter by a factor of $37.6/(10 \times 10) = 0.376$. So the limit gets better only by a factor of $1/0.376 = 2.65$ with a factor of 10 increase in exposure.

5.1.2 Likelihood for discovery

Let's consider now an experiment where one observes a number of events N, assumed to follow a Poisson distribution with an expectation value $E[N] = N_s(\sigma) + N_b$. Here $N_s(\sigma)$ represents the mean number of events from a signal model, which we take to be a known value; N_b is the expected number from background processes. In a real analysis, the value of N_b may have some uncertainty and could be itself treated as a nuisance parameter, but in this example we will take its value to be known. The data thus consist of two measured values: N and $N_b^{\rm Exp}$, the measured value of the background events. We have one parameter of interest, σ, and one nuisance parameter, N_b.

An important special case of the counting experiment above mentioned corresponds to the case in which the mean background N_b is known with negligible uncertainty and can be treated as a constant. If we regard N_b as known, the data consist only of N and thus the likelihood function can be written as in Eq. 5.5.

The test statistic for discovery q_0 can be written as [380, 381]

$$q_0 = \begin{cases} -2\ln\frac{\mathcal{L}(0)}{\mathcal{L}(\hat{\sigma})} & \hat{\sigma} \geq 0, \\ 0 & \hat{\sigma} < 0\ . \end{cases} \tag{5.11}$$

For sufficiently large N_b we can use the asymptotic formula for the significance

$$Z_0 = \sqrt{q_0} = \begin{cases} \sqrt{2\left(N \ln \frac{N}{N_b} + N_b - N\right)} & \hat{\sigma} \geq 0, \\ 0 & \hat{\sigma} < 0. \end{cases} \tag{5.12}$$

To approximate the median significance assuming the nominal signal hypothesis we replace N by the Asimov value $N_s + N_b$ to obtain

$$\text{med}[Z_0|1] = \sqrt{q_{0,\text{A}}} = \sqrt{2\left((N_s + N_b)\ln(1 + N_s/N_b) - N_s\right)}\,, \tag{5.13}$$

where Z_0 is the discovery significance in units of sigmas.

Expanding the logarithm in N_s/N_b one finds

$$\text{med}[Z_0|1] = \frac{N_s}{\sqrt{N_b}}\left(1 + \mathcal{O}(N_s/N_b)\right)\,. \tag{5.14}$$

Although $Z_0 \approx N_s/\sqrt{N_b}$ is widely used for cases where $N_s + N_b$ is large, it is important to underline that this final approximation is strictly valid only for $N_s \ll N_b$.

Fig. 5.2 shows the number of WIMP-like events that an experiment would need to observe in order to reject the null hypothesis at $5\,\sigma$ as a function of the number of expected background events, N_b, when the background model predicts the background with negligible uncertainty. When the model predicts 0.1 background events, just 4.3 WIMP-like events are statistically significant to claim a detection at the $5\,\sigma$ level. However, if an experiment expects to see one background event, the number of WIMP-like events needed for a discovery increases to 10.6. This means that a dark matter experiment expecting one background event will need approximately 2.5 times more WIMP interactions to claim a detection, compared to an experiment which plans to run background-free. The requirement becomes increasingly more restrictive if the expected number of background events is greater than 10.

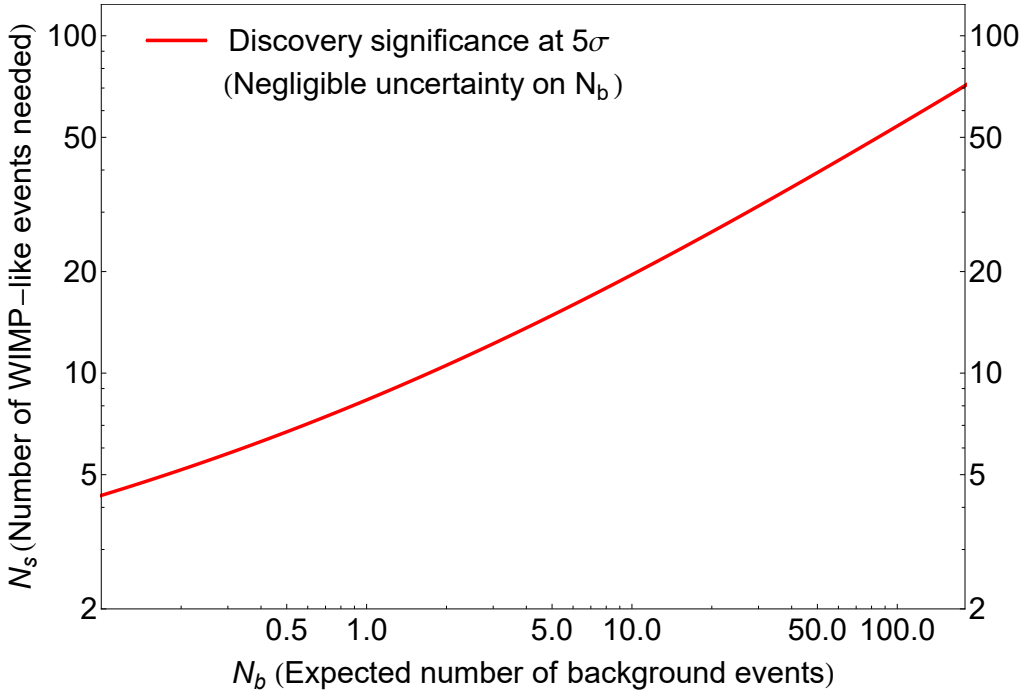

Fig. 5.2.: Number of WIMP-like signal events needed to claim a WIMP observation at the $5\,\sigma$ level, based on the predicted background rate of the experiment for negligible background uncertainty, in a log-log scale.

5.2 CEnNS background contribution

In previous sections, it has been shown that, for the case of zero background, the formula to obtain the 90% C.L. for a given WIMP mass is that in Eq. 5.8. Indeed, this is the procedure used to draw the 90 C.L. in an experiment like DarkSide-50 for which the background content did not exceed 0.1 in the corresponding exposure. Instead, for DarkSide-20k, there will be a non negligible background contribution from CEnNS that has to be taken into account. In this section, I will show the predictions for such a background in DarkSide-20k.

Coherent scattering of neutrinos on complex nuclei was proposed in 1974 [254, 382] as a prominent probe to study neutral-current (NC) ν-nucleus processes. Only in 2017 the COHERENT experiment [188] observed at 6.7 σ confidence level for the first time CEnNS with a small scintillator detector made of sodium-doped CsI exposed to a low-energy neutrino flux generated in the Spallation Neutron Source (SNS) at the Oak Ridge National Laboratory. Such a neutrino detection constitutes an excellent probe to search for a plethora of conventional neutrino physics applications and new-physics open issues. To this purpose, great

experimental effort has been put and new experiments have been proposed to be performed at facilities with stopped-pion neutrino beams, based on promising nuclear detectors like those of the COHERENT experiment [188, 383] and others [384] at the SNS, or alternative setups at the Booster Neutrino Beam (BNB) at Fermilab [385]. The nuclear ν-detectors adopted by the relevant experiments include liquid noble gases, such as ^{20}Ne, ^{40}Ar, ^{132}Xe as well as ^{76}Ge and CsI[Na] detection materials [386].

While being conceptually highly interesting and allowing measurements of electroweak observables at low momentum transfer, the process is also of phenomenological importance for future dark matter direct detection experiments [256], which is the main focus of this chapter.

5.3 Neutrino-nucleus cross section

As predicted in the SM neutrinos can scatter off coherently with a nucleus through a neutral current process. The coherence of the process is determined by the length scale of the interaction which in turn is related to the inverse of the momentum exchanged between the neutrino and the nucleus. The differential cross section depends on the neutrino energy E_ν, the nucleus mass m_N and the nuclear recoil energy E_r

$$\frac{d\sigma(E_\nu, E_r)}{dE_r} = \frac{G_f^2}{4\pi} Q_w^2 m_N \left(1 - \frac{m_N E_r}{2E_\nu^2}\right) |F(q^2)|^2 \,, \tag{5.15}$$

where G_f is the Fermi coupling constant, $Q_w = N - (1 - 4\sin^2\theta_w)Z$ is the weak hypercharge with N the number of neutrons, Z the atomic number and θ_w is the weak mixing angle. The nucleus mass is denoted by m_N while $|F(q^2)|^2$ is the nuclear form factor[2] as a function of the momentum transfer q, which in turn is related to the recoil energy through $q^2 \simeq 2ME_r$. From kinematics it can be shown that the recoil energy of the nucleus E_r can be related to $c_\theta \equiv \cos\theta$, where θ is defined as the scattering angle between the momenta of the initial neutrino and the final nucleus, such that

$$E_r = \frac{2m_N E_\nu^2 c_\theta^2}{(m_N + E_\nu)^2 - E_\nu^2 c_\theta^2} \,. \tag{5.16}$$

[2] In this section I will use the standard Helm form factor parametrization but I will examine the limits of this choice in Chap. 7.

For a given value of E_ν, the maximal recoil energy $E_r^{\max}$ is reached at $\theta = 0$:

$$E_r^{\max}(E_\nu) = \frac{2E_\nu^2}{m_N + 2E_\nu} \,. \tag{5.17}$$

In Tab. 5.1 the maximum neutrino energy, $E_\nu^{\max}$, and maximum recoil energy of a xenon target, $E_{r_{\mathrm{Xe}}}^{\max}$, and an argon target, $E_{r_{\mathrm{Ar}}}^{\max}$, corresponding to the maximum neutrino energy are shown for different neutrino components. In the last column the neutrino flux for each component is shown together with its uncertainty.
The minimum neutrino energy needed to impart a recoil energy E_r to the nucleus is

$$E_\nu^{\min} = \frac{1}{2}\left(E_r + \sqrt{E_r(E_r + 2m_N)}\right) \simeq \sqrt{\frac{m_N E_r}{2}} \tag{5.18}$$

in which the expression on the right holds in the limit $m_N \gg E_\nu$. The integrated cross section is given by

$$\sigma(E_\nu) = \int_0^{E_r^{\max}(E_\nu)} \frac{d\sigma(E_\nu, E_r)}{dE_r} dE_r \,. \tag{5.19}$$

ν **type**	$\mathbf{E}_\nu^{\max}$ **(MeV)**	$\mathbf{E}_{\mathbf{r}_{\mathrm{Xe}}}^{\max}$ **(keV)**	$\mathbf{E}_{\mathbf{r}_{\mathrm{Ar}}}^{\max}$ **(keV)**	ν **flux** $(\mathrm{cm}^{-2}\,\mathrm{s}^{-1})$
pp	0.42341	2.94×10^{-3}	9.62×10^{-3}	$(5.98 \pm 0.006) \times 10^{10}$
$^{7}\mathrm{Be}_{384.3}$	0.3843	2.42×10^{-3}	7.92×10^{-3}	$(4.84 \pm 0.48) \times 10^{8}$
$^{7}\mathrm{Be}_{861.3}$	0.8613	0.0122	0.0398	$(4.35 \pm 0.35) \times 10^{9}$
pep	1.440	0.0340	0.1112	$(1.44 \pm 0.012) \times 10^{8}$
$^{13}\mathrm{N}$	1.199	0.02355	0.07712	$(2.97 \pm 0.14) \times 10^{8}$
$^{15}\mathrm{O}$	1.732	0.04914	0.1610	$(2.23 \pm 0.15) \times 10^{8}$
$^{17}\mathrm{F}$	1.740	0.04959	0.16241	$(5.52 \pm 0.17) \times 10^{6}$
$^{8}\mathrm{B}$	16.360	4.383	14.346	$(5.58 \pm 0.14) \times 10^{6}$
hep	18.784	5.778	18.910	$(8.04 \pm 1.30) \times 10^{3}$
DSNB	91.201	136.0	444.0	85.5 ± 42.7
Atm.	981.748	15.54×10^{3}	49.09×10^{3}	10.5 ± 2.1

Tab. 5.1.: Total neutrino fluxes with corresponding uncertainties. The maximum neutrino energy, $E_\nu^{\max}$, and maximum recoil energy of a xenon target, $E_{r_{\mathrm{Xe}}}^{\max}$, and an argon target, $E_{r_{\mathrm{Ar}}}^{\max}$, are also shown.

In Fig. 5.3 I show the CEnNS differential cross section in Eq. 5.15 for argon nuclei for different neutrino energies, while in Fig. 5.4 I show the comparison between argon and xenon differential cross sections in a log-log scale for a fixed neutrino energy of E_ν=200 MeV. The minimum in the cross section for xenon near between 90 and 100 keV recoil energy is related to the form factor and it indicates the diffraction minimum as a consequence of the loose of coherency (see Fig. 3.1).

In Fig. 5.5 I show the comparison between the integrated cross section in Eq. 5.19 for argon and xenon nuclei as a function of the neutrino energy. Since the CEnNS cross section is roughly proportional to N^2, the cross section for xenon is bigger than for an argon nuclei.

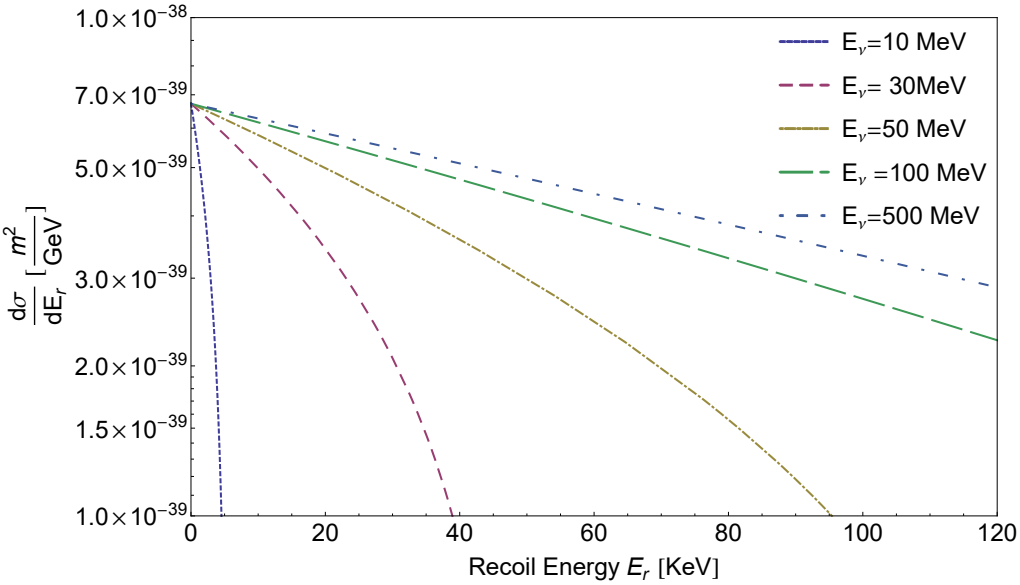

Fig. 5.3.: CEnNS differential cross section in Eq. 5.15 for argon nuclei for five different neutrino energies, (E_ν=10, 30, 50, 100 and 500) MeV as a function of the recoil energy E_r in keV.

The important quantity for the final calculation of the number of neutrino background events for DarkSide-20k or other future Xenon DM experiments like XENONnT, LZ or Darwin is the neutrino differential rate per unit of exposure and the final total integrated number. To do this calculation one needs to derive the total neutrino flux, dN/dE_ν at Earth. This will be presented in the next section.

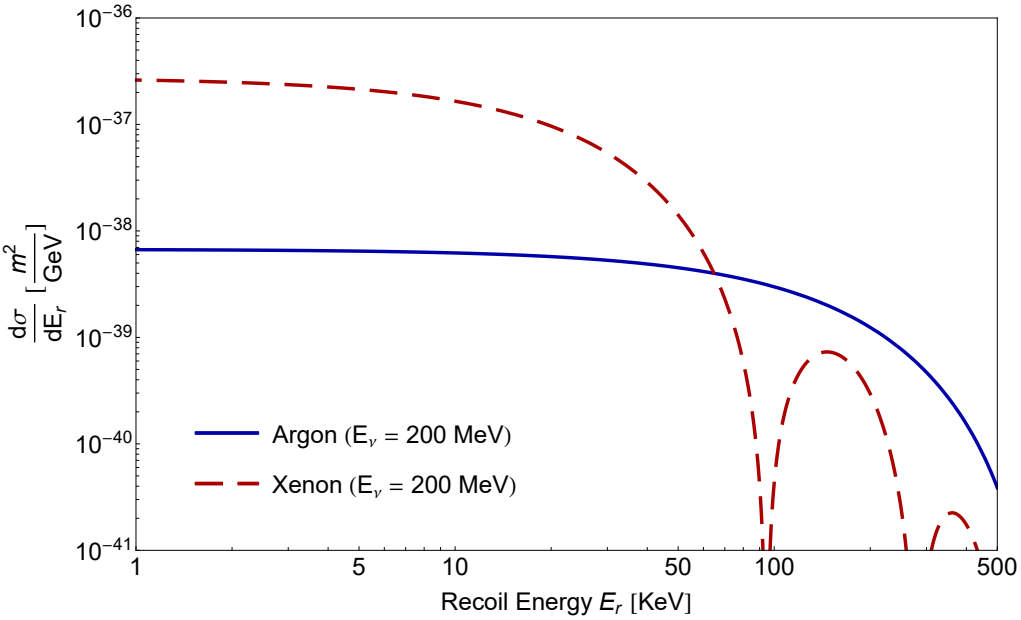

Fig. 5.4.: CEnNS differential cross section in Eq. 5.15 in a log-log scale for argon (solid blue line) and xenon (dashed red line) nuclei for a fixed neutrino energy (E_ν=200 MeV) as a function of the recoil energy E_r in keV.

5.4 Neutrino Fluxes

Direct detection experiments like DarkSide-20k will be sensitive to the flux of solar, atmospheric, and diffuse supernova neutrinos. In this section I will discuss the respective neutrino fluxes examining their respective uncertainties. Afterwards, I will evaluate the neutrino background event rate starting from the description of the single neutrino flux components.

The main neutrino fluxes at Earth could be divided into three categories: Solar, atmospheric and diffuse supernovae neutrinos. Solar neutrinos are produced by the nuclear synthesis reactions inside the Sun such as the proton-proton (*pp*) or Carbon-Nitrogen-Oxygen (*CNO*) chains. They are characterized by energies lower than $\sim$ 20 MeV. Another important flux is represented by the Diffuse Supernova Neutrino Background (DSNB) which derives from all the past supernova explosions in the Universe. DSNB flux covers energies up to about a hundred of MeV. The last component is constituted by atmospheric neutrinos produced through cosmic ray collisions in the Earth atmosphere. The energy range of interest is approximately 10-1000 MeV. In the following, I will examine these components in more details.

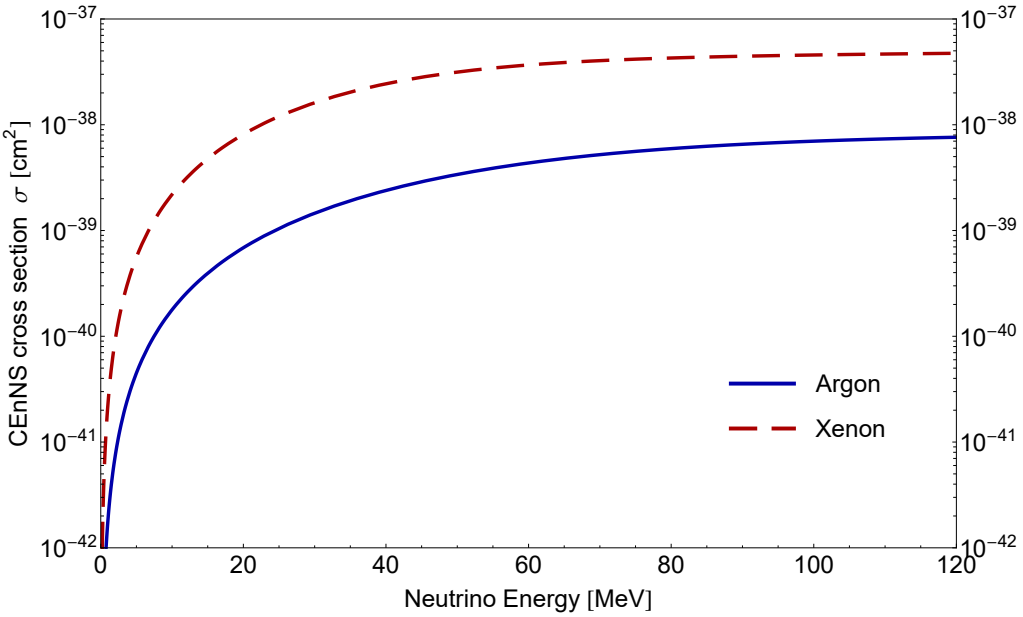

Fig. 5.5.: Integrated CEnNS cross section in Eq. 5.19 for argon (solid blue line) and xenon nuclei (dashed red line) as a function of the neutrino energy E_ν in MeV.

5.4.1 Solar neutrinos

Direct dark matter detection experiments that are sensitive to neutrino-nucleus coherent scattering are primarily sensitive to two sources of solar neutrinos, so called ^{8}B and hep neutrinos. The ^{8}B neutrinos arise from the decay $^8\text{B} \rightarrow {}^7\text{Be}^* + e^+ + \nu_e$, which occurs in approximately 0.02% of the terminations of the pp chain. The total flux measured with the neutral current interaction of ^{8}B solar neutrinos is $\phi_{NC} = 5.58 \pm 0.14 \times 10^6$ cm^{-2} s^{-1} [387]. The hep neutrinos arise from the reaction $^3\text{He} + \text{p} \rightarrow {}^4\text{He} + e^+ + \nu_e$, which occurs in approximately 2×10^{-5}% of the terminations of the pp chain. At the lowest neutrino energies, electron capture reaction on ^{7}Be is the second largest neutrino source that leads to two monoenergetic neutrino lines at 384.3 and 861.3 keV with a branching ratio of 10% and 90% respectively due to the ^{7}Li excited state. According to the BS05(OP) solar model, we chose a ^{7}Be neutrino flux of 4.84×10^9 cm^{-2} s^{-1} with a theoretical uncertainty of about 10.5% [388]. Dark matter detectors would be also sensitive to CNO neutrinos. The uncertainty in the solar composition is the dominant source of uncertainty in the CNO neutrino fluxes.

Through neutrino-electron scattering, dark matter detection experiments are also sensitive to neutrinos produced directly in the pp chain. As already said, the total

flux of neutrinos produced in the pp chain is 5.98×10^{10} cm^{-2} s^{-1}. Because the neutrino-electron scattering cross section is flavour dependent, in this case we must consider the flavour composition of the neutrino flux that arrives on the Earth. For the energies that we are sensitive to, the electron neutrino survival probability is approximately 55% [389]. Following Ref. [388], the pp neutrino flux has an uncertainty of about 0.1%.

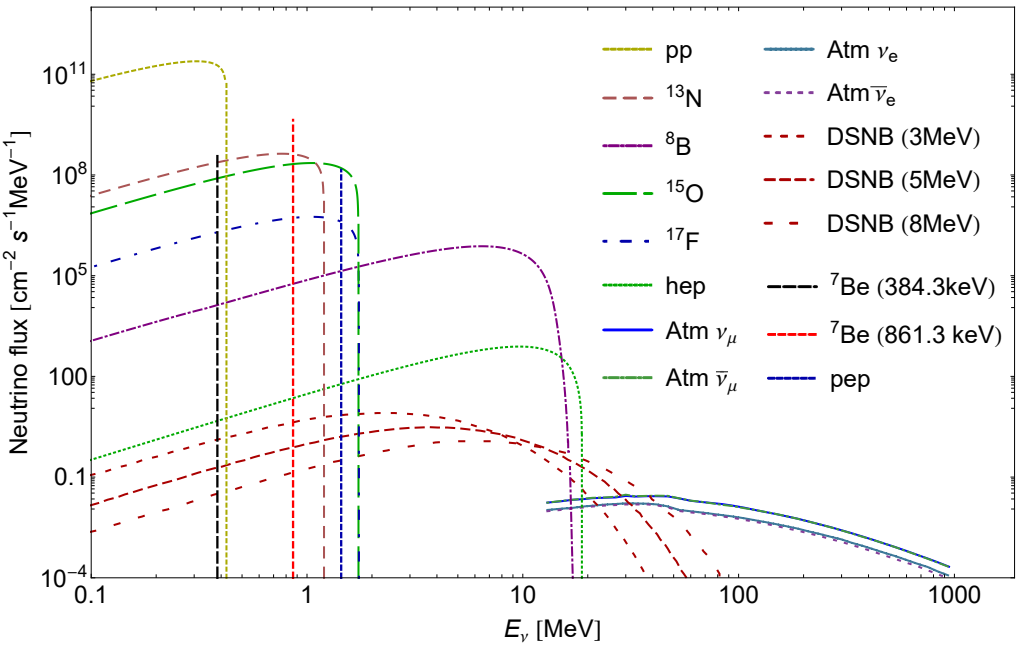

Fig. 5.6.: Relevant neutrino fluxes which are backgrounds to direct dark matter detection experiments: Solar, atmospheric, and diffuse supernovae neutrinos [390].

5.4.2 Atmospheric neutrinos

Atmospheric neutrinos are produced through cosmic ray collisions in the Earth's atmosphere. The collisions produce pions which then decay to muon and electron neutrinos and antineutrinos. The atmospheric neutrino flux has been detected by several experiments: Super-Kamiokande [391], SNO [392], MINOS [393], and IceCube [394]. In these experiments, the direction of the detected muon is reconstructed. Modern direct dark matter detectors do not have directional sensitivity and are mainly sensitive to the low component of the atmospheric neutrino flux, *i.e.* less than approximately 100 MeV. At these energies, the uncertainty on the predicted atmospheric neutrino flux is approximately 20% [395]. Due to a cutoff in the rigidity of cosmic rays induced by the Earth's geomagnetic field at

low energies, the atmospheric neutrino flux is larger for detectors that are nearer to the poles [395].

5.4.3 Diffuse supernova neutrinos

The diffuse supernova neutrino background (DSNB) is the flux from the past history of all supernova explosions in the Universe. The DSNB flux is a convolution of the core-collapse supernova rate as a function of redshift with the neutrino spectrum per supernova. The core-collapse rate is derived from the star-formation rate and stellar initial mass function; for a recent review on the predicted DSNB flux see Beacom [396]. The neutrino spectrum of a core-collapse supernova is believed to be similar to a Fermi-Dirac spectrum, with temperatures in the range 3-8 MeV. Following [396], I will consider a systematic uncertainty on the DSNB flux of 50%.

Figure 5.6 presents the relevant neutrino fluxes that will be a background for dark matter direct detection. Shown are the different contributions from solar, atmospheric, and diffuse supernova neutrinos. Note that I did not considered geoneutrinos nor reactor neutrinos in this study. Indeed, as shown in [397], the contribution of the geoneutrinos to the neutrino-induced recoil energy spectrum is at least 2 orders of magnitude below the solar neutrino contribution over the whole energy range. The reactor neutrinos are strongly dependent on the location of the experiment with respect to the surrounding nuclear reactors and on the power of these reactors. While this contribution should be estimated independently for each experiment, I will not consider them in the following and I will therefore only discuss the case of cosmic neutrinos as shown in Fig. 5.6.

5.5 Event rate for argon and xenon

The neutrino differential rate is given by

$$\frac{dR}{dE_r} = \eta \times \int_{E_\nu^{min}} \frac{dN}{dE_\nu} \times \frac{d\sigma(E_\nu, E_r)}{dE_r} dE_\nu \ , \tag{5.20}$$

where η is the number of nucleus targets per unit of detector active mass and dN/dE_ν represents the total neutrino flux that has been described in Sec.5.4. This CEnNS differential rate is shown in Fig. 5.8 for xenon and in Fig. 5.9 for argon

as a function of the recoil energy for all neutrino components and for the sum of them. In the top plot a large recoil energy range is considered while in the bottom plot only the interesting region for future DM detectors is shown. Most of the solar neutrinos are at very low recoiling energies (below 0.2 keV), except the ^{8}B and hep neutrinos that will dominate the event rate from 0.2 to 5 (18) keV for xenon (argon). Above these energies, atmospheric neutrinos will dominate with a subdominant contribution from the diffuse supernova background neutrinos. In the top panel of Fig. 5.10 it is shown the comparison between the xenon and argon differential rate. The two curves show a similar behaviour, which reflects the neutrino spectrum. However, since the two nuclei masses are quite different, the maximum recoil energy for argon is bigger than for xenon (see Tab. 5.1), resulting in a shift between the two curves which increase with the recoil energy. The second ingredient which change between xenon and argon is the CEnNS differential cross section in Eq. 5.15. Since the latter depends in a complicated way mainly on the nuclei mass, the recoil energy, the number of neutrons and the form factor, it is not trivial to predict which differential cross section is larger for a given neutrino energy. For example, considering a neutrino energy of 200 MeV the differential cross section for xenon is larger than the argon one for recoil energies below about 65 keV, as it can be seen in Fig. 5.4. Above that energy the argon differential cross section remains larger. In Fig. 5.7 the recoil energy for which the differential cross sections in argon and xenon become the same is plotted as a function of the neutrino energy. In particular, the orange area indicates for a given neutrino energy the maximum recoil energy for which the xenon differential cross section dominates. Conversely, in the blue area the argon dominates. For large neutrino energies ($\gtrsim 100\,$MeV) the recoil energy for which the argon cross section becomes dominant is almost flat ($\sim 60\,$keV). This is due to the fact that in xenon at these energies the loss of coherency starts to became important and we are already above the first diffraction minimum.

Until now I have studied in detail the behaviour of the differential rates for xenon and argon. However, the interesting quantity for a future DM detector is the integrated number of coherent neutrino background events. The integrated number of neutrino events reads

$$N_\nu(E_{\text{th}}) = \int_{E_{\text{th}}}^{E_{\text{up}}} \frac{dR}{dE_r} dE_r \,, \tag{5.21}$$

in which the value of E_{up} represents the upper limit of the nucleus recoil energy. In Fig. 5.11 and Fig. 5.12 the integrated number of neutrino events is shown as a

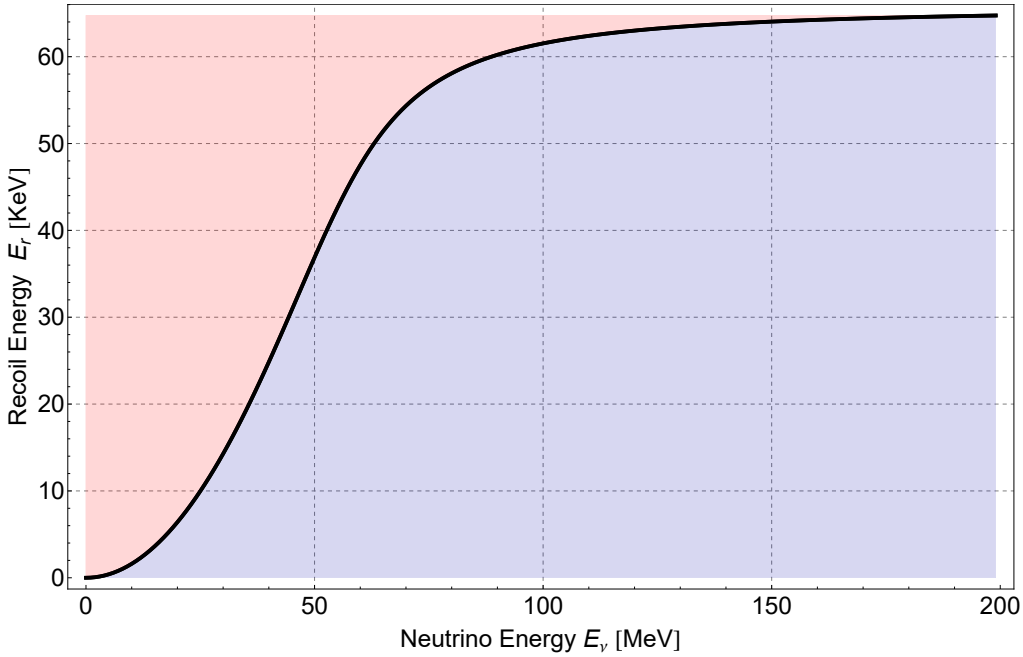

Fig. 5.7.: Recoil energy in keV for which the differential cross sections in argon and xenon are equal, as a function of the neutrino energy in MeV. The orange area indicates for a given neutrino energy the maximum recoil energy for which the xenon differential cross section dominates. Conversely, in the blue area the argon differential cross section is larger.

function of the threshold energy for xenon and argon respectively, having fixed the upper energy to $E_{\text{up}} = 400\,\text{keV}$[3]. For example for $E_{\text{th}} = 5\,\text{keV}$ in xenon we will have ~ 0.04 neutrinos per tonne in a year. This number rapidly increases by a factor ~ 100 if one lower the threshold to $\sim$ 2 keV. This increment is due to the contribution of boron and hep neutrinos, setting a natural threshold energy for xenon experiments. For argon instead taking $E_{\text{th}} = 30\,\text{keV}$ we have ~ 0.019 neutrinos per tonne in a year which increase by a factor ~ 100 for $E_{\text{th}} \sim 6\,\text{keV}$. This is better visible looking at the comparison plot between xenon and argon event rates shown in Fig. 5.13.

5.5.1 One neutrino isoevent curve for argon and xenon

As we have seen in previous sections, the WIMP sensitivity depends crucially on the number of background events. In this section, following Ref. [256], an

[3] Note that this choice is arbitrary since argon and xenon experiments have in general very different upper energies. However, since most of the events are concentrated at lower energies this choice doesn't have a large impact on the integrated number of neutrino events.

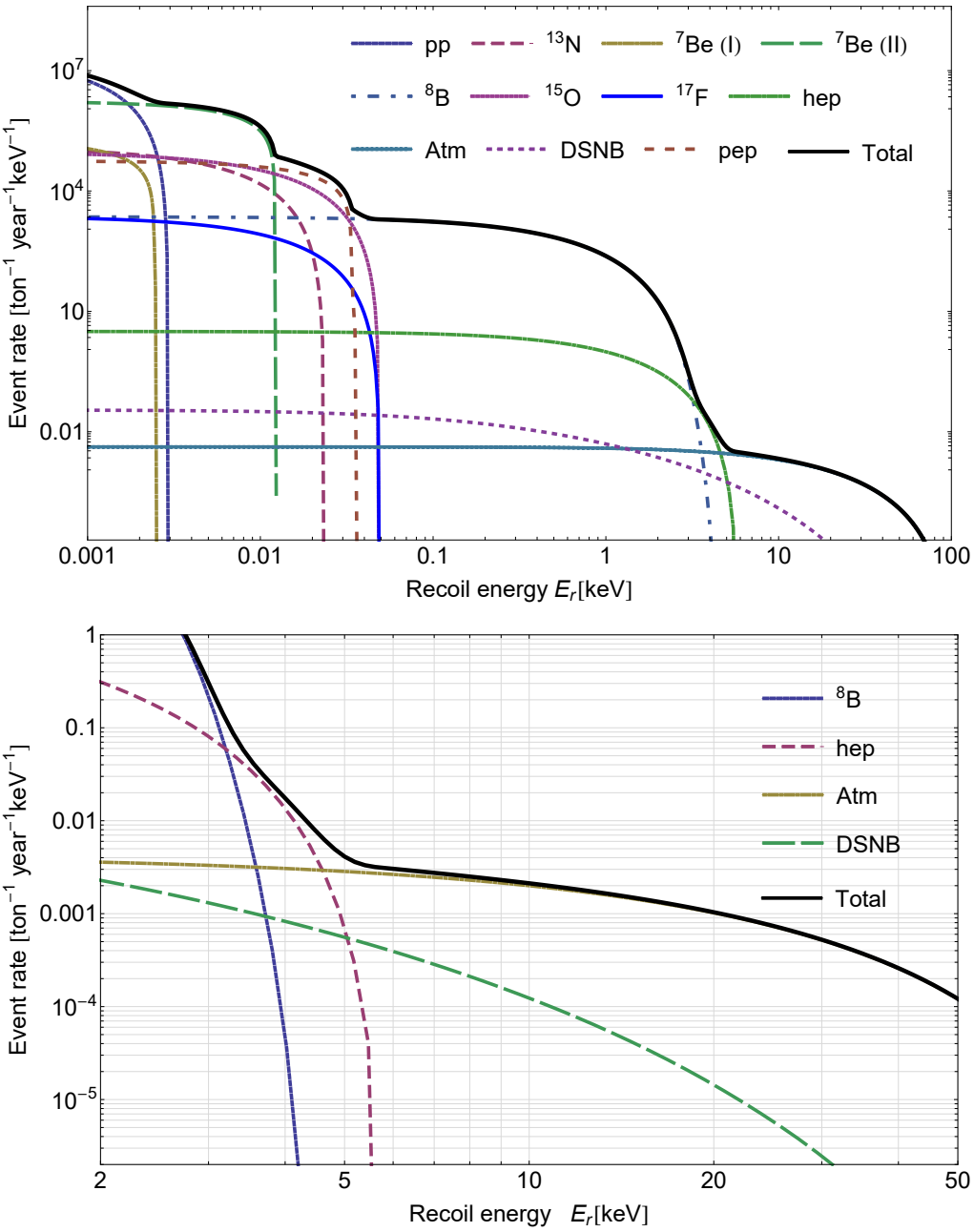

Fig. 5.8.: **Upper panel**: Differential rate for CEnNS in xenon (Eq. 5.20) as a function of the recoil energy E_r in keV.
Lower panel: The same as the upper panel zoomed in the interesting recoil energy range for future xenon DM detectors.

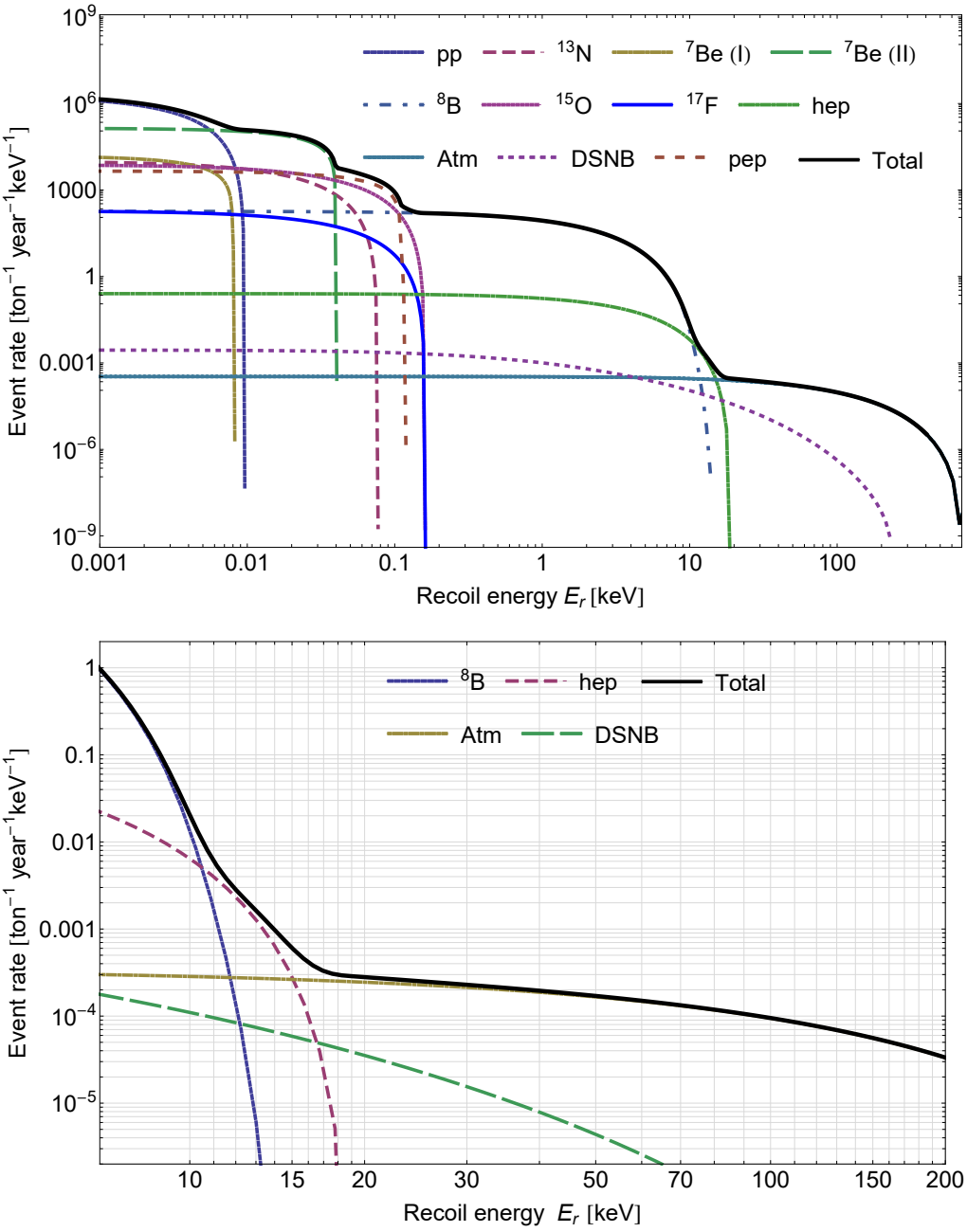

Fig. 5.9.: **Upper panel**: Differential rate for CEnNS in argon (Eq. 5.20) as a function of the recoil energy E_r in keV.
Lower panel: The same as the upper panel zoomed in the interesting recoil energy range for future argon DM detectors such as DarkSide-20k.

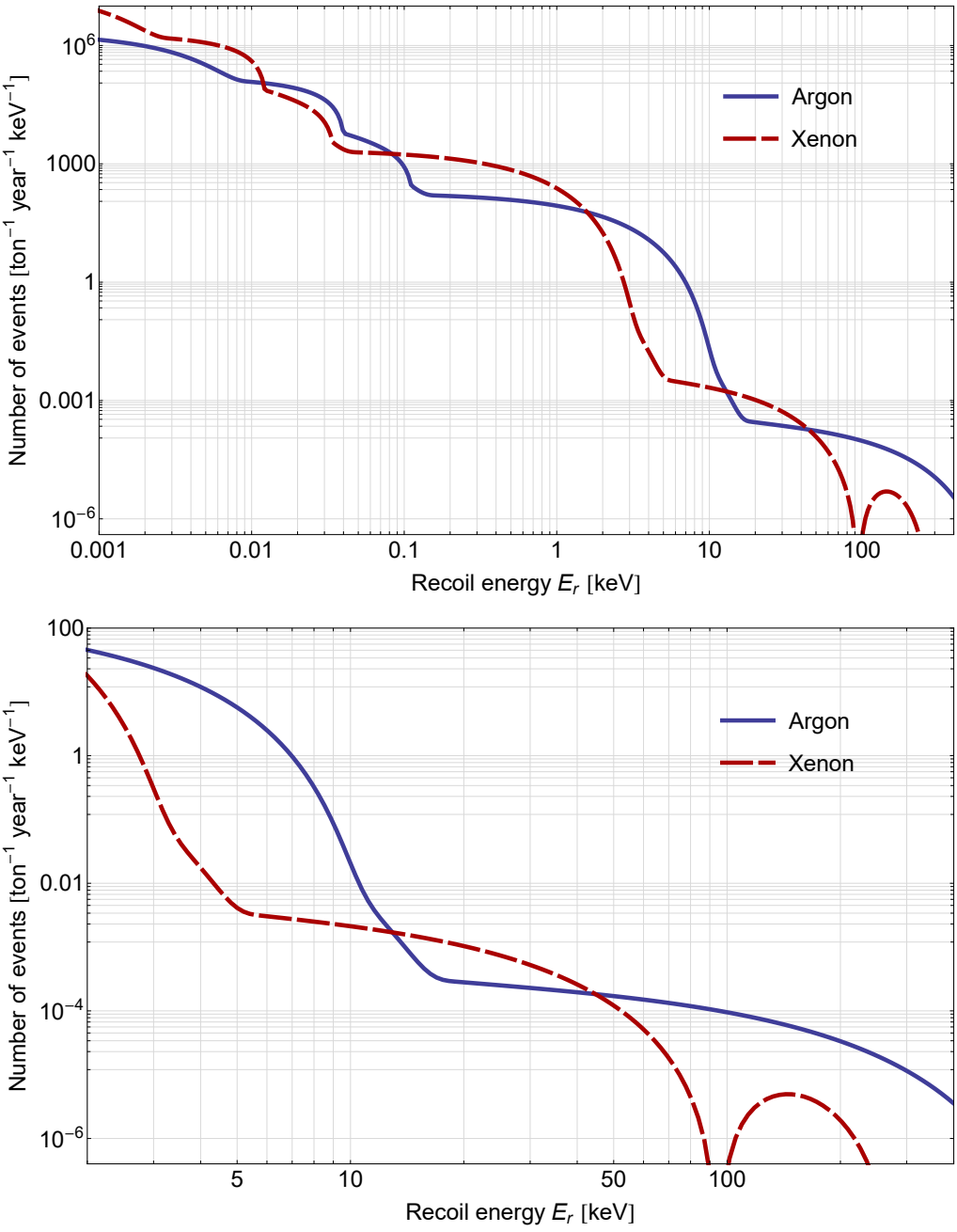

Fig. 5.10.: **Upper panel**: Differential rate for CEnNS in argon (solid blue line) and in xenon (dashed red line) (see Eq. 5.20) as a function of the recoil energy E_r in keV.
Lower panel: The same as the upper panel zoomed in the interesting recoil energy range for future DM detectors.

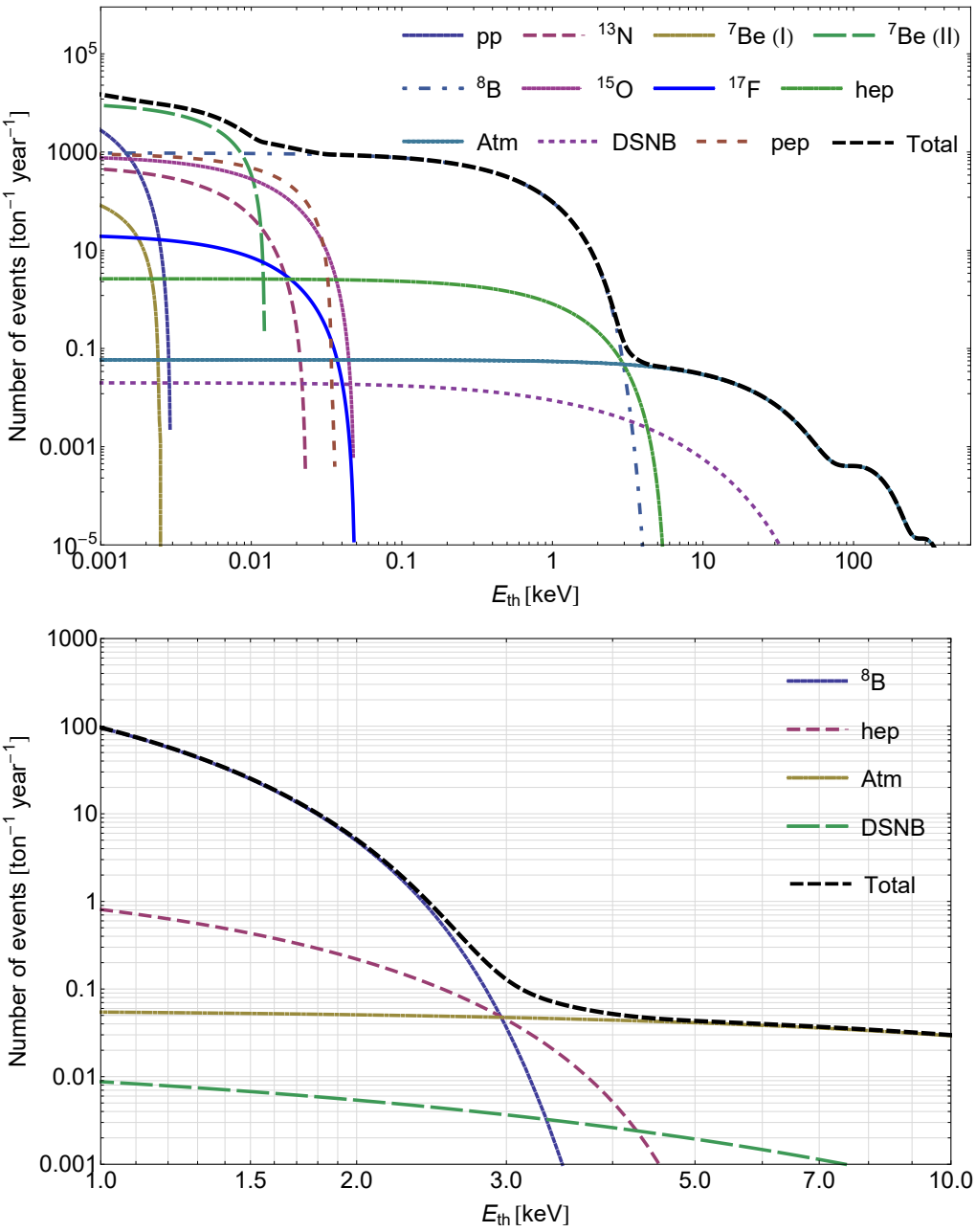

Fig. 5.11.: **Upper panel**: Integrated number of CEnNS events as defined in Eq. 5.21 for xenon as a function of the threshold energy E_{th} in keV for E_{up}=400 keV. **Lower panel:** The same as the upper panel zoomed in the interesting recoil energy range for future DM detectors.

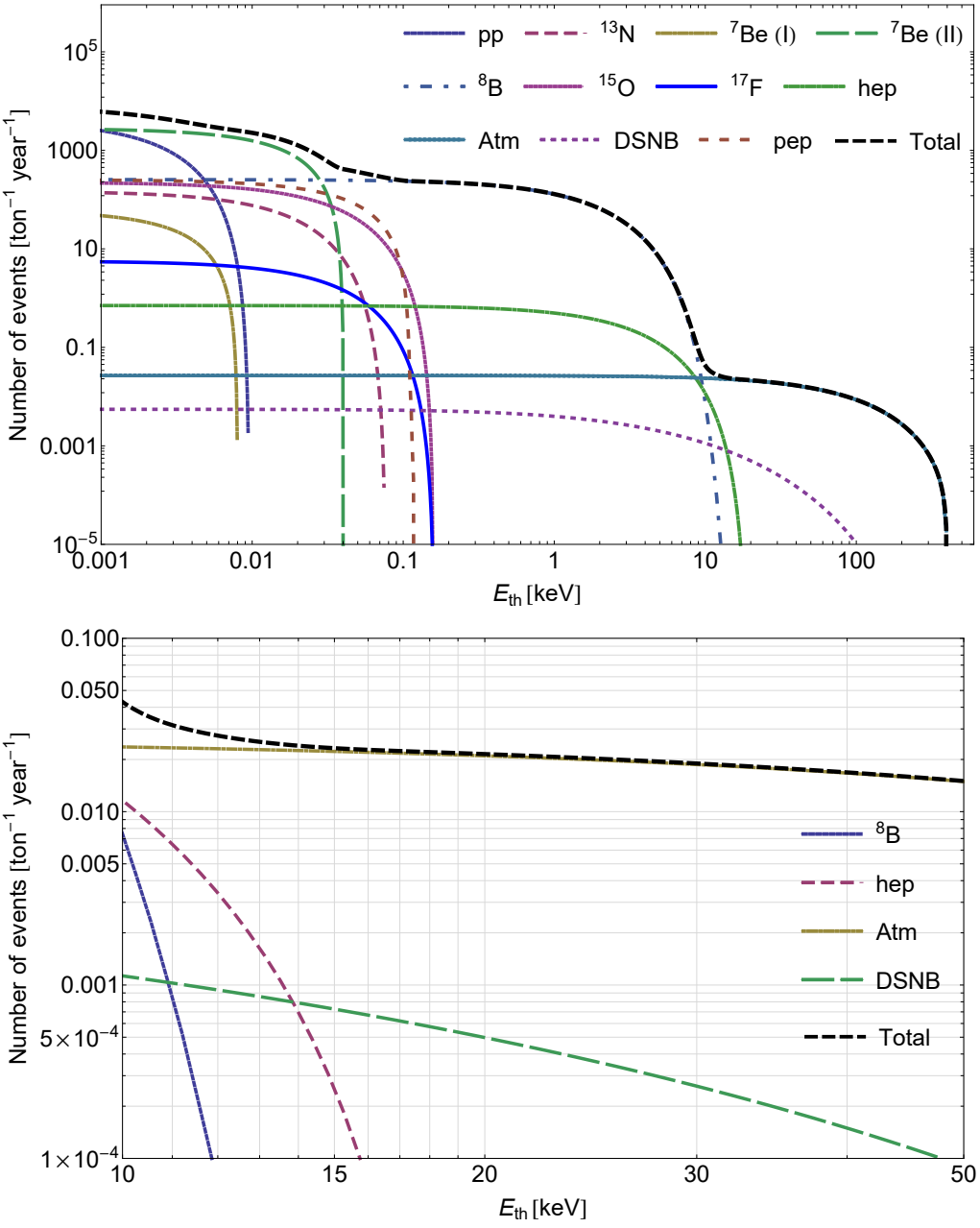

Fig. 5.12.: **Upper panel**: Integrated number of CEnNS events as defined in Eq. 5.21 for argon as a function of the threshold energy E_{th} in keV for E_{up}=400 keV. **Lower panel:** The same as the upper panel zoomed in the interesting recoil energy range for future DM detectors such as DarkSide-20k.

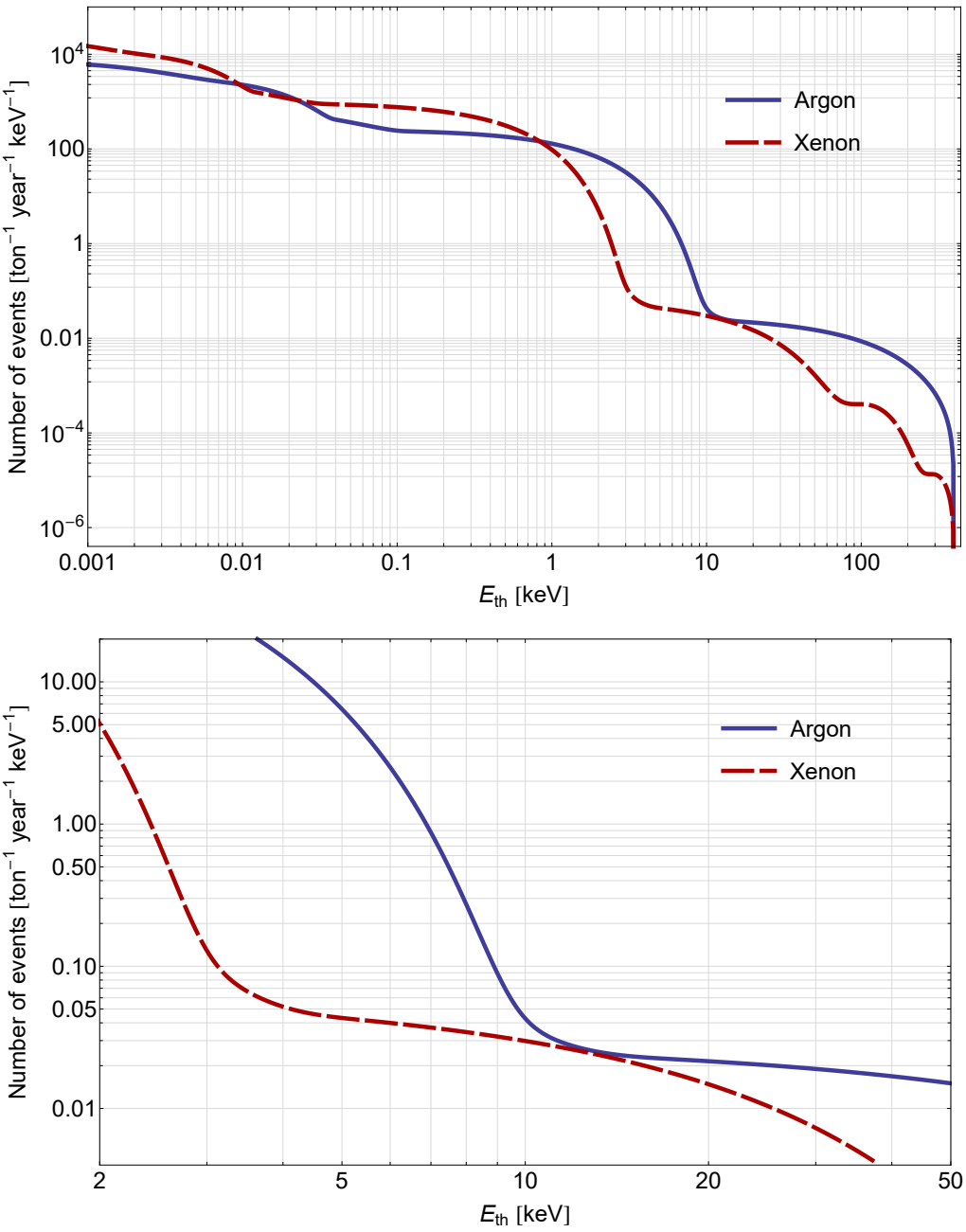

Fig. 5.13.: **Upper panel**: Integrated number of CEnNS events as defined in Eq. 5.21 for argon (solid blue line) and xenon (dashed red line) as a function of the threshold energy E_{th} in keV for E_{up}=400 keV.
Lower panel: The same as the upper panel zoomed in the interesting recoil energy range for future DM detectors.

alternative and more instructive way to quantify the impact of the neutrino CEnNS background on the WIMP sensitivity is presented. It is in fact possible to represent this background as a line in the WIMP-nucleon cross section vs WIMP mass plane considering an ideal argon or xenon experiment.

Generating a big number of background-free exclusion limits, which are defined as isovalues of WIMP events (2.3 at 90% C.L.), as a function of the WIMP mass, with varying thresholds from 0.001 to 400 keV it is possible to adjust each curve's exposure such that each experiment expects a neutrino background of one event; see coloured solid lines in Fig. 5.14 for argon (top) and xenon (bottom).
By taking the lowest cross section from all the limits as a function of the WIMP mass, one can draw the line in the WIMP-nucleon cross section vs WIMP mass plane that corresponds to the best background-free sensitivity estimate achievable at each WIMP mass for a one neutrino event exposure, see dashed black line in Fig. 5.14. This curve will be referred to as one neutrino isoevent curve. This follows from the construction of the line, which joins the mass-dependent threshold/exposure pairs that optimize the background-free sensitivity estimate at each mass while having a background of one neutrino event. In Fig. 5.15 the comparison between the one neutrino isoevent curve for argon and xenon as a function of the WIMP mass is shown. As visible, in case of a background of one neutrino the sensitivity of an argon experiment is slightly lower than a xenon one for WIMP masses above about 6 GeV. This is mostly due to the fact that the integrated number of neutrino events in argon are larger than for xenon above threshold energies of ~ 10 keV (see Fig. 5.13). Having fixed the upper energy to 400 keV clearly the argon suffers more of this background than xenon being a lighter nuclei (see discussion in Sec. 5.5). This choice of the upper threshold has been done just for illustrative purposes in order to simplify the comparison between xenon and argon. However, in order to properly quantify the impact of neutrino background for real argon and xenon experiments one has to determine the signal to background ratio in the correct energy range for these experiments. For example a typical energy range for argon is 30-200 keV, while for xenon is 3-50 keV. Moreover, xenon experiments suffer also of the standard electroweak neutrino scattering on electrons, having a reduced capability in rejecting the electron recoil (ER) backgrounds. All these considerations will be explain in more detail in Sec. 5.7.

Looking in more detail into Fig. 5.15, it is noticeable that between WIMP masses of 5 to 10 GeV there is a sudden change in the WIMP sensitivity corresponding

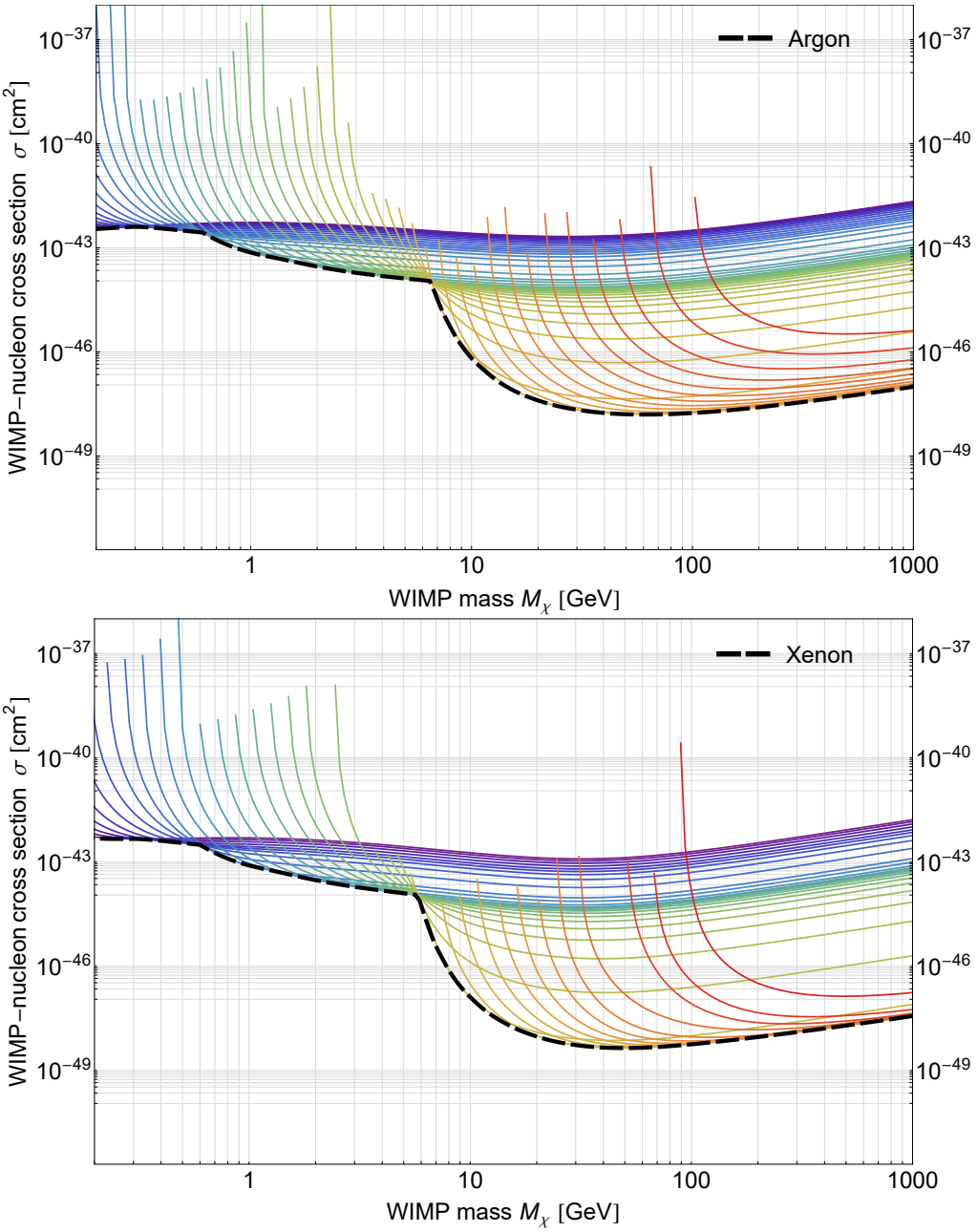

Fig. 5.14.: **Upper panel**: Set of derived background-free sensitivity curves for exposures that correspond to one coherent neutrino event, for different thresholds from 0.001 (purple) to 400 keV (red) considering argon as a target. The dashed black line is constructed by joining the best sensitivity for each WIMP mass, and represents a one neutrino event contour line in the WIMP-nucleon cross section vs WIMP mass plane. **Lower panel:** The same plot for xenon as a target.

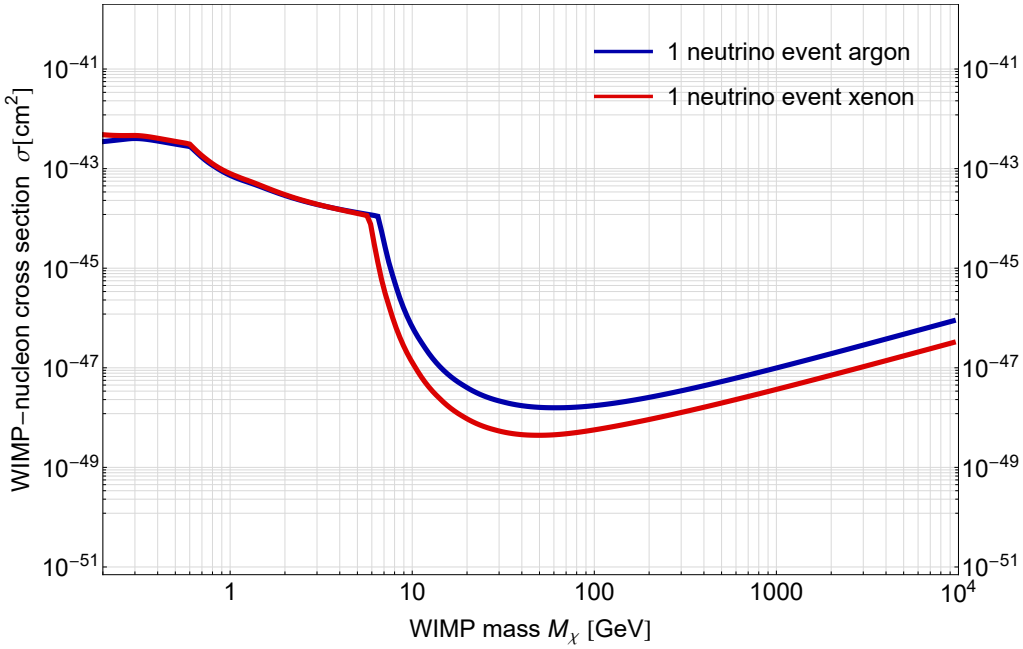

Fig. 5.15.: Comparison between the one neutrino isoevent curve for argon (blue line) and xenon (red line) as a function of the WIMP mass in GeV.

to exposures leading to one neutrino event. A Xe(Ar)-based experiment needs to have a threshold below 4 (13) keV to have sensitivity to WIMPs below ∼6.3 (7.1) GeV. As already mentioned in the previous sections, below 4 (13) keV the ^{8}B and hep neutrinos start to become important, and their much larger rate implies that one needs a much lower exposure to obtain one neutrino event. On the other hand, for WIMP masses above ∼10 GeV, a better WIMP sensitivity can be achieved by a Xe (Ar)-based experiment by increasing the threshold even further above 4 (13) keV. In this way the experiment becomes mainly insensitive to the solar neutrinos and only atmospheric neutrinos remain as the dominant neutrino background. The much lower neutrino flux implies a much larger exposure to attain one neutrino event. One can deduce from Fig. 5.15 that aiming at detecting a light WIMP (below 10 GeV) with a cross section below 10^{-45} cm^2 or a WIMP heavier than 20 GeV with a cross section below 10^{-48} cm^2 will be very challenging due to the presence of a consistent neutrino background. Notice that for argon the abrupt drop around 6 GeV occurs at slightly larger masses (around 7 GeV). This kinematic effect will be discussed in the next section.

5.6 Kinematic differences in WIMP and neutrino reconstruction

We have seen that neutrino can scatter off a nucleus producing a nuclear recoil almost indistinguishable from a WIMP event. However, due to differences in mass and energies between neutrinos and WIMP we will have a different kinematic behaviour between the two. In this section I will analyse these effects in more detail. In Fig. 5.16 the coloured line indicates the maximum recoil energy (see Eq. 5.17) generated by a neutrino given a certain neutrino energy (see right y-axis). The y-axis on the left indicates instead the minimum WIMP mass that can be inferred interpreting the neutrino scattering as a WIMP event. Indeed, since in Standard Halo Model a WIMP can have a maximum speed given by $v = v_E + v_{\rm esc} = 232 + 544$ km/s $= 776$ km/s (see Sec. 3.3) as seen by a detector at Earth, the corresponding recoil energy would determine an univocal minimum WIMP mass that can be detected. For example a ^{8}B neutrino would generate a maximum recoil energy of $\sim$ 14.4 (4.4) keV in argon (xenon), see top (bottom) plot of Fig. 5.16. In turn, this recoil energy would be produced by a WIMP with mass equal or greater than 7.6 (6.7) GeV. On the other hand, an atmospheric neutrino with energy $\sim$ 70 MeV would generate a maximum recoil energy of $\sim$ 262 (80) keV in argon (xenon) that would be produced by a WIMP with mass equal or greater than 98 (35) GeV. So, from masses above 98 (35) GeV, the sensitivity to WIMP is determined mostly by the atmospheric neutrino flux (see Fig. 5.15).

It is interesting to investigate how a neutrino false positive WIMP detection signal could be interpreted analysing the data under the WIMP only hypothesis. For these purposes, I introduce the WIMP only likelihood function defined as follows [398, 347]:

$$\mathscr{L}(M_\chi, \sigma) = \frac{N_\chi^{\rm N}}{\rm N!} e^{-N_\chi} \prod_{i=1}^{\rm N} f_\chi(E_{r_i}), \tag{5.22}$$

where f_χ is the unit normalized energy distribution for WIMP-induced nuclear recoils and N_χ is the expected number of WIMP events for a given WIMP mass and WIMP-nucleon cross section (σ) defined as:

$$N_\chi = \int_{E_{\rm th}}^{E_{\rm up}} \frac{dR}{dE_r} dE_r, \tag{5.23}$$

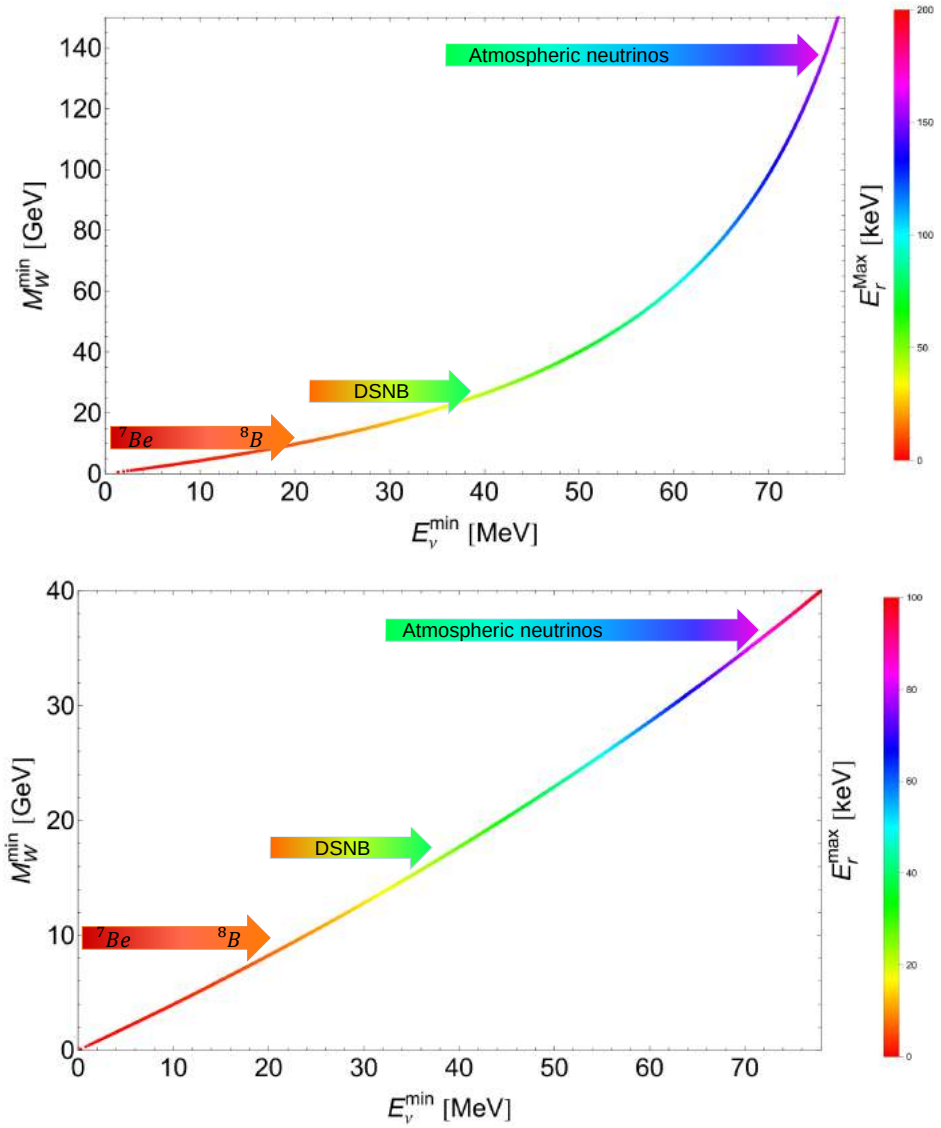

Fig. 5.16.: **Upper panel**: The coloured line indicates the maximum recoil energy (see Eq. 5.17) generated by a neutrino of a given energy (see right y-axis) in argon. The y-axis on the left indicates instead the minimum WIMP mass that can be inferred interpreting the neutrino scattering as a WIMP event.
Lower panel: The same as the upper panel for xenon.

where $E_{\rm th}$ is the nuclear recoil energy threshold and $E_{\rm up}$ is the upper limit which is taken to be equal to 400 keV.
In order to study how a neutrino signal could be interpreted as a potential WIMP signal, I computed the maximum likelihood distribution of several Monte Carlo pseudo-experiments that only contain neutrino-induced nuclear recoils. Also, I have varied the total exposure such that the expected number of neutrino events for each threshold energy is about 500 events, which is roughly the number of neutrino events which define the so-called "neutrino floor"[4].

The resulting distributions for various energy thresholds are presented in Fig. 5.17 for a xenon target (top and middle panels) and argon target (lower panel) where the different symbols and colours correspond to the various energy thresholds considered: 1 eV, 10 eV, 100 eV, 1 keV, 2.5 keV, 5 keV, 7.5 keV, and 10 keV (30 keV for argon only). From the different distributions, one can deduce that for energy thresholds of the order of 1 keV and below, the reconstructed WIMP mass from neutrino background only data should lie within the range of 3 to 30 GeV in the case of Xe-based experiments, while for Ar-based this results in a range of 2-20 GeV. The general tendency when increasing the energy threshold is that the reconstructed WIMP mass gets higher and the cross section lower. The first effect is easily explained by the fact that when the energy threshold increases, the experiment is less sensitive to the lower-energy (but higher flux) neutrinos, and thus the higher-energy neutrinos have a more dominant role, inducing a larger fraction of higher recoil energies which mimics higher WIMP masses. The reduction of the reconstructed cross section comes from the fact that the CEnNS background is composed of several components that have different end point energies, inducing significant reductions of the event rate when increasing the energy threshold. As a matter of fact, as the reconstructed WIMP mass and cross section drastically depend on the energy threshold, this suggests that the total CEnNS spectrum is not well fitted by a WIMP only hypothesis on the whole energy range from 1 eV to 400 keV.

In Fig. 5.18 the comparison between argon and xenon distributions of the maximum likelihood of the CEnNS background under the WIMP only hypothesis for a set of different experimentally interesting thresholds (1 keV, 5 keV, 10 keV) is shown. For 1 keV threshold a neutrino in xenon would be reconstructed as a WIMP mass between 5.5-9 GeV and a WIMP-nucleon cross section between

[4]The concept of "neutrino floor" will be introduced later. For the purpose of this section it is just necessary to know that it corresponds to a background of 500 neutrino events.

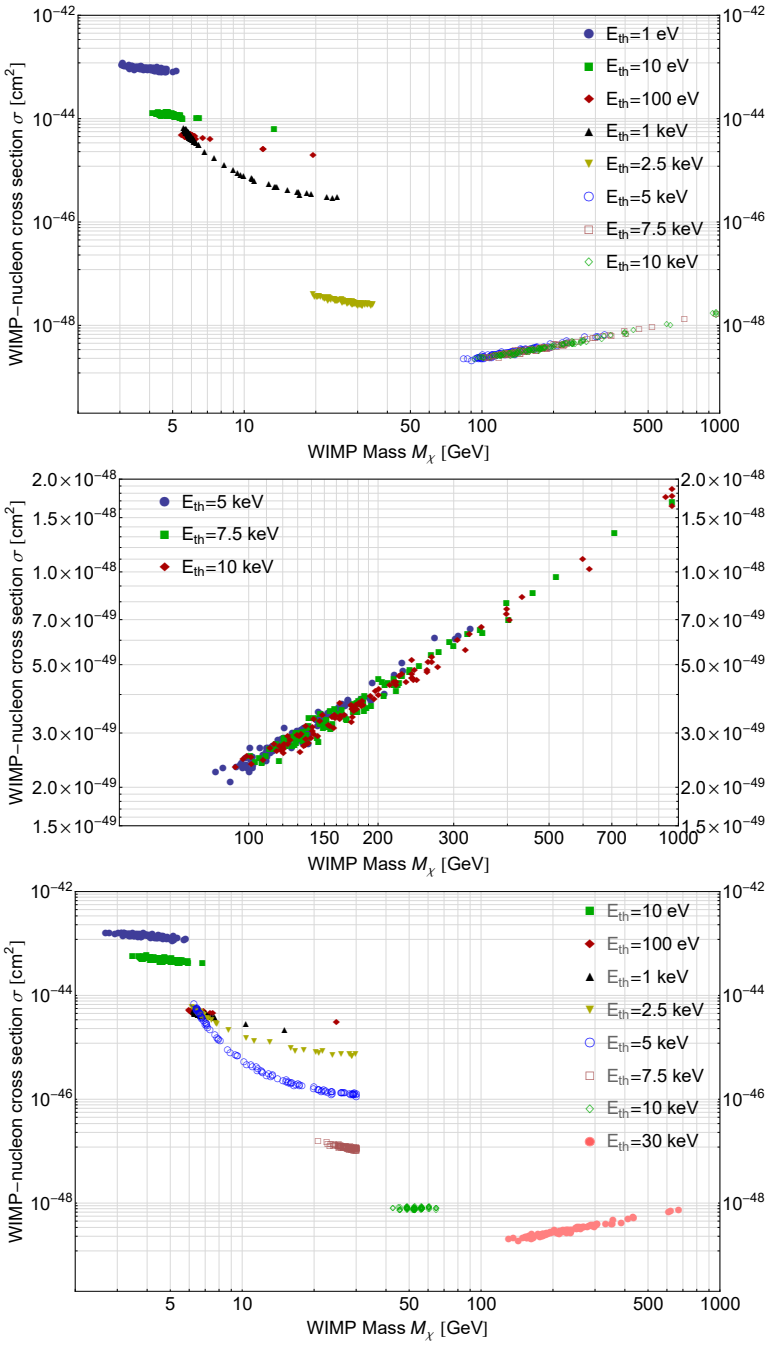

Fig. 5.17.: **Upper panel**: Distributions of the maximum likelihood of the CEnNS background under the WIMP only hypothesis for a xenon target. The different symbols and colours correspond to the energy threshold considered: 1 eV, 10 eV, 100 eV, 1 keV, 2.5 keV, 5 keV, 7.5 keV, and 10 keV. These distributions have been computed by adjusting the experiment exposure such that there is a total of about 500 expected neutrino events for each different energy threshold.
Middle panel: Zoom of the upper panel in the high WIMP mass (>100 GeV) region.
Lower panel: Same as upper panel for an argon target. Note that an additional energy threshold of 30 keV has been considered.

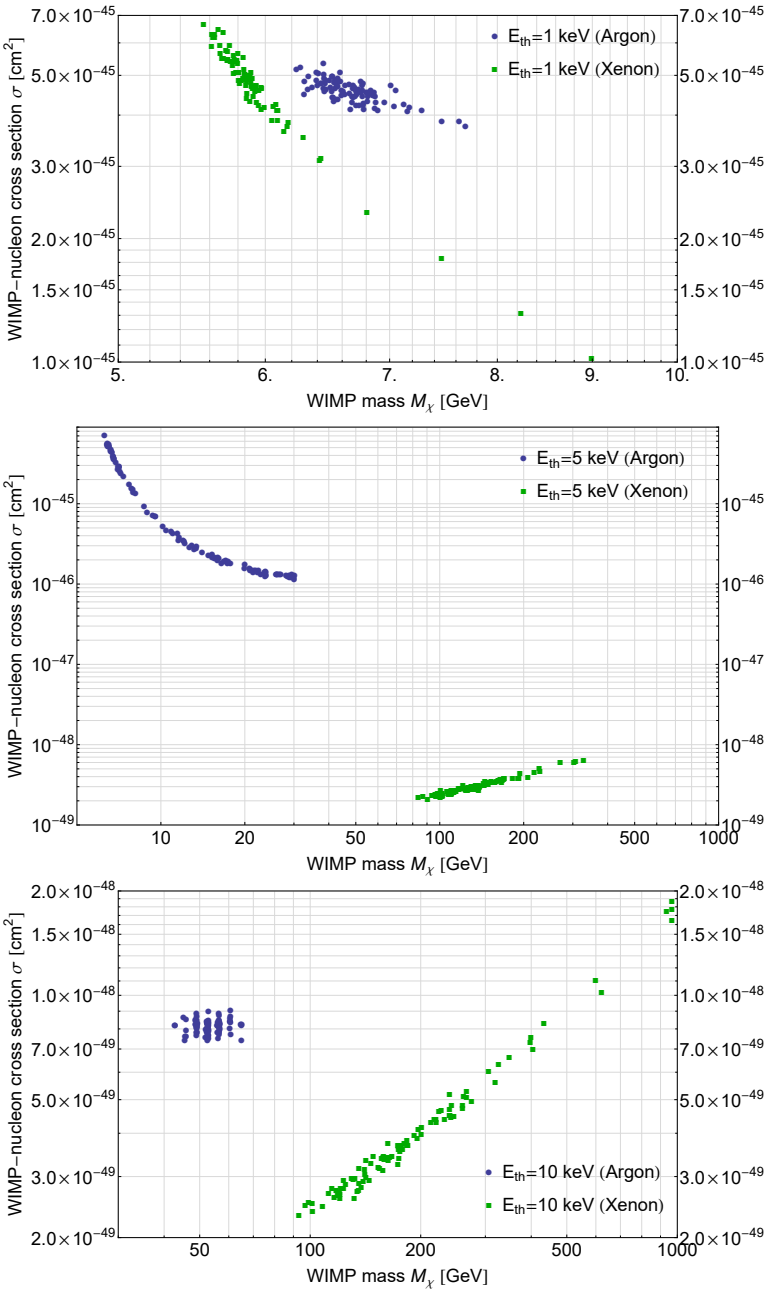

Fig. 5.18.: Comparison between argon (blue) and xenon (green) distributions of the maximum likelihood in Fig.5.17 of the CEnNS background under the WIMP only hypothesis for energy thresholds of 1 keV (upper panel), 5 keV (middle panel), and 10 keV (lower panel).

1-7$\times 10^{-45}$ cm^2. In argon this would correspond instead to a WIMP mass between 6.2-8 GeV and a WIMP-nucleon cross section between 3.8-5.5$\times 10^{-45}$ cm^2. Using the mean reconstructed values of M_χ and σ from the aforementioned distributions to derive the spectrum of a given WIMP model and comparing it with the total CEnNS-induced nuclear recoil energy spectrum we obtain the distributions in Fig. 5.19. This comparison allows to assess how well the CEnNS spectrum is fitted by a WIMP only hypothesis. As it is possible to see, the WIMP only hypothesis fits the total CEnNS background reasonably well. It is easy to understand that the neutrino background could only mimic very well a WIMP detection in the case where the energy threshold is high enough such that there is only one very dominant contribution or a smooth superposition of different neutrino components, such as ^{8}B and hep neutrinos or atmospheric and diffuse supernova neutrinos. Thus, one could vary the energy threshold of the experiment to get a consistency check of the WIMP hypothesis.

By looking at the distributions for 5 keV and 10 keV energy thresholds (middle and bottom panel of Fig. 5.19, respectively) one can notice that there is a large separation between the WIMP reconstructed physics parameters in argon and xenon. The combination of the results of argon and xenon experiments (or in general different nuclei) can thus be exploited to disentangle the neutrino events from a genuine WIMP signal [399].

From all these studies one can conclude that the solar neutrinos tend to be reconstructed at low WIMP masses with high cross sections while the DSNB and atmospheric neutrinos are at much higher WIMP masses and much lower cross sections. One can easily deduce that the neutrino background will start to become important when an experiment will start to reach sensitivities down to 10^{-45} cm^2 (10^{-48} cm^2) for the light (heavy) WIMP range.

Until now, I have discussed different scenarios for argon and xenon experiments considering a wide range for the energy thresholds. This has been done for illustrative purposes, since most of the energy thresholds considered are beyond the current and also near future possibilities for xenon and argon experiments. In the following, I will concentrate on argon and I will restrict the energy range to that of interest for DarkSide-20k. As seen in 4.4.2 the NR acceptance for DarkSide-20k is in the range 20-200 keV and so it will be sensitive to diffuse supernova and atmospheric neutrinos. In Fig. 5.20 I show the comparison for

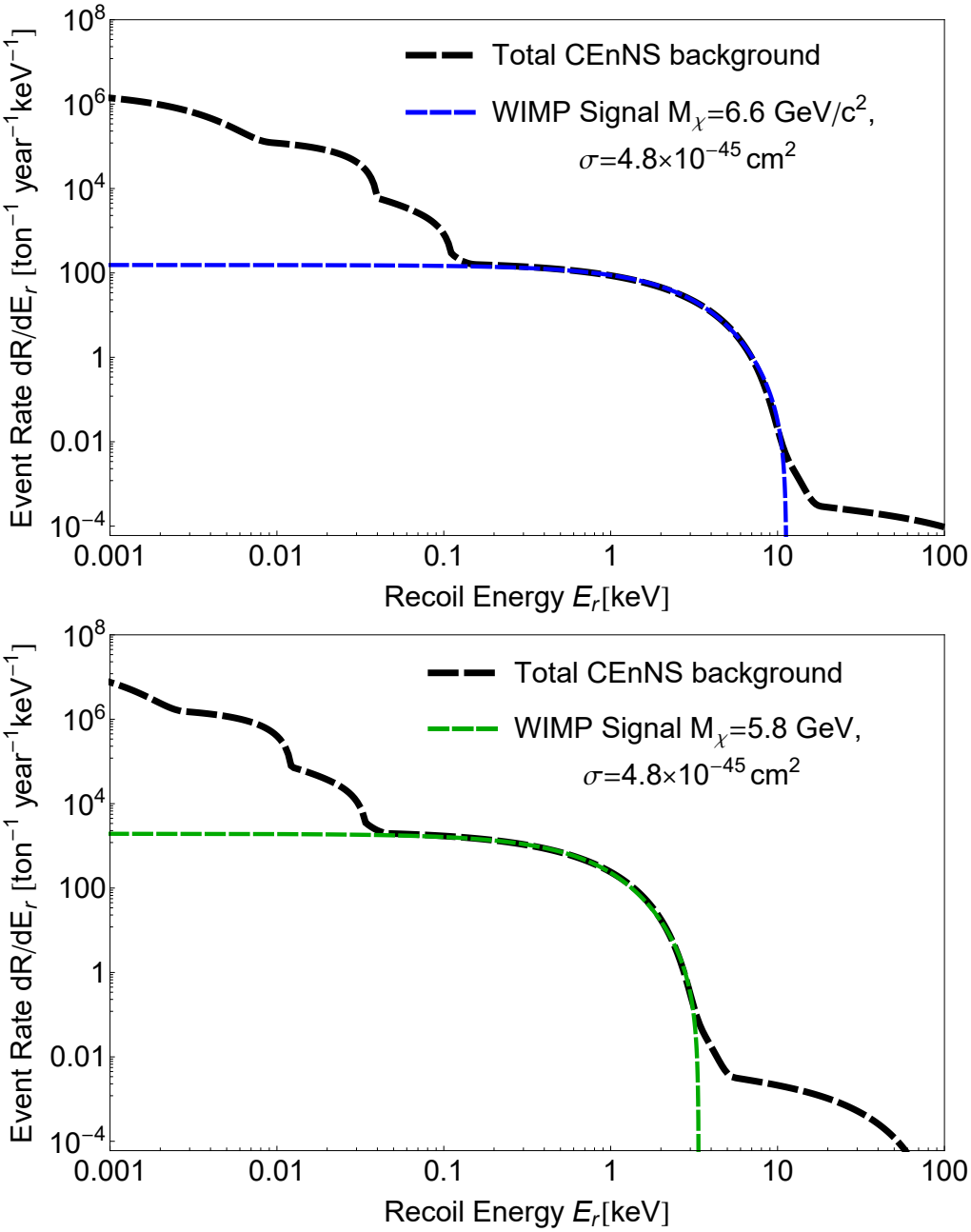

Fig. 5.19.: Comparison between the nuclear recoil event rate as a function of energy from the CEnNS background (dashed black line) and the best fit WIMP models for an energy thresholds of 1 keV deduced from the upper panel of Fig. 5.18, in the case of an argon (upper panel) and xenon (lower panel) target.

argon between the differential rate as a function of the recoil energy for a 200 GeV (top panel) and 1 TeV (bottom panel) WIMP signal and the CEnNS background differential rate. The WIMP-nucleon cross sections have been chosen such that the total number of WIMP events in the integration range 20-200 keV matches

the total number of neutrino background events in the same energy range, which is about 1.87 events/(100 tonne year). As visible, the two distributions slightly differ. In particular, having made the assumption to have the same number of WIMP and neutrino events[5] it is possible to see that the two curves have different slopes and they intercept around 70 keV. This implies that one could expect a small gain in sensitivity when using a complete likelihood analysis including the spectral information. Moreover, restricting the integration range up to $\sim$70 keV, at least in this example, should maximize the signal to background ratio.

[5]Note that this represents the worst scenario. In reality in order to exclude at 90% C.L. the background hypothesis, with such a level of background, one needs at least about 4 WIMP events, see Sec. 5.1.1.

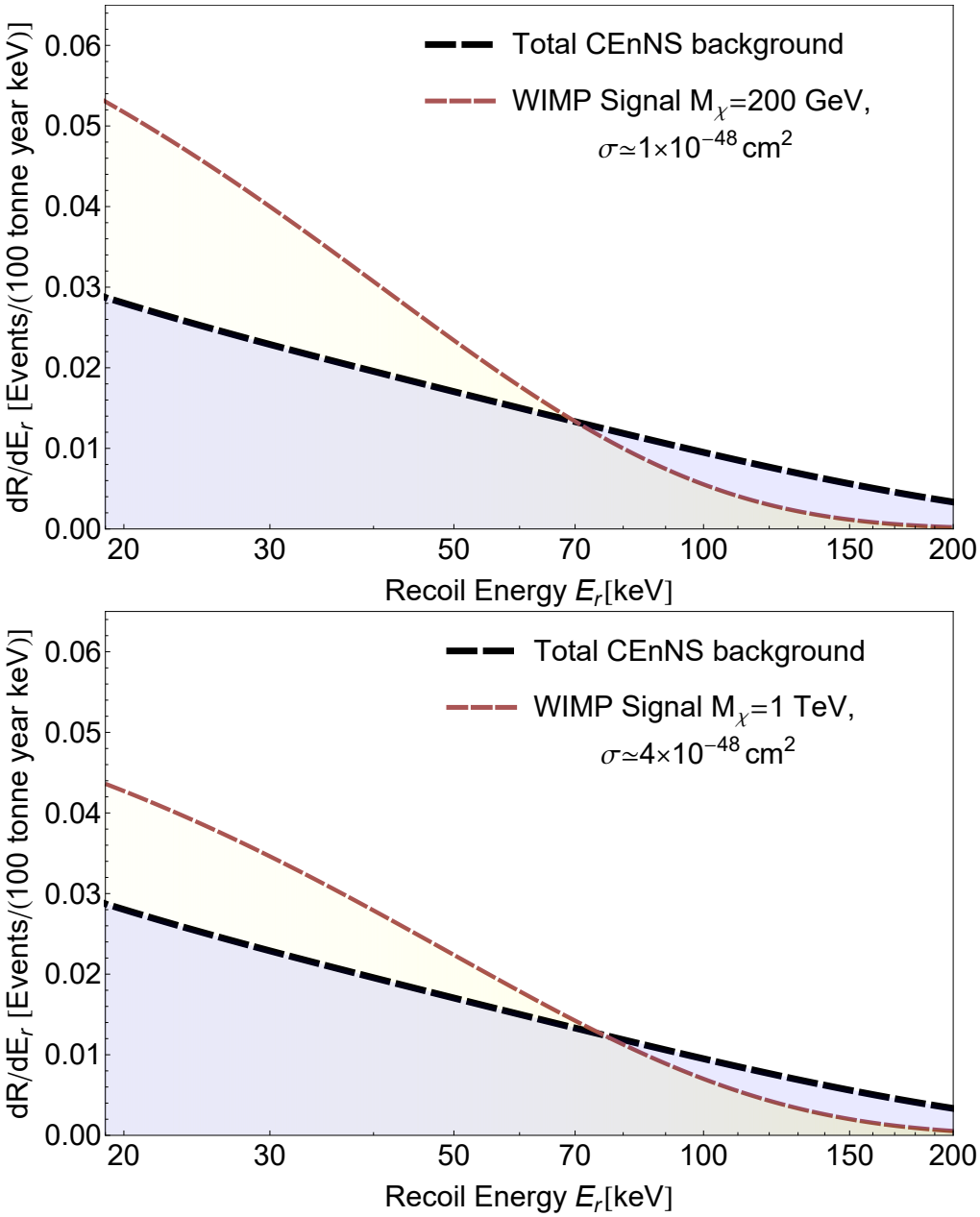

Fig. 5.20.: Comparison for an argon target between the differential event rate as a function of the nuclear recoil energy for the CEnNS background (dashed black line) and for a 200 GeV (top panel) and 1 TeV (bottom panel) WIMP signal (dashed red line). The different values of the WIMP-nucleon cross section have been chosen such that they give the same number of neutrino and WIMP events when integrating between 20 and 200 keV recoil energies.

5.6.1 DarkSide-20k and Argo/GADMC detector sensitivity

Until now I have discussed the general implications of the CEnNS background for an argon detector capable of collecting $\mathcal{O}(100)$ tonne year exposure, without including the nuclear recoil energy acceptance (see Sec. 4.4.2 and Fig. 4.9) which characterize a particular experiment. In this section I will, first of all, derive the number of CEnNS background including the experimental acceptance for DarkSide-20k and its nominal exposures. Secondly, given this number, I will draw the 90% WIMP-nucleon cross-section sensitivity limits following the statistical discussion made in Sec. 5.1.

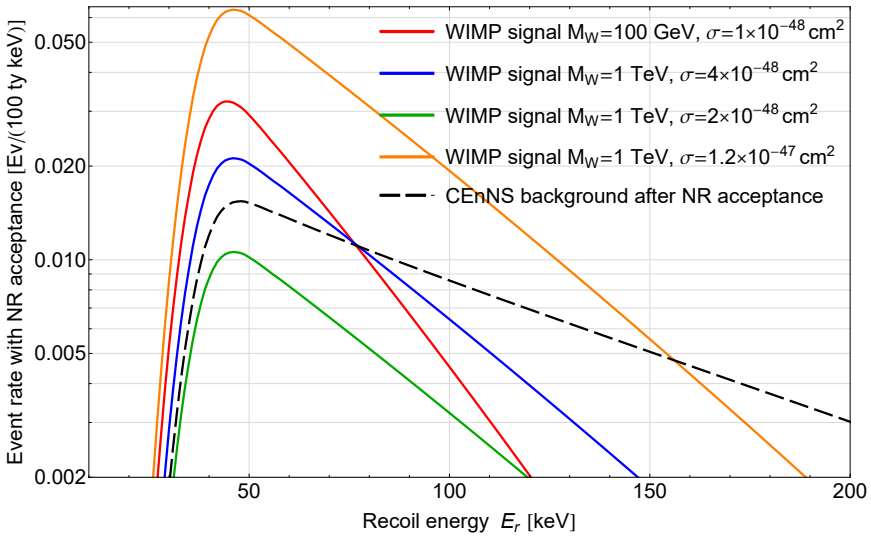

Fig. 5.21.: Differential rate as a function of the recoil energy convoluted by the DarkSide-20k nuclear recoil acceptance for CEnNS (dashed black line) and for WIMPs with different masses and WIMP-nucleon cross-sections: red line (M_χ =100 GeV and $\sigma = 1 \times 10^{-48}$ cm^2), blue line (M_χ =1 TeV and $\sigma = 4 \times 10^{-48}$ cm^2), green line (M_χ =1 TeV and $\sigma = 2 \times 10^{-48}$ cm^2) and orange line (M_χ =1 TeV and $\sigma = 1.2 \times 10^{-47}$ cm^2).

In Fig. 5.21 it is possible to judge the effect of the acceptance looking at the acceptance corrected WIMP and CEnNS spectra for different WIMP masses and cross sections. As visible, the curves change significantly modifying the assumptions and they cross the CEnNS spectrum at different values of the recoil energy. This is suggesting that there will be an optimal energy upper limit for which we maximize the WIMP signal to neutrino background ratio. Before to show the effect of the energy upper limit, E_{up}, on the sensitivity let us calculate the total number of CEnNS background as a function of it. To do that one needs to integrate the CEnNS differential spectra corrected by the DarkSide-20k ac-

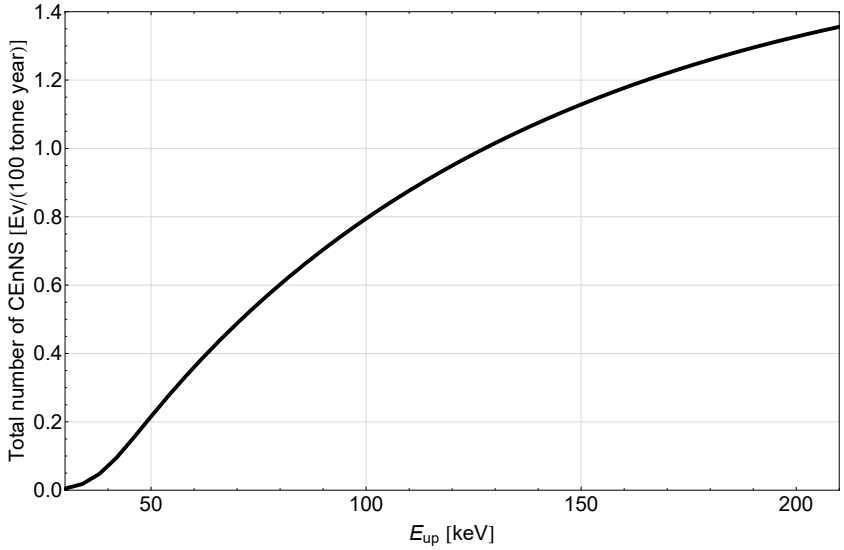

Fig. 5.22.: Total number of CEnNS background events in DarkSide-20k as a function of the upper energy limit, E_{up}, in keV.

ceptance for different values of E_{up}. The result of this is shown in Fig. 5.22. Considering E_{up}=200 keV, the number of coherent neutrino background events expected is 1.33±0.26 $(100\ \text{tonne}\ \text{year})^{-1}$, which halves at around E_{up}=86 keV. The uncertainty on the number of coherent neutrino background events can be determined considering that after applying the NR acceptance, the only neutrino sources that contribute are the atmospheric and the diffuse supernova neutrinos. Namely, their contribution is 1.31±0.26 $(100\ \text{tonne}\ \text{year})^{-1}$ and 0.016±0.008 $(100\ \text{tonne}\ \text{year})^{-1}$, respectively, where the uncertainty has been determined propagating the uncertainty on the corresponding fluxes.

With this information in mind we can calculate the final DarkSide-20k sensitivity. This can be done following the discussion in Sec. 5.1.1 for the case of a non zero background with 20% uncertainty. The WIMP-nucleon cross-section sensitivity at 90% C.L. as a function of the WIMP mass for DarkSide-20k for a total exposure of 100 tonne year is shown in Fig. 5.23 for different upper energy limits. The curves do not vary significantly considering $80 < E_{up}[\text{keV}] < 300$, however there is a slight improvement when considering $E_{up} = 150$-200 keV.

For this reason I decided to take $E_{up} = 200$ keV for the final determination of the DarkSide-20k sensitivity curves for the two exposures of 100 and 200 tonne year. In addition to this, I have estimated the sensitivity curves for a future argon

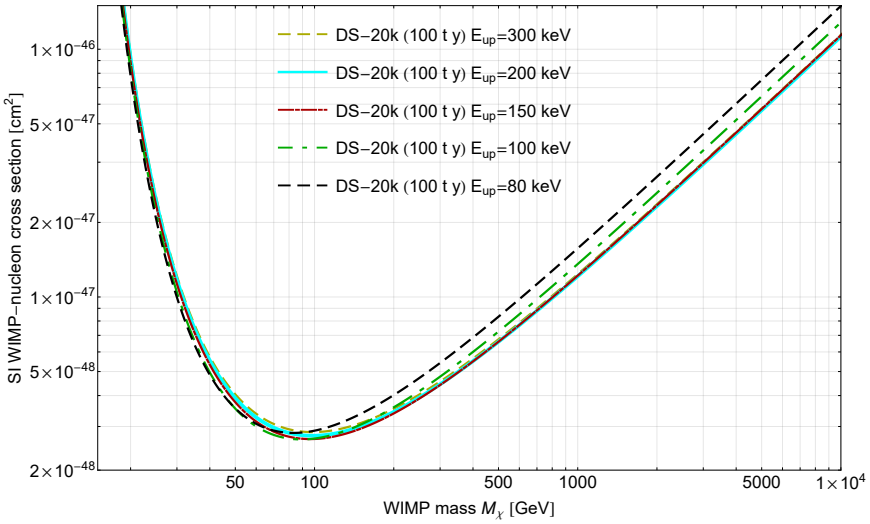

Fig. 5.23.: WIMP-nucleon cross-section sensitivity at 90% C.L. for DarkSide-20k for a total exposure of 100 tonne year for different upper energy limits.

detector, that is usually referred to as Argo or GADMC[6] capable of collecting an exposure of 2000 tonne year or even 3000 tonne year free of backgrounds other than CEnNS. Moreover, I have considered that at the time of operation of this detector the uncertainty on the number of neutrino events will be reduced to about 5%. Indeed, some recent works show the feasibility of improving already now the uncertainty on the muon-neutrino flux related to the primary cosmic rays of (5–15)%, depending on energy, which is about a factor of two smaller than the previously determined uncertainty [400]. These curves are shown in Fig. 5.24. Future DarkSide-20k experiment with an exposure of 100 tonne year will be able to exclude cross sections down to 2.8×10^{-48} cm^2 for a WIMP mass of ∼100 GeV. Future GADMC for 3000 tonne year exposure will be able to exclude cross sections down to 3×10^{-49} cm^2 for the same WIMP mass. Instead, for a WIMP mass of about 1 TeV, DarkSide-20k experiment with an exposure of 100 tonne year will be able to exclude cross sections down to 1.2×10^{-47} cm^2, whereas the same number for future GADMC for 3000 tonne year exposure is 1.5×10^{-48} cm^2. Note that the cross section does not scale as 1/MT because of the presence of the neutrino irreducible backgrounds, that in the last case is of the order of 40 events. This saturation effect is usually indicated using the so-called *neutrino floor*. In particular, in Fig. 5.24 the neutrino floor for a xenon target has been superimposed. The latter represents a discovery limit defined such that if the true WIMP model lies above this limit, then a given experiment has a 90% probability

[6]Note that the details of this far future detectors are not defined yet.

to get at least a 3σ WIMP detection and it has been calculated assuming two particular low energy thresholds, 3 eV and 4 keV, such that a fixed number of 500 neutrino events from coherent neutrino scattering on nuclei are expected. Note that the concept of neutrino floor can be misleading. Indeed, it represents a discovery limit @3σ for xenon and we are comparing it to 90% exclusion curves for argon. Despite these two share some common assumptions, they vehiculate different information. However, even if the neutrino floor is derived using some arbitrary assumptions, in the dark matter community it is often used to represent a hard limit for the WIMP-nucleon cross sections that can be reached by future experiments due to the presence of neutrino background. I have included it in Fig. 5.24 just for "historical reasons", since the sensitivity curves that I previously discussed already include the proper saturation effect due to such a background. A proper way to compare sensitivities for xenon and argon taking into account the CEnNS background has been already presented in Sec. 5.5.1.

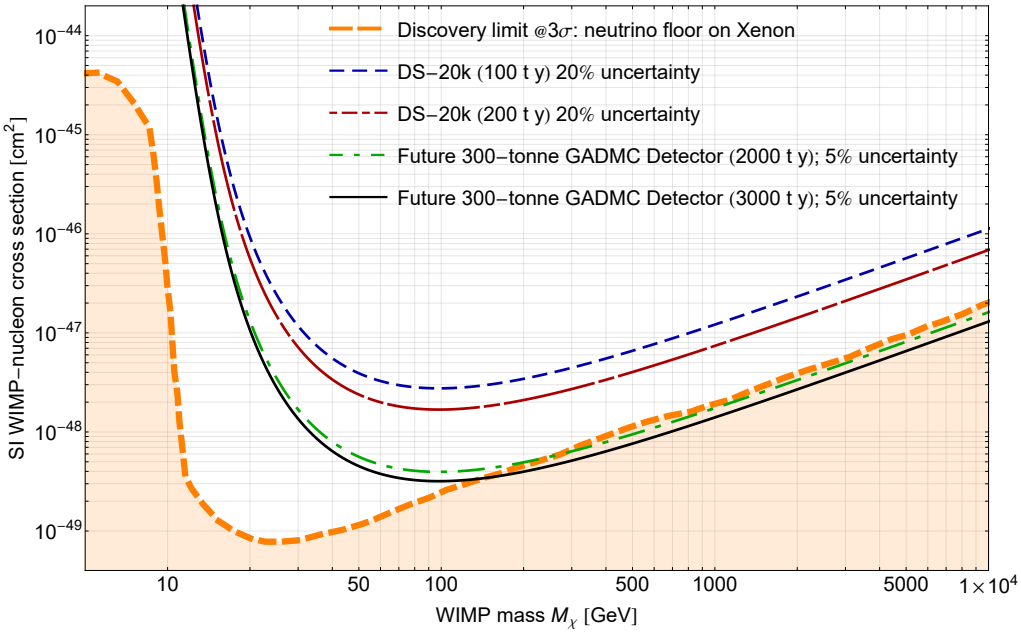

Fig. 5.24.: WIMP-nucleon cross-section sensitivity at 90% C.L. for DarkSide-20k for a total exposure of 100 tonne year (dashed blue line), and 200 tonne year considering a total 20% of background uncertainty. Sensitivity of a future 300-tonne GADMC detector for 2000 tonne year (dashed dot green line) and 3000 tonne year (solid black line) considering a total 5% of background uncertainty are also shown, superimposed with the neutrino floor for a xenon target (dashed orange line), which represents the discovery limit @3σ [256].

5.6.2 ARIA impact on sensitivity curves

The sensitivity curves that I have just discussed have been derived considering a NR acceptance that has a low threshold at around 30 keV due to the presence of ^{39}Ar combined with the excellent electron recoil rejection capabilities of argon. However, they do not exploit yet a possible depletion factor of ^{39}Ar coming from the ARIA project (see Sec. 4.3). The NR acceptance derived considering a realistic depletion factor of 100, that will maintain the ER background to a level of 0.1 events for the total exposure of 100 tonne year, is shown in Fig. 5.25. For comparison, the standard DarkSide-20k acceptance is also shown. Using this new NR acceptance we obtain the sensitivity curve for DarkSide-20k, with the usage of ARIA, shown in Fig. 5.26. As visible from Fig. 5.27, with the inclusion of ARIA, we gain a factor 5 in sensitivity at low WIMP masses which decrease to a factor 20% for high WIMP masses.

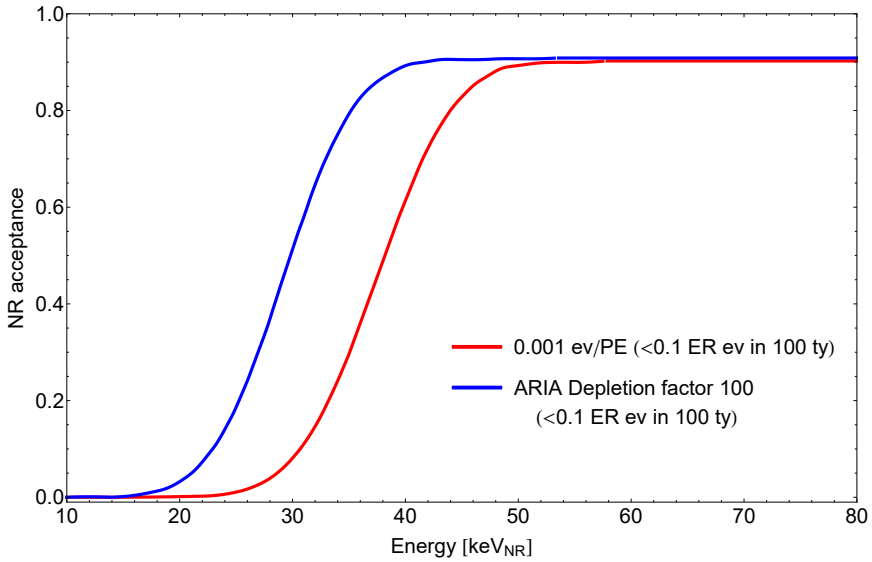

Fig. 5.25.: Nuclear recoil (NR) acceptance for DarkSide-20k, with the condition to have less than 0.1 electron recoil (ER) events from ^{39}Ar. From right to left NR acceptance for the baseline condition which correspond to have <0.1 ER events in the total 100 tonne year exposure without including the possible reduction from ARIA (red line) and NR acceptance including a depletion factor of 100 which maintains a total of less than 0.1 ER events (red line).

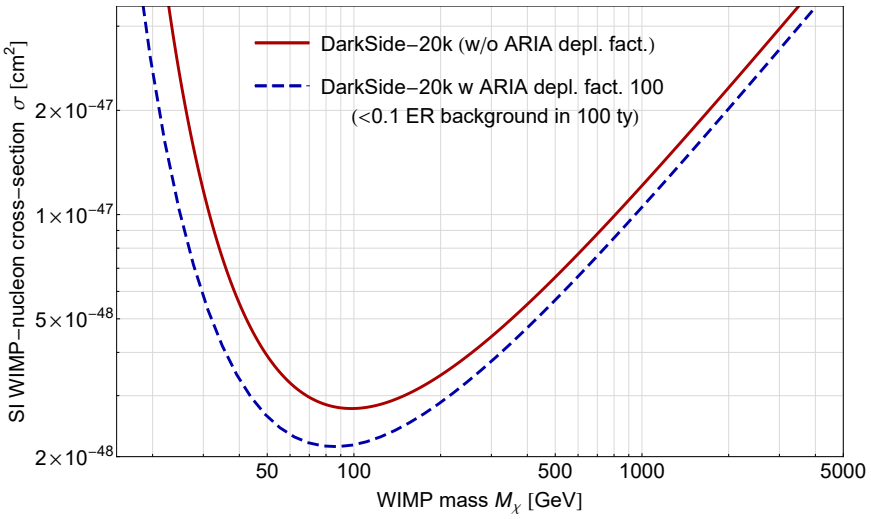

Fig. 5.26.: WIMP-nucleon cross-section sensitivity at 90% C.L. for DarkSide-20k without considering the depletion factor of ARIA (red solid line) and considering a ER ^{39}Ar depletion factor of 100 (dashed blue line) for a total exposure of 100 tonne year.

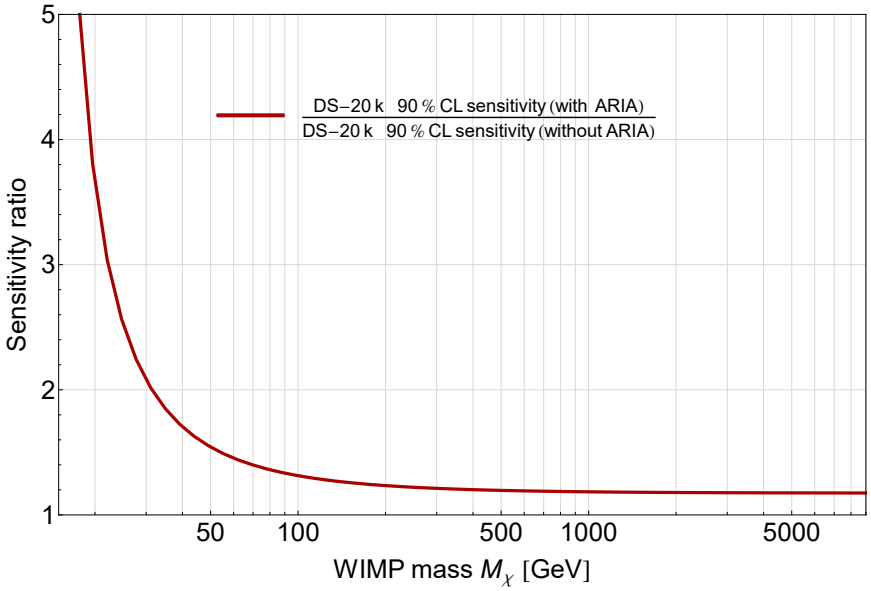

Fig. 5.27.: Ratio between WIMP-nucleon cross-section sensitivity at 90% C.L. for DarkSide-20k with the inclusion of ARIA and without it.

5.7 Argon-xenon comparison in view of standard electroweak interactions on electrons

In this section I want to compare the potentialities of future dark matter detectors for a possible WIMP discover or, in the worst scenario, in exploring and excluding lower and lower WIMP-nucleon cross sections. Since the light WIMP range (below 10 GeV) will be explored by LHC and the neutrino background will stronger limit the sensitivity already at the order of cross sections near 10^{-45} cm^2 (see Fig. 5.15), I will consider only the heavier mass range (above 20 GeV) for which the exploration of cross sections down to 10^{-48} cm^2 is still feasible (see Fig. 5.24). In this mass range the leading technology is represented by large dual-phase liquid noble TPCs at ton-scale, in particular those that use xenon and argon. From the discussion of Sec.5.5.1, it seems that xenon and argon behave very similarly regarding the one neutrino isoevent sensitivity curve. However in that section other kinds of backgrounds have been neglected. I have also demonstrated that the argon technology as used by DarkSide-20k will be able to reach a level for which all other kinds of background apart form CEnNS will be reduced to a negligible amount. This is possible especially thanks to the extraordinary ER rejection power of argon that is able to remove, for example, the electron recoil contribution due to solar neutrino scattering. Here, I will examine this fact in more detail for both argon and xenon, showing that the latter could suffer from this kind of ER backgrounds.

If an experiment does not reach sufficiently high power in electronic recoil background rejection, such background processes should be accounted for in the estimation of WIMP sensitivity or of the discovery reach of it. In the following, I will discuss the main neutrino-electron scattering processes that are relevant for neutrino energies below 1-10 MeV [401] which is the standard neutrino electron electroweak interaction. As the pp neutrinos provide the dominant contribution to the solar neutrino flux and the maximum recoil energy induced by these neutrinos is about 260 keV, we can safely neglect the other neutrino components to the total neutrino-induced electronic recoil background. Also, in the following calculations, I will neglect atomic effects and consider the electrons from the atomic cloud as being free [401, 402].

Standard neutrino-electron electroweak interaction

At tree level, the neutrino-electron electroweak interaction proceeds through the exchange of a Z boson (neutral current) and the exchange of a W boson (charged current) which is only possible in the case of an incoming electron neutrino. The resulting expression of the cross section is as follows [401, 403]:

$$\frac{d\sigma(E_\nu, E_r)}{dE_r} = \frac{G_f^2 m_e}{2\pi}\left[(g_v + g_a)^2 + (g_v - g_a)^2\left(1 - \frac{E_r}{E_\nu}\right)^2 + (g_a^2 - g_v^2)\frac{m_e E_r}{E_\nu^2}\right], \tag{5.24}$$

where m_e is the electron mass, g_v and g_a are the vectorial and axial coupling respectively and are defined such that:

$$g_v = 2\sin^2\theta_w - \frac{1}{2} \qquad g_a = \frac{1}{2}. \tag{5.25}$$

In the particular case $\nu_e + e \to \nu_e + e$, the interference due to the additional charged current contribution implies a shift in the vectorial and axial coupling constants such that $g_{v,a} \to g_{v,a} + 1$. One can easily derive that the $\nu_e + e \to \nu_e + e$ cross section is about one order of magnitude larger than in the case of $\nu_l + e \to \nu_l + e$ (where $l = \mu, \tau$). In this case one has to take into account neutrino oscillation from the solar core to the Earth-based detector when computing this neutrino-electron background. In first approximation the survival probability of ν_e below 1 MeV is constant in energy and equal to about 0.55 [389]. The remaining component is distributed between ν_μ and ν_τ which have the same expression of the cross section. In Fig. 5.28 the total neutrino electron cross section $\sigma_{\nu-e^-}$ as a function of the neutrino energy, is shown.

In Fig. 5.29 the differential rate for $\nu + e^- \to \nu + e^-$ contribution in xenon (upper panel) and argon (lower panel) is shown by the solid red line superimposed to the already shown CEnNS contributions. Differently from the CEnNS background this contribution can be somehow distinguished from a possible NR induced by a WIMP. However, the capability in rejecting this background varies significantly between xenon and argon technologies. Indeed, the pulse shape discrimination (PSD) tool in argon allows to reach an ER rejection of 6.7×10^{-8} (see Sec. 4.1.2). Taking into account this already experimentally proved ER rejection factor the $\nu + e^- \to \nu + e^-$ contribution from solar neutrinos in argon is significantly reduced and it is depicted in Fig. 5.29 (lower panel) by a dashed red line. It is clear

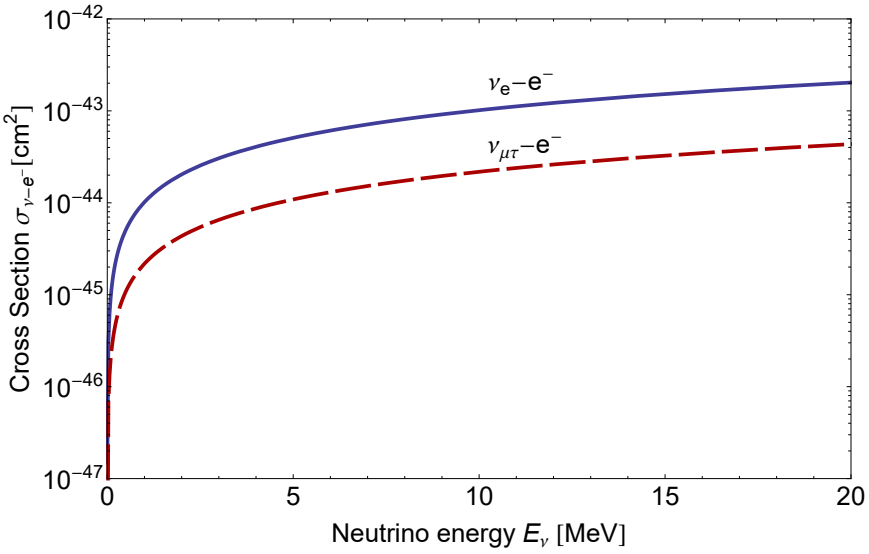

Fig. 5.28.: Neutrino-electron electroweak cross section for $\nu_e - e^-$ (solid blue line) and $\nu_{\mu\tau} - e^-$ (dashed red line) as a function of the neutrino energy in MeV.

that in argon this background is completely negligible since it is almost three orders of magnitude smaller than the CEnNS from atmospheric neutrinos. On the other hand, xenon does not have a PSD tool, relying on the ratio between S1 and S2 to distinguish NR from ER. Unfortunately this method is less powerful than the PSD one, allowing an ER rejection efficiency in the range 99.5-99.9% for a NR acceptance that varies from 50% to 30%, respectively, as stated in the XENON1T physics reach paper [312]. The other xenon competitor experiment, LZ, in its technical proposal considers a background rejection of 99.5% for a signal acceptance of 50% for all WIMP masses, but the collaboration claims a discrimination between electron and nuclear recoil events which is potentially able to reach the value of 99.99% [313]. Finally the ambitious DARWIN project, aiming to explore cross sections at the neutrino floor as DarkSide-20k will do, assumes an ER rejection level of 99.98% at 30% nuclear recoil acceptance using an S2/S1-based rejection of ERs. This corresponds to a rejection factor of 2×10^{-4}. For comparing the level of neutrino induced ER between argon and xenon I assumed this latter rejection factor even if it is very optimistic. In Fig. 5.29 (upper panel) this contribution is shown with a solid (dashed) red line before (after) the ER rejection factor. As you can see for xenon this background component is comparable to the CEnNS background from atmospheric neutrinos. Solar neutrinos will thus become a relevant background source at WIMP-nucleon cross sections of the order of 10^{-48}cm^2.

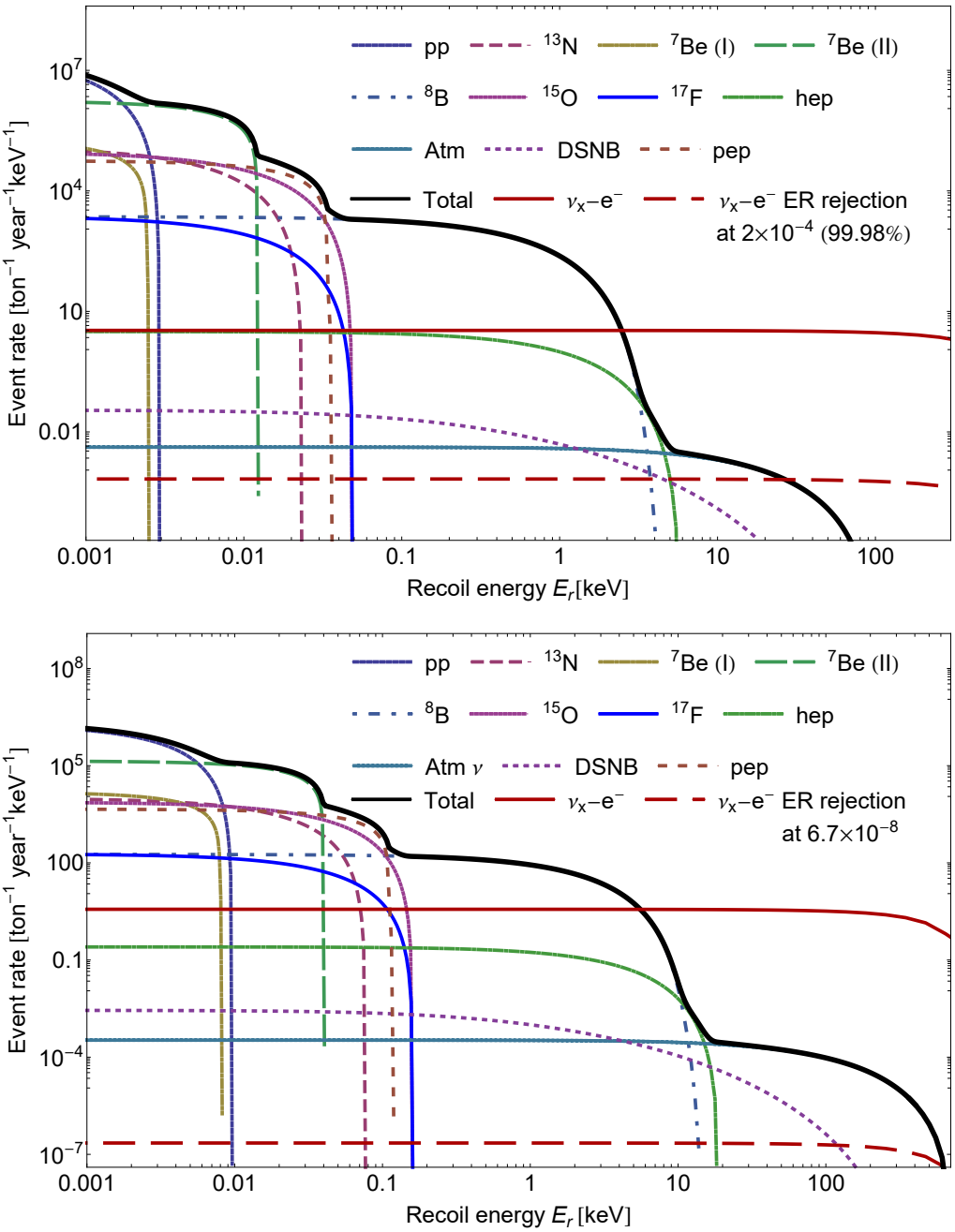

Fig. 5.29.: **Upper panel**: Differential rate for CEnNS in xenon as Fig. 5.11. Solid and dashed red lines correspond to the $\nu_x - e^-$ weak interaction rate before and that after the consideration of an electron recoil (ER) rejection factor at 2.2×10^{-4} (99.98 %).
Lower panel: Differential rate for CEnNS in argon as Fig. 5.12. Solid and dashed red lines correspond to the $\nu_x - e^-$ weak interaction rate before and that after the consideration of an electron recoil (ER) rejection factor at 6.7×10^{-8}.

To quantify the impact of this background, in Fig. 5.30 I show the event rate of CEnNS, neutrino-induced electron scattering (ES) recoils and a WIMP of 1 TeV mass and for a cross section of $6 \times 10^{-48}\,\mathrm{cm}^2$ in $(\mathrm{tonne\,year\,keV})^{-1}$ for xenon (upper panel) and argon (lower panel). In this case, for the ER rejection in xenon I considered the more realistic value as in LZ of 99.5% with a signal acceptance of 50%. For argon instead I applied the experimentally measured ER rejection and 90% signal acceptance. As clearly visible in argon the WIMP signal lies above the CEnNS background while in xenon the $\nu - e^-$ ER background overwhelms the signal. In xenon, integrating in the 6-30 keV nuclear recoil energy range (which corresponds to 1.5-6.5 keV electron recoil energy), the integrated number of CEnNS neutrinos is 0.017 events/(tonne year) and 0.083 events/(tonne year) from ES for a total of 0.1 events/(tonne year) to be compared to 0.05 WIMP events/(tonne year) for the chosen parameters. So there is almost a factor of two more background than signal. In argon, integrating in the range 30-200 keV we have 0.015 events/(tonne year) from CEnNS, a negligible contribution from ES neutrinos and 0.02 WIMP events/(tonne year) and so in this case the WIMP signal is greater than the background. Note that in this section I am not even considering further sources of background that affect xenon only, like the contribution of the neutrino double beta decay of ^{136}Xe, the ^{222}Rd and the presence of krypton. All these contributions sum up to a final event rate of the same order of the CEnNS contribution.

To conclude, in this chapter the DarkSide-20k sensitivity has been calculated for different exposures. It has been shown that the main source of background is represented by the coherent elastic neutrino nucleus scattering and that this background is basically irreducible using only the recoil energy information. In the next chapter, I will explore a new possibility to discriminate such a background using the recoil direction information. Up to now none of the current detectors at ton scale exploits this information but it will be essential for future searchers.

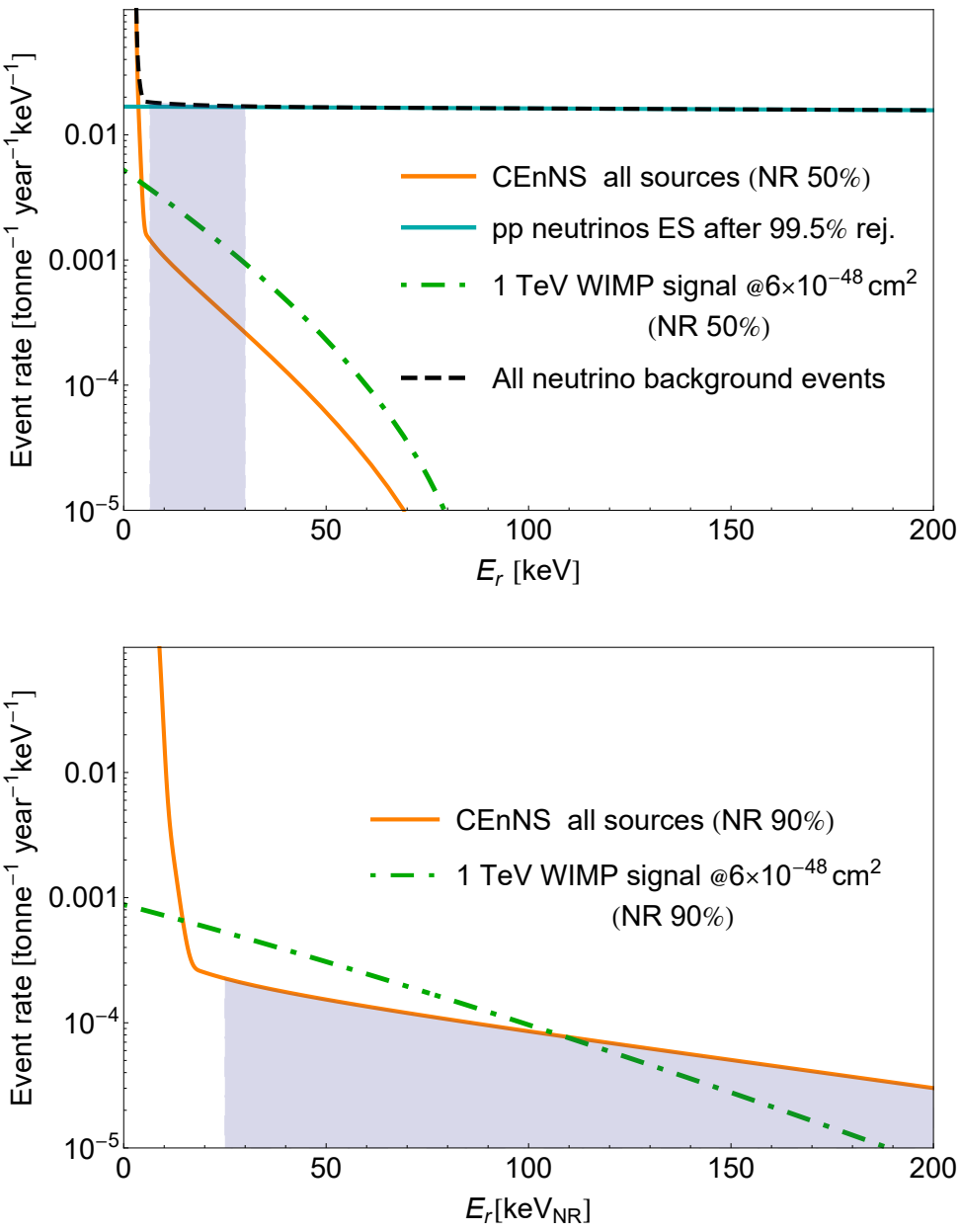

Fig. 5.30.: **Upper panel**: Neutrino backgrounds and signals in xenon. The grey dashed region shows the expected energy ROI for dark matter search, and the dashed dotted green line shows the expected signal from a 1 TeV WIMP with a SI cross-section per nucleon of 6×10^{-48}cm^2. Xenon backgrounds are dominated by electron recoils from elastic scattering of pp neutrinos on electrons. **Lower panel:** Same as the upper panel for argon. The electron recoil backgrounds are negligible due to the very strong pulse-shape discrimination; limiting backgrounds are from coherent scattering of atmospheric neutrinos.

6 Directional dark matter detection

Contents

6.1 Directional detectors and columnar recombination 164
6.2 Cross section and differential rates 167
6.3 Recoil directional signals at LNGS 173
6.4 Seasonal effects 176
6.5 Statistical analysis for a directional signal 180
6.6 Conclusions 188

As explained in Chap. 5 the near future DM experiments such as DarkSide-20k, XENONnT and LZ will be sensitive to the irreducible background from CEnNS that will limit the sensitivity or the discovery potential to WIMPs. This background will be even more problematic for future argon detectors like Argo (or GADMC), capable of collecting O(1000) tonne year exposure, or xenon detectors, like DARWIN for 200 tonne year scale, because the number of neutrino background events will be of the order of tens of events. Since, the WIMP and neutrino spectra are quite similar (see Figs. 5.19 and 5.20) the use of the likelihood test statistic would help just a bit in discriminating the WIMP signal from the background. However, for even large exposures the discovery of DM will be a difficult task in the presence of this background. A way to improve WIMP sensitivity is to reduce the energy threshold, however, the presence of the ^{8}B neutrinos will determine a natural limit. For example, moving from 35 keV (approximatively the DarkSide-20k energy threshold) to 10 keV, the number of neutrino background increases by a factor 100 for argon. The same factor will be achieved in a xenon detector moving from 6.5 keV to 3 keV. Roughly speaking, this implies that going under 10 keV (3 keV) for future argon (xenon) detector will be prohibitive as the number of neutrino background will saturate the sensitivity. In order to discriminate this background from a WIMP signal one needs to exploit a different feature. This feature is the incoming direction of the WIMP or the neutrino and, in this chapter, I will examine the potential of a DM detector capable to discriminate the recoil nucleus direction. In the following, such a detector will be referred to as

directional detector. I will show that the expected event rate varies by a large factor $(4-8)$ when considering nuclear recoil directions going from the zenith to the horizon and, at fixed angular direction, it varies by about the same factor with a sidereal-day[1] period considering a possible directional detector located at INFN Laboratori Nazionali del Gran Sasso (LNGS). In Sec. 6.5 I will show that the angular resolution of the detector will imply important consequences on the experimental sensitivity to such a rate variation. I will prove that the event-rate variations as a function of the sidereal time and as a function of the polar angle are very robust and are largely independent on details of the WIMP interaction and of the WIMP velocity distribution. They are direct consequences of the solar system motion through the Galaxy and of the Earth motion around the Sun.

6.1 Directional detectors and columnar recombination

A possibility for non-directional detectors to verify if a signal is a genuine WIMP signal is to exploit the knowledge that the latter is expected to modulate over the year [404, 204] (see Sec. 3.3.1). However, this seasonal modulation is expected to be smaller than 10% and background sources exist that have similar seasonal modulations. For instance the DAMA collaboration [405] reported an observation of such a modulation, but it is controversial due to the difficulties in excluding that this effect could come from possible sources of background.

A large mass detector with sensitivity to the direction of the recoiling nuclei would constitute a considerable breakthrough in the search for DM, as I will show in this chapter. A directional detector would allow to prove that the detected new particle is indeed a dark matter candidate. For the sake of concreteness, a detector located at the latitude[2] of the LNGS, where the DarkSide-20k experiment [3] will be located, is considered.

Isotropic backgrounds (*e.g.:* Diffuse supernovae and atmospheric neutrinos), backgrounds from sources within the solar system (*e.g.:* solar neutrinos), or backgrounds with the periodicity of local day (*e.g.:* backgrounds that depend on

[1] The sidereal day is about four minutes shorter than the solar day. It correspond to $23^{\mathrm{h}}\ 56^{\mathrm{m}}\ 4.0916^{\mathrm{s}}$.
[2] The LNGS coordinates are 42° 28' N 13° 33' E.

the temperature or the atmospheric density) can be considerably reduced using the angular and time information provided by a directional detector.

Several prototypes of directional detectors exist [406, 407], generally based on the attempt to perform an imaging of the nuclear recoil trajectory. These detectors aim at achieving high spatial resolutions and are usually limited in mass, thus being capable to collect limited exposures. On the other hand, non-directional DM detectors have already reached exposures greater than 10^4 kg-day, [361, 408] excluding spin independent WIMP-nucleon cross sections greater than about 10^{-46}cm^2.

As argued in [409], a promising technique for a very large-mass detector with directional DM capability would be to exploit the phenomenon called *Columnar Recombination* (CR) in a noble liquid Time Projection Chamber. An argon-based detector sensitive to the effect of CR, would combine directional sensitivity with the ability to collect exposures of several hundreds of tonnes year [3]. In noble liquid TPCs the recoiling nucleus produces both scintillation and ionization. CR models [274] predict that the amount of signal due to ionization that can be collected in the presence of an electric field $\boldsymbol{\mathcal{E}}$ should depend on the angle θ_r between $\boldsymbol{\mathcal{E}}$ and the track (the average direction of the straggling nucleus). The ionization signal is expected to be maximal when $\theta_r = 90°$, since electrons drift in a direction perpendicular to the region around the recoil track where ions are present, minimizing recombination. On the contrary, it should be minimal when $\theta_r = 0°$, since electrons drift along the region where ions are present, with high probability of recombination. The ionization signal from the collected electrons would be a function of the component of the electric field perpendicular to the track, $\mathcal{E}_\perp = \mathcal{E} \sin\theta_r$, and, therefore would carry, together with the scintillation signal, information on the average direction of the recoiling nucleus (see the schematic representation in Fig. 6.1).

Columnar recombination in a LAr TPC would thus provide signatures for the orientation of the ionizing tracks relative to the direction of the electric field. Evidence for this effect has been collected for α particles and protons [410, 411]. The SCENE experiment [412, 359], a small two-phase LAr TPC designed for calibration of nuclear-recoil responses, gave a hint for the same directional signature in the scintillation response of nuclear recoils of about 57 keV, approximately the energy at which, following the argument in [409], one might expect the ion range to be sufficient to form a track with a definite direction. However, the

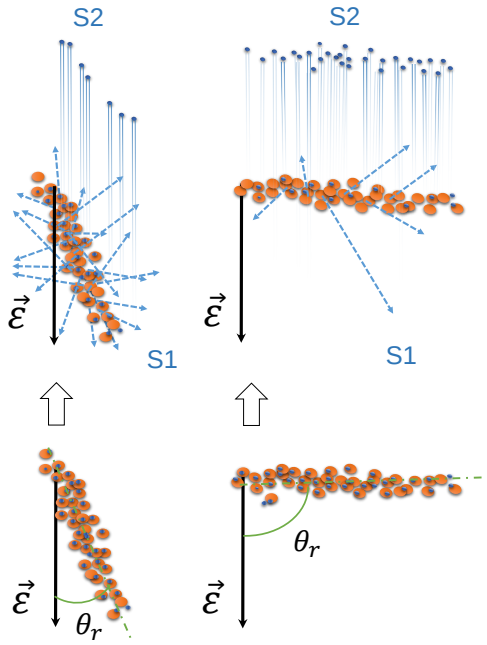

Fig. 6.1.: Schematic representation of the columnar recombination effect on the primary scintillation light, S1, after the recombination between electrons and argon dimers for the case of a recoil ionization track almost parallel to the TPC electric field $\mathcal{E}$ (left) or perpendicular to it (right). The survived electrons are accelerated by the electric field and produce the secondary electroluminescence light, S2, in the gas pocket.

corresponding ionization response measured in SCENE did not show the same hint for a directional effect [359].

In order to better investigate the CR effect, in a recent work [4] we derived a new model describing the recombination of electron-ion pairs in ionizing tracks in the presence of a drift field. The physical distributions characterizing the electron-ion cloud after thermalization, from which the recombination takes place, are largely unknown, and the recombination angular dependence is strongly affected by this initial condition. In this work, we introduced a novel model for the description of electron-ion recombination process in LAr TPCs which takes into account the dependence on the electron-ion pairs distribution obtained after thermalization. Indeed, the two classical models in use to date, the columnar [274] and box models [413], both fail to reproduce the accurate data reported by the ArgoNeuT experiment for proton tracks [414]. This new model describes the initial distribution of the electron ion cloud as that of an elongated ellipsoid,

with a single adimensional parameter, R, accounting for the aforementioned elongation. By proper tuning of the parameter, this model is brought to coincide with the box model in the limit for R = 1, and with the columnar model in the limit $R \to \infty$. By solving the equations describing the evolution of the electron-ion cloud, we determined that the dependence of the recombination fraction upon the angle between track and drift field is described by the function $f(\theta_r, R) = \sqrt{\sin^2\theta_r + \cos^2\theta_r/R^2}$. The model successfully reproduces the proton ArgoNeuT data [414] for a specific choice of the parameter R, which is extracted from a fit to the aforementioned data. Although the portability of this study for neutrons- or WIMPs-induced nuclear recoils is quite hard, it is expected that specialized experiments can clarify the situation. Therefore, a small prototype has been proposed with the aim to improve the SCENE measurement, as part of the DarkSide-20k proposal. Its name is RED (REcoil Directionality) and the experimental details can be found in Ref. [3].

General aspects of DM directional detection have been discussed in a number of works [415, 416, 417, 418, 419]. In the following, an active mass of 100 tonne (which in terms of number of WIMP events is equivalent to a 20 tonne active mass detector running for 5 years) is considered, with a detector at LNGS as in the DarkSide-20k experiment [3].

6.2 Cross section and differential rates

In a given reference frame, let's assume $\mathbf{v}_i$ is the velocity of the incoming WIMP of mass M_χ, $\mathbf{u}$ is the velocity of the recoiling nucleus of mass m_N, $\mathbf{q} = m_N\mathbf{u}$ is the nucleus momentum and $E_r = q^2/(2m_N)$ is the corresponding energy. The azimuthal and zenith angles of the recoiling nucleus are ϕ_r and θ_r, while ϑ is the angle between the incoming WIMP direction and the recoiling nucleus, as shown in Fig. 6.2. In general, recoil rates are convolutions of the scattering cross section and the incoming velocity distribution. A point-like cross section in the center of mass is constant and can be parametrized by the total WIMP-nucleus cross section $\sigma_{\chi-N}$. For a spin-independent interaction with equal couplings for neutrons and protons, $\sigma_{\chi-N}$ can be expressed in terms of the WIMP-nucleon cross section σ_n as $\sigma_{\chi-N}/\mu_N^2 = A^2\sigma_n/\mu_p^2$, where A is the atomic mass and μ_N and μ_p are the WIMP-nucleus and the WIMP-nucleon reduced masses, respectively. The finite size of the nucleus is taken into account by introducing the Helm nuclear form factor, see Sec. 3.1.4.

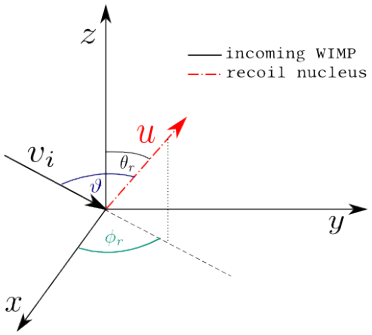

Fig. 6.2.: Schematic view of a WIMP-nucleus scattering. The incoming WIMP with velocity $\mathbf{v}_i$ hits the nucleus that recoils in the direction of the momentum $\mathbf{q} = m_N \mathbf{u}$ whose azimuthal and zenith angles are ϕ_r and θ_r. The angle between u and $\mathbf{v}_i$ is ϑ.

In the frame where the target nucleus is at rest, the double-differential cross section depends on the cosine of the angle between the incoming WIMP and the recoiling nucleus $\hat{\mathbf{v}}_i \cdot \hat{\mathbf{q}} = \cos\vartheta$ as

$$\begin{aligned} \frac{\mathrm{d}^2\sigma(q, \hat{\mathbf{v}}_i \cdot \hat{\mathbf{q}})}{\mathrm{d}q^2\, d\Omega} &= \frac{\mathrm{d}^2\sigma(q, \cos\vartheta)}{2m_N\, \mathrm{d}E_r 2\pi\, \mathrm{d}\cos\vartheta} \\ &= \frac{\sigma_{\chi-N}}{8\pi\mu_N^2 v_i} F^2(q)\, \delta\left(\mathbf{v}_i \cdot \hat{\mathbf{q}} - \frac{q}{2\mu_N}\right) . \end{aligned} \tag{6.1}$$

Given a velocity distribution for the incoming WIMP $f(\mathbf{v}_i)$, normalized so that $\int f(\mathbf{v})\mathrm{d}\mathbf{v} = 1$, and a WIMP mass density ρ, the double-differential recoil rate per unit mass, *i.e.* the rate per target nucleus divided by the nucleus mass m_N, as a function of the nuclear recoil energy, E_r, and of the recoil direction $\hat{\mathbf{q}}$ is

$$\begin{aligned} \frac{\mathrm{d}^2 R(E_r, \hat{\mathbf{q}})}{\mathrm{d}E_r\, \mathrm{d}\Omega_r} &= \frac{2\rho}{M_\chi} \int v \frac{\mathrm{d}^2\sigma(q, \hat{\mathbf{v}} \cdot \hat{\mathbf{q}})}{\mathrm{d}q^2\, \mathrm{d}\Omega} f(\mathbf{v})\, \mathrm{d}\mathbf{v} \\ &= \frac{\rho\, \sigma_{\chi-N} F^2(q)}{M_\chi 4\pi\, \mu_N^2} \int \delta\left(\mathbf{v} \cdot \hat{\mathbf{q}} - \frac{q}{2\mu_N}\right) f(\mathbf{v})\, \mathrm{d}\mathbf{v} \\ &= \frac{\rho}{M_\chi} \frac{\sigma_{\chi-N} F^2(q)}{4\pi\mu_N^2} \hat{f}(v_{min}, \hat{\mathbf{q}}) , \end{aligned} \tag{6.2}$$

where $v_{min} = q/(2\mu_N) = \sqrt{2m_N E_r}/(2\mu_N)$ is the minimal WIMP velocity that can give momentum q or energy E_r to the recoiling nucleus and $\hat{f}(v_{min}, \hat{\mathbf{q}})$ is the 3-dimensional Radon transform [420] of the velocity distribution $f(\mathbf{v})$.
As done in Sec. 3.3 I assume the Standard Halo Model (SHM), *i.e.* an isotropic Maxwell-Boltzmann WIMP velocity distribution of width σ_v in a reference frame

at rest with respect to the Galactic center. In a reference frame with velocity $\mathbf{V}$ relative to the Galactic center, the velocity distribution is

$$f(\mathbf{v}) = \frac{1}{\sqrt{(2\pi\sigma_v^2)^3}} \exp\left[-\frac{1}{2}\left(\frac{\mathbf{v}+\mathbf{V}}{\sigma_v}\right)^2\right] \tag{6.3}$$

and the corresponding Radon transform is

$$\hat{f}\,(v_{min}, \hat{\mathbf{q}}) = \frac{1}{\sqrt{2\pi\sigma_v^2}} \exp\left[-\frac{1}{2}\left(\frac{v_{min}+\hat{\mathbf{q}}\cdot\mathbf{V}}{\sigma_v}\right)^2\right] . \tag{6.4}$$

Therefore, if recoils are measured in a frame at rest with respect to the center of the Galaxy, $\mathbf{V} = 0$ and the rate is isotropic. Similarly, when measured in a frame at rest with respect to the Sun, $\mathbf{V}$ is the Sun velocity relative to the galactic center $\mathbf{V}_{SG}$, which points towards the galactic coordinates [421] (ℓ_c=90°, b_c=0°), roughly the direction of the Cygnus constellation, and has magnitude $V_{SG} \approx v_0 = 220$ km/s, where v_0 is the Galactic orbital speed at the Sun position. For an Earthbound laboratory, the velocity $\mathbf{V}$ can be decomposed as $\mathbf{V} = \mathbf{V}_{SG} + \mathbf{V}_{ES}$, where $\mathbf{V}_{ES}$ is the Earth velocity relative to the Sun, which has magnitude $V_{ES} \approx 30$ km/s, about ten times smaller than v_0. The laboratory velocity relative to the Earth center has been neglected, since it is almost two orders of magnitude smaller than $\mathbf{V}_{ES}$.

If a detector collects events of energy $E_{th} < E_r < E_{up}$, the direction-dependent recoil rate per unit mass, obtained by substituting the Radon transform from Eq. (6.4) in Eq. (6.3) and integrating over the energy range, becomes

$$\frac{\mathrm{d}R(E_{th}, E_{up}, \hat{\mathbf{q}})}{\mathrm{d}\Omega_r} = \int_{E_{th}}^{E_{up}} \mathrm{d}E_r \frac{\mathrm{d}^2R(E_r, \hat{\mathbf{q}})}{\mathrm{d}E_r\,\mathrm{d}\Omega_r} . \tag{6.5}$$

The study presented in this thesis focuses on the use of polar detectors *i.e.* detectors that give only information on the angle θ_r between the recoil track and a fixed axis. If the fixed axis is the vertical direction, the relevant recoil rate is

$$\frac{\mathrm{d}R(E_{th}, E_{up}, \cos\theta_r)}{\mathrm{d}\cos\theta_r} = \int_0^{2\pi} \mathrm{d}\phi_r \int_{E_{th}}^{E_{up}} \mathrm{d}E_r \, \frac{\mathrm{d}^2R(E_r, \hat{\mathbf{q}})}{\mathrm{d}E_r\,\mathrm{d}\Omega_r} , \tag{6.6}$$

which, after integrating out ϕ_r, depends on $\cos\theta_r$. In addition, if a detector cannot distinguish signals from recoil tracks differing by 180°, events that differ by 180°

are summed together. The relevant rate is the so-called "folded" angular recoil rate [422]:

$$\frac{\mathrm{d}R_F(|\cos\theta_r|)}{\mathrm{d}|\cos\theta_r|} \equiv \frac{\mathrm{d}R}{\mathrm{d}\cos\theta_r}(\cos\theta_r) + \frac{\mathrm{d}R}{\mathrm{d}\cos\theta_r}(-\cos\theta_r)\,, \tag{6.7}$$

which depends only on $|\cos\theta_r|$. Dependences of the recoil rates on other variables are not shown.

Unless explicitly stated, in this chapter I will show results for a LAr detector using the reference values $M_\chi = 200$ GeV, $m_N = 0.923\,A$, where A is the argon atomic mass, $\rho = 0.3$ GeV cm^{-3}, and $\sigma_v = v_0/\sqrt{2}$. Rates are given for a reference cross section $\sigma_n = 10^{-46}$ cm^2, which is of the order of the last limits set by the LUX, XENON1T and PandaX-II collaborations [361, 275, 269], for recoil energies from $E_{th} = 50$ keV to $E_{up} = 200$ keV, and for an active mass of 100 tonne[3]. Note that the anisotropy of all rates in Eqs. (6.5), (6.6), and (6.7) depends only on the velocity $\mathbf{V}$. In a given frame, which fixes $\mathbf{V}$, one can choose different angular coordinate systems. If the angular coordinate system is time dependent, *e.g.* a coordinate system fixed to the rotating Earth, the direction of $\mathbf{V}$ in that system becomes time dependent. In a frame at rest with respect to the Earth and using Galactic coordinates, $\mathbf{V}_{SG}$ is constant and only $\mathbf{V}_{ES}$ rotates with the annual periodicity of the Earth revolution. Since $\mathbf{V}_{ES}$ is an order of magnitude smaller than $\mathbf{V}_{SG}$, the WIMP apparent direction $-\mathbf{V} = -(\mathbf{V}_{SG} + \mathbf{V}_{ES})$ rotates with annual periodicity around the fixed $\mathbf{V}_{SG}$ direction with an opening angle of about one tenth of radiant. In this frame the peaked angular distribution is the main signature of the signal and allows for background reduction. In the laboratory coordinate system, the coordinates and, therefore, the apparent direction of $\mathbf{V}$ makes an additional rotation with the periodicity of a sidereal day and an amplitude that depends on the latitude. This specific periodicity is also a characteristic signature and provides more background suppression.

6.2.1 Recoil rate in Galactic angular coordinates

Figures 6.3 and 6.4 show results in a reference frame at rest with respect to the Sun in Galactic coordinates to demonstrate the potentialities of a directional detector independently of the location, as it has been extensively done in the past, and to discuss the influence of the threshold energy $E_{\rm th}$. All other results in this

[3] This choice for the threshold energy is motivated by hints from the SCENE experiment [359] for directional dependence in the scintillation signal at energy of 57.3 keV.

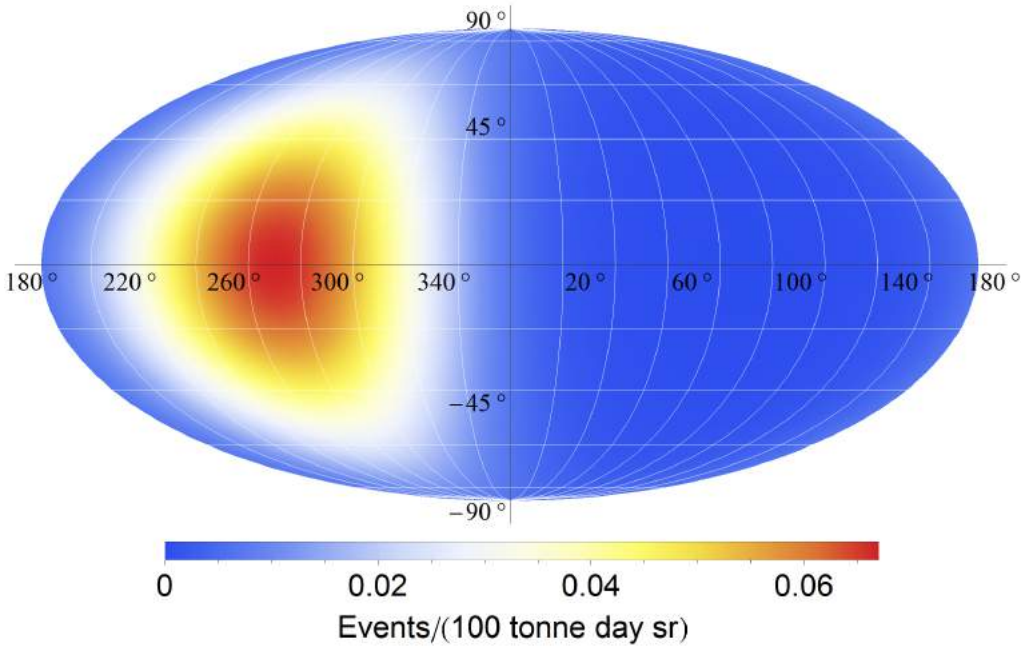

Fig. 6.3.: Recoil rate in argon, Eq (6.5), on a Mollweide equal area projection map of the celestial sphere in galactic coordinates. The horizontal axis is the galactic longitude $0° < \ell < 360°$ and the vertical axis is the galactic latitude $-90° < b < 90°$. The WIMP mass is 200 GeV, the WIMP-nucleon cross section is 10^{-46}cm^2 and the energy interval considered is $(50\ \text{keV} \leq E_r \leq 200\ \text{keV})$. The colour scale represents units of events/(100 tonne · day · sr).

chapter will be given for a detector located at the latitude of LNGS in the local coordinate system with the polar axis pointing in the vertical direction. Indeed, the potentialities of a directional detector and, more specifically, the signature in the angular recoil rate of the detector motion through the WIMP halo are best illustrated in Galactic coordinates in a frame at rest with the Sun. In this coordinate system, $\hat{x}$ points from the Sun towards the Galactic center, $\hat{y}$ in the direction of the Solar motion and $\hat{z}$ towards the Galactic north pole; therefore, $\mathbf{V} = v_0\hat{y}$. In Fig. 6.3 we show the angular recoil rate of Eq. (6.5) for argon on a Mollweide equal area projection map. The horizontal axis is the galactic longitude $0° < \ell < 360°$ (the counterclockwise angle from the $\hat{x}$ axis) and the vertical axis is the galactic latitude $-90° < b < 90°$ ($90° - b$ is the angle from the $\hat{z}$ axis). To obtain the total number of events that are expected for an exposure of 100 tonne year (five years of DarkSide-20k), one has to integrate over the solid angle and multiply for 365 days. This results in a number of WIMPs above 50 keV of about 74. With the same assumption on the WIMP mass and the WIMP-nucleon cross section, the total number of WIMP events expected from DarkSide-20k for 5

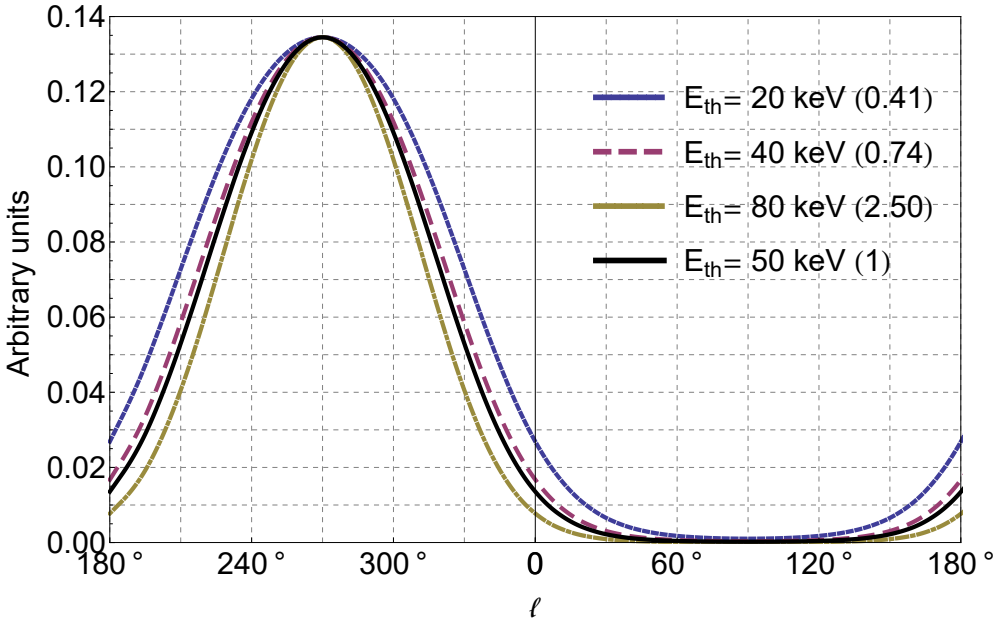

Fig. 6.4.: Recoil rate in arbitrary units for argon as a function of the galactic longitude ℓ in degrees. The WIMP mass is assumed to be 200 GeV and the recoil energy is integrated between E_{th} and 200 keV, where $E_{th} = 20$, 40, 50 and 80 keV. With respect to the curve for $E_{th} = 50$ keV the other curves have been rescaled to have the same maximum. As shown in the legend the rescaling factors are: 0.41, 0.74, 2.50, respectively.

years of data taking including the NR acceptance, is about 100 since it includes events below 50 keV, which I conservatively did not include when considering a directional detector.

The recoil rate is clearly anisotropic [416] and points at coordinates $(\ell = 270°, b = 0°)$ opposite to the direction of the Sun motion throughout the Galaxy. Since the expected signal in the SHM is rotationally symmetric around the Sun direction, the width of the forward peak is better shown on a one dimensional plot as a function of the galactic longitude ℓ, obtained integrating over the galactic latitude b (Fig. 6.4). The units on the y-axis are events/(100 tonne day $180/\pi$), such that after integration one obtain about 0.2 events/(100 tonne day). In Fig. 6.4 the effect of different energy thresholds is considered. Indeed, it shows that the width of the peak is slightly reduced for higher recoil energies, thus increasing the correlation between the recoil direction and the apparent WIMP arrival direction, even if the width of the peak is dominated by the WIMP transverse velocity distribution. Indeed, in a liquid the straggling of the recoiling nucleus

will broaden further the peak. A higher threshold, in addition, lowers the total rate as it can be quantitatively seen from the normalization factors.

6.3 Recoil directional signals at LNGS

In this section I will consider WIMP scattering in a reference frame at rest relative to a detector situated at LNGS with the $\hat{z}$ axis along the vertical. In this frame, the angle between the recoiling nucleus and the vertical axis is called θ_r. In particular I will study the expected rates, Eqs. (6.5) and (6.7), as a function of $\cos\theta_r$ and of the time of the day. The effect of a finite angular resolution will be also considered.

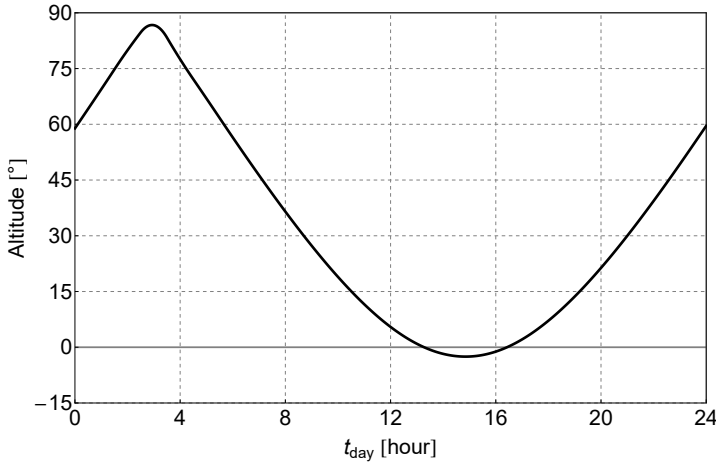

Fig. 6.5.: Altitude (angle from the horizon) of the Cygnus constellation as seen at LNGS as a function of the time in the summer solstice. The horizontal line at 0 corresponds to the horizon.

Figure 6.5 shows the Cygnus constellation altitude at the LNGS location as a function of the time from the midnight of the Summer Solstice (SS), providing a clear picture of the daily dependence of the expected recoil *average* direction. As already discussed, the correlation between the Cygnus direction and the WIMP wind changes by at most a tenth of a radiant during the year because of the Earth revolution around the Sun. As the cross section in Eq. (6.2) peaks in the forward direction, when Cygnus is close to the zenith, nuclei recoil mainly towards the nadir, and when Cygnus is close to the horizon, nuclei recoil mainly in the horizontal plane, as depicted in Fig. 6.6. The most important qualitative feature in Fig. 6.5 is that Cygnus spans the whole range of polar directions from zenith to horizon during the day at the LNGS latitude, thus allowing a strong

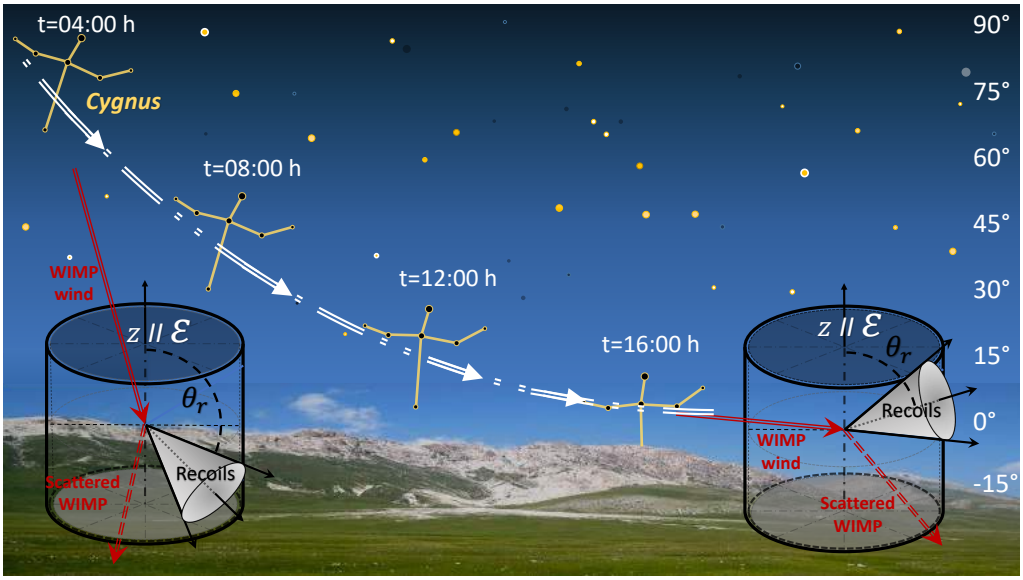

Fig. 6.6.: Altitude of the Cygnus constellation in the sky as seen by an observer at LNGS as a function of the time of the summer solstice. The WIMP apparent wind at 04:00 h (16:00 h) will induce nuclear recoils mostly parallel (perpendicular) to the electric TPC field, $\mathcal{E}$.

correlation between time and polar angle of the recoils. Thus, the angle between the expected average WIMP direction with the vertical electric field in the LAr TPC spans the entire range between 0° and 90° during the day. Since the Cygnus polar angle period is the sidereal day, this correlation is lost during the year if local solar time is used.

6.3.1 Differential rates as functions of the polar angle

Figure 6.7 shows the differential recoil rate, Eq. (6.6), as a function of $\cos\theta_r$ for the SS day (solid black line). This rate is more than twice as high for negative values of $\cos\theta_r$ than for positive values, since Cygnus is most of the time above the horizon. Freezing the position of the Cygnus in the sky at a given time of the SS day for the whole day, one obtains the different dashed lines in Fig. 6.7. One clearly sees that there is a strong dependence on the time of the day. Indeed, the asymmetry in $\cos\theta_r$ (the angle between the recoil direction and the z axis) is larger when Cygnus is high in the sky, *e.g.*, at hour 4, while it is smaller when it is close to the horizon, *e.g.*, at hour 16.

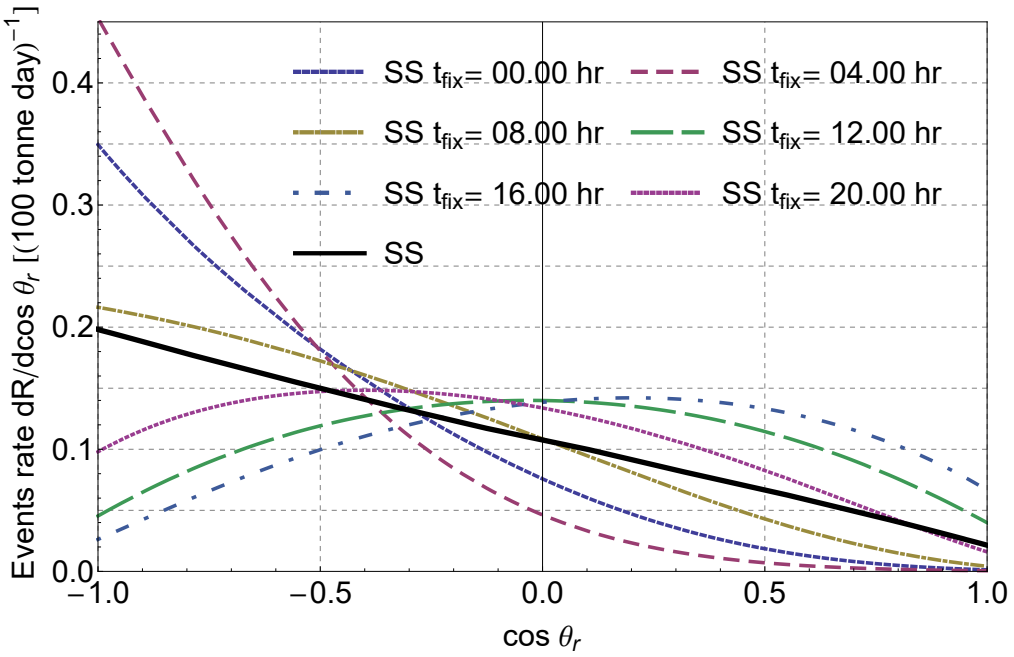

Fig. 6.7.: Differential recoil rate as a function of the cosine of the polar angle θ_r (the angle between the recoil direction and the z axis) at the latitude of LNGS for the SS day (solid black line). The six dashed curves show the differential recoil rate obtained freezing the position of the Cygnus in the sky at a given time (four-hour apart from each other) of the SS day for the whole day.

Figure 6.8 shows the "folded" differential recoil rate introduced in Eq. (6.7), which is the relevant rate for a polar detector. The angular and time dependences of the rate remain quite strong even without the information on which side of the track the head is. When Cygnus is close to the zenith (horizon) the rate is peaked at $|\cos\theta_r| \sim 1$ ($|\cos\theta_r| \sim 0$).

6.3.2 Vertical and horizontal event categories

A simple and robust analysis of the time and angular dependency of the event rate of WIMP collisions is achieved by separating the candidate event sample into two categories that require only a minimal amount of angular information. Events can be categorized as horizontal events (HOR), defined by $|\cos\theta_r| < 0.5$ or $60^\circ < \theta_r < 120^\circ$, and vertical events (VER), defined by $|\cos\theta_r| > 0.5$ (see Fig. 6.9).

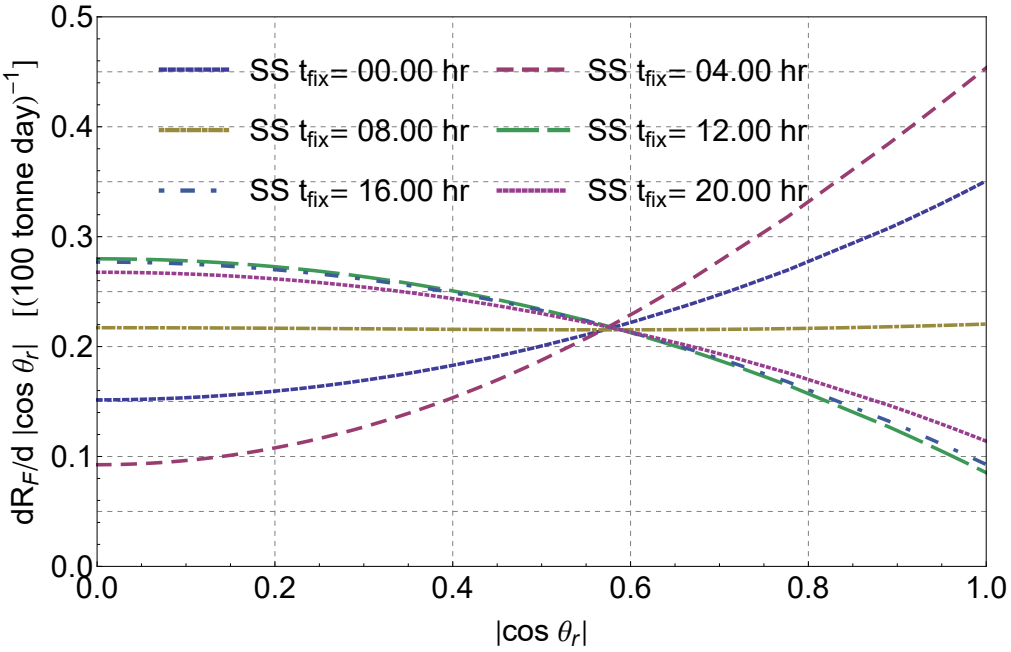

Fig. 6.8.: Same as figure 6.7 for the "folded" rate in Eq. (6.7).

Figure 6.10 shows horizontal and vertical WIMP event rates as a function of the time of the day. At the latitude of LNGS, the time signature of an anisotropic WIMP wind is evident in spite of the very crude angular classification. In the same figure we also show the ratio $R = \mathrm{HOR}/\mathrm{VER}$ of horizontal to vertical events. For the given choice of parameters, R changes during the day by a factor of ~ 4.

6.4 Seasonal effects

As already discussed in Section 6.2, the Earth velocity within the Galaxy and, therefore, the velocity relative to the average WIMP velocity $\mathbf{V} = \mathbf{V}_{SG} + \mathbf{V}_{ES}$ changes during the year due to the annual rotation of orbital velocity $\mathbf{V}_{ES}$. Since $|\mathbf{V}_{SG}| \approx 220$ km/s and $|\mathbf{V}_{ES}| \approx 30$ km/s with an angle of about 60° between $\mathbf{V}_{SG}$ and the ecliptic, the module $|\mathbf{V}|$ changes by about $\pm 15/220 \approx \pm 7\%$ during the year causing a similar change of the WIMP flux, while the annual change of direction is about a tenth of radiant (see Fig. 3.7). In Fig. 6.11 the WIMP differential rate as a function of the nuclear recoil energy is shown for the SS day and half an year later. A small differences are visible among the two curves. The

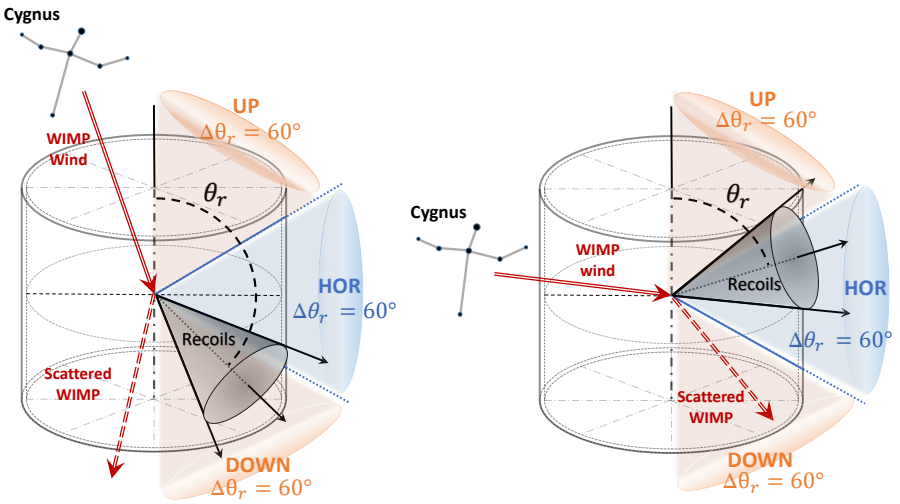

Fig. 6.9.: Schematic view of the two categories in which events are divided, namely horizontal (HOR) and vertical (VER=UP+DOWN) events for two different Cygnus altitudes in the sky.

feature that the recoil spectra cross at about 20 keV is better visible plotting the so-called modulation amplitude, defined as

$$A_1(E_r) \approx \frac{1}{2}\left[\frac{dR}{dE_r}(E_r, \text{Day}_1) - \frac{dR}{dE_r}(E_r, \text{Day}_2)\right], \tag{6.8}$$

as shown in Fig. 6.12 for $\text{Day}_1 = SS$ and Day_2 half an year later. As visible, the amplitude of the modulation is small relative to the average rate. Moreover, the modulation changes sign at low recoil energies (small $v_{\min}$), in this case at about 21.5 keV. Incidentally, this phase reversal can be used to constrain the WIMP mass.

The annual change of the average WIMP speed produces a corresponding change of the total rate, which reaches its maximum around the end of May and its minimum around the end of November, as clearly visible in Fig. 6.13 (upper panel). This has been obtained by integrating the differential recoil rate in Fig. 6.11 in the range 50-200 keV for each day of the year. In addition to the time-varying motion of a detector due to the orbit of the Earth about the Sun, there is a time-varying motion due to the rotation of the Earth about its axis, leading to a daily (diurnal) modulation in the recoil rate. This daily modulation is shown in the insert of Fig. 6.13 for the month of August for reference. Since the rotational velocity (at most 0.5 km/s near the equator) is significantly smaller than the orbital velocity (30 km/s), the daily modulation signal is much smaller than

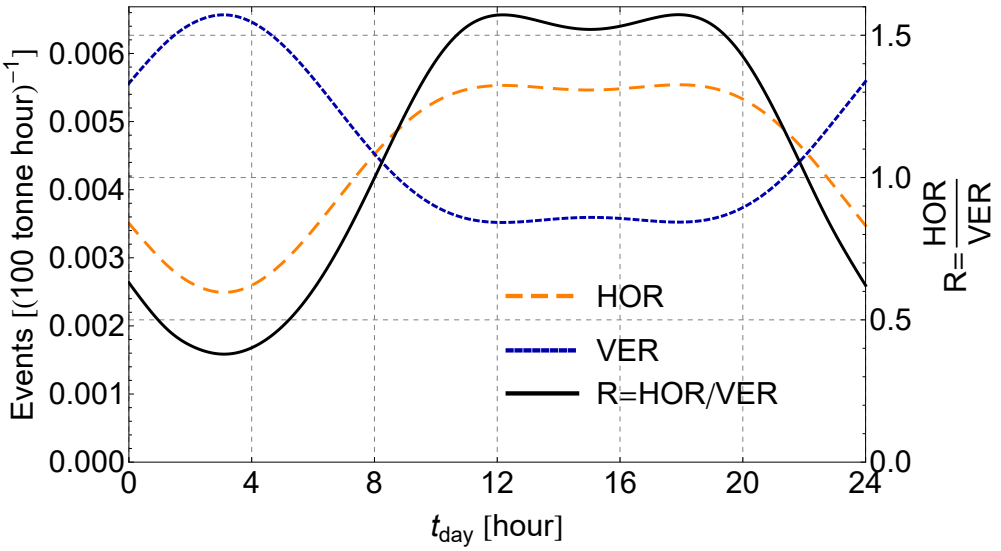

Fig. 6.10.: Horizontal (HOR), corresponding to $|\cos\theta_r| < 0.5$ or $60^\circ < \theta_r < 120^\circ$ (long dashes) and vertical (VER), corresponding to $|\cos\theta_r| > 0.5$ (short dashes) event rates as a function of time in events per 100 tonne per hour (left scale). The solid line shows the ratio $R = \mathrm{HOR}/\mathrm{VER}$ (right scale). Curves are drawn for the summer solstice day.

the annual modulation signal and, unfortunately, much more difficult to detect. For this reason, the daily modulation in the recoil rate is typically ignored in modulation searches. Note that this daily modulation is related but different from the daily modulation in the recoil direction, which is a much larger effect as already shown in Fig. 6.10.

Coming back to the annual modulation, in Fig. 6.13 (lower panel) I show the effect of three different threshold energies $E_{th} = 40$, 50, and 60 keV to the percentage annual variation. As expected [423, 424] the larger the energy threshold the larger the percentage annual modulation.

Figure 6.14 (upper panel) shows the daily variation of the ratio R at four times of the year; the signal time structure changes during the year as function of the local time. The Cygnus, *i.e.* the WIMP direction, returns exactly in the same position in the sky after a sidereal day, which is about four minutes shorter than the solar day. This annual drift of the angular signal as a function of the solar time can be used to characterize the WIMP signal with respect to other effects that also produce daily variations but with solar-day periodicity [425].

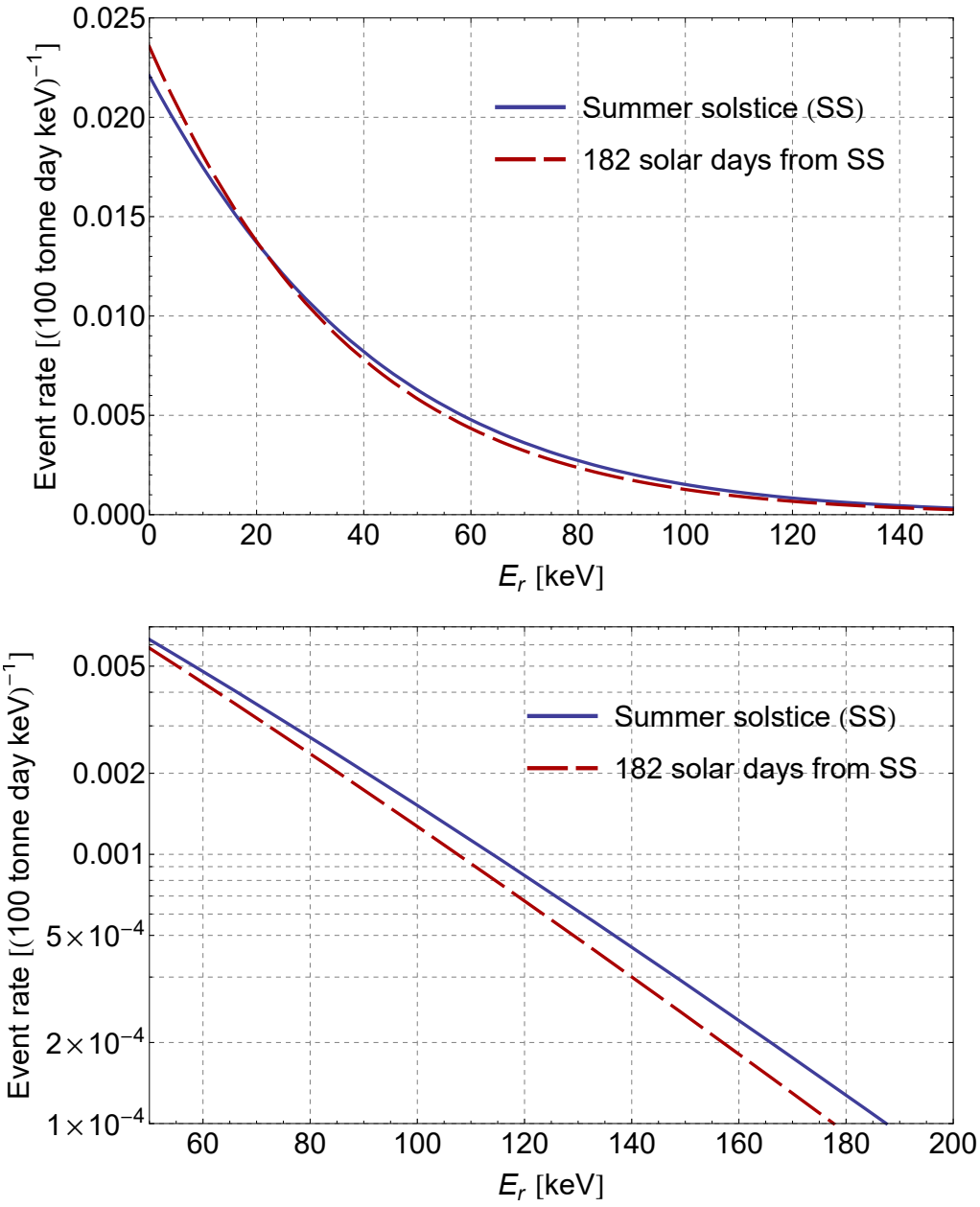

Fig. 6.11.: **Upper panel**: WIMP differential rate as a function of the recoil energy for the summer solstice (SS) (solid blue line) and half a year later (dashed red line).
Lower panel: Same as upper plot in the energy range of interest (50-200 keV) in logarithmic scale.

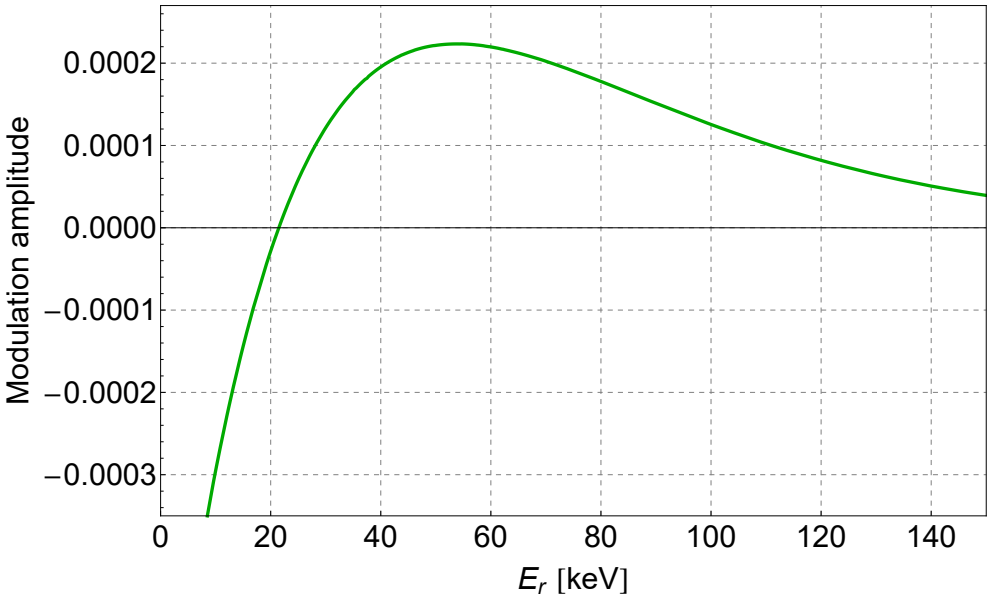

Fig. 6.12.: Modulation amplitude as a function of the recoil energy as defined in Eq. 6.8 for $\text{Day}_1 = SS$ and Day_2 half an year later.

If the sidereal time is used to time-stamp events, the annual drift is eliminated and it is possible to compare and average events rates taken at different days, see Fig. 6.14 (lower panel). Note that part of the seasonal variation of HOR and VER cancels out in their ratio R. Figure 6.15 shows the HOR and VER daily event rates taken at four times of the year and the annual rates of HOR and VER events computed by summing the contributions at each sidereal day.

The much larger time variation of the directional signal relative to the seasonal variation of the non-directional signal is evident by comparing Fig. 6.13 to Fig. 6.14 (lower panel), or also in Fig. 6.14 (upper panel) or Fig. 6.15. However one should use the combination of seasonal and directional modulations to better characterize the nature of the signal.

6.5 Statistical analysis for a directional signal

A path through the discovery process of DM searches may proceed initially through the observation of a number of candidates that significantly exceed the small expected background level. However, after rejecting the background-only hy-

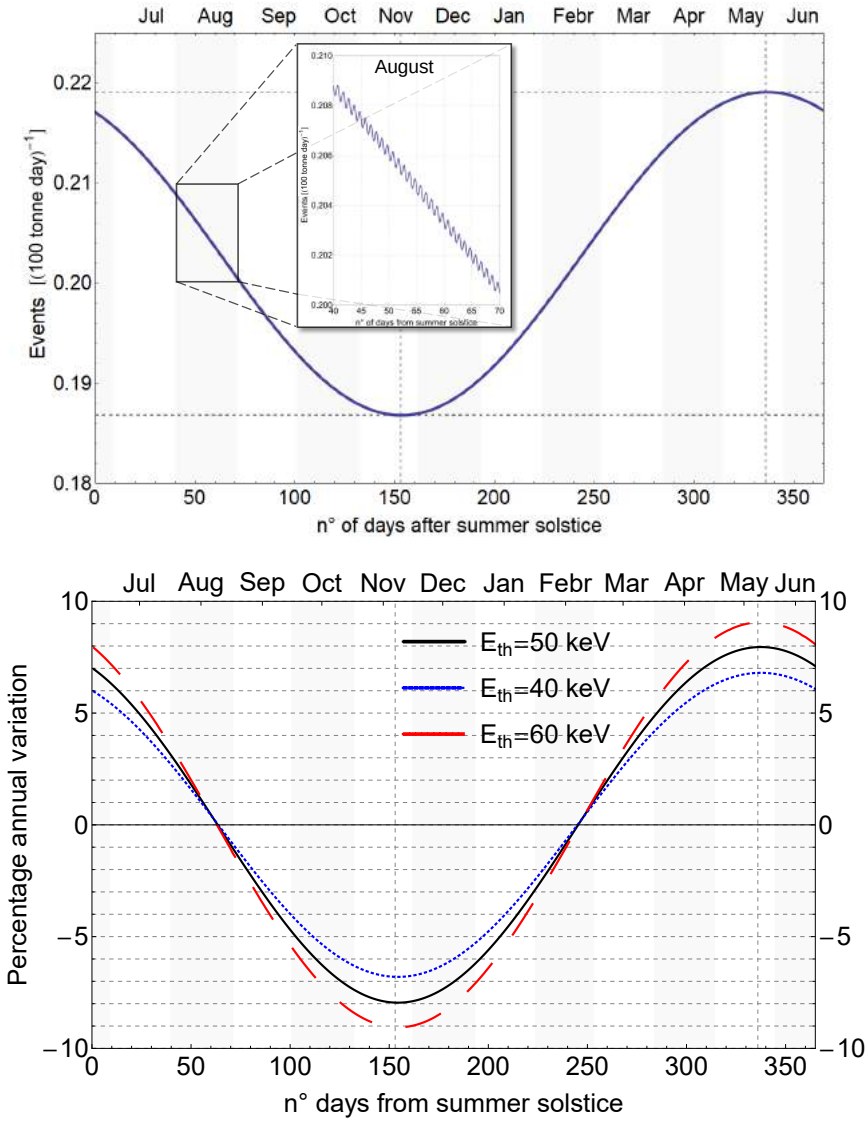

Fig. 6.13.: **Upper panel**: Annual WIMP modulation for $E_{th} = 50$ keV at LNGS as a function of the number of the days after the summer solstice (SS). The minimum event rate is found at 154 days after SS, while the maximum is for 337 days after the SS (∼24th May). The insert shows the daily modulation rate in August. **Lower panel:** Percentage annual variation of the event rate as a function of the number of days from the SS for three different recoil energy thresholds. The solid line corresponds to $E_{th} = 50$ keV, the dotted line corresponds to $E_{th} = 40$ keV, and the dashed line corresponds to $E_{th} = 60$ keV. The corresponding average daily rates are about 0.21, 0.27, and 0.15 events per day for a 100 tonne active mass.

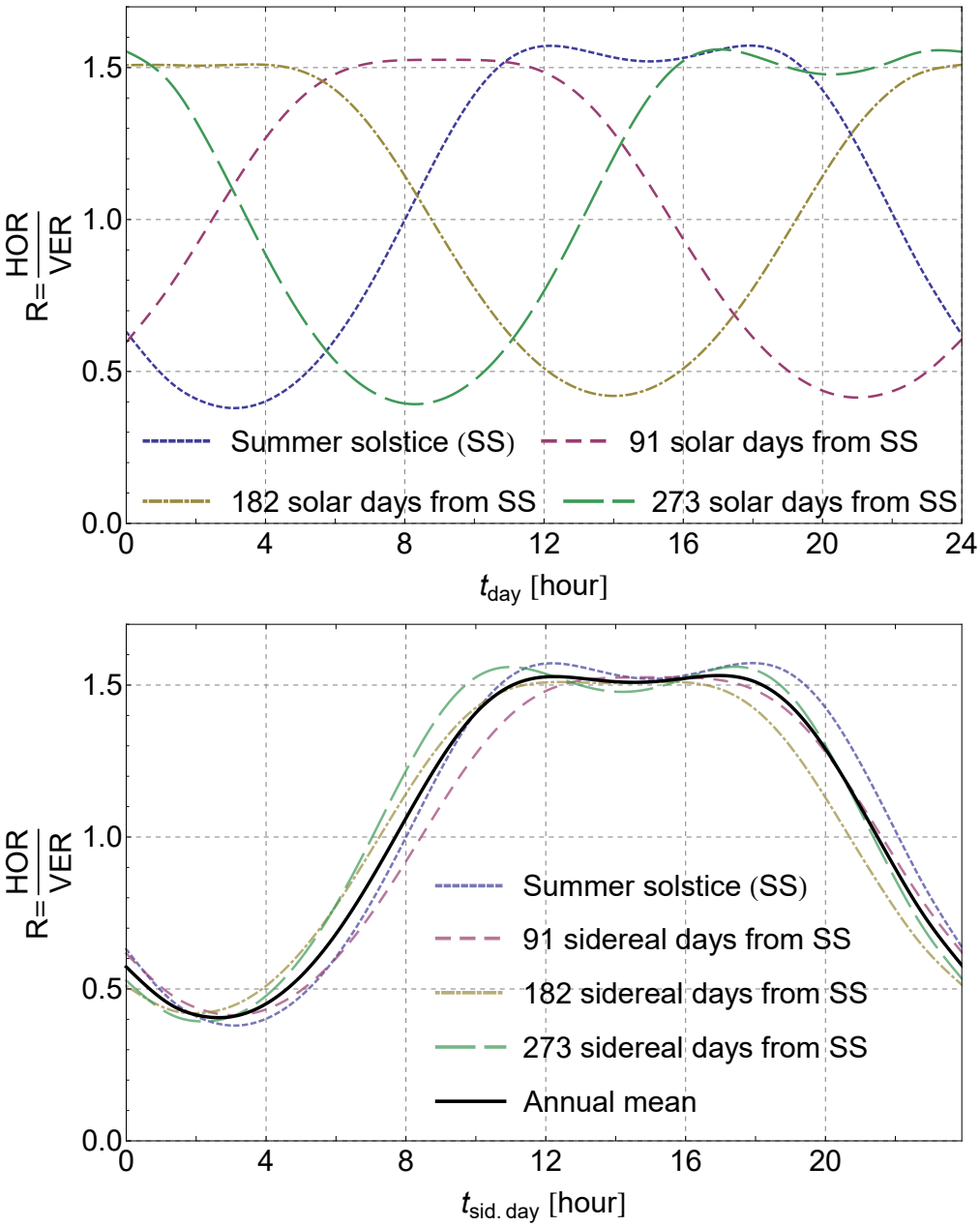

Fig. 6.14.: **Upper panel**: Ratio R of expected number of events along the horizontal and the vertical direction in an argon detector located at LNGS as function of the time of the day at four different solar days of the year. R is defined in Fig. 6.10 and in the text referring to it. **Lower panel:** Ratio of HOR and VER $R = \mathrm{HOR}/\mathrm{VER}$ at each hour of a sidereal day for four different sidereal days of the year.

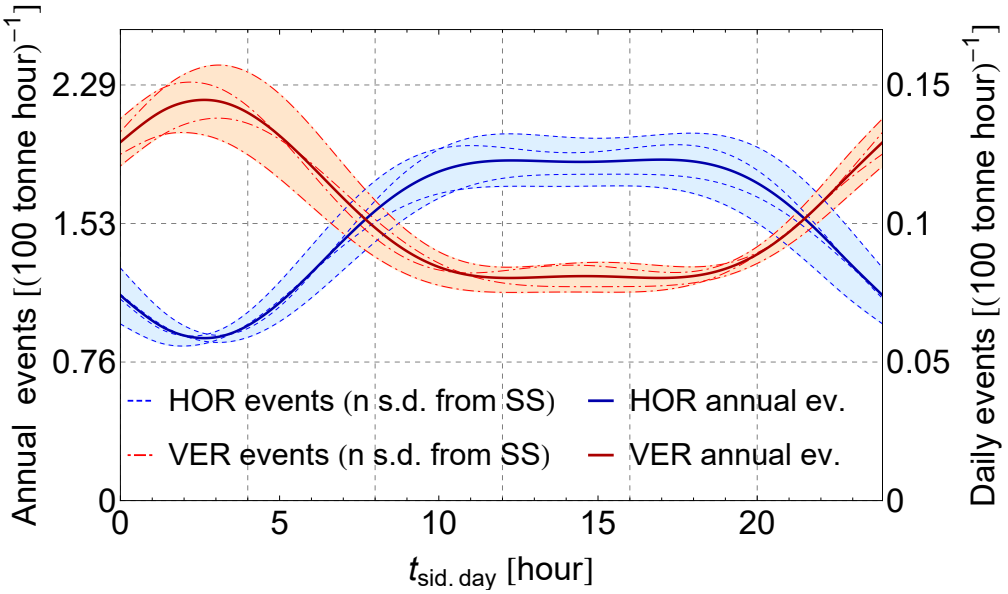

Fig. 6.15.: Solid red and blue lines (left y-scale): annual sum of HOR $\equiv |\cos\theta_r| < 0.5$) and vertical (VER $\equiv |\cos\theta_r| > 0.5$) events expected at each hour of a sidereal day, respectively. Dashed red and blue lines(right y-scale): events at each hour of a given sidereal day, namely the day of the SS, and 91, 182, 273 days after it.

pothesis, the study of angular properties of the observed nuclear recoils can corroborate the belief that the observed signal can be attributed to DM interactions. In Sec. 6.3 I have discussed semi-quantitatively the power of angular discrimination by using a crude classification in horizontal and vertical events. Here, I want to quantitatively discuss the number of events necessary to discriminate the hypothesis of a DM signal with preferential incoming direction from the Cygnus constellation against the alternative hypothesis of an isotropic signal. I am considering only the isotropic hypothesis for the background since the major background contribution for a possible DM detector with threshold energy above 50 keV is represented by atmospheric neutrinos. Indeed, I have already shown that atmospheric neutrinos due to cosmic ray collisions are responsible for the neutrino floor for WIMP masses above 100 GeV and will limit the discovery of SI cross sections below approximately 10^{-48} cm^2, see Sec. 5.5.1. The atmospheric neutrino flux peaks near the horizon, at nadir angle $\cos\Theta \simeq 0$, and it is expected to be up-down symmetric at Gran Sasso latitude (see Fig. 35b of [426]). At high energies, the flux is very nearly symmetric about $\cos\Theta \simeq 0$, while it is practically flat with respect to the azimuthal angle. However, this preferential direction of the neutrino flux is almost lost in the recoil spectrum, which depends only weakly

on it (compared with other neutrino components and particularly WIMP recoils). I will instead briefly discuss the case of the solar neutrino background later.

Being justified the hypothesis of a mainly isotropic background, one needs to derive the number of candidate events necessary to prove at a certain confidence level that they come from a preferential direction. To do so, the negative logarithm of the likelihood ratio is taken as test statistic t to discriminate between the hypotheses of a directional signal from the Cygnus constellation (Cyg) against an isotropic signal (iso) ($\mathbf{V}$ as in Section 6.2 or $\mathbf{V} = 0$, respectively). Such test statistic can also be extended in order to take into account the effect of systematic uncertainties for realistic applications [427]. The test statistic is defined as

$$t(\mathbf{x}^{(1)}, \cdots, \mathbf{x}^{(N)}) = -\ln \frac{\mathcal{L}_{\mathrm{Cyg}}(\mathbf{x}^{(i)})}{\mathcal{L}_{\mathrm{iso}}(\mathbf{x}^{(i)})}\,, \tag{6.9}$$

where $\mathcal{L}_{\mathrm{Cyg,iso}}(\mathbf{x}^{(i)})$ are the likelihood functions corresponding to the two hypotheses. Given a sample of N independent WIMP like events, the two likelihood functions are given by the products of the probability density function (PDF) values $f_{\mathrm{Cyg,iso}}(\mathbf{x}^{(i)})$ corresponding to each WIMP interaction candidate:

$$\mathcal{L}_{\mathrm{Cyg,iso}}(\mathbf{x}^{(1)}, \cdots, \mathbf{x}^{(N)}) = \prod_{i=1}^{N} f_{\mathrm{Cyg,iso}}(\mathbf{x}^{(i)})\,, \tag{6.10}$$

where the vector $\mathbf{x}^{(i)}$ contains the variables used to characterize the event (i). Here, I use the two variables θ_{rec}, the recoil polar angle in the laboratory, and θ_{Cyg}, the polar angle of the Cygnus constellation at the time of the event in the laboratory: $\mathbf{x}^{(i)} \equiv (\theta^{(i)}_{\mathrm{rec}}, \theta^{(i)}_{\mathrm{Cyg}})$. Additional variables such as the recoil energy or the time of the year could provide additional information and, in principle, better discrimination between the two hypotheses, our conclusions are conservative in this respect. The same method can be used to study alternative models for WIMP distribution or backgrounds.

The PDFs $f_{\mathrm{Cyg,iso}}(\mathbf{x}^{(i)})$ have been sampled generating 10^{10} simulated interaction recoils for each hypothesis and binning the allowed kinematic range of each variable $\theta^{(i)}_{\mathrm{rec}}$ and $\theta^{(i)}_{\mathrm{Cyg}}$ with 100 bins. In the simulation the energy has been smeared by 10 keV in order to account for the energy resolution and an energy threshold of 50 keV has been used. In addition I compared the case of perfect resolution of the recoil angle in the laboratory frame to a resolution smeared by

a Gaussian distribution with a 400 mrad width, which is enough to distinguish between horizontal and vertical events.

Given an assumed number N of WIMP like interaction candidate events, 10^7 pseudo-samples of N events each were generated for each of the four cases, namely events from Cygnus direction or isotropic and with the two angular resolutions. The test statistic, t, of Eq. (6.9) has been evaluated for each pseudo-sample and stored into histograms with a fine binning. Just as an example, Fig. 6.16 shows the distribution of the test statistic t defined in Eq. (6.9) for the case of ideal (top panel) and 400 mrad resolution (bottom panel) with $N = 50$. The directional (isotropic) distribution is peaked at negative (positive) values. The expected p-value is computed from the distribution of the test statistic $t_{\rm iso}$ corresponding to the null (isotropic) hypothesis by considering the percentage of pseudo-sample with t below $t_{\rm Cyg,0}$, where $t_{\rm Cyg,0}$ is the median of the distribution of the test statistic $t_{\rm Cyg}$ corresponding to Cygnus direction hypothesis. The corresponding one- or two-standard-deviation excursions are calculated by considering instead of $t_{\rm Cyg,0}$ the boundaries of the one- or two-standard-deviation interval for the test statistic $t_{\rm Cyg}$.

The expected p-values as a function of the observed number of DM interaction candidate events are shown in Fig. 6.17 for ideal angular resolution (top) and for a 400 mrad resolution (bottom). In the case of an ideal resolution, a 3σ evidence of a directional signal is expected to be achieved with about 100 candidate events. For an angular resolution of 400 mrad, a 3σ evidence can be achieved with about 250 events.

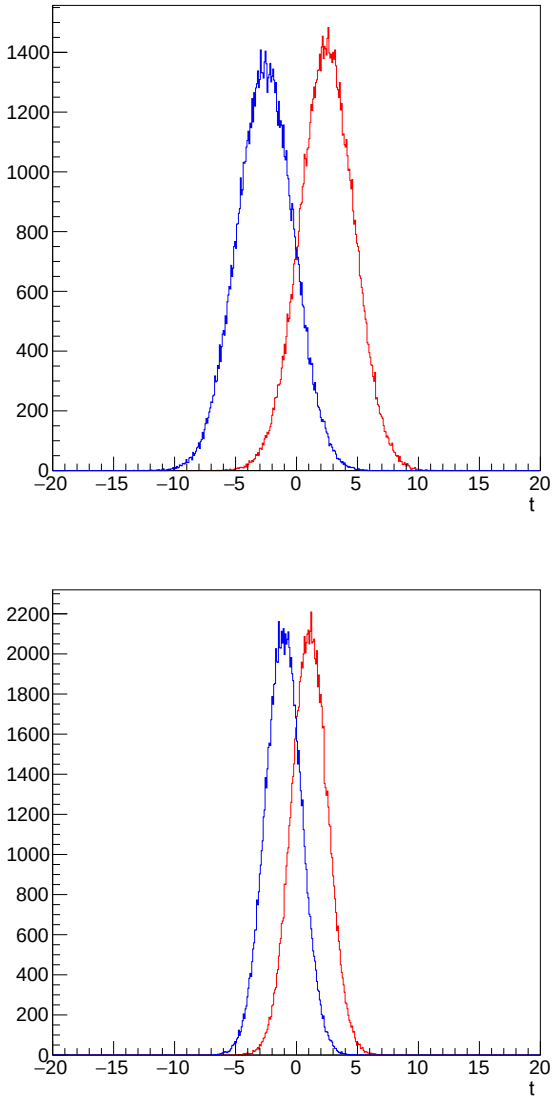

Fig. 6.16.: Distribution of the likelihood-ratio test statistic t for ideal resolution (top) and for a resolution of 400 mrad (bottom) for $N = 50$ observed DM candidates. The blue (red) curves that peak at negative (positive) values of t correspond to the hypothesis of incoming particles from the Cygnus direction (of isotropic signal).

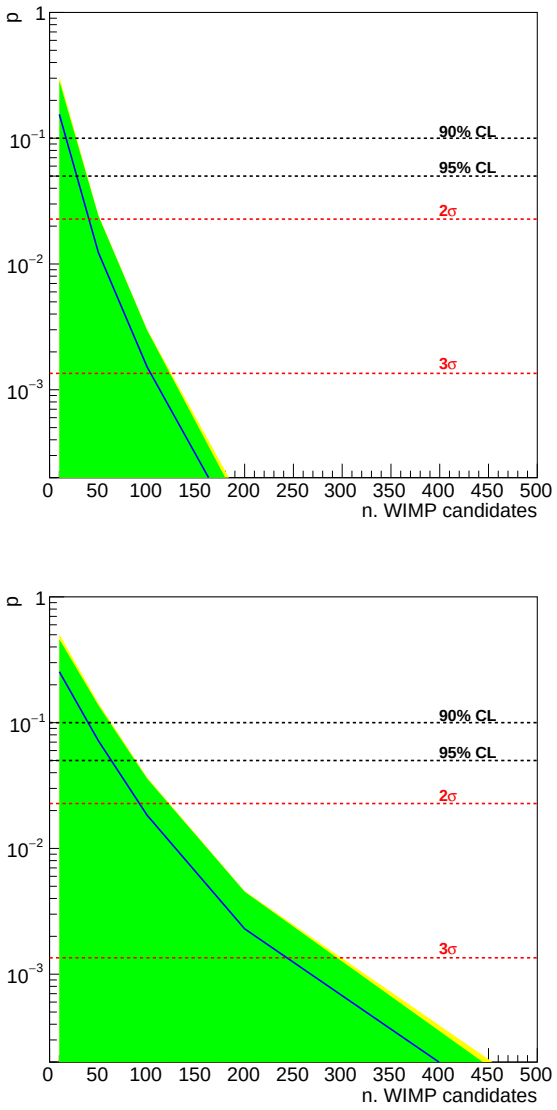

Fig. 6.17.: Expected p-value (blue line) of the null hypothesis (isotropic signal) as a function of the observed number of DM interaction candidate events for ideal resolution (top) and for a resolution of 400 mrad (bottom). The green and yellow bands show the excursion range at one and two standard deviations. The horizontal lines show from top to bottom the 90% and 95% CL exclusion and the 2σ and 3σ significance levels.

6.6 Conclusions

To conclude, in this chapter I have examined the sensitivity of a large scale dark matter liquid argon experiment to the directionality of the dark matter signal, under the assumption that it is possible, above a certain threshold, to measure the direction of the recoiling nucleus. This may indeed be possible with double phase liquid argon detectors, if the suggested dependence of columnar recombination on the alignment of the recoil momentum with the electric field can be experimentally demonstrated.

With a likelihood-ratio based statistical approach I showed that, using the angular information alone, 100 events are sufficient to reject the hypothesis of an isotropic background at 3 sigma level. This is in the ballpark of the number of events that can be observed by DarkSide-20k for a 100 tonne year exposure assuming a WIMP-nucleon cross-section of 10^{-46} cm^2 at 200 GeV WIMP mass. Larger exposures would probe directionality at smaller cross sections. Note that this result is rather conservative because it is telling us that, when a directional experiment such that described in this chapter is capable of collecting 100 (250) events for ideal (realistic) angular resolution, one is able to confirm if those events come from the preferential direction of Cygnus. This would mean that it is likely that they are dark matter candidates if one assumes the SHM. This result clearly helps in disentangling the background and WIMP hypotheses even in the worst case of an isotropic neutrino background. Recall that we are using only the directional information as a discrimination tool. Adding more information, like the arrival time, the energy spectra distribution and the estimation of the total number of predicted background events one can expect that a lower number of WIMP candidates are needed to claim an observation.

In Sec. 5.6 I have shown that lowering the energy threshold, experiments are sensitive to lower WIMP masses (in the range of about 1-10 GeV). However, this is the region in which the ^8B neutrinos saturate the sensitivity. In this case the directionality would help a lot in disentangling the signal from the background hypothesis since the latter is not even isotropic but it has a precise direction, namely the Sun. Indeed, the path in the sky for the Cygnus as view from the LNGS and the Sun is very different as showed in Fig. 6.18. In figure it is shown the position in the sky of the Sun and of the Cygnus as observed from the LNGS laboratory. If one observes the position of the Sun at the same time from a fixed

position over the course of the year, it results in a characteristic 8-shaped diagram, called analemma. The orange points show those analemmas for observations

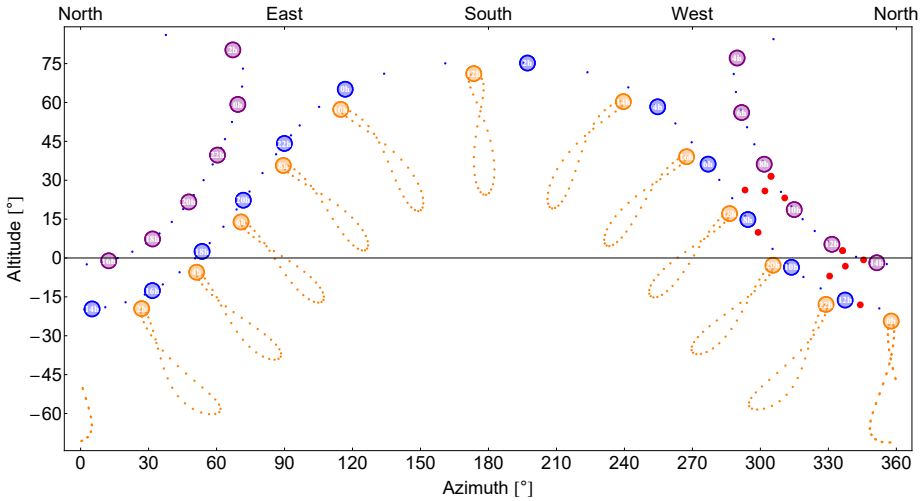

Fig. 6.18.: The orange points show the position of the sun analemmas every two hours, while the blue points show the path in the sky followed by two of the stars (Albireo and Deneb) of the Cygnus constellation as observed at the LNGS laboratory. The red points indicate the Cygnus position at about 9h and 12h of the 2017 SS to better understand the path of the blue points. The solid horizontal line is the horizon. As demonstrated here, the Sun's position does not coincide with that of Cygnus at any time.

made every two hours starting from the left at midnight. The highlighted orange circles indicate the sun position at 2017 SS. The blue small points indicate instead the path in the sky followed by two of the stars (Albireo and Deneb) of the Cygnus constellation during the year. To better understand such a path on the right it is possible to see the entire Cygnus constellation at different time of the day with red points. The path followed by the Cygnus constellation is the same every day, but due to the shift between sidereal and solar time its position is not the same at the same time of different days. In the figure the time stamps in blue and purple correspond to the position of Albireo and Deneb respectively. As visible, taking as an example the midday the sun is high in the sky while Albireo and Deneb are close to the horizon. In general for different time and days a similar separation remains. This fact suggests that a directional experiment should in principle be able to disentangle the WIMP from the Solar neutrino contributions in the observed data.

In view of the evidence presented in this chapter, and in consideration of the strong exclusion bounds already achieved by null observations performed by non-directional dark matter detectors, it is of utmost importance the development of

experimental technologies able to couple directional sensitivity with large fiducial masses (many tonnes) and the ability to collect large exposures free of background from β/γ events and neutron-induced nuclear recoils. One possible avenue would be offered by the presence of the signature of columnar recombination in nuclear recoils in a liquid argon time projection chamber, where this effect has already been observed for α particles and protons. Dedicated experiments performed on monochromatic, pulsed neutron beams will allow to explore the possible presence of this signature.

7 Experimental constraint of coherent neutrino scattering

Contents

7.1 The COHERENT experiment 193
7.2 CEnNS cross section with the inclusion of the neutron form factor 197
7.3 Parametrization of the neutron and proton form factors . . . 200
7.4 Fitting procedure of the COHERENT data 203
7.5 Implications of COHERENT results for dark matter searches . 210

In the previous chapters I have shown how the neutrino background coming from coherent elastic neutrino nucleus scattering plays a crucial role in the determination of the sensitivity to WIMPs of future dark matter detectors like DarkSide-20k. The calculation of the number of neutrino background events and the related "neutrino floor" [256] have been carried out using the standard Helm form factor (FF) with the Lewin-Smith (LS) prescription which parametrizes the nuclear part of the scattering cross section. As already said in Sec. 3.1.4, the use of the Helm form factor within the dark matter community is established for reasons of simplicity and uniformity in confronting different experimental exclusion curves. The Helm form factor however represents the distribution of protons and not the distribution of all the nucleons in the nucleus, since it has been obtained through the electron scattering data in Fricke et al. compilation [428] which probe only the charged distribution. However, in the most simple model which assumes equal coupling between WIMP and protons and WIMP and neutrons, $f_P = f_N$, the approximation that the form factor of the neutron distribution equals that of the protons $F_N \approx F_P = F$ leads to a small correction (less then few percent) of the WIMP rate prediction, which is not critical when determining exclusion limits in the case of a negative WIMP observation. Moreover, this correction in the WIMP rate prediction is negligible with respect to other assumptions that are made like that on the velocity distribution, which is assumed to be Maxwellian while the N-body simulation in the case of the Milky Way tell us that the deviation

from that model is large. However, when searching for a new phenomena the aim is to exclude or confirm a model, starting from the simplest one, within a certain confidence level. For this reason the dark matter community has so far widely tested mainly the simplest model of WIMP interaction. In literature, also the CEnNS differential cross-section is usually parametrized using a single Helm form factor with the LS parametrization. However in this case this prescription is not suitable because the neutrino coupling is weighted by the Q_w^2 factor (see Eq. 5.15), thus the contribution of ν-proton scattering is lower than ν-neutron one because of the presence of the factor $(1 - 4\sin^2\theta_w) \simeq 0.0454$. For this reason neutrinos probe mostly the distribution of the neutrons inside the nucleus, and the coherency is determined by the rms neutron radius which is a very poorly known quantity for most of the nuclei. The CEnNS reaction has been introduced in 1974 [254, 429] but it has been observed only in 2017 by the COHERENT collaboration [188] mainly due to the challenging task to reach energy thresholds of the order of $\sim 5\,$keV. The COHERENT experiment observed this process at 6.7σ confidence level for the first time using a 14.6 kg sodium-doped CsI scintillator exposed to a low-energy neutrino flux generated in the Spallation Neutron Source (SNS) at Oak Ridge National Laboratory. The collaboration observed 134 ± 22 CEnNS candidates instead of 173 ± 48 events predicted by the Standard Model, which is 77 ± 16 per cent of the SM value. This deficit of events have been explained in terms of Non Standard neutrino Interactions (NSI) by some authors [430, 431] resulting in limits on NSI parameter space for a vector mediator lighter than 50 MeV or for NS coupling between neutrinos and up and down quarks. However, in these works and also in the COHERENT paper the SM prediction has been written in terms of a unique nuclear form factor.

A better understanding of CEnNS has implications in many fields and it includes the possibility to search for sterile neutrinos, a neutrino magnetic moment [432, 433, 434], non-standard interactions mediated by new particles [435, 436], improved constraints on the value of the weak nuclear charge [437] and on the process occurring during stellar collapse [438, 439]. In this chapter, I will present a method to obtain valuable information about the neutron distribution of nuclei using CEnNS as a probe. The deficit and also the spectral distribution of the COHERENT events can be well fitted assuming that the rms radius of the neutron distribution is bigger than the corresponding proton radius. This implies that the reduction of events due to loss of coherence is more pronounced and it is potentially able to explain the deficit without implying the use of NSI or the reduction due to oscillation of standard neutrinos into sterile ones [440]. This

results in the first experimental constraint of the CEnNS phenomenology and would provide a better understanding of the neutrino background for future direct dark matter experiments.

In the following I will explain the method to obtain the first measurement [1] of the average CsI neutron density radius fitting the COHERENT data and how this information can be used to obtain a more reliable constraint on the neutrino background for DarkSide-20k.

7.1 The COHERENT experiment

In this section I will briefly describe the COHERENT experiment, the method to extract information on the neutron distribution and all the relevant formulas.

The Spallation Neutron Source (SNS) at Oak Ridge National Laboratory generates the most intense pulsed neutron beams in the world, produced by the interactions of accelerator-driven high-energy ($\simeq$ 1 GeV) protons striking a mercury target. Spallation sources give a significant yield of neutrinos, generated when pions, which are created as a consequence of proton interactions in the target, decay at rest. The resulting low neutrino energies are appropriate for CEnNS detection [441]. Three neutrino flavors are produced (prompt muon neutrinos ν_μ, delayed electron neutrinos ν_e, and delayed muon antineutrinos $\bar{\nu}_\mu$), each with characteristic energy and time distributions (see Fig. 7.1), and all having a similar CEnNS cross section for a given energy. During beam operation, approximately 5×10^{20} protons-on-target (POT) are delivered per day, each proton returning $\simeq$ 0.08 isotropically-emitted neutrinos per flavor.

Prompt neutrons escaping the iron and steel shielding monolith surrounding the mercury target would swamp a CEnNS detector sited at the SNS instrument bay. Neutron-induced nuclear recoils would largely dominate over neutrino-induced recoils, making experimentation impossible. The CsI detector has been for this reason located in a basement corridor, called the “neutrino alley” which offers more than 12 m of additional void free neutron-moderating materials in the line-of-sight to the SNS target monolith. An overburden of 8 meters of water equivalent (m.w.e.) provides an additional reduction in backgrounds associated with cosmic rays. The CsI[Na] CEnNS detector and shielding were installed in the corridor location nearest to the SNS target (see Fig. 7.3).

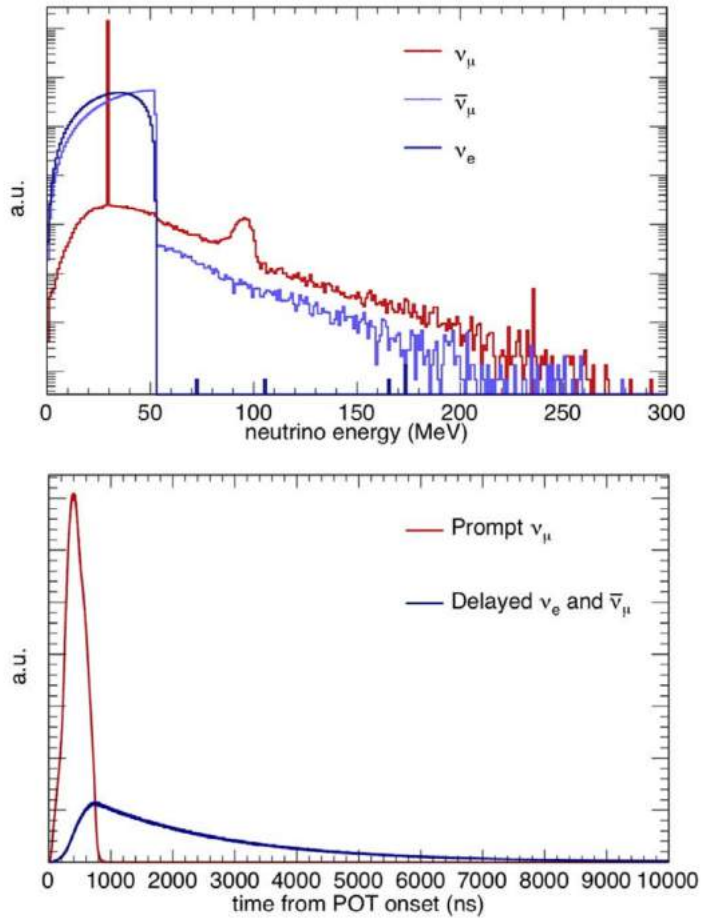

Fig. 7.1.: Simulation of the energy distribution (upper panel) and arrival time (lower panel) of SNS neutrinos to the COHERENT detector. Neutrinos above the endpoint of the Michel spectrum ($\simeq$ 52.8 MeV) arise from decay-in-flight and muon capture, giving a negligible signal rate ($<$ 1%) signal rate. Delayed neutrinos follow the 2.2 μs time constant characteristic of muon decay. Figure from [188], my reproduction of the neutrino flux at SNS is in Fig. 7.2.

The advantages of sodium-doped CsI as a CEnNS detection material is that heavy caesium and iodine nuclei provide large cross-sections, and nearly-identical response to CEnNS while generating sufficient scintillation for the detection of nuclear recoil energies down to a few keV.

In Fig. 7.4 is represented the main result obtained by the COHERENT collaboration, derived from fifteen months of accumulated live-time. When comparing CsI[Na] signals occurring before POT triggers, and those taking place immediately after, the collaboration observes a high-significance excess in the second group of signals, visible in both the energy spectrum and the distribution of signal-arrival

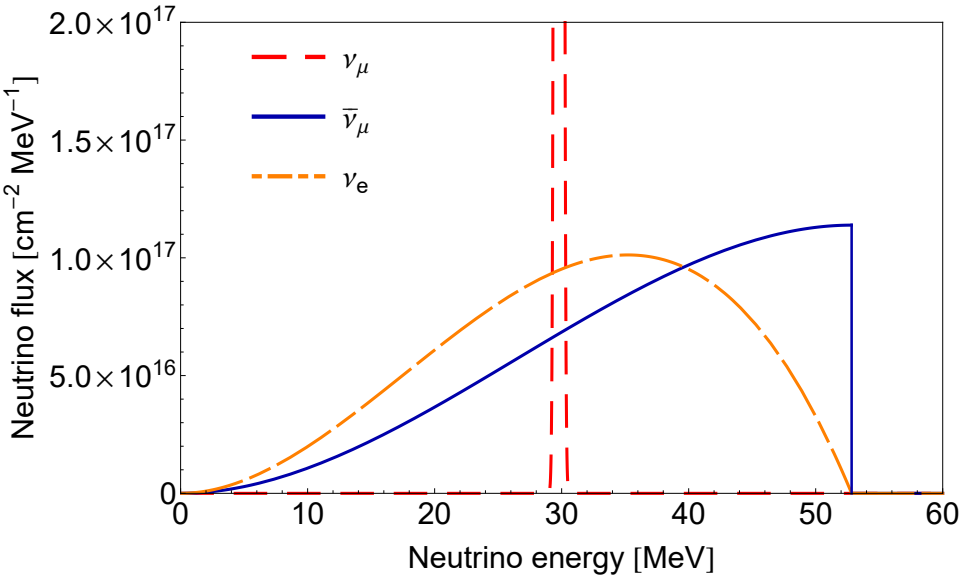

Fig. 7.2.: Neutrino flux at SNS from stopped pion decays, $\pi^+ \rightarrow \mu^+ + \nu_\mu$, and two delayed components of $\bar{\nu}_\mu$ and ν_e from the subsequent muon decays, $\mu^+ \rightarrow e^+ + \bar{\nu}_\mu + \nu_e$ (see Eq. 7.16). Here I have neglected neutrinos from decay-in-flight and muon capture which is a negligible contribution.

times. This excess appears only during times of neutrino production ("Beam ON" in the figure). The excess follows the expected CEnNS signature very closely, containing only a minimal contamination from beam-associated backgrounds. Neutrino-induced neutrons (NINs) have a negligible contribution, even smaller than that from prompt neutrons, which is shown in the figure. The formation of the excess is strongly correlated to the instantaneous power on target. All neutrino flavors emitted by the SNS contribute to reconstructing the excess, as expected from a neutral current process. Stacked histograms in Fig. 7.4 display the Standard Model CEnNS predictions for prompt ν_μ and delayed ν_e and $\bar{\nu}_\mu$, emissions. Consistency with the Standard Model is observed at the one-sigma level (134 $\pm$ 22 events observed, 173 $\pm$ 48 predicted).

The CEnNS predictions used by the collaboration were generated by convolving the simulated neutrino flux (Fig. 7.1) at the CsI[Na] detector position with the CEnNS differential cross-section described in [442]. In its prediction, the collaboration uses a unique nuclear form factor for neutrons and protons (one for Cs and one for I) as described in [443], that for simplicity I will refer to as Klein FF. The Klein FF (see Fig. 7.5) is an approximation of the the Woods-Saxon

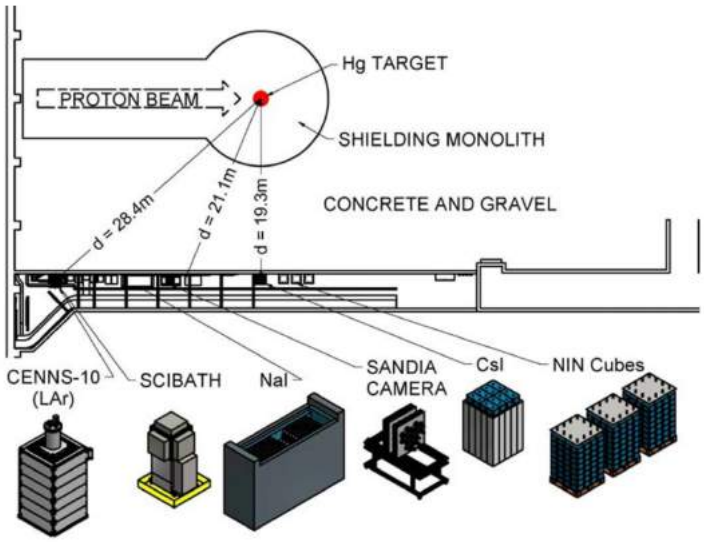

Fig. 7.3.: Schematic view of the COHERENT detectors populating the "neutrino alley" at the SNS. Locations in this basement corridor profit from more than 19 m of continuous shielding against beam-related neutrons, and a modest 8 meter of water equivalent overburden able to reduce cosmic-ray induced backgrounds. The CsI[Na] detector is located at a distance of 19.3 m from the intense neutrino source.

distribution as a hard sphere, with radius R_A, convoluted with a Yukawa potential with range $r = 0.7$ fm. The Fourier transform of this convolution is the product of the two individual transforms:

$$F(q^2) = \frac{4\pi\rho_0}{Aq^3}\Big[\sin(qR_a) - qR_a\cos(qR_A)\Big]\ \Big[\frac{1}{1+a^2q^2}\Big]. \tag{7.1}$$

The use of a unique nuclear form factor in the CEnNS cross section formula introduces a big approximation which is that the distributions of neutrons and protons are equal. I will relax this hypothesis introducing two distinct form factors, one for protons and a separate one for neutrons. Exploiting the fact that proton form factors are relatively well known it is possible to measure the for the first time the average rms radius of CsI neutron distribution, fitting the COHERENT data. The idea is that the deficit registered can be explained with the help of the neutron form factor and a rms neutron radius bigger than the corresponding proton one. In the next section I will present the main formulas and the fitting method.

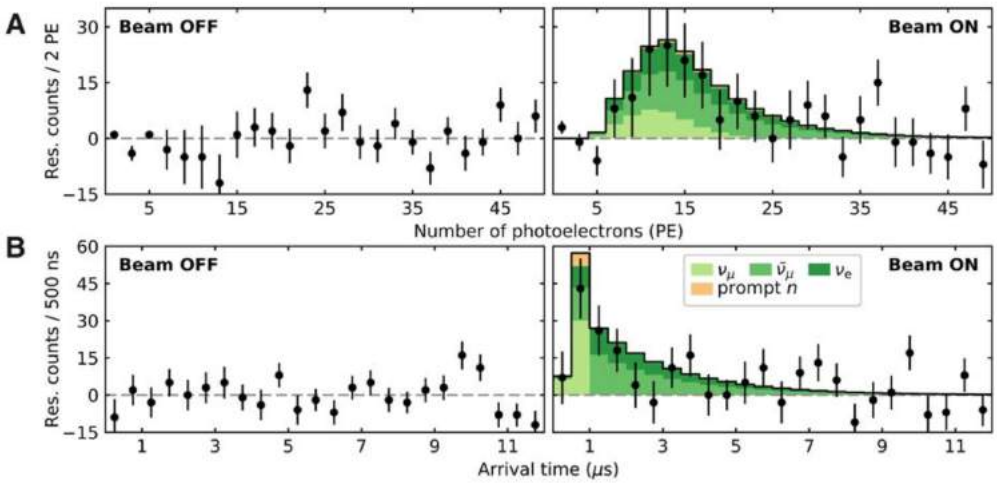

Fig. 7.4.: Observation of coherent elastic neutrino nucleus Scattering. Residual differences (data points) between CsI[Na] signals in the 12 μs following POT triggers, and those in a 12-μs window before, as a function of their (A) energy (number of photoelectrons detected), and of (B) event arrival time (onset of scintillation). These residuals are shown for 153.5 live-days of SNS inactivity ("Beam OFF") and 308.1 live-days of neutrino production ("Beam ON"), over which 7.48 GWhr of energy ($\simeq 1.76\times10^{23}$) was delivered to the mercury target. Approximately 1.17 photoelectrons are expected per keV of cesium or iodine nuclear recoil energy. Characteristic excesses closely following the Standard Model CEnNS prediction with a unique form factor as implemented by the collaboration (histograms) are observed for periods of neutrino production only, with a rate correlated to instantaneous beam power. Figure from [188].

7.2 CEnNS cross section with the inclusion of the neutron form factor

The differential cross section for coherent elastic scattering of a neutrino with a nucleus $\mathcal{N}$ with Z protons and N neutrons with the inclusion of the neutron form factor can be written[1] as [444, 445]

$$\frac{d\sigma_{\nu\text{-}\mathcal{N}}}{dE_r}(E,E_r) \simeq \frac{G_{\rm f}^2 m_{\mathcal{N}}}{4\pi}\left(1-\frac{m_{\mathcal{N}}E_r}{2E^2}\right) \times\left[NF_N(q^2)-\epsilon ZF_Z(q^2)\right]^2, \tag{7.2}$$

where $G_{\rm f}$ is the Fermi constant, $m_{\mathcal{N}}$ is the nuclear mass, $F_N(q^2)$ and $F_Z(q^2)$ are, respectively, the nuclear neutron and proton form factors, and $\epsilon = 1-4\sin^2\vartheta_{\rm w} = 0.0454\pm0.0003$, using the low-energy PDG value of the weak mixing angle $\vartheta_{\rm W}$

[1] For a simple derivation see App. A.

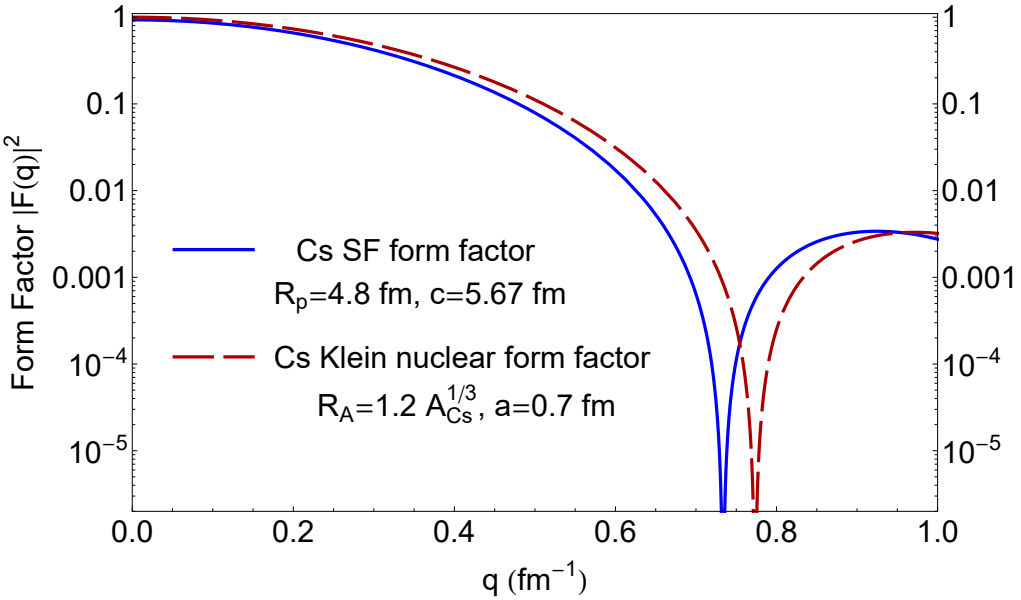

Fig. 7.5.: Comparison between the nuclear Klein form factor (red dashed line) used in [188] and the proton Symmetrized Fermi form factor (blue solid line) described in Eq. 7.7.

[446]. This choice is motivated by the fact that the momentum transfer in the CEnNS reaction is small. Because of the small value of ϵ, the neutron contribution is dominant. Hence, measurements of the process give information on the nuclear neutron form factor, which is more difficult to obtain than the information on the proton nuclear form factor, that can be obtained with elastic electron-nucleus scattering and other electromagnetic processes (see Refs. [187, 447]). Knowledge of these form factors is important, because form factors are the Fourier transform of the corresponding charge distribution. Electromagnetic processes probe the nuclear proton distribution, whereas neutral-current weak interaction processes are mainly sensitive to the nuclear neutron distribution. Also hadron scattering experiments give information on the nuclear neutron distribution, but their interpretation depends on the model used to describe non-perturbative strong interactions (see Refs. [448, 449, 450, 451]). Before the COHERENT experiment, the only measurement of the nuclear neutron distribution with neutral-current weak interactions was done with parity-violating asymmetry, A_{PV}, in the electron scattering on ^{208}Pb in the PREX experiment [213]. Before going into the details of the method used to extract the neutron radius using CEnNS is instructive to review the first measurement of R_n using A_{PV}.

7.2.1 The PREX measurement and its implications

Due to the fact that the weak charge of the neutron is much larger than that of the proton [452], the Z^0 boson, that carries the weak force, couples primarily to neutrons. Thus, a measurement of parity violation in electron scattering provides a model-independent probe of neutron densities that is free from most strong-interaction uncertainties.

One system of particular interest is the doubly-magic nucleus ^{208}Pb, which has 44 more neutrons than protons; some of these extra neutrons are expected to be found in the surface, where they form a neutron-rich skin. The thickness of this skin is sensitive to nuclear dynamics and provides fundamental nuclear structure information. A number of mean-field-theory models [453, 454, 455, 456, 457] predicts values consistent with a radius of the point-neutron distribution R_n between 0.0 – 0.4 fm, larger than that of the point-proton distribution R_p. The value of the neutron radius of ^{208}Pb has important implications for models of nuclear structure and their application in atomic physics and astrophysics. There is a strong correlation between R_n of ^{208}Pb and the pressure of neutron matter, in particular measuring R_n one can constrain the equation of state (EOS), the pressure as a function of density, of neutron matter. There is also a correlation between R_n and the radius of a neutron star r_{NS} [458, 459]. In general, a larger R_n implies a stiffer EOS and a larger r_{NS}.

In the Born approximation, the parity violating cross-section asymmetry for longitudinally polarized electrons elastically scattered from an unpolarized nucleus, A_{PV}, is proportional to the weak form factor $F_W(Q^2)$. This is the Fourier transform of the weak charge density, which is closely related to the neutron density, and therefore the neutron density can be extracted from an electro-weak measurement [452] of

$$A_{PV} = \frac{\sigma_R - \sigma_L}{\sigma_R + \sigma_L} \approx \frac{G_f Q^2}{4\pi\alpha\sqrt{2}} \frac{F_W(Q^2)}{F_{ch}(Q^2)} \,, \tag{7.3}$$

where $\sigma_{R(L)}$ is the differential cross section for elastic scattering of right and left handed longitudinally polarized electrons, α the fine structure constant and $F_{ch}(Q^2)$ is the Fourier transform of the known charge density.

The PREX collaboration reported the first measurement of the parity-violating asymmetry A_{PV} in the elastic scattering of polarized electrons from ^{208}Pb. The

result $A_{PV} = 0.656 \pm 0.060\,(\text{stat}) \pm 0.014\,(\text{syst})$ ppm corresponds to a difference between the radii of the neutron and proton distributions $R_n - R_p = 0.33^{+0.16}_{-0.18}$ fm and provides the first electroweak observation of the neutron skin which is expected in a heavy, neutron-rich nucleus.

7.3 Parametrization of the neutron and proton form factors

In the case of the COHERENT experiment, the coherent elastic scattering is measured on ^{133}Cs and ^{127}I, which contribute incoherently, leading to the total cross section

$$\frac{d\sigma_{\nu\text{-CsI}}}{dE_r} = \frac{d\sigma_{\nu\text{-Cs}}}{dE_r} + \frac{d\sigma_{\nu\text{-I}}}{dE_r}, \tag{7.4}$$

with $N_{\text{Cs}} = 78$, $Z_{\text{Cs}} = 55$, $N_{\text{I}} = 74$, and $Z_{\text{I}} = 53$. I neglect the small axial contribution due to the unpaired valence proton [442].

The proton and neutron form factors are the Fourier transform of the nuclear proton and neutron densities. The proton structures of ^{133}Cs and ^{127}I have been studied with muonic atom spectroscopy [187] and the data were fitted with Fermi density distributions of the form

$$\rho_{\text{F}}(r) = \frac{\rho_0}{1 + e^{(r-c)/a}}, \tag{7.5}$$

where ρ_0 is a normalization factor and a is a parameter which quantifies the surface thickness $t = 4a \ln 3$, which was fixed at 2.30 fm. The fit of the data yielded $c_{\text{Cs}} = 5.6710 \pm 0.0001$ fm and $c_{\text{I}} = 5.5931 \pm 0.0001$ fm, which correspond to the proton rms radii $R_p^{\text{Cs}} = \langle r_p^2 \rangle_{\text{Cs}}^{1/2} = 4.804$ fm and $R_p^{\text{I}} = \langle r_p^2 \rangle_{\text{I}}^{1/2} = 4.749$ fm, respectively. Hence, the proton structures of ^{133}Cs and ^{127}I are similar. Since it is expected that also their neutron structures are similar and the current uncertainties of the COHERENT data do not allow to distinguish between them, I consider in Eq. (7.4) the approximation

$$F_{N,\text{Cs}}(q^2) \simeq F_{N,\text{I}}(q^2) \simeq F_N(q^2). \tag{7.6}$$

I fitted the COHERENT data under this approximation assuming proton form factors $F_Z(q^2)$ for ^{133}Cs and ^{127}I given by the Fourier transform of a symmetrized Fermi (SF) distribution $\rho_{\text{SF}}(r) = \rho_{\text{F}}(r) + \rho_{\text{F}}(-r) - 1$, which is practically equiv-

alent to a Fermi distribution and gives an analytic expression for the form factor [460]:

$$F_Z^{\text{SF}}(q^2) = \frac{3}{qc\,[(qc)^2 + (\pi qa)^2]} \left[\frac{\pi qa}{\sinh(\pi qa)}\right] \times \left[\frac{\pi qa \sin(qc)}{\tanh(\pi qa)} - qc\cos(qc)\right]. \tag{7.7}$$

In order to get information on the neutron distribution of ^{133}Cs and ^{127}I in the approximation in Eq. (7.6), I considered the following parametrizations of the neutron form factor $F_N(q^2)$:

1. A symmetrized Fermi form factor $F_N^{\text{SF}}(q^2)$ analogous to that in Eq. (7.7). In this case, the neutron rms radius is given by

$$R_n^2 = \frac{3}{5}\,c^2 + \frac{7}{5}\,(\pi a)^2. \tag{7.8}$$

   Since the COHERENT data are not sensitive to the surface thickness, I consider the same value of $t = 2.30\,\text{fm}$ as for the proton form factor. I verified that the results of the fit are practically independent of small variations of the value of the surface thickness.

2. The Helm form factor [185]

$$F_N^{\text{Helm}}(q^2) = 3\,\frac{j_1(qR_0)}{qR_0}\,e^{-q^2s^2/2}, \tag{7.9}$$

   where $j_1(x) = \sin(x)/x^2 - \cos(x)/x$ is the spherical Bessel function of order one and R_0 is the box (or diffraction) radius. In this case, the neutron rms radius is given by

$$R_n^2 = \frac{3}{5}\,R_0^2 + 3s^2. \tag{7.10}$$

   The parameter s quantifies the surface thickness. In this case I consider the value $s = 0.9\,\text{fm}$ which was determined for the proton form factor of similar nuclei [461]. Also in this case, I verified that the results of the fit are practically independent of small variations of the value of the surface thickness.

In Fig. 7.6 I have shown the comparison between the integrated CEnNS cross section (Eq. 5.19) for Cesium obtained by the COHERENT collaboration with the

inclusion of the neutron form factor as in Eq. 7.2. The cross section used in [188] considered only a global nuclear form factor while my implementation make use of the SF form factor for protons (with the experimental value $c_{\rm Cs} \simeq 5.67\,\text{fm}$ and $R_p^{\rm Cs} = \langle r_p^2 \rangle_{\rm Cs}^{1/2} \simeq 4.8\,\text{fm}$), and the Helm form factor for neutrons (with $R_n^{\rm Cs} \simeq 4.8\,\text{fm}$, and $s = 0.9\,\text{fm}$). In this case I have chosen a value for the neutron rms radius which is identical to the proton one, just for comparison. As it is possible to see, with the inclusion of the neutron form factor the cross section for Cs, even in the case of equal values of the neutron and proton radius, deviates from the implementation of the COHERENT collaboration [188]. In the next section, I will describe the fitting procedure used in order to obtain information about the neutron distribution.

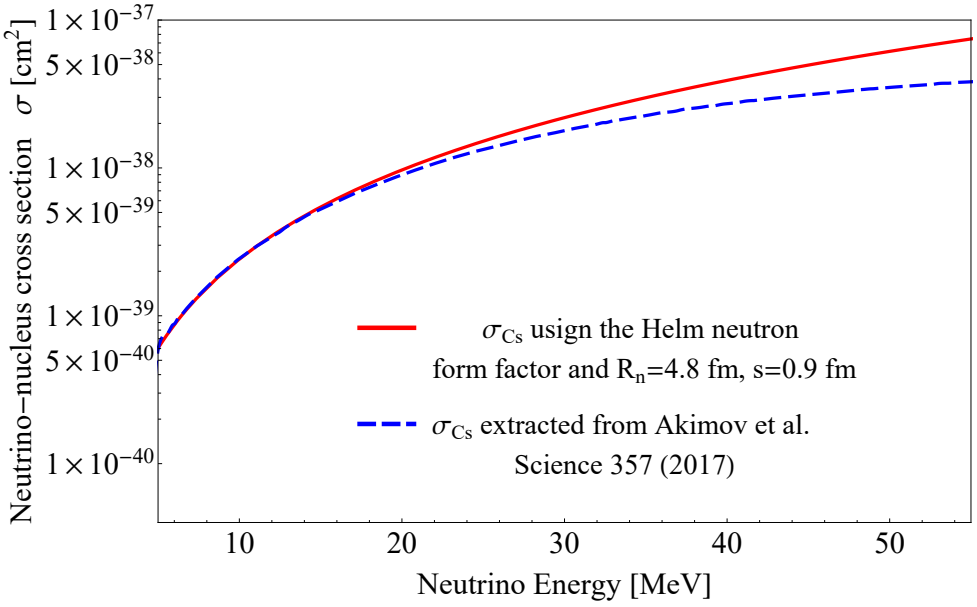

Fig. 7.6.: Integrated CEnNS cross section (see Eq. 5.19) for Cs obtained by the COHERENT collaboration [188] (dashed blue line), and the implementation described in this thesis with the inclusion of the neutron form factor (see Eq. 7.2) (solid red line) as a function of the neutrino energy in MeV. The COHERENT measurement involves neutrino energies in the range ∼16-53 MeV, the lower bound defined by the lowest nuclear recoil energy measured, the upper bound by SNS neutrino emissions.

7.4 Fitting procedure of the COHERENT data

In order to extract a value for R_n I fitted the COHERENT data in Fig. 3A of Ref. [188] (see panel A right of Fig. 7.4) with the least-squares function

$$\chi^2 = \sum_{i=4}^{15} \left(\frac{N_i^{\text{exp}} - (1+\alpha)\, N_i^{\text{th}} - (1+\beta)\, B_i}{\sigma_i} \right)^2 + \left(\frac{\alpha}{\sigma_\alpha} \right)^2 + \left(\frac{\beta}{\sigma_\beta} \right)^2 . \tag{7.11}$$

For each energy bin i, N_i^{exp} and N_i^{th} are, respectively, the experimental and theoretical number of events, B_i is the estimated number of background events extracted from Fig. S13 of Ref. [188], and σ_i is the statistical uncertainty. The parameters α and β are nuisance parameters which quantify, respectively, the systematic uncertainty of the signal rate and the systematic uncertainty of the background rate. The corresponding standard deviations are $\sigma_\alpha = 0.28$ and $\sigma_\beta = 0.25$ [188]. I did not considered the first three energy bins in Fig. 3A of Ref. [188], which do not give any information on neutrino-nucleus scattering because they correspond to the detection of less than 6 photoelectrons, for which the acceptance function in Fig. S9 of Ref. [188] vanishes. My reproduction of the acceptance function is provided in figure 7.7.

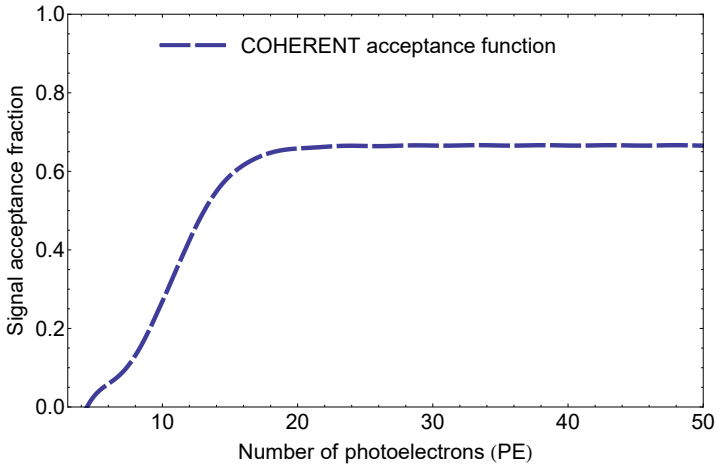

Fig. 7.7.: Acceptance function of COHERENT search data. The acceptance points have been extracted from fig. S9 [188] and then fitted to obtain this acceptance curve.

I considered only the 12 energy bins from $i = 4$ to $i = 15$ for which the COHERENT collaboration fitted the quenching factor in Fig. S10 of Ref. [188] and obtained

the linear relation between the observed number of photoelectrons $N_{\rm PE}$ and the nuclear kinetic recoil energy E_r given by

$$N_{\rm PE} = 1.17 \left(\frac{E_r}{\rm keV} \right). \tag{7.12}$$

The theoretical number of coherent elastic scattering events $N_i^{\rm th}$ in each energy bin i depends on the nuclear neutron form factor and it is given by

$$N_i^{\rm th} = N_{\rm CsI} \int_{E_r^i}^{E_r^{i+1}} dE_r \int_{E_{\rm min}} dE\, A(E_r) \frac{dN_\nu}{dE} \frac{d\sigma_{\nu\text{-CsI}}}{dE_r}. \tag{7.13}$$

where $N_{\rm CsI}$ is the number of CsI in the detector (given by $N_{\rm A} M_{\rm det}/M_{\rm CsI}$, where $N_{\rm A}$ is the Avogadro number, $M_{\rm det} = 14.6\,$kg, is the detector mass, and $M_{\rm CsI} = 259.8$ is the molar mass of CsI), $E_{\rm min} = \sqrt{m_{\mathcal{N}} E_r/2}$, $A(E_r)$ is the acceptance function given in Fig. S9 of Ref. [188] and dN_ν/dE is the neutrino flux integrated over the experiment lifetime. As anticipated, neutrinos at the SNS consist of a prompt component of monochromatic ν_μ from stopped pion decays, $\pi^+ \to \mu^+ + \nu_\mu$, and two delayed components of $\bar{\nu}_\mu$ and ν_e from the subsequent muon decays, $\mu^+ \to e^+ + \bar{\nu}_\mu + \nu_e$. The total flux dN_ν/dE is the sum of

$$\frac{dN_{\nu_\mu}}{dE} = \eta\, \delta\left(E - \frac{m_\pi^2 - m_\mu^2}{2m_\pi} \right), \tag{7.14}$$

$$\frac{dN_{\nu_{\bar{\mu}}}}{dE} = \eta\, \frac{64E^2}{m_\mu^3} \left(\frac{3}{4} - \frac{E}{m_\mu} \right), \tag{7.15}$$

$$\frac{dN_{\nu_e}}{dE} = \eta\, \frac{192E^2}{m_\mu^3} \left(\frac{1}{2} - \frac{E}{m_\mu} \right), \tag{7.16}$$

for $E \leq m_\mu/2 \simeq 52.8\,$MeV, with the normalization factor $\eta = r N_{\rm POT}/4\pi L^2$, where $r = 0.08$ is the number of neutrinos per flavor that are produced for each proton on target, $N_{\rm POT} = 1.76 \times 10^{23}$ is the number of proton on target and $L = 19.3\,$m is the distance between the source and the COHERENT CsI detector [188]. Each of the components of the total flux is shown in Fig. 7.2.

Figure 7.8 shows the COHERENT data as a function of the nuclear kinetic recoil energy E_r. I first compared the data with the predictions in the case of full coherence, i.e. all nuclear form factors equal to unity. Figure 7.8 shows that the corresponding histogram does not fit the data. Hence, albeit the COHERENT data represent the first measurement of coherent elastic neutrino-nucleus scattering, the scattering is not fully coherent and the data give information on the nuclear

structure. Indeed, as already said, the COHERENT collaboration [188] explained the data using the form factor in Ref. [443] with fixed value of the parameters, i.e. assuming the value of the nuclear rms radius.

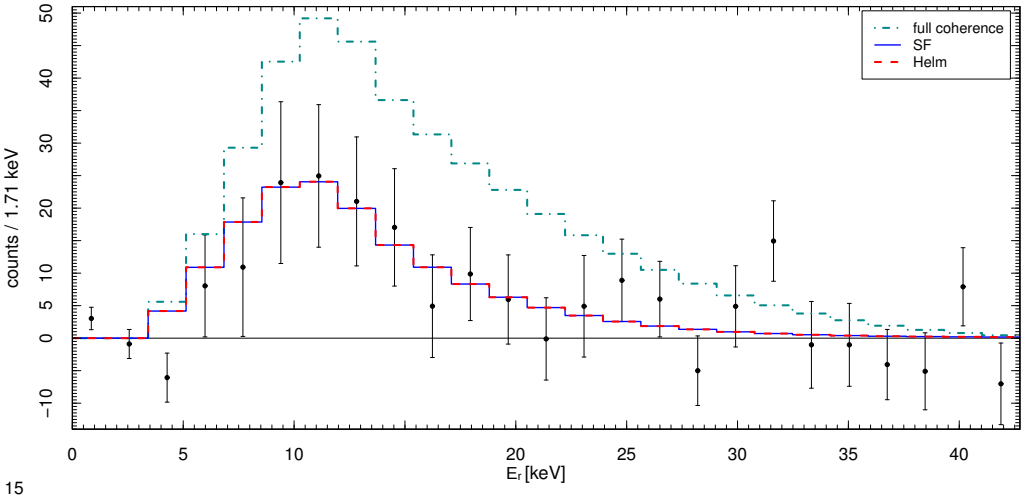

Fig. 7.8.: COHERENT data [188] versus the nuclear kinetic recoil energy E_r. The histograms represent the theoretical prediction in the case of full coherence (cyan dash-dotted) and the best fits obtained using the symmetrized Fermi (SF) distribution (blue solid) and Helm (red dashed) form factors.

I fitted the COHERENT data in order to get information on the value of the neutron rms radius R_n, which is determined by the minimization of the χ^2 in Eq. (7.11) using the symmetrized Fermi and Helm form factors. In both cases I obtained a minimum χ^2 which is smaller than the χ^2 corresponding to full coherence by 5.5. Hence, the hypothesis of full coherence has a p-value of 1.9% and there is a 2.3σ evidence of the nuclear structure suppression of the coherence.

Figure 7.8 shows the best-fit results that I obtained using the symmetrized Fermi and Helm form factors. Figure 7.9 shows the corresponding marginal values of the χ^2 as a function of R_n. One can see from both figures that the two parameterizations of the neutron form factor fit equally well the data and give practically the same result:

$$R_n = 5.5^{+0.9}_{-1.1}\,\text{fm}. \tag{7.17}$$

This is the first determination of the neutron rms radius of a nucleus obtained with neutrino-nucleus scattering data. Note also that it is practically model-independent, because it coincides for the symmetrized Fermi and Helm form factors which correspond to reasonable descriptions of the nuclear density. As a

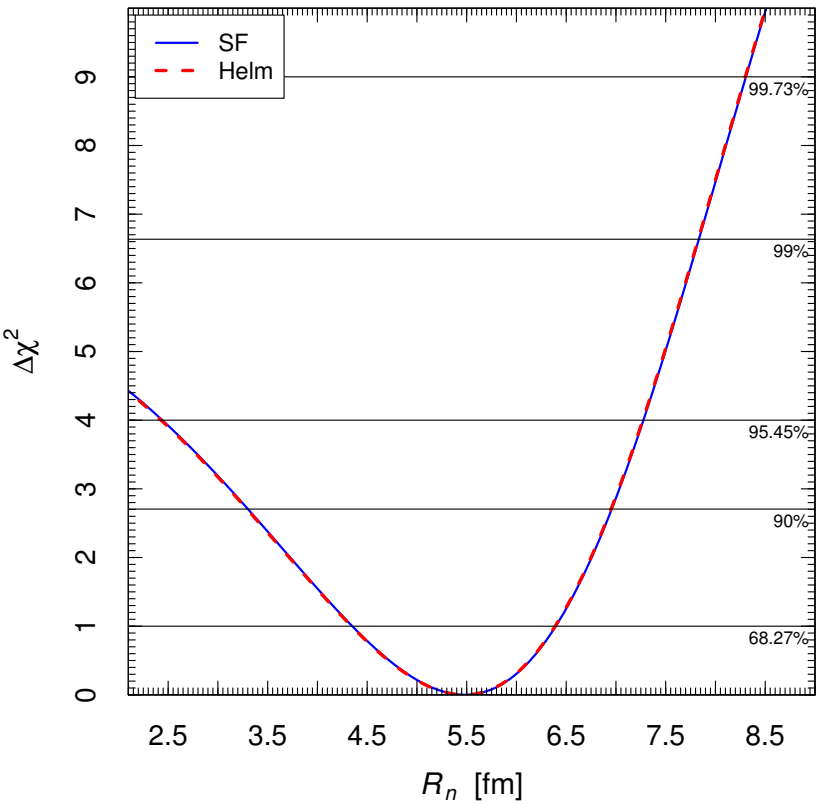

Fig. 7.9.: $\Delta\chi^2 = \chi^2 - \chi^2_{\text{min}}$ as a function of the neutron rms radius R_n obtained from the fit of the data of the COHERENT experiment [188] using the symmetrized Fermi (SF) and Helm form factors.

qualitatively example I show in Fig 7.12 the average CsI neutron density (Eq. 7.7 and Eq. 3.40) as a function of the neutron radius corresponding to the SF and Helm form factors obtained using the central value of R_n presented in Eq. 7.17.

As already stated above, the neutron rms radius was determined before only for ^{208}Pb from the parity-violating measurements of the PREX experiment [213]. The authors of Ref. [462] found $R_n(^{208}\text{Pb}) = 5.75 \pm 0.18\,\text{fm}$. Our best-fit value of R_n for ^{127}I and ^{133}Cs, obtained assuming that the two nuclei have similar structures, is correctly smaller than that of the heavier ^{208}Pb nucleus.

Table 7.1 shows the theoretical values of the proton and neutron rms radii of ^{133}Cs and ^{127}I obtained with nuclear mean field models. All the models predict values of R_p which are in approximate agreement with the experimental ones in Eqs. (7.3) and (7.3). Due to the large uncertainty, the average CsI value of R_n that we obtained in Eq. (7.17) is compatible with all the model calculations. It tends to favour values of R_n that are larger than all the model calculations in

	^{133}Cs			^{127}I			CsI		
Model	R_p	R_n	ΔR_{np}	R_p	R_n	ΔR_{np}	R_p	R_n	ΔR_{np}
SHF SkM* [463]	4.76	4.90	0.13	4.71	4.84	0.13	4.73	4.86	0.13
SHF SkP [464]	4.79	4.91	0.12	4.72	4.84	0.12	4.75	4.87	0.12
SHF SkI4 [465]	4.73	4.88	0.15	4.67	4.81	0.14	4.70	4.83	0.14
SHF Sly4 [456]	4.78	4.90	0.13	4.71	4.84	0.13	4.73	4.87	0.13
SHF UNEDF1 [466]	4.76	4.90	0.15	4.68	4.83	0.15	4.71	4.87	0.15
RMF NL-SH [467]	4.74	4.93	0.19	4.68	4.86	0.19	4.71	4.89	0.18
RMF NL3 [453]	4.75	4.95	0.21	4.69	4.89	0.20	4.72	4.92	0.20
RMF NL-Z2 [468]	4.79	5.01	0.22	4.73	4.94	0.21	4.76	4.97	0.21

Tab. 7.1.: Theoretical values in units of fermi of the proton and neutron rms radii of ^{133}Cs and ^{127}I and the CsI average obtained with nonrelativistic Skyrme-Hartree-Fock (SHF) and relativistic mean field (RMF) nuclear models.

Table 7.1, but more precise measurements are needed in order to truly test the models.

Another quantity of interest is the difference between the neutron and proton rms radii $R_n - R_p$, which is usually referred to as "neutron skin" [469]. The values of R_p for ^{127}I and ^{133}Cs determined in Ref. [187] are around 4.78 fm, with a difference of about 0.05 fm. Hence, for the neutron skin, I obtain

$$\Delta R_{np} \equiv R_n - R_p \simeq 0.7^{+0.9}_{-1.1}\,\text{fm}. \tag{7.18}$$

Unfortunately, the uncertainty is large and it does not allow to claim a determination of the neutron skin. One can only note that the best-fit value indicates the possibility of a value that is larger than the model-predicted values obtained in Ref. [469], which are between about 0.1 and 0.3 fm. Indeed, some models predicts for Cs $\Delta R_{np} = 0.158(37)\,\text{fm}$ [470], $\Delta R_{np} = 0.23\,\text{fm}$ (see Fig. 10 of [471]). However, also in the case of ^{208}Pb the theoretical models predicted a value of the neutron skin lower than the experimental value of $0.33^{+0.16}_{-0.18}$ fm found in [460]. In Fig. 7.10 the predictions for the neutron skin of different nuclei are reported as a function of the predicted values of ΔR^{208}_{np} [472]. Taking into account that the experimental value of ΔR^{208}_{np} lies outside the predicted range in this figure, according to this model values as large as 0.3 fm can be feasible for Cs.

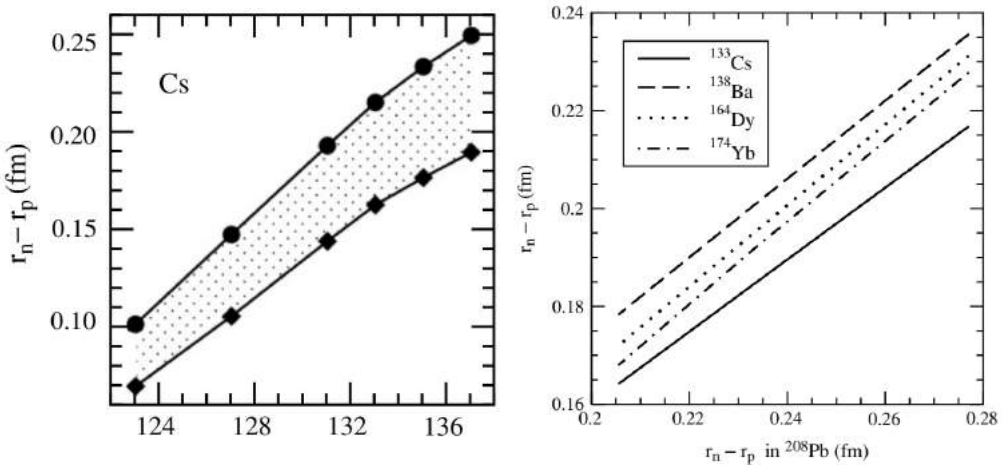

Fig. 7.10.: Variation of the neutron skin in Cs isotope chains for the two effective field theory models considered in [472] (Left) and the correlation between the neutron skin of Cs and that of Pb (Right). Figure form [472].

7.4.1 Future sensitivity of R_n

Future data of the COHERENT experiment may lead to a better determination of the neutron rms radius R_n. Figure 7.11 shows an estimation of the sensitivity of the COHERENT experiment as a function of the number of protons on target with the current systematic uncertainties, with half the current systematic uncertainties, and with one quarter of the current systematic uncertainties. The effect of the beam-off background, extracted from the statistical uncertainties of Fig. 3A of Ref. [188], has been included. From Fig. 7.11 one can see that the current sensitivity gives a relative uncertainty $\Delta R_n/R_n \simeq 17\%$, which is in approximate agreement with the uncertainty of the determination of R_n in Eq. (7.17). With the current systematic uncertainties and ten times the current number of protons on target, the data of the COHERENT experiment will allow to determine R_n within about 0.5 fm. If the systematic uncertainties are reduced by half or one quarter, R_n can be determined within about 0.4 or 0.3 fm, respectively. Such a measurement would also decrease the uncertainty on the value of the neutron skin allowing a more meaningful comparison with the model predictions in Table 7.1.

Since R_p is relatively well known, a measurement of R_n allows to determine the neutron skin ΔR_{np}. Information on this quantity is eagerly awaited because ΔR_{np} is correlated with several properties characterizing neutron-rich matter (see

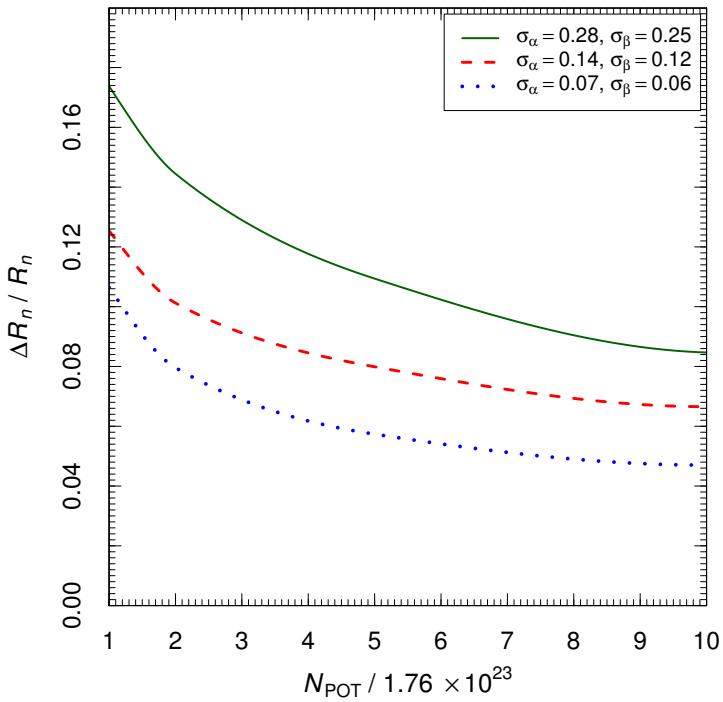

Fig. 7.11.: Projected relative uncertainty of the possible determination of the neutron rms radius R_n with the data of the COHERENT experiment as a function of the number N_{POT} of protons on target in units of the current number (1.76×10^{23}) for the current systematic uncertainties (solid green curve), half the current systematic uncertainties (dashed red curve), and one quarter of the current systematic uncertainties (dotted blue curve).

Refs. [473, 474, 475, 476, 477]). A larger neutron skin would suggest a stiffer EOS and imply a larger neutron star radius R_{NS}. Since the neutron star binding energy is inversely proportional to R_{NS}, a larger R_{NS} implies a smaller gravitational binding energy, which can be tested by observing the intense neutrino burst of a core collapse supernova.

The neutron skin is also correlated with several other nuclear quantities, e.g. with the slope of bulk symmetry energy, with the slope of binding energy of neutron matter, and with the symmetry correction to the incompressibility (see Ref. [478] for a review).

On August 17, 2017 the Advanced LIGO and Advanced Virgo gravitational-wave detectors made their first observation of a binary neutron star inspiral [163]. From this observation the collaboration was able to infer not only the component masses of the binary but also the tidal deformability parameter, which is related to the neutron star EOS and to the neutron skin [479, 459].

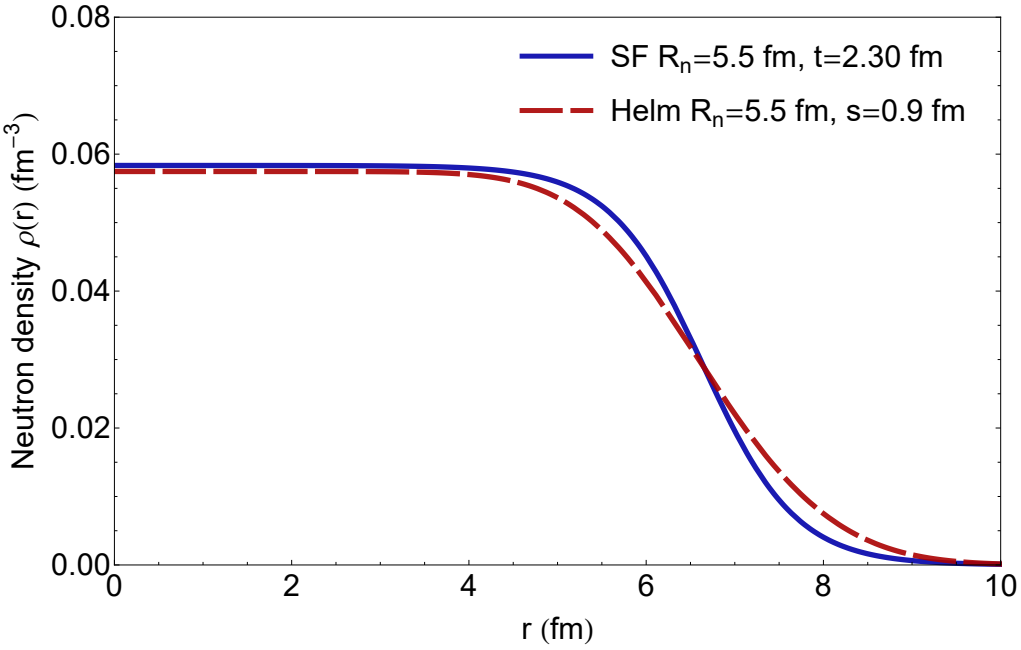

Fig. 7.12.: Average CsI neutron density as a function of the neutron radius in fm corresponding to SF (solid blue line) and Helm (dashed red line) form factors obtained using the central value of R_n presented in Eq. 7.17.

7.5 Implications of COHERENT results for dark matter searches

In this section I will analyse the implications of the results described in the previous sections for dark matter searches and in particular the impact on the irreducible CEnNS background. As we have seen, the COHERENT data suggest that, in order to obtain a better fit, we need to distinguish between the proton and the neutron form factor. The fact that the neutron distribution radius is quite different from that of the proton has been already suggested by the PREX measurement. COHERENT data confirms this observation hinting an even larger difference. In Fig. 7.13 I show the comparison between the SF proton form factor and the neutron one evaluated with the experimental constraint inputs coming from the electron scattering data from [187] and the COHERENT data as I explained in the sections before, respectively. It is possible to see that there is a sizeable difference among the two in the ROI of the COHERENT energy range. One can evaluate how this difference impacts the number of CEnNS neutrino background expected for future DM detectors. Since caesium and iodine have similar atomic and mass numbers to that of xenon, it is possible to make a

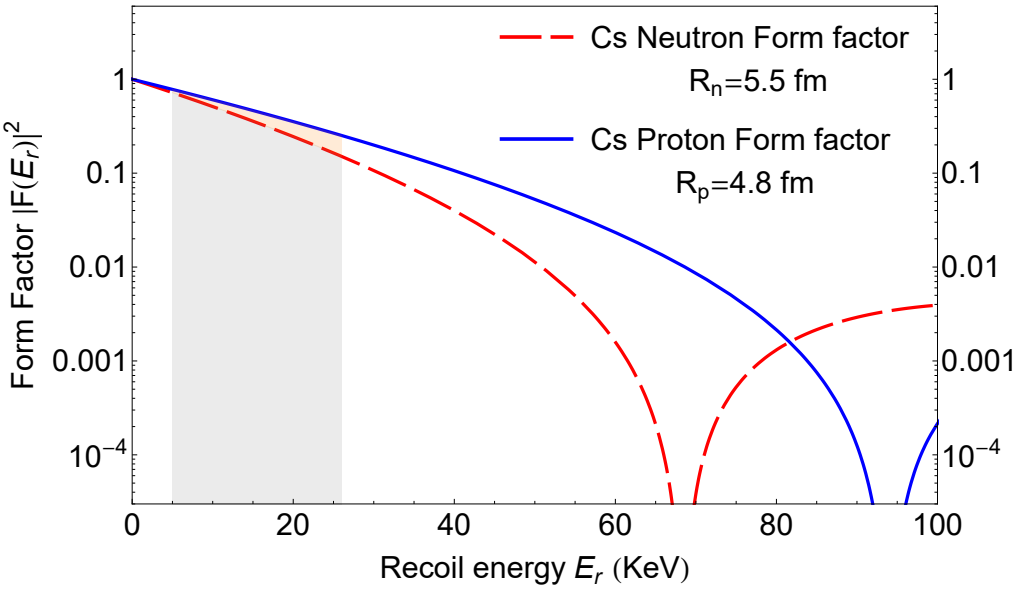

Fig. 7.13.: Comparison between the Cs SF proton form factor and the neutron one with the experimental constraints coming from [187] and the COHERENT data ([1] and this thesis) respectively, as a function of the recoil energy. The grey band highlights the COHERENT data fit region, while the orange band shows the difference between the two form factors.

preliminary study for experiments like DARWIN, XENONnT and LZ that use such a noble element as a target. In Fig. 7.14 I show the ratio between the differential cross-section including the neutron form factor in Eq. 7.2 and that with a unique Helm nuclear form factor using the LS parametrization in Eq. 5.15, for the energy ROI of xenon experiments. The ratio varies between approximately one and two in the region where most of the events are expected but it grows up to five at large energies ~ 50 keV. This implies that the total number of CEnNS background events would be smaller than previously estimated.

For DarkSide-20k I cannot quantitatively calculate the impact of the neutron form factor since argon has a quite different atomic and mass number than caesium and iodine. However, the COHERENT data-taking continues, with neutrino production expected to increase soon by up to 30%, compared to the average delivered during the initial period. In addition to CsI[Na], the COHERENT collaboration presently operates also a 28 kg single-phase liquid argon (LAr) detector, that would give precious information about the argon response to CEnNS. Moreover, presently planned expansion includes an almost one ton LAr detector with nuclear/electron recoil discrimination capability. This would represent a unique opportunity to experimentally constrain the physics parameters related to CEnNS, in particular

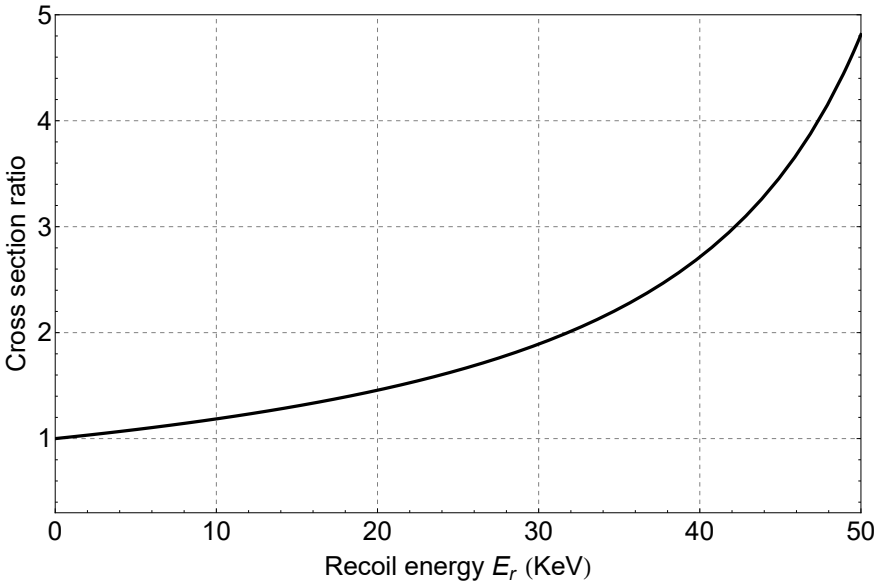

Fig. 7.14.: Ratio between the differential cross-section including the neutron form factor in Eq. 7.2 and that with a unique Helm nuclear form factor using the LS parametrization in Eq. 5.15, for the energy ROI of xenon experiments.

the argon neutron distribution. In this way I will be capable to precisely determine the expected number of neutrino background events which represents the most insidious background of future DM experiments. This will have a large impact on the final WIMP sensitivity that can be reached, as explained in Chap. 5.

8 Conclusions

In this thesis, the 90% confidence level (C.L.) WIMP-nucleon sensitivity curve for DarkSide-20k, a dual-phase liquid argon time projection chamber (TPC) of 20 tonne active mass to be built at LNGS, has been derived for the first time. The sensitivity curve depends crucially on the background content of the experiment. As shown in the third chapter, thanks to its extraordinary capability in distinguishing nuclear from electron recoils, DarkSide-20k will be able to keep the instrumental background content to less than 0.1 events for a total exposure of 100 tonne year. However, it will be affected by Coherent Elastic neutrino-Nucleus Scattering (CEnNS), that induces nuclear recoils almost indistinguishable from those potentially induced by WIMPs. The detailed calculation of the expected number of CEnNS in the DarkSide-20k exposure and the study of the spectral distribution of those events has been carried out for the first time in this thesis. It has been demonstrated that this background will be the dominant one for DarkSide-20k, despite the fact that it was neglected until this work. All these studies have been described in the fourth chapter, followed by a discussion on the impact of CEnNS background for future xenon and argon DM detectors clarifying the concept of the so-called “neutrino floor”.

It has been found that, in the nuclear recoil energy range needed to achieve the excellent electron recoil background rejection in liquid argon, only atmospheric and diffuse supernova neutrinos are energetic enough to produce nuclear recoils in the WIMP region of interest. In particular, the number of CEnNS candidates has been estimated to be 1.33 ± 0.26, considering an exposure of 100 tonne year and after the inclusion of the experimental DarkSide-20k nuclear recoil acceptance. It has been understood that the atmospheric neutrino contribution is the dominant one, being the diffuse supernova neutrino contribution negligible. The reported uncertainty on the predicted CEnNS candidates is dominated by the uncertainty on the atmospheric neutrino fluxes.
Taking into account the impact of this background, the WIMP-nucleon sensitivity at 90% C.L. has been determined. DarkSide-20k will be able to exclude WIMP-nucleon cross section down to $2.8 \times 10^{-48}\,\mathrm{cm}^2$ ($1.2 \times 10^{-47}\,\mathrm{cm}^2$) for a WIMP

mass of 100 GeV (1 TeV). Moreover, the impact of ARIA purification process and the possible gain in sensitivity due to the reduction of the ^{39}Ar background content has been discussed. Similarly, a preliminary sensitivity curve for a yet to be defined far future liquid argon experiment capable of collecting an exposure between 1000-3000 tonne year has been determined. This study suggests that cross sections down to 10^{-48} cm^2 could be explored at 1 TeV WIMP mass, reaching the "ultimate limit" of dark matter searches and becoming the most sensitive DM experiment ever proposed.

At these exposures, the sensitivity will be strongly affected by the irreducible CEnNS background. In these optics, it is of utmost importance to find a way to distinguish a neutrino from a WIMP interaction. One possible avenue would be offered by the presence of the signature of columnar recombination in nuclear recoils using a liquid argon TPC. The latter can provide information on the incident direction of the incoming particle. Since WIMPs are expected to come preferentially from the Cygnus constellation, this technique would greatly help in disentangling WIMP signal from background.
In chapter six, the potentiality of a directional tonne-scale DM detector located at LNGS has been illustrated. In particular, it has been derived that the expected event rate varies by a large factor $(4-8)$ when considering nuclear recoil directions going from the zenith to the horizon and, at fixed angular direction, it varies by about the same factor with a sidereal-day periodicity. With a likelihood-ratio based statistical approach it has been shown that, using the angular information alone, 100 (250) events are sufficient to reject the hypothesis of an isotropic background at 3σ level considering an ideal (realistic) angular resolution. All these studies corroborated the motivation for the construction of a small prototype dual-phase TPC called RED, which is part of the DarkSide program and currently in his commissioning phase, that aims to prove the directional sensitivity using a beam of neutrons. This study confirms that the development of experimental technologies able to couple directional sensitivity with large fiducial masses (many tonnes) and the ability to collect large exposures free of background from β/γ events and neutron-induced nuclear recoils is a priority for future dark matter detectors.

While waiting for a technique able to remove the irreducible CEnNS background, it is essential to constrain more precisely the expected number of CEnNS, since the WIMP sensitivity depends crucially on it. The uncertainty on the prediction of the CEnNS scattering cross section affects significantly the number of expected

CEnNS events and it is dominated by the nuclear form factor parametrization. Since neutrinos couple preferentially with neutrons, the lack of knowledge of the neutron distribution, or better of the neutron distribution radius, plays a fundamental role. In this contest, the first experimental observation made in 2017 by the COHERENT Collaboration of a CEnNS process, provides a valuable occasion to experimentally constrain for the first time the CEnNS phenomenology. Analysing the COHERENT data, the first determination of the average neutron radius of ^{133}Cs and ^{127}I has been obtained, as explained in the seventh chapter. The practically model-independent value of $R_n = 5.5^{+0.9}_{-1.1}$ fm has been derived. Moreover, the COHERENT data show a 2.3σ evidence of the nuclear structure suppression of the full coherence. The difference between the neutron and proton rms radii, known as the "neutron skin", has also been derived, giving $R_n - R_p \simeq 0.7^{+0.9}_{-1.1}$ fm. Even if the uncertainty is considerable, the best-fit value indicates the possibility of a neutron skin larger than the model-predicted values which lie between about 0.1 and 0.3 fm. This study has many consequences for nuclear physics models and implications for the equation of state of neutron stars.

To conclude, all the studies carried out in this thesis project have significant impact for the development and the understanding of future argon dark matter detectors. The outcome of these studies represents a fundamental part of the DarkSide-20k proposal and it is of remarkable importance also for fields outside the dark matter one.

A

Derivation of the SM coherent ν-nucleus cross sections

The CEnNS reactions (Fig. A.1) that take place in nuclei are represented by

$$\nu_\alpha(\tilde{\nu}_\alpha) + (A, Z) \rightarrow \nu_\alpha(\tilde{\nu}_\alpha) + (A, Z)\,, \tag{A.1}$$

where $\alpha = e, \mu, \tau$.

The effective (quark-level) SM ν-nucleus interaction Lagrangian, $\mathcal{L}_{\rm SM}$, at low and intermediate neutrino energies can be written as [445]

$$\mathcal{L}_{\rm SM} = -2\sqrt{2}G_f \sum_{\substack{f=u,d \\ \alpha=e,\mu,\tau}} g_P^f \left[\bar{\nu}_\alpha \gamma_\rho L \nu_\alpha\right] \left[\bar{f}\gamma^\rho P f\right]\,, \tag{A.2}$$

where $g_L^u = \frac{1}{2} - \frac{2}{3}\sin^2\theta_w$ and $g_R^u = -\frac{2}{3}\sin^2\theta_w$ are the left- and right-handed couplings of the u-quark to the Z-boson and $g_L^d = -\frac{1}{2} + \frac{1}{3}\sin^2\theta_w$, $g_R^d = \frac{1}{3}\sin^2\theta_w$ are the corresponding couplings of the d-quark and θ_w is the Weinberg mixing angle [480].

For coherent ν-nucleus scattering, the SM angle-differential cross section reads

$$\frac{d\sigma_{{\rm SM},\nu_\alpha}}{d\cos\theta} = \frac{G_f^2}{2\pi} E_\nu^2 \left(1 + \cos\theta\right) \left|\langle gs||\hat{\mathcal{M}}_0(q)||gs\rangle\right|^2\,. \tag{A.3}$$

The operator $\hat{\mathcal{M}}_0$ in the nuclear matrix element of the latter equation is the Coulomb operator which is equal to the product of the zero-order spherical Bessel function times the zero-order spherical harmonic [481, 480]. This matrix element can be cast in the form [482]

$$\left|\mathcal{M}^{\rm SM}_{V,\nu_\alpha}\right|^2 \equiv \left|\langle gs||\hat{\mathcal{M}}_0(q)||gs\rangle\right|^2 = \left[g_V^p Z F_Z(q^2) + g_V^n N F_N(q^2)\right]^2\,, \tag{A.4}$$

where, the polar-vector couplings of protons g_V^p and neutrons g_V^n with the Z boson are written as $g_V^p = 2(g_L^u + g_R^u) + (g_L^d + g_R^d) = \frac{1}{2} - 2\sin^2\theta_w$ and $g_V^n = (g_L^u + g_R^u) + 2(g_L^d + g_R^d) = -\frac{1}{2}$, respectively. As it can be easily seen, the vector

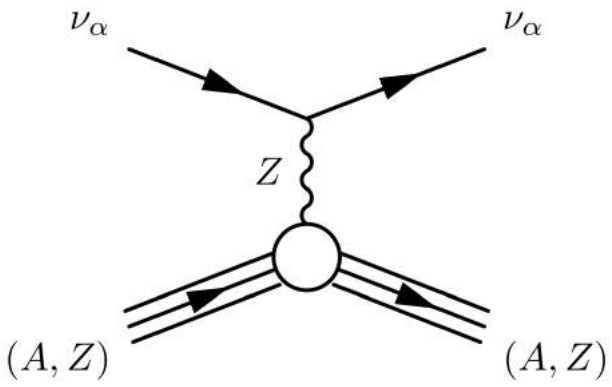

Fig. A.1.: Effective Feynman diagram contributing to coherent neutrino-nucleus scattering within the SM.

contribution of all protons is very small ($g_V^p \sim 0.04$), hence the coherence in Eq. A.4 essentially refers to all neutrons only of the studied nucleus. After some straightforward elaboration the differential cross section with respect to the nuclear recoil energy, E_r, takes the form

$$\frac{d\sigma_{\mathrm{SM},\nu_\alpha}}{dE_r} = \frac{G_f^2\, m_N}{\pi}\left(1 - \frac{m_N\, E_r}{2E_\nu^2}\right)\left|\langle gs||\hat{\mathcal{M}}_0(q)||gs\rangle\right|^2 . \tag{A.5}$$

Bibliography

[1] M. Cadeddu, C. Giunti, Y. F. Li, and Y. Y. Zhang. "Average CsI neutron density distribution from COHERENT data". In: *Phys. Rev. Lett.* 120.7 (2018), p. 072501. arXiv: 1710.02730 [hep-ph] (cit. on pp. 5, 48, 193, 211).

[2] M. Cadeddu and Emmanuele Picciau. "Impact of neutrino background prediction for next generation dark matter xenon detector". In: *J. Phys. Conf. Ser.* 956.1 (2018), p. 012014 (cit. on p. 5).

[3] C. E. Aalseth et al. "DarkSide-20k: A 20 Tonne Two-Phase LAr TPC for Direct Dark Matter Detection at LNGS". In: *Arxiv:1707.08145 (Accepted by European Physical Journal Plus)* (2017). arXiv: 1707.08145 [physics.ins-det] (cit. on pp. 5, 73, 80, 82, 85, 164, 165, 167).

[4] V. Cataudella, A.. de Candia, G.. De Filippis, et al. "Directional modulation of electron-ion pairs recombination in liquid argon". In: *JINST* 12.12 (2017), P12002 (cit. on pp. 5, 166).

[5] M. Cadeddu et al. "Recoil Directionality Studies in Two-Phase Liquid Argon TPC Detectors". In: *EPJ Web Conf.* 164.07036 (2017) (cit. on p. 5).

[6] M. Cadeddu et al. "Potential for an argon directional dark matter detector". In: *Arxiv:1704.03741 (to be submitted to JHEP)* (2017). arXiv: 1704.03741 [astro-ph.CO] (cit. on p. 5).

[7] Giuliana Fiorillo and Matteo Cadeddu. *Directionality in Dark Matter search*. Vol. NOW2016. 2017, p. 091 (cit. on p. 5).

[8] M. Cadeddu. "Dark Matter search with directional sensitivity". In: *Nuovo Cim.* C40.1 (2017), p. 66 (cit. on p. 5).

[9] Matteo Cadeddu. *A directional Dark Matter argon detector at LNGS*. Vol. 689. 1. 2016, p. 012015 (cit. on p. 5).

[10] P. Agnes et al. "Results from the first use of low radioactivity argon in a dark matter search". In: *Phys. Rev.* D93.8 (2016). [Addendum: Phys. Rev. D 95, no. 6, 069901 (2017)], p. 081101. arXiv: 1510.00702 [astro-ph.CO] (cit. on pp. 5, 80).

[11] P. Agnes et al. “The veto system of the DarkSide-50 experiment”. In: *JINST* 11.03 (2016), P03016. arXiv: 1512.07896 [physics.ins-det] (cit. on p. 5).

[12] P. Agnes et al. “The Electronics and Data Acquisition System for the DarkSide-50 Veto Detectors”. In: *JINST* 11.12 (2016), P12007. arXiv: 1606.03316 [physics.ins-det] (cit. on p. 5).

[13] P. Agnes et al. “Simulation of argon response and light detection in the DarkSide-50 dual phase TPC”. In: *JINST* 12.10 (2017), P10015. arXiv: 1707.05630 [physics.ins-det] (cit. on p. 5).

[14] P. Agnes et al. “Effect of Low Electric Fields on Alpha Scintillation Light Yield in Liquid Argon”. In: *JINST* 12.01 (2017), P01021. arXiv: 1611.00241 [physics.ins-det] (cit. on p. 5).

[15] P. Agnes et al. “CALIS - a CALibration Insertion System for the DarkSide-50 dark matter search experiment”. In: *JINST no. 12 T12004* (2016). arXiv: 1611.02750 [physics.ins-det] (cit. on p. 5).

[16] C. E. Aalseth et al. “Cryogenic Characterization of FBK RGB-HD SiPMs”. In: *JINST* 12.09 (2017), P09030. arXiv: 1705.07028 [physics.ins-det] (cit. on p. 5).

[17] F Zwicky. In: *Helv. Phys. Acta.* 6 (1933), pp. 110–127 (cit. on p. 10).

[18] J. S. Sanders, A. C. Fabian, E. Churazov, et al. “Linear Structures in the Core of the Coma Cluster of Galaxies”. In: *Science* 341.6152 (Sept. 2013), pp. 1365–1368. arXiv: 1309.4866 (cit. on p. 10).

[19] R. Fusco-Femiano and John P. Hughes. “Nonpolytropic model for the Coma Cluster”. In: *Astrophys. J.* 429 (July 1994), pp. 545+ (cit. on p. 10).

[20] Nobuyoshi Makino. “Maximum radial extension of the Coma cluster”. In: *Publ. Astron. Soc. Jpn.* 46.2 (1994), pp. 139–146 (cit. on p. 10).

[21] K.G. Begeman, A.H. Broeils, and R.H. Sanders. “Extended rotation curves of spiral galaxies: Dark haloes and modified dynamics”. In: *Mon. Not. R. Astron. Soc.* 249 (1991), p. 523 (cit. on pp. 11, 33).

[22] M. Persic, P. Salucci, and F. Stel. “The universal rotation curve of spiral galaxies – I. The dark matter connection”. In: *Mon. Not. R. Astron. Soc.* 281.1 (July 1996), pp. 27–47. eprint: astro-ph/9506004 (cit. on p. 11).

[23] A. Bosma. “21-cm line studies of spiral galaxies. I - Observations of the galaxies NGC 5033, 3198, 5055, 2841, and 7331. II - The distribution and kinematics of neutral hydrogen in spiral galaxies of various morphological types”. In: *Astron. J.* 86 (Dec. 1981), pp. 1791+ (cit. on p. 11).

[24] A. Bosma. “21-cm line studies of spiral galaxies. II. The distribution and kinematics of neutral hydrogen in spiral galaxies of various morphological types.” In: *Astron. J.* 86 (Dec. 1981), pp. 1825+ (cit. on p. 11).

[25] Julio F. Navarro, Carlos S. Frenk, and Simon D. M. White. “The Structure of Cold Dark Matter Halos”. In: *Astrophys. J.* 462 (May 1996), pp. 563+. eprint: astro-ph/9508025 (cit. on pp. 11, 19).

[26] A. J. Deason, V. Belokurov, N. W. Evans, and J. An. “Broken degeneracies: the rotation curve and velocity anisotropy of the Milky Way halo: Broken degeneracies”. In: *Mon. Not. R. Astron. Soc.: Lett.* 424.1 (July 2012), pp. L44–L48. arXiv: 1204.5189 (cit. on p. 11).

[27] Martín López-Corredoira. “Milky Way rotation curve from proper motions of red clump giants”. In: *Astron. Astrophys.* 563 (Mar. 2014), A128+. arXiv: 1402.3551 (cit. on p. 11).

[28] Pijushpani Bhattacharjee, Soumini Chaudhury, and Susmita Kundu. “Rotation curve of the Milky way out to $\sim$ 200 kpc”. In: *Astrophys. J.* 785.1 (Apr. 2014), pp. 63+. arXiv: 1310.2659 (cit. on p. 11).

[29] Euaggelos E. Zotos. “Classifying orbits in galaxy models with a prolate or an oblate dark matter halo component”. In: *Astron. Astrophys.* 563 (2014), A19. arXiv: 1404.4194 [astro-ph.GA] (cit. on p. 12).

[30] Adam G. Riess, Alexei V. Filippenko, Peter Challis, et al. “Observational Evidence from Supernovae for an Accelerating Universe and a Cosmological Constant”. In: *Astrophys. J.* 116.3 (Sept. 1998), pp. 1009–1038. eprint: astro-ph/9805201 (cit. on p. 15).

[31] S. Perlmutter, G. Aldering, G. Goldhaber, et al. “Measurements of and from 42 High-Redshift Supernovae”. In: *Astrophys. J.* 517.2 (June 1999), pp. 565–586. eprint: astro-ph/9812133 (cit. on p. 15).

[32] Edward W. Kolb and Michael S. Turner. *The Early Universe*. Reading, Massachusetts: Addison-Wesley, Feb. 1990. Chap. 9 (cit. on pp. 15, 24).

[33] George R. Blumenthal, S. M. Faber, Joel R. Primack, and Martin J. Rees. “Formation of galaxies and large-scale structure with cold dark matter”. In: *Nature* 311.5986 (Oct. 1984), pp. 517–525 (cit. on p. 15).

[34] P. A. R. Ade et al. “Planck 2015 results. XIII. Cosmological parameters”. In: *Astron. Astrophys.* 594 (2016), A13. arXiv: 1502.01589 [astro-ph.CO] (cit. on pp. 15–17, 26).

[35] G. Hinshaw, D. Larson, E. Komatsu, et al. “Nine-year Wilkinson Microwave Anisotropy Probe (WMAP) Observations: Cosmological Parameter Results”. In: *Astrophys. J. Suppl. Ser.* 208.2 (Oct. 2013), pp. 19+ (cit. on p. 15).

[36] Kyle S. Dawson, David J. Schlegel, Christopher P. Ahn, et al. “The Baryon Oscillation Spectroscopic Survey of SDSS-III”. In: *Astron. J.* 145.1 (Jan. 2013), pp. 10+ (cit. on p. 15).

[37] T. D. Kitching, A. F. Heavens, J. Alsing, et al. “3D Cosmic Shear: Cosmology from CFHTLenS”. In: (Jan. 2014). arXiv: 1401.6842 (cit. on p. 15).

[38] Liping Fu, Martin Kilbinger, Thomas Erben, et al. “CFHTLenS: Cosmological constraints from a combination of cosmic shear two-point and three-point correlations”. In: (Apr. 2014). arXiv: 1404.5469 (cit. on p. 15).

[39] Will J. Percival, Carlton M. Baugh, Joss Bland-Hawthorn, et al. “The 2dF Galaxy Redshift Survey: the power spectrum and the matter content of the Universe”. In: *Mon. Not. R. Astron. Soc.* 327.4 (Nov. 2001), pp. 1297–1306 (cit. on p. 15).

[40] Donald G. York, J. Adelman, John E. Anderson, et al. “The Sloan Digital Sky Survey: Technical Summary”. In: *Astron. J.* 120 (Sept. 2000), pp. 1579–1587. eprint: astro-ph/0006396 (cit. on p. 15).

[41] N. Suzuki, D. Rubin, C. Lidman, et al. “The Hubble Space Telescope Cluster Supernova Survey: V. Improving the Dark Energy Constraints Above z>1 and Building an Early-Type-Hosted Supernova Sample”. In: *Astrophys. J.* 746.1 (May 2011), pp. 85+. arXiv: 1105.3470 (cit. on p. 15).

[42] Pol Mollitor, Emmanuel Nezri, and Romain Teyssier. “Baryonic and dark matter distribution in cosmological simulations of spiral galaxies”. In: (May 2014). arXiv: 1405.4318 (cit. on p. 18).

[43] M. Vogelsberger, S. Genel, V. Springel, et al. “Properties of galaxies reproduced by a hydrodynamic simulation”. In: *Nature* 509.7499 (May 2014), pp. 177–182. arXiv: 1405.1418 (cit. on p. 18).

[44] M. Vogelsberger, S. Genel, D. Sijacki, et al. “A model for cosmological simulations of galaxy formation physics”. In: *Mon. Not. R. Astron. Soc.* 436.4 (Oct. 2013), pp. 3031–3067. arXiv: 1305.2913 (cit. on p. 18).

[45] Volker Springel, Simon D. M. White, Adrian Jenkins, et al. “Simulations of the formation, evolution and clustering of galaxies and quasars”. In: *Nature* 435.7042 (June 2005), pp. 629–636. eprint: astro-ph/0504097 (cit. on p. 18).

[46] V. Springel, J. Wang, M. Vogelsberger, et al. “The Aquarius Project: the subhaloes of galactic haloes”. In: *Mon. Not. R. Astron. Soc.* 391.4 (Dec. 2008), pp. 1685–1711. arXiv: 0809.0898 (cit. on p. 19).

[47] G Kauffmann, Simon D.M. White, and B. Guiderdoni. “The Formation and Evolution of Galaxies Within Merging Dark Matter Haloes”. In: *Mon. Not. R. Astron. Soc.* 264 (1993), p. 201 (cit. on p. 19).

[48] Matthew G. Walker, Mario Mateo, Edward W. Olszewski, et al. “A Universal Mass Profile for Dwarf Spheroidal Galaxies?” In: *Astrophys. J.* 704.2 (Oct. 2009), pp. 1274+ (cit. on p. 19).

[49] V. Belokurov, M. G. Walker, N. W. Evans, et al. “Big Fish, Little Fish: Two New Ultra-faint Satellites of the Milky Way”. In: *Astrophys. J. Lett.* 712.1 (Mar. 2010), pp. L103–L106. arXiv: 1002.0504 (cit. on p. 19).

[50] Anatoly Klypin, Andrey V. Kravtsov, Octavio Valenzuela, and Francisco Prada. “Where Are the Missing Galactic Satellites?” In: *Astrophys. J.* 522.1 (Sept. 1999), pp. 82–92 (cit. on p. 19).

[51] Stacy Y. Kim, Annika H. G. Peter, and Jonathan R. Hargis. “There is No Missing Satellites Problem”. In: (2017). arXiv: 1711.06267 [astro-ph.CO] (cit. on p. 19).

[52] Michael Boylan-Kolchin, James S. Bullock, and Manoj Kaplinghat. “Too big to fail? The puzzling darkness of massive Milky Way subhaloes”. In: *Mon. Not. R. Astron. Soc. Lett.* 415.1 (May 2011), pp. L40–L44. arXiv: 1103.0007 (cit. on p. 19).

[53] Shea Garrison-Kimmel, Michael Boylan-Kolchin, James S. Bullock, and Evan N. Kirby. “Too Big to Fail in the Local Group”. In: (Apr. 2014). arXiv: 1404.5313 (cit. on p. 19).

[54] W. J. G. de Blok. “The Core-Cusp Problem”. In: *Adv. Astron.* 2010.1-2 (Oct. 2010), pp. 1–14. arXiv: 0910.3538 (cit. on p. 19).

[55] John Dubinski and R. G. Carlberg. “The structure of cold dark matter halos”. In: *Astrophys. J.* 378 (Sept. 1991), pp. 496+ (cit. on p. 19).

[56] Paolo Salucci. “The constant-density region of the dark haloes of spiral galaxies”. In: *Mon. Not. R. Astron. Soc.* 320.1 (Jan. 2001), pp. L1–L5 (cit. on p. 19).

[57] Fiorenza Donato, Gianfranco Gentile, and Paolo Salucci. “Cores of dark matter haloes correlate with stellar scalelengths”. In: *Mon. Not. R. Astron. Soc.* 353.2 (Sept. 2004), pp. L17–L22. eprint: astro-ph/0403206 (cit. on p. 19).

[58] E. Hayashi, J. F. Navarro, C. Power, et al. “The inner structure of ΛCDM haloes – II. Halo mass profiles and low surface brightness galaxy rotation curves”. In: *Mon. Not. R. Astron. Soc.* 355.3 (Dec. 2004), pp. 794–812. eprint: astro-ph/0310576 (cit. on p. 19).

[59] Matthias Gritschneder and Douglas N. C. Lin. “Explaining the Observed Velocity Dispersion of Dwarf Galaxies by Baryonic Mass Loss during the First Collapse”. In: *Astrophys. J.* 765.1 (Mar. 2013), pp. 38+ (cit. on p. 20).

[60] N. C. Amorisco, J. Zavala, and T. J. L. de Boer. “DARK MATTER CORES IN THE FORNAX AND SCULPTOR DWARF GALAXIES: JOINING HALO ASSEMBLY AND DETAILED STAR FORMATION HISTORIES”. In: *Astrophys. J.* 782.2 (Feb. 2014), pp. L39+. arXiv: 1309.5958 (cit. on p. 20).

[61] A. Del Popolo, J. A. S. Lima, Julio C. Fabris, and Davi C. Rodrigues. “A unified solution to the small scale problems of the ΛCDM model”. In: (Apr. 2014). arXiv: 1404.3674 (cit. on p. 20).

[62] B. Moore, T. Quinn, F. Governato, J. Stadel, and G. Lake. “Cold collapse and the core catastrophe”. In: *Mon. Not. R. Astron. Soc.* 310.4 (Dec. 1999), pp. 1147–1152. eprint: astro-ph/9903164 (cit. on p. 20).

[63] Paul Bode, Jeremiah P. Ostriker, and Neil Turok. “Halo Formation in Warm Dark Matter Models”. In: *Astrophys. J.* 556.1 (May 2001), pp. 93–107. eprint: astro-ph/0010389 (cit. on p. 20).

[64] Andrea V. Macciò and Fabio Fontanot. “How cold is dark matter? Constraints from Milky Way satellites”. In: *Mon. Not. R. Astron. Soc. Lett.* 404.1 (May 2010), pp. L16–L20 (cit. on p. 20).

[65] A. De Rújula, S. L. Glashow, and Uri Sarid. “Charged dark matter”. In: *Nucl. Phys. B* 333.1 (Mar. 1990), pp. 173–194 (cit. on p. 20).

[66] Atsushi Kudo and Masahiro Yamaguchi. “Inflation with low reheat temperature and cosmological constraint on stable charged massive particles”. In: *Phys. Lett. B* 516.1-2 (Sept. 2001), pp. 151–155 (cit. on p. 20).

[67] T. Hemmick, D. Elmore, T. Gentile, et al. “Search for low-Z nuclei containing massive stable particles”. In: *Phys. Rev. D* 41.7 (Apr. 1990), pp. 2074–2080 (cit. on p. 20).

[68] Martin L. Perl, Peter C. Kim, Valerie Halyo, et al. “The Search for Stable, Massive, Elementary Particles”. In: *Int. J. Mod. Phys. A* 16.12 (Feb. 2001), pp. 2137–2164. eprint: hep-ex/0102033 (cit. on p. 20).

[69] S. N. Gninenko, N. V. Krasnikov, and A. Rubbia. “Search for millicharged particles in reactor neutrino experiments: a probe of the PVLAS anomaly”. In: *Phys. Rev. D* 75.7 (Mar. 2007), p. 075014. eprint: hep-ph/0612203 (cit. on p. 20).

[70] Alessandro Melchiorri, Antonello Polosa, and Alessandro Strumia. “New bounds on millicharged particles from cosmology”. In: *Phys. Lett. B* 650.5-6 (May 2007), pp. 416–420. eprint: hep-ph/0703144 (cit. on p. 20).

[71] Priyamvada Natarajan, Abraham Loeb, Jean-Paul Kneib, and Ian Smail. “Constraints on the Collisional Nature of the Dark Matter from Gravitational Lensing in the Cluster A2218”. In: *Astrophys. J.* 580.1 (Oct. 2002), pp. L17–L20. eprint: astro-ph/0207045 (cit. on p. 20).

[72] Xuelei Chen, Steen Hannestad, and Robert J. Scherrer. “Cosmic microwave background and large scale structure limits on the interaction between dark matter and baryons”. In: *Phys. Rev. D* 65.12 (Apr. 2002), p. 123515. eprint: astro-ph/0202496 (cit. on p. 21).

[73] Santiago D. L. Amigo, William M. Cheung, Zhiqi Huang, and Siew-Phang Ng. “Cosmological constraints on decaying dark matter”. In: *J. Cosmol. Astropart. Phys.* 2009.06 (June 2009), p. 005. arXiv: 0812.4016 (cit. on p. 21).

[74] Nicole F. Bell, Ahmad J. Galea, and Kalliopi Petraki. “Lifetime Constraints for Late Dark Matter Decay”. In: *Phys. Rev. D* 82.2 (July 2010), p. 023514. arXiv: 1004.1008 (cit. on p. 21).

[75] Daniel Feldman, Zuowei Liu, Pran Nath, and Gregory Peim. “Multicomponent dark matter in supersymmetric hidden sector extensions”. In: *Phys. Rev. D* 81.9 (May 2010), p. 095017. arXiv: 1004.0649 (cit. on p. 21).

[76] David Tytler, John M. O’Meara, Nao Suzuki, and Dan Lubin. “Review of Big Bang Nucleosynthesis and Primordial Abundances”. In: *Physica Scripta* T85.1 (Jan. 2000), pp. 12+. eprint: astro-ph/0001318 (cit. on p. 21).

[77] Brian Fields and Subir Sarkar. “Big-Bang nucleosynthesis (Particle Data Group mini-review)”. In: *J. Phys. G.* 33.1 (Oct. 2006), pp. 1–1232. eprint: astro-ph/0601514 (cit. on p. 21).

[78] Michele Maggiore. “Gravitational Wave Experiments and Early Universe Cosmology”. In: *Phys. Rep.* 331.6 (Feb. 2000), pp. 283–367. eprint: gr-qc/9909001 (cit. on p. 22).

[79] Richard H. Cyburt, Brian D. Fields, Keith A. Olive, and Evan Skillman. “New BBN limits on Physics Beyond the Standard Model from He4”. In: *J. Astropart. Phys.* 23.3 (Aug. 2005), pp. 313–323. eprint: astro-ph/0408033 (cit. on p. 22).

[80] Karsten Jedamzik. “Big Bang Nucleosynthesis Constraints on Hadronically and Electromagnetically Decaying Relic Neutral Particles”. In: *Phys. Rev. D* 74.10 (Nov. 2006), p. 103509. eprint: hep-ph/0604251 (cit. on p. 22).

[81] J. R. Bond and A. S. Szalay. “The collisionless damping of density fluctuations in an expanding universe”. In: *Astrophys. J.* 274 (Nov. 1983), pp. 443–468 (cit. on p. 22).

[82] D. Boyanovsky, H. J. de Vega, and N. Sanchez. “The dark matter transfer function: free streaming, particle statistics and memory of gravitational clustering”. In: *Phys. Rev. D* 78.6 (Sept. 2008), p. 063546. arXiv: 0807.0622 (cit. on p. 22).

[83] Olivier Wantz and E. P. S. Shellard. “Axion Cosmology Revisited”. In: *Phys. Rev. D* 82.12 (Feb. 2011), p. 123508. arXiv: 0910.1066 (cit. on p. 22).

[84] Vijay K. Narayanan, David N. Spergel, Romeel Davé, and Chung-Pei Ma. “Constraints on the Mass of Warm Dark Matter Particles and the Shape of the Linear Power Spectrum from the L[CLC]y[/CLC] Forest”. In: *The Astrophysical Journal* 543.2 (Nov. 2000), pp. L103–L106. eprint: astro-ph/0005095 (cit. on p. 22).

[85] Kevork Abazajian, Eric R. Switzer, Scott Dodelson, Katrin Heitmann, and Salman Habib. “The Nonlinear Cosmological Matter Power Spectrum with Massive Neutrinos I: The Halo Model”. In: *Phys. Rev. D* 71.4 (Feb. 2005), p. 043507. eprint: astro-ph/0411552 (cit. on p. 23).

[86] Roland de Putter, Olga Mena, Elena Giusarma, et al. “NEW NEUTRINO MASS BOUNDS FROM SDSS-III DATA RELEASE 8 PHOTOMETRIC LUMINOUS GALAXIES”. In: *Astrophys. J.* 761.1 (Dec. 2012), pp. 12+. arXiv: 1201.1909 (cit. on p. 23).

[87] Jason Kumar, Jonathan L. Feng, George Alverson, Pran Nath, and Brent Nelson. “WIMPless Dark Matter”. In: *AIP Conf. Proc.* 1200 (Sept. 2010), pp. 1059–1062. arXiv: 0909.2877 (cit. on p. 23).

[88] S. W. Hawking. “Gravitationally collapsed objects of very low mass”. In: *Mon. Not. R. Astron. Soc.* 152 (1971), p. 75 (cit. on p. 23).

[89] R. Foot. “Mirror dark matter: Cosmology, galaxy structure and direct detection”. In: *Int. J. Mod. Phys. A* 29.11n12 (Apr. 2014), pp. 1430013+. arXiv: 1401.3965 (cit. on p. 23).

[90] Andreas Birkedal, Andrew Noble, Maxim Perelstein, and Andrew Spray. "Little Higgs dark matter". In: *Phys. Rev. D* 74.3 (Aug. 2006), p. 035002. eprint: hep-ph/0603077 (cit. on p. 23).

[91] Marco Cirelli, Nicolao Fornengo, and Alessandro Strumia. "Minimal Dark Matter". In: *Nucl. Phys. B* 753.1-2 (July 2007), pp. 178–194. eprint: hep-ph/0512090 (cit. on p. 23).

[92] Gerard Jungman, Marc Kamionkowski, and Kim Griest. "Supersymmetric Dark Matter". In: *Phys. Rep.* 267.5-6 (June 1995), pp. 195–373. eprint: hep-ph/9506380 (cit. on pp. 23, 38, 40, 69).

[93] Gordon L. Kane and Stephen P. Martin. "A Supersymmetry Primer". In: *Perspectives on Supersymmetry II*. Vol. 21. Singapore: World Scientific, Sept. 2011, pp. 1–153. eprint: hep-ph/9709356 (cit. on p. 23).

[94] G. Gelmini and P. Gondolo. "DM production mechanisms". In: *Particle Dark Matter*. Ed. by Gianfranco Bertone. Cambridge: Cambridge University Press, Sept. 2010. Chap. 7, pp. 121–141. arXiv: 1009.3690 (cit. on p. 24).

[95] Kim Griest. "Three exceptions in the calculation of relic abundances". In: *Phys. Rev. D* 43.10 (May 1991), pp. 3191–3203 (cit. on p. 24).

[96] John Ellis, J. S. Hagelin, D. V. Nanopoulos, K. Olive, and M. Srednicki. "Supersymmetric relics from the big bang". In: *Nucl. Phys. B* 238.2 (June 1984), pp. 453–476 (cit. on p. 24).

[97] Bibhushan Shakya. "The Status of Neutralino Dark Matter". In: (Dec. 2013). arXiv: 1312.7505 (cit. on p. 25).

[98] Ki-Young Choi and Osamu Seto. "Light Dirac right-handed sneutrino dark matter". In: *Phys. Rev. D* 88.3 (Aug. 2013), p. 035005. arXiv: 1305.4322 (cit. on p. 25).

[99] Frank D. Steffen. "Gravitino Dark Matter and Cosmological Constraints". In: *J. Cosmol. Astropart. Phys.* 2006.09 (Sept. 2006), p. 001. eprint: hep-ph/0605306 (cit. on p. 25).

[100] M. J. Duff. "Kaluza-Klein Theory in Perspective". In: (Oct. 1994). eprint: hep-th/9410046 (cit. on p. 25).

[101] Thomas Appelquist, Hsin-Chia Cheng, and Bogdan A. Dobrescu. "Bounds on Universal Extra Dimensions". In: *Phys. Rev. D* 64.3 (June 2001), p. 035002. eprint: hep-ph/0012100 (cit. on p. 25).

[102] Hsin-Chia Cheng, Konstantin T. Matchev, and Martin Schmaltz. "Radiative Corrections to Kaluza-Klein Masses". In: *Phys. Rev. D* 66.3 (Apr. 2002), p. 036005. eprint: hep-ph/0204342 (cit. on p. 25).

[103] Geraldine Servant and Tim M. P. Tait. "Is the Lightest Kaluza-Klein Particle a Viable Dark Matter Candidate?" In: *Nucl. Phys. B* 650.1-2 (Sept. 2002), pp. 391–419. eprint: hep-ph/0206071 (cit. on p. 25).

[104] Lars Bergström. “Dark matter candidates”. In: *New Journal of Physics* 11.10 (Oct. 2009), pp. 105006+. arXiv: 0903.4849 (cit. on p. 25).

[105] Steen H. Hansen, Julien Lesgourgues, Sergio Pastor, and Joseph Silk. “Constraining the window on sterile neutrinos as warm dark matter”. In: *Mon. Not. R. Astron. Soc.* 333.3 (Feb. 2002), pp. 544–546. eprint: astro-ph/0106108 (cit. on p. 26).

[106] Kevork Abazajian and Savvas M. Koushiappas. “Constraints on Sterile Neutrino Dark Matter”. In: *Phys. Rev. D* 74.2 (July 2006), p. 023527. eprint: astro-ph/0605271 (cit. on p. 26).

[107] Xiangdong Shi and George M. Fuller. “A New Dark Matter Candidate: Nonthermal Sterile Neutrinos”. In: *Phys. Rev. Lett.* 82.14 (Apr. 1999), pp. 2832–2835. eprint: astro-ph/9810076 (cit. on p. 26).

[108] R. D. Peccei and Helen R. Quinn. “CP Conservation in the Presence of Pseudoparticles”. In: *Phys. Rev. Lett.* 38.25 (June 1977), pp. 1440–1443 (cit. on p. 27).

[109] P. Sikivie and Q. Yang. “Bose-Einstein Condensation of Dark Matter Axions”. In: *Phys. Rev. Lett.* 103.11 (Sept. 2009), p. 111301. arXiv: 0901.1106 (cit. on p. 27).

[110] Georg Raffelt. “AXIONS IN ASTROPHYSICS AND COSMOLOGY”. In: (Mar. 1995). eprint: hep-ph/9502358 (cit. on p. 27).

[111] Peter W. Graham, Igor G. Irastorza, Steven K. Lamoreaux, Axel Lindner, and Karl A. van Bibber. “Experimental Searches for the Axion and Axion-Like Particles”. In: *Ann. Rev. Nucl. Part. Sci.* 65 (2015), pp. 485–514. arXiv: 1602.00039 [hep-ex] (cit. on p. 27).

[112] M. Arik, S. Aune, K. Barth, et al. “CAST solar axion search with $3^{H}ebuffergas : Closingthehotdarkmattergap$”. In: *Phys. Rev. Lett.* 112.9 (July 2013), p. 091302. arXiv: 1307.1985 (cit. on p. 27).

[113] Asimina Arvanitaki, Savas Dimopoulos, Sergei Dubovsky, Nemanja Kaloper, and John March-Russell. “String axiverse”. In: *Phys. Rev. D* 81.12 (June 2010), p. 123530. arXiv: 0905.4720 (cit. on p. 27).

[114] Lisa Edelhäuser, Thomas Flacke, and Michael Krämer. “Constraints on models with universal extra dimensions from dilepton searches at the LHC”. In: *J. High Energy Phys.* 2013.8 (Aug. 2013). arXiv: 1302.6076 (cit. on p. 28).

[115] Takuya Kakuda, Kenji Nishiwaki, Kin-ya Oda, Naoya Okuda, and Ryoutaro Watanabe. “Phenomenological constraints on universal extra dimensions at LHC and electroweak precision test”. In: (Apr. 2013). arXiv: 1304.6362 (cit. on p. 28).

[116] ATLAS Collaboration. https://atlas.web.cern.ch/Atlas/GROUPS/PHYSICS/CombinedSummaryPlots/SUSY/ATLAS_SUSY_Summary/ATLAS_SUSY_Summary.pdf. 2017 (cit. on p. 29).

[117] CMS Collaboration. https://twiki.cern.ch/twiki/pub/CMSPublic/PhysicsResultsSUS/Moriond2017_BarPlot.pdf. 2013 (cit. on p. 29).

[118] Hao Zhang, Qing-Hong Cao, Chuan-Ren Chen, and Chong S. Li. “Effective Dark Matter Model: Relic density, CDMS II, Fermi LAT and LHC”. In: *J. High Energy Physics* 2011.8 (Aug. 2011). arXiv: 0912.4511 (cit. on p. 29).

[119] Ning Zhou, David Berge, and Daniel Whiteson. “Mono-everything: Combined limits on dark matter production at colliders from multiple final states”. In: *Phys. Rev. D* 87.9 (May 2013), p. 095013. arXiv: 1302.3619 (cit. on p. 29).

[120] Patrick J. Fox, Roni Harnik, Joachim Kopp, and Yuhsin Tsai. “Missing Energy Signatures of Dark Matter at the LHC”. In: *Phys. Rev. D* 85.5 (Sept. 2011), pp. 056011+. arXiv: 1109.4398 (cit. on p. 29).

[121] Howard Baer, Eun-Kyung Park, and Xerxes Tata. “Collider, direct and indirect detection of supersymmetric dark matter”. In: *New J. Phys.* 11.10 (Oct. 2009), pp. 105024+. arXiv: 0903.0555 (cit. on p. 29).

[122] O. Buchmueller, Matthew J. Dolan, and Christopher McCabe. “Beyond effective field theory for dark matter searches at the LHC”. In: *J. High Energy Phys.* 2014.1 (Jan. 2014). arXiv: 1308.6799 (cit. on p. 29).

[123] Giorgio Busoni, Andrea De Simone, Enrico Morgante, and Antonio Riotto. “On the Validity of the Effective Field Theory for Dark Matter Searches at the LHC”. In: *Phys. Lett. B* 728 (Dec. 2013), pp. 412–421. arXiv: 1307.2253 (cit. on p. 29).

[124] Christian Laner Ogilvy. *Searches for dark matter at CMS in events with missing transverse energy*. Tech. rep. CMS-CR-2017-165. Geneva: CERN, 2017 (cit. on p. 29).

[125] Philip Bechtle, Torsten Bringmann, Klaus Desch, et al. “Constrained supersymmetry after two years of LHC data: a global view with Fittino”. In: *Journal of High Energy Physics* 2012.6 (June 2012). arXiv: 1204.4199 (cit. on p. 29).

[126] Philip Bechtle, Klaus Desch, Herbert K. Dreiner, et al. “Constrained Supersymmetry after the Higgs Boson Discovery: A global analysis with Fittino”. In: (Oct. 2013). arXiv: 1310.3045 (cit. on p. 29).

[127] M. Ackermann, M. Ajello, A. Albert, et al. “Fermi LAT search for dark matter in gamma-ray lines and the inclusive photon spectrum”. In: *Physical Review D* 86.2 (July 2012), p. 022002. arXiv: 1205.2739 (cit. on p. 30).

[128] E. Charles et al. “Sensitivity Projections for Dark Matter Searches with the Fermi Large Area Telescope”. In: *Phys. Rept.* 636 (2016), pp. 1–46. arXiv: 1605.02016 [astro-ph.HE] (cit. on p. 30).

[129] A. Albert et al. “Searching for Dark Matter Annihilation in Recently Discovered Milky Way Satellites with Fermi-LAT”. In: *Astrophys. J.* 834.2 (2017), p. 110. arXiv: 1611.03184 [astro-ph.HE] (cit. on p. 30).

[130] M. Ackermann et al. “The Fermi Galactic Center GeV Excess and Implications for Dark Matter”. In: *Astrophys. J.* 840.1 (2017), p. 43. arXiv: 1704.03910 [astro-ph.HE] (cit. on p. 30).

[131] M. Boezio, M. Pearce, P. Picozza, et al. “PAMELA and indirect dark matter searches”. In: *New J. Phys.* 11.10 (Oct. 2009), pp. 105023+ (cit. on p. 30).

[132] M. Aguilar, G. Alberti, B. Alpat, et al. “First Result from the Alpha Magnetic Spectrometer on the International Space Station: Precision Measurement of the Positron Fraction in Primary Cosmic Rays of 0.5–350 GeV”. In: *Physical Review Letters* 110.14 (Apr. 2013) (cit. on p. 30).

[133] O. Adriani, G. C. Barbarino, G. A. Bazilevskaya, et al. “A statistical procedure for the identification of positrons in the PAMELA experiment”. In: *Astropart. Phys.* 34.1 (Aug. 2010), pp. 1–11 (cit. on p. 30).

[134] M. Ackermann, M. Ajello, A. Allafort, et al. “Measurement of Separate Cosmic-Ray Electron and Positron Spectra with the Fermi Large Area Telescope”. In: *Phys. Rev. Lett.* 108.1 (Jan. 2012), pp. 011103+ (cit. on p. 30).

[135] Alejandro Ibarra, Anna S. Lamperstorfer, and Joseph Silk. “Dark matter annihilations and decays after the AMS-02 positron measurements”. In: *Phys. Rev. D* 89.6 (Mar. 2014), p. 063539. arXiv: 1309.2570 (cit. on p. 30).

[136] Joachim Kopp. “Constraints on dark matter annihilation from AMS-02 results”. In: *Phys. Rev.* D88 (2013), p. 076013. arXiv: 1304.1184 [hep-ph] (cit. on p. 30).

[137] G. Ambrosi et al. “Direct detection of a break in the teraelectronvolt cosmic-ray spectrum of electrons and positrons”. In: (2017). arXiv: 1711.10981 [astro-ph.HE] (cit. on p. 30).

[138] Gustavo A. Medina Tanco, Elisabete M. de Gouveia Dal Pino, and Jorge E. Horvath. “Deflection of Ultra–HighEnergy Cosmic Rays by the Galactic Magnetic Field: From the Sources to the Detector”. In: *Astrophys. J.* 492.1 (Jan. 1998), pp. 200–204 (cit. on p. 30).

[139] J. Lavalle, Q. Yuan, D. Maurin, and X. J. Bi. “Full calculation of clumpiness boost factors for antimatter cosmic rays in the light of Lambda-CDM N-body simulation results”. In: *Astron. Astrophys.* 479.2 (Feb. 2008), pp. 427–452. arXiv: 0709.3634 (cit. on p. 30).

[140] M. Ackermann, A. Albert, B. Anderson, et al. “Dark Matter Constraints from Observations of 25 Milky Way Satellite Galaxies with the Fermi Large Area Telescope”. In: *Phys. Rev. D* 89.4 (Feb. 2014), p. 042001. arXiv: 1310.0828 (cit. on p. 30).

[141] Christoph Weniger. “A tentative gamma-ray line from Dark Matter annihilation at the Fermi Large Area Telescope”. In: *J. Cosmol. Astropart. Phys.* 2012.08 (Aug. 2012), p. 007. arXiv: 1204.2797 (cit. on p. 31).

[142] E. Bloom, E. Charles, E. Izaguirre, et al. “Search of the Earth Limb Fermi Data and Non-Galactic Center Region Fermi Data for Signs of Narrow Lines”. In: (Mar. 2013). arXiv: 1303.2733 (cit. on p. 31).

[143] Wilfried Buchmüller and Mathias Garny. “Decaying vs. annihilating dark matter in light of a tentative gamma-ray line”. In: *J. Cosmol. Astropart. Phys.* 2012.08 (Aug. 2012), p. 035. arXiv: 1206.7056 (cit. on p. 31).

[144] Timothy Cohen, Mariangela Lisanti, Tracy R. Slatyer, and Jay G. Wacker. “Illuminating the 130 GeV gamma line with continuum photons”. In: *J. High Energy Phys.* 2012.10 (Oct. 2012). arXiv: 1207.0800 (cit. on p. 31).

[145] A. Abramowski, F. Acero, F. Aharonian, et al. “Search for Photon-Linelike Signatures from Dark Matter Annihilations with H.E.S.S.” In: *Phys. Rev. Lett.* 110.4 (Jan. 2013). arXiv: 1301.1173 (cit. on p. 31).

[146] J. Aleksić, S. Ansoldi, L. A. Antonelli, et al. “Optimized dark matter searches in deep observations of Segue 1 with MAGIC”. In: *J. Cosmol. Astropart. Phys.* 2014.02 (Feb. 2014), p. 008. arXiv: 1312.1535 (cit. on p. 31).

[147] V. A. Acciari, T. Arlen, T. Aune, et al. “VERITAS SEARCH FOR VHE GAMMA-RAY EMISSION FROM DWARF SPHEROIDAL GALAXIES”. In: *Astrophys. J.* 720.2 (Sept. 2010), pp. 1174–1180. arXiv: 1006.5955 (cit. on p. 31).

[148] M. Doro, J. Conrad, D. Emmanoulopoulos, et al. “Dark matter and fundamental physics with the Cherenkov Telescope Array”. In: *J. Astropart. Phys.* 43 (Mar. 2013), pp. 189–214 (cit. on p. 31).

[149] J. Zornoza. “Search for dark matter in the Sun with the ANTARES neutrino telescope in the CMSSM and mUED frameworks”. In: *Nucl. Instrum. Methods* 725 (Oct. 2013), pp. 76–79. arXiv: 1204.5290 (cit. on p. 31).

[150] M. G. Aartsen, R. Abbasi, Y. Abdou, et al. “The IceCube Neutrino Observatory Part IV: Searches for Dark Matter and Exotic Particles”. In: (Sept. 2013). arXiv: 1309.7007 (cit. on p. 31).

[151] M. G. Aartsen et al. “Search for Neutrinos from Dark Matter Self-Annihilations in the center of the Milky Way with 3 years of IceCube/DeepCore”. In: *Eur. Phys. J.* C77.9 (2017), p. 627. arXiv: 1705.08103 [hep-ex] (cit. on p. 31).

[152] Mark W. Goodman and Edward Witten. “Detectability of certain dark-matter candidates”. In: *Phys. Rev. D* 31.12 (June 1985), pp. 3059–3063 (cit. on pp. 32, 35, 38).

[153] Andrzej K. Drukier, Katherine Freese, and David N. Spergel. “Detecting cold dark-matter candidates”. In: *Phys. Rev. D* 33.12 (June 1986), pp. 3495–3508 (cit. on pp. 32, 35).

[154] M. Milgrom. “A modification of the Newtonian dynamics as a possible alternative to the hidden mass hypothesis”. In: *Astrophys. J.* 270 (July 1983), pp. 365–370 (cit. on p. 32).

[155] M. Milgrom. “A modification of the Newtonian dynamics - Implications for galaxies”. In: *Astrophys. J.* 270 (1983), pp. 371+ (cit. on p. 32).

[156] M. Milgrom. “A Modification of the Newtonian Dynamics - Implications for Galaxy Systems”. In: *Astrophys. J.* 270 (July 1983), pp. 384+ (cit. on p. 32).

[157] Oleg Y. Gnedin, David H. Weinberg, James Pizagno, Francisco Prada, and Hans-Walter Rix. “Dark Matter Halos of Disk Galaxies: Constraints from the Tully-Fisher Relation”. In: *Astrophys. J.* (Dec. 2007), pp. 1115+ (cit. on p. 33).

[158] Stacy S. McGaugh. “The Baryonic Tully-Fisher Relation of Galaxies with Extended Rotation Curves and the Stellar Mass of Rotating Galaxies”. In: *Astrophys. J.* 632.2 (2005), pp. 859–871. eprint: astro-ph/0506750 (cit. on p. 33).

[159] Jacob D. Bekenstein. “Relativistic gravitation theory for the MOND paradigm”. In: *Phys. Rev. D* 70.8 (2005), pp. 083509+. eprint: astro-ph/0403694 (cit. on p. 33).

[160] Mu-Chen Chiu, Chung-Ming Ko, and Yong Tian. “Theoretical Aspects of Gravitational Lensing in TeVeS”. In: *Astrophys. J.* 636.2 (Oct. 2005), pp. 565–574. eprint: astro-ph/0507332 (cit. on p. 33).

[161] Constantinos Skordis. “Tensor-vector-scalar cosmology: Covariant formalism for the background evolution and linear perturbation theory”. In: *Phys. Rev. D* 74.10 (Nov. 2006), p. 103513 (cit. on p. 33).

[162] S. Boran, S. Desai, E. O. Kahya, and R. P. Woodard. “GW170817 Falsifies Dark Matter Emulators”. In: (2017). arXiv: 1710.06168 [astro-ph.HE] (cit. on p. 33).

[163] B.P. Abbott et al. “GW170817: Observation of Gravitational Waves from a Binary Neutron Star Inspiral”. In: *Phys. Rev. Lett.* 119.16 (2017), p. 161101. arXiv: 1710.05832 [gr-qc] (cit. on pp. 33, 209).

[164] B. P. Abbott et al. “Gravitational Waves and Gamma-rays from a Binary Neutron Star Merger: GW170817 and GRB 170817A”. In: *Astrophys. J.* 848.2 (2017), p. L13. arXiv: 1710.05834 [astro-ph.HE] (cit. on p. 33).

[165] Erik P. Verlinde. “Emergent Gravity and the Dark Universe”. In: *SciPost Phys.* 2.3 (2017), p. 016. arXiv: 1611.02269 [hep-th] (cit. on p. 33).

[166] Mariano Cadoni, Roberto Casadio, Andrea Giusti, Wolfgang Mueck, and Matteo Tuveri. “Effective Fluid Description of the Dark Universe”. In: *Phys. Lett.* B776 (2018), p. 242. arXiv: 1707.09945 [gr-qc] (cit. on p. 33).

[167] R. H. Sanders. “The published extended rotation curves of spiral galaxies: Confrontation with Modified Dynamics”. In: *Astrophys. J.* 473.1 (June 1996), pp. 117–129. eprint: astro-ph/9606089 (cit. on p. 33).

[168] W. J. G. de Blok and S. S. McGaugh. “Testing Modified Newtonian Dynamics with Low Surface Brightness Galaxies --Rotation curve fits-”. In: *Astrophys. Jo.* 508.1 (May 1998), pp. 132–140. eprint: astro-ph/9805120 (cit. on p. 33).

[169] Robert H. Sanders and Stacy S. McGaugh. “Modified Newtonian Dynamics as an Alternative to Dark Matter”. In: *Ann. Rev. Astron. Astrophys.* 40.1 (Apr. 2002), pp. 263–317. eprint: astro-ph/0204521 (cit. on p. 34).

[170] Garry W. Angus, HuanYuan Shan, HongSheng Zhao, and Benoit Famaey. “On the Proof of Dark Matter, the Law of Gravity and the Mass of Neutrinos”. In: *Astrophys. J.* 654.1 (Nov. 2006), pp. L13–L16. eprint: astro-ph/0609125 (cit. on p. 34).

[171] Scott Dodelson and Michele Liguori. “Can Cosmic Structure form without Dark Matter?” In: *Phys. Rev. Lett.* 97.23 (Aug. 2006). eprint: astro-ph/0608602 (cit. on p. 34).

[172] Anže Slosar, Alessandro Melchiorri, and Joseph Silk. “Test of modified Newtonian dynamics with recent Boomerang data”. In: *Phys. Rev. D* 72.10 (Nov. 2005), p. 101301. eprint: astro-ph/0508048 (cit. on p. 34).

[173] J. Zuntz, T. G. Zlosnik, F. Bourliot, P. G. Ferreira, and G. D. Starkman. “Vector field models of modified gravity and the dark sector”. In: *Phys. Rev. D* 81.10 (Feb. 2010), p. 104015. arXiv: 1002.0849 (cit. on p. 34).

[174] D. G. Cerdeño and A. M. Green. “Direct detection of WIMPs”. In: *Particle Dark Matter*. Ed. by Gianfranco Bertone and Gianfranco Bertone. Cambridge: Cambridge University Press, Feb. 2010. Chap. 17, pp. 347–369. arXiv: 1002.1912 (cit. on pp. 35, 38, 42).

[175] Andriy Kurylov and Marc Kamionkowski. “Generalized Analysis of Weakly-Interacting Massive Particle Searches”. In: *Phys. Rev. D* 69.6 (July 2003), p. 063503. eprint: hep-ph/0307185 (cit. on pp. 37, 69).

[176] Katherine Freese, J. Frieman, and A. Gould. “Signal modulation in cold-dark-matter detection”. In: *Phys. Rev. D* 37.12 (June 1988), pp. 3388–3405 (cit. on p. 37).

[177] A. Liam Fitzpatrick, Wick Haxton, Emanuel Katz, Nicholas Lubbers, and Yiming Xu. “The effective field theory of dark matter direct detection”. In: *J. Cosmol. Astropart. Phys.* 2013.02 (Feb. 2013), p. 004. arXiv: 1203.3542 (cit. on pp. 38, 69).

[178] J. M. Alarcón, J. Martin Camalich, and J. A. Oller. “Chiral representation of the N scattering amplitude and the pion-nucleon sigma term”. In: *Phys. Rev. D* 85.5 (Mar. 2012), p. 051503. arXiv: 1110.3797 (cit. on pp. 39, 69).

[179] Gunnar S. Bali, Sara Collins, Meinulf Göckeler, et al. “Strange and light quark contributions to the nucleon mass from lattice QCD”. In: *Phys. Rev. D* 85.5 (Mar. 2012), p. 054502. arXiv: 1111.1600 (cit. on pp. 39, 69).

[180] M. Shifman, A. Vainshtein, and V. Zakharov. “Remarks on Higgs-boson interactions with nucleons”. In: *Phys. Lett. B* 78.4 (Oct. 1978), pp. 443–446 (cit. on p. 40).

[181] Marco Cirelli, Eugenio D. Nobile, and Paolo Panci. “Tools for model-independent bounds in direct dark matter searches”. In: *J. Cosmol. Astropart. Phys.* 2013.10 (Oct. 2013), p. 019. arXiv: 1307.5955 (cit. on pp. 40, 69).

[182] J. Engel. “Nuclear form factors for the scattering of weakly interacting massive particles”. In: *Phys. Lett. B* 264.1-2 (July 1991), pp. 114–119 (cit. on p. 41).

[183] J. Engel, S. Pittel, and P. Vogel. “NUCLEAR PHYSICS OF DARK MATTER DETECTION”. In: *Int. J. Mod. Phys. E* 01.01 (Mar. 1992), pp. 1–37 (cit. on pp. 41, 69).

[184] B. J. Kavanagh. “Confronting astrophysical uncertainties in the direct detection of dark matter”. In: *PhD Thesis* University of Nottingham (2014) (cit. on pp. 41, 65).

[185] Richard Helm. “Inelastic and Elastic Scattering of 187-Mev Electrons from Selected Even-Even Nuclei”. In: *Phys. Rev.* 104.5 (Dec. 1956), pp. 1466–1475 (cit. on pp. 45, 66–68, 201).

[186] J. D. Lewin and P. F. Smith. “Review of mathematics, numerical factors, and corrections for dark matter experiments based on elastic nuclear recoil”. In: *Astropart. Phys.* 6 (1996), pp. 87–112 (cit. on pp. 46, 47).

[187] G. Fricke, C. Bernhardt, K. Heilig, et al. “Nuclear Ground State Charge Radii from Electromagnetic Interactions”. In: *Atom. Data Nucl. Data Tabl.* 60 (1995), pp. 177–285 (cit. on pp. 46, 198, 200, 207, 210, 211).

[188] D. Akimov et al. “Observation of Coherent Elastic Neutrino-Nucleus Scattering”. In: *Science* 357.6356 (2017), pp. 1123–1126. arXiv: 1708.01294 [nucl-ex] (cit. on pp. 48, 122, 123, 192, 194, 197, 198, 202–206, 208).

[189] M. Cannoni. “Reanalysis of nuclear spin matrix elements for dark matter spin-dependent scattering”. In: *Phys. Rev. D* 87.7 (Apr. 2013), p. 075014. arXiv: 1211.6050 (cit. on p. 49).

[190] M. Ressell and D. Dean. “Spin-dependent neutralino-nucleus scattering for A127 nuclei”. In: *Phys. Rev. C* 56.1 (July 1997), pp. 535–546. eprint: hep-ph/9702290 (cit. on p. 49).

[191] John Ellis and R. A. Flores. “Realistic predictions for the detection of supersymmetric dark matter”. In: *Nucl. Phys. B* 307.4 (Oct. 1988), pp. 883–908 (cit. on p. 49).

[192] J. Engel and P. Vogel. “Spin-dependent cross sections of weakly interacting massive particles on nuclei”. In: *Phys. Rev. D* 40.9 (Nov. 1989), pp. 3132–3135 (cit. on p. 49).

[193] Francesco Iachello, Lawrence M. Krauss, and Giuseppe Maino. “Spin-dependent scattering of weakly interacting massive particles in heavy nuclei”. In: *Phys. Lett. B* 254.1-2 (Jan. 1991), pp. 220–224 (cit. on p. 49).

[194] David G. Cerdeno, Mattia Fornasa, Ji-Haeng Huh, and Miguel Peiro. “Nuclear uncertainties in the spin-dependent structure functions for direct dark matter detection”. In: *Phys. Rev. D* 87.2 (Sept. 2012), p. 023512. arXiv: 1208.6426 (cit. on p. 49).

[195] J. A. Fillmore and P. Goldreich. “Self-similar gravitational collapse in an expanding universe”. In: 281 (June 1984), pp. 1–8 (cit. on p. 51).

[196] J. Dubinski and R. G. Carlberg. “The structure of cold dark matter halos”. In: 378 (Sept. 1991), pp. 496–503 (cit. on p. 51).

[197] Julio F. Navarro, Aaron Ludlow, Volker Springel, et al. “The diversity and similarity of simulated cold dark matter haloes”. In: *Monthly Notices of the Royal Astronomical Society* 402.1 (2010), pp. 21–34. eprint: /oup/backfile/content_public/journal/mnras/402/1/10.1111_j.1365-2966.2009.15878.x/1/mnras0402-0021.pdf (cit. on p. 51).

[198] B. Moore, T. Quinn, F. Governato, J. Stadel, and G. Lake. “Cold collapse and the core catastrophe”. In: *Monthly Notices of the Royal Astronomical Society* 310.4 (1999), pp. 1147–1152. eprint: /oup/backfile/content_public/journal/mnras/310/4/10.1046_j.1365-8711.1999.03039.x/1/310-4-1147.pdf (cit. on p. 52).

[199] J. Einasto. “On the Construction of a Composite Model for the Galaxy and on the Determination of the System of Galactic Parameters”. In: *Trudy Astrofizicheskogo Instituta Alma-Ata* 5 (1965), pp. 87–100 (cit. on p. 52).

[200] Jurg Diemand, Michael Kuhlen, and Piero Madau. “Dark matter substructure and gamma-ray annihilation in the Milky Way halo”. In: *Astrophys. J.* 657 (2007), pp. 262–270. arXiv: astro-ph/0611370 [astro-ph] (cit. on p. 53).

[201] J. Diemand, M. Kuhlen, P. Madau, et al. “Clumps and streams in the local dark matter distribution”. In: *Nature* 454 (2008), pp. 735–738. arXiv: 0805.1244 [astro-ph] (cit. on p. 53).

[202] Joachim Stadel, Doug Potter, Ben Moore, et al. “Quantifying the heart of darkness with GHALO - a multi-billion particle simulation of our galactic halo”. In: *Mon. Not. Roy. Astron. Soc.* 398 (2009), pp. L21–L25. arXiv: 0808.2981 [astro-ph] (cit. on p. 53).

[203] A. K. Drukier, Katherine Freese, and D. N. Spergel. “Detecting Cold Dark Matter Candidates”. In: *Phys. Rev.* D33 (1986), pp. 3495–3508 (cit. on p. 53).

[204] Katherine Freese, Joshua A. Frieman, and Andrew Gould. *Signal Modulation in Cold Dark Matter Detection*. Vol. 37. 1998, pp. 3388–3405 (cit. on pp. 53, 164).

[205] Martin C. Smith, Gregory R. Ruchti, Amina Helmi, et al. “The RAVE survey: constraining the local Galactic escape speed”. In: *Mon. Not. R. Astron. Soc.* 379.2 (Aug. 2007), pp. 755–772. eprint: astro-ph/0611671 (cit. on p. 53).

[206] T. Piffl, C. Scannapieco, J. Binney, et al. “The RAVE survey: the Galactic escape speed and the mass of the Milky Way”. In: *Astron. Astrophys.* 562 (Feb. 2014), A91+. arXiv: 1309.4293 (cit. on p. 53).

[207] F. J. Kerr and Donald Lynden-Bell. “Review of galactic constants”. In: *Mon. Not. Roy. Astron. Soc.* 221 (1986), p. 1023 (cit. on pp. 54, 55).

[208] M. J. Reid et al. “Trigonometric Parallaxes of Massive Star Forming Regions: VI. Galactic Structure, Fundamental Parameters and Non-Circular Motions”. In: *Astrophys. J.* 700 (2009), pp. 137–148. arXiv: 0902.3913 [astro-ph.GA] (cit. on pp. 54, 55).

[209] Paul J. McMillan and James J. Binney. “The uncertainty in Galactic parameters”. In: *Mon. Not. Roy. Astron. Soc.* 402 (2010), p. 934. arXiv: 0907.4685 [astro-ph.GA] (cit. on pp. 54, 55).

[210] Jo Bovy, David W. Hogg, and Hans-Walter Rix. “Galactic masers and the Milky Way circular velocity”. In: *Astrophys. J.* 704 (2009), pp. 1704–1709. arXiv: 0907.5423 [astro-ph.GA] (cit. on pp. 54, 55).

[211] Christopher Savage, Katherine Freese, and Paolo Gondolo. “Annual Modulation of Dark Matter in the Presence of Streams”. In: *Phys. Rev.* D74 (2006), p. 043531. arXiv: astro-ph/0607121 [astro-ph] (cit. on p. 56).

[212] Christopher McCabe. “The Astrophysical Uncertainties Of Dark Matter Direct Detection Experiments”. In: *Phys. Rev.* D82 (2010), p. 023530. arXiv: 1005.0579 [hep-ph] (cit. on pp. 56, 79).

[213] S. Abrahamyan et al. “Measurement of the Neutron Radius of ^{208}Pb Through Parity-Violation in Electron Scattering”. In: *Phys. Rev. Lett.* 108 (2012), p. 112502. arXiv: 1201.2568 [nucl-ex] (cit. on pp. 68, 198, 206).

[214] B. Borasoy and Ulf-G. “Baryon masses and pion-nucleon σ-term to second order in the quark masses”. In: *Phys. Lett. B* 365.1-4 (Aug. 1995), pp. 285–291. eprint: hep-ph/9508354 (cit. on p. 69).

[215] M. M. Pavan, I. I. Strakovsky, R. L. Workman, and R. A. Arndt. “The pion-nucleon Sigma term is definitely large: results from a G.W.U. analysis of pion nucleon scattering data”. In: (Nov. 2001). eprint: hep-ph/0111066 (cit. on p. 69).

[216] L. Alvarez-ruso, T. Ledwig, M. J. Vicente Vacas, and J. Martin-camalich. “THE NUCLEON MASS AND PION-NUCLEON SIGMA TERM FROM A CHIRAL ANALYSIS OF N_f = 2 + 1 LATTICE QCD WORLD DATA”. In: *Int. J. Mod. Phys.: Conf. Ser.* 26 (Jan. 2014), pp. 1460089+. arXiv: 1402.1031 (cit. on p. 69).

[217] J. Ashman, B. Badelek, G. Baum, et al. “A measurement of the spin asymmetry and determination of the structure function g1 in deep inelastic muon-proton scattering”. In: *Phys. Lett. B* 206.2 (May 1988), pp. 364–370 (cit. on p. 69).

[218] R. L. Jaffe and Aneesh Manohar. “The g1 problem: Deep inelastic electron scattering and the spin of the proton”. In: *Nucl. Phys. B* 337.3 (June 1990), pp. 509–546 (cit. on p. 69).

[219] D. Adams. “Spin Structure of the Proton from Polarized Inclusive Deep-Inelastic Muon-Proton Scattering”. In: *Phys. Rev. D* 56.9 (Feb. 1997), pp. 5330–5358. eprint: hep-ex/9702005 (cit. on p. 69).

[220] Di Qing, Xiang-Song Chen, and Fan Wang. “Spin content of the nucleon in a valence and sea quark mixing model”. In: *Phys. Rev. C* 57.1 (Jan. 1998), R31–R34 (cit. on p. 69).

[221] Anthony Thomas. “Interplay of Spin and Orbital Angular Momentum in the Proton”. In: *Phys. Rev. Lett.* 101.10 (Sept. 2008), pp. 102003+ (cit. on p. 69).

[222] Jonathan L. Feng, Jason Kumar, Danny Marfatia, and David Sanford. “Isospin-Violating Dark Matter”. In: *Phys. Lett. B* 703.2 (Oct. 2011), pp. 124–127. arXiv: 1102.4331 (cit. on pp. 69, 78).

[223] Jason Kumar. “PROBING ISOSPIN-VIOLATING DARK MATTER”. In: *Int. J. Mod. Phys.: Conf. Ser.* 10 (Jan. 2012), pp. 115–122. arXiv: 1201.0217 (cit. on p. 69).

[224] Koichi Hamaguchi, Seng P. Liew, Takeo Moroi, and Yasuhiro Yamamoto. “Isospin-Violating Dark Matter with Colored Mediators”. In: (Mar. 2014). arXiv: 1403.0324 (cit. on p. 69).

[225] Kai Schmidt-Hoberg, Florian Staub, and Martin W. Winkler. “Constraints on light mediators: confronting dark matter searches with B physics”. In: *Phys. Lett. B* 727.4-5 (Oct. 2013), pp. 506–510. arXiv: 1310.6752 (cit. on p. 69).

[226] Haipeng An, Lian-Tao Wang, and Hao Zhang. “Dark matter with t-channel mediator: a simple step beyond contact interaction”. In: (Mar. 2014). arXiv: 1308.0592 (cit. on p. 69).

[227] Maxim Pospelov and Tonnis T. Veldhuis. “Direct and indirect limits on the electromagnetic form factors of WIMPs”. In: *Phys. Lett. B* 480.1-2 (Mar. 2000), pp. 181–186. eprint: hep-ph/0003010 (cit. on p. 69).

[228] Chiu M. Ho and Robert J. Scherrer. “Anapole dark matter”. In: *Phys. Lett. B* 722.4-5 (May 2013), pp. 341–346. arXiv: 1211.0503 (cit. on p. 69).

[229] JiJi Fan, Matthew Reece, and Lian-Tao Wang. “Non-relativistic effective theory of dark matter direct detection”. In: *J. Cosmol. Astropart. Phys.* 2010.11 (Nov. 2010), p. 042. arXiv: 1008.1591 (cit. on p. 69).

[230] Riccardo Catena and Piero Ullio. “A novel determination of the local dark matter density”. In: *JCAP* 1008 (2010), p. 004. arXiv: 0907.0018 [astro-ph.CO] (cit. on p. 70).

[231] Fabrizio Nesti and Paolo Salucci. “The Dark Matter halo of the Milky Way, AD 2013”. In: *JCAP* 1307 (2013), p. 016. arXiv: 1304.5127 [astro-ph.GA] (cit. on p. 70).

[232] Silvia Garbari, Chao Liu, Justin I. Read, and George Lake. “A new determination of the local dark matter density from the kinematics of K dwarfs”. In: *Mon. Not. Roy. Astron. Soc.* 425 (2012), p. 1445. arXiv: 1206.0015 [astro-ph.GA] (cit. on p. 70).

[233] Fabio Iocco, Miguel Pato, Gianfranco Bertone, and Philippe Jetzer. “Dark Matter distribution in the Milky Way: microlensing and dynamical constraints”. In: *JCAP* 1111 (2011), p. 029. arXiv: 1107.5810 [astro-ph.GA] (cit. on p. 70).

[234] P. Salucci, F. Nesti, G. Gentile, and C. F. Martins. “The dark matter density at the Sun’s location”. In: *Astron. Astrophys.* 523 (2010), A83. arXiv: 1003.3101 [astro-ph.GA] (cit. on p. 70).

[235] R. Schönrich, J. Binney, and W. Dehnen. “Local kinematics and the local standard of rest”. In: 403 (Apr. 2010), pp. 1829–1833. arXiv: 0912.3693 (cit. on p. 71).

[236] Ralph Schönrich. “Galactic rotation and solar motion from stellar kinematics: Galactic rotation and the solar motion”. In: *Mon. Not. R. Astron. Soc.* 427.1 (Nov. 2012), pp. 274–287. arXiv: 1207.3079 (cit. on p. 71).

[237] Jo Bovy, Carlos A. Prieto, Timothy C. Beers, et al. “The Milky Way’s circular velocity curve between 4 and 14 kpc from APOGEE data”. In: *Astrophys. J.* 759.2 (Sept. 2012), pp. 131+. arXiv: 1209.0759 (cit. on p. 71).

[238] J. Binney and S. Tremaine. *Galactic Dynamics: Second Edition*. Princeton University Press, 2008 (cit. on p. 71).

[239] Martin C. Smith et al. “The RAVE Survey: Constraining the Local Galactic Escape Speed”. In: *Mon. Not. Roy. Astron. Soc.* 379 (2007), pp. 755–772. arXiv: astro-ph/0611671 [astro-ph] (cit. on p. 71).

[240] N. W. Evans, C. M. Carollo, and P. T. de Zeeuw. “Triaxial haloes and particle dark matter detection”. In: *Mon. Not. R. Astron. Soc.* 318.4 (Nov. 2000), pp. 1131–1143. eprint: astro-ph/0008156 (cit. on p. 71).

[241] Lawrence M. Widrow. “Distribution Functions for Cuspy Dark Matter Density Profiles”. In: *Astrophys. J. Suppl. Ser.* 131.1 (Nov. 2000), pp. 39–46 (cit. on p. 71).

[242] Mariangela Lisanti, Louis E. Strigari, Jay G. Wacker, and Risa H. Wechsler. “The Dark Matter at the End of the Galaxy”. In: *Phys. Rev. D* 83 (Oct. 2011), p. 023519. arXiv: 1010.4300 (cit. on p. 71).

[243] Mark Vogelsberger, Amina Helmi, Volker Springel, et al. “Phase-space structure in the local dark matter distribution and its signature in direct detection experiments”. In: *Mon. Not. R. Astron. Soc.* 395.2 (May 2009), pp. 797–811. arXiv: 0812.0362 (cit. on p. 72).

[244] Michael Kuhlen, Neal Weiner, Jürg Diemand, et al. “Dark matter direct detection with non-Maxwellian velocity structure”. In: *J. Cosmol. Astropart. Phys.* 02.02 (Feb. 2010), p. 030. arXiv: 0912.2358 (cit. on p. 72).

[245] Yao-Yuan Mao, Louis E. Strigari, Risa H. Wechsler, Hao-Yi Wu, and Oliver Hahn. “Halo-to-Halo Similarity and Scatter in the Velocity Distribution of Dark Matter”. In: *Astrophys. J.* 764.1 (Dec. 2012), p. 35. arXiv: 1210.2721 (cit. on p. 72).

[246] Amina Helmi, Simon D. M. White, and Volker Springel. “The Phase space structure of a dark matter halo: Implications for dark matter direct detection experiments”. In: *Phys. Rev.* D66 (2002), p. 063502. arXiv: astro-ph/0201289 [astro-ph] (cit. on p. 72).

[247] J. I. Read, L. Mayer, A. M. Brooks, F. Governato, and G. Lake. “A dark matter disc in three cosmological simulations of Milky Way mass galaxies”. In: *Mon. Not. R. Astron. Soc.* 397.1 (July 2009), pp. 44–51. arXiv: 0902.0009 (cit. on p. 72).

[248] J. I. Read, T. Bruch, L. Baudis, et al. “A Dark Matter Disc in the Milky Way”. In: *AIP Conf. Proc.* 1240 (Jan. 2010), p. 391. arXiv: 0901.2938 (cit. on p. 72).

[249] Annalisa Pillepich, Michael Kuhlen, Javiera Guedes, and Piero Madau. “THE DISTRIBUTION OF DARK MATTER IN THE MILKY WAY’S DISK”. In: *Astrophys. J.* 784.2 (Apr. 2014), pp. 161+. arXiv: 1308.1703 (cit. on p. 72).

[250] Anne M. Green. “Dependence of direct detection signals on the WIMP velocity distribution”. In: *J. Cosmol. Astropart. Phys.* 10.10 (Oct. 2010), p. 034. arXiv: 1009.0916 (cit. on p. 72).

[251] Annika H. G. Peter. “WIMP astronomy and particle physics with liquid-noble and cryogenic direct-detection experiments”. In: *Phys. Rev. D* 83.12 (June 2011), p. 125029. arXiv: 1103.5145 (cit. on p. 72).

[252] Malcolm Fairbairn, Tom Douce, and Jace Swift. “Quantifying Astrophysical Uncertainties on Dark Matter Direct Detection Results”. In: *J. Astropart. Phys.* 47 (2013), pp. 45–53. arXiv: 1206.2693 (cit. on p. 72).

[253] D. Acosta-Kane et al. “Discovery of underground argon with low level of radioactive 39Ar and possible applications to WIMP dark matter detectors”. In: *Nucl. Instrum. Meth.* A587 (2008). [J. Phys. Conf. Ser.120,042015(2008)], pp. 46–51. arXiv: 0712.0381 [astro-ph] (cit. on p. 73).

[254] Daniel Z. Freedman. “Coherent neutrino nucleus scattering as a probe of the weak neutral current”. In: *Phys. Rev.* D9 (1974), pp. 1389–1392 (cit. on pp. 74, 122, 192).

[255] Blas Cabrera, Lawrence M. Krauss, and Frank Wilczek. “Bolometric Detection of Neutrinos”. In: *Phys. Rev. Lett.* 55 (1985), p. 25 (cit. on p. 74).

[256] J. Billard, L. Strigari, and E. Figueroa-Feliciano. “Implication of neutrino backgrounds on the reach of next generation dark matter direct detection experiments”. In: *Phys. Rev.* D89.2 (2014), p. 023524. arXiv: 1307.5458 [hep-ph] (cit. on pp. 74, 79, 80, 123, 131, 153, 191).

[257] V. Chepel and H. Araujo. “Liquid noble gas detectors for low energy particle physics”. In: *JINST* 8 (2013), R04001. arXiv: 1207.2292 [physics.ins-det] (cit. on p. 74).

[258] R. Bernabei et al. “The DAMA/LIBRA apparatus”. In: *Nucl. Instrum. Meth.* A592 (2008), pp. 297–315. arXiv: 0804.2738 [astro-ph] (cit. on pp. 74, 77, 80).

[259] R. Bernabei et al. “Final model independent result of DAMA/LIBRA-phase1”. In: *Eur. Phys. J.* C73 (2013), p. 2648. arXiv: 1308.5109 [astro-ph.GA] (cit. on pp. 74, 77).

[260] S. C. Kim et al. “New Limits on Interactions between Weakly Interacting Massive Particles and Nucleons Obtained with CsI(Tl) Crystal Detectors”. In: *Phys. Rev. Lett.* 108 (2012), p. 181301. arXiv: 1204.2646 [astro-ph.CO] (cit. on pp. 74, 77).

[261] B. Ahmed et al. “The NAIAD experiment for WIMP searches at Boulby mine and recent results”. In: *Astropart. Phys.* 19 (2003), pp. 691–702. arXiv: hep-ex/0301039 [hep-ex] (cit. on p. 75).

[262] Z. Ahmed et al. “Dark Matter Search Results from the CDMS II Experiment”. In: *Science* 327 (2010), pp. 1619–1621. arXiv: 0912.3592 [astro-ph.CO] (cit. on p. 75).

[263] G. Angloher et al. “Results from 730 kg days of the CRESST-II Dark Matter Search”. In: *Eur. Phys. J.* C72 (2012), p. 1971. arXiv: 1109.0702 [astro-ph.CO] (cit. on pp. 75, 78, 80).

[264] C. E. Aalseth et al. “CoGeNT: A Search for Low-Mass Dark Matter using p-type Point Contact Germanium Detectors”. In: *Phys. Rev.* D88 (2013), p. 012002. arXiv: 1208.5737 [astro-ph.CO] (cit. on pp. 75, 77, 80).

[265] C. E. Aalseth et al. “Search for An Annual Modulation in Three Years of CoGeNT Dark Matter Detector Data”. In: (2014). arXiv: 1401.3295 [astro-ph.CO] (cit. on p. 75).

[266] E. Armengaud et al. “Performance of the EDELWEISS-III experiment for direct dark matter searches”. In: *JINST* 12.08 (2017), P08010. arXiv: 1706.01070 [physics.ins-det] (cit. on p. 75).

[267] E. Aprile et al. “The XENON1T Dark Matter Experiment”. In: (2017). arXiv: 1708.07051 [astro-ph.IM] (cit. on pp. 75, 82).

[268] Daniel S Akerib, H M Araújo, X Bai, et al. *First Results from the LUX Dark Matter Experiment at the Sanford Underground Research Facility*. Vol. 112. 9. 2014, p. 091303 (cit. on p. 75).

[269] Xiangyi Cui et al. “Dark Matter Results From 54-Ton-Day Exposure of PandaX-II Experiment”. In: (2017). arXiv: 1708.06917 [astro-ph.CO] (cit. on pp. 75, 77, 79, 80, 170).

[270] P. Benetti et al. “First results from a Dark Matter search with liquid Argon at 87 K in the Gran Sasso Underground Laboratory”. In: *Astropart. Phys.* 28 (2008), pp. 495–507. arXiv: astro-ph/0701286 [astro-ph] (cit. on pp. 76, 80).

[271] E. Behnke et al. “First Dark Matter Search Results from a 4-kg CF_3I Bubble Chamber Operated in a Deep Underground Site”. In: *Phys. Rev.* D86.5 (2012). [Erratum: Phys. Rev.D90,no.7,079902(2014)], p. 052001. arXiv: 1204.3094 [astro-ph.CO] (cit. on p. 76).

[272] M. Felizardo et al. “The SIMPLE Phase II Dark Matter Search”. In: *Phys. Rev.* D89.7 (2014), p. 072013. arXiv: 1404.4309 [hep-ph] (cit. on p. 76).

[273] S. Archambault et al. “Constraints on Low-Mass WIMP Interactions on ^{19}F from PICASSO”. In: *Phys. Lett.* B711 (2012), pp. 153–161. arXiv: 1202.1240 [hep-ex] (cit. on p. 76).

[274] George Jaffé. *Zur Theorie der Ionisation in Kolonnen. II*. Vol. 393. 7. WILEY-VCH Verlag, 1929, pp. 977–1008 (cit. on pp. 76, 165, 166).

[275] E. Aprile et al. “First Dark Matter Search Results from the XENON1T Experiment”. In: (2017). arXiv: 1705.06655 [astro-ph.CO] (cit. on pp. 77, 79, 80, 170).

[276] D. S. Akerib et al. “Results from a search for dark matter in the complete LUX exposure”. In: *Phys. Rev. Lett.* 118.2 (2017), p. 021303. arXiv: 1608.07648 [astro-ph.CO] (cit. on pp. 77, 79, 80).

[277] R. Agnese et al. “WIMP-Search Results from the Second CDMSlite Run”. In: *Phys. Rev. Lett.* 116.7 (2016), p. 071301. arXiv: 1509.02448 [astro-ph.CO] (cit. on pp. 77, 78, 80).

[278] K. Abe et al. “Direct dark matter search by annual modulation in XMASS-I”. In: *Phys. Lett.* B759 (2016), pp. 272–276. arXiv: 1511.04807 [astro-ph.CO] (cit. on p. 77).

[279] Jonathan H. Davis. “The Past and Future of Light Dark Matter Direct Detection”. In: *Int. J. Mod. Phys.* A30.15 (2015), p. 1530038. arXiv: 1506.03924 [hep-ph] (cit. on pp. 77, 78).

[280] E. Aprile et al. “Search for magnetic inelastic dark matter with XENON100”. In: *JCAP* 1710.10 (2017), p. 039. arXiv: 1704.05804 [astro-ph.CO] (cit. on p. 77).

[281] G. Barello, Spencer Chang, and Christopher A. Newby. “A Model Independent Approach to Inelastic Dark Matter Scattering”. In: *Phys. Rev.* D90.9 (2014), p. 094027. arXiv: 1409.0536 [hep-ph] (cit. on p. 77).

[282] Eugenio Del Nobile, Graciela B. Gelmini, Andreea Georgescu, and Ji-Haeng Huh. “Reevaluation of spin-dependent WIMP-proton interactions as an explanation of the DAMA data”. In: *JCAP* 1508.08 (2015), p. 046. arXiv: 1502.07682 [hep-ph] (cit. on p. 77).

[283] Graciela B. Gelmini. “Light WIMPs”. In: (2016). arXiv: 1612.09137 [hep-ph] (cit. on pp. 77, 78).

[284] E. Aprile et al. “Search for WIMP Inelastic Scattering off Xenon Nuclei with XENON100”. In: *Phys. Rev.* D96.2 (2017), p. 022008. arXiv: 1705.05830 [hep-ex] (cit. on p. 77).

[285] Joachim Kopp, Viviana Niro, Thomas Schwetz, and Jure Zupan. “DAMA/LIBRA and leptonically interacting Dark Matter”. In: *Phys. Rev.* D80 (2009), p. 083502. arXiv: 0907.3159 [hep-ph] (cit. on p. 77).

[286] C. E. Aalseth et al. “Search for an Annual Modulation in a P-type Point Contact Germanium Dark Matter Detector”. In: *Phys. Rev. Lett.* 107 (2011), p. 141301. arXiv: 1106.0650 [astro-ph.CO] (cit. on p. 77).

[287] C. E. Aalseth et al. “Results from a Search for Light-Mass Dark Matter with a P-type Point Contact Germanium Detector”. In: *Phys. Rev. Lett.* 106 (2011), p. 131301. arXiv: 1002.4703 [astro-ph.CO] (cit. on p. 77).

[288] C. E. Aalseth et al. “Maximum Likelihood Signal Extraction Method Applied to 3.4 years of CoGeNT Data”. In: (2014). arXiv: 1401.6234 [astro-ph.CO] (cit. on p. 77).

[289] Jonathan H. Davis, Christopher McCabe, and Celine Boehm. “Quantifying the evidence for Dark Matter in CoGeNT data”. In: *JCAP* 1408 (2014), p. 014. arXiv: 1405.0495 [hep-ph] (cit. on p. 77).

[290] Q. Yue et al. “Limits on light WIMPs from the CDEX-1 experiment with a p-type point-contact germanium detector at the China Jingping Underground Laboratory”. In: *Phys. Rev.* D90 (2014), p. 091701. arXiv: 1404.4946 [hep-ex] (cit. on p. 78).

[291] G. K. Giovanetti et al. “A Dark Matter Search with MALBEK”. In: *Phys. Procedia* 61 (2015), pp. 77–84. arXiv: 1407.2238 [nucl-ex] (cit. on p. 78).

[292] Eugenio Del Nobile, Graciela B. Gelmini, Paolo Gondolo, and Ji-Haeng Huh. “Halo-independent analysis of direct detection data for light WIMPs”. In: *JCAP* 1310 (2013), p. 026. arXiv: 1304.6183 [hep-ph] (cit. on p. 78).

[293] M. Kuźniak, M. G. Boulay, and T. Pollmann. “Surface roughness interpretation of 730 kg days CRESST-II results”. In: *Astropart. Phys.* 36 (2012), pp. 77–82. arXiv: 1203.1576 [astro-ph.IM] (cit. on p. 78).

[294] G. Angloher et al. “Results on low mass WIMPs using an upgraded CRESST-II detector”. In: *Eur. Phys. J.* C74.12 (2014), p. 3184. arXiv: 1407.3146 [astro-ph.CO] (cit. on p. 78).

[295] R. Agnese et al. “Silicon Detector Dark Matter Results from the Final Exposure of CDMS II”. In: *Phys. Rev. Lett.* 111.25 (2013), p. 251301. arXiv: 1304.4279 [hep-ex] (cit. on pp. 78, 80).

[296] R. Agnese et al. “Maximum Likelihood Analysis of Low Energy CDMS II Germanium Data”. In: *Phys. Rev. D* (2014). [Phys. Rev.D91,052021(2015)]. arXiv: 1410.1003 [astro-ph.CO] (cit. on p. 78).

[297] R. Agnese et al. “Search for Low-Mass Weakly Interacting Massive Particles Using Voltage-Assisted Calorimetric Ionization Detection in the SuperCDMS Experiment”. In: *Phys. Rev. Lett.* 112.4 (2014), p. 041302. arXiv: 1309.3259 [physics.ins-det] (cit. on p. 78).

[298] Graciela B. Gelmini, Ji-Haeng Huh, and Samuel J. Witte. “Assessing Compatibility of Direct Detection Data: Halo-Independent Global Likelihood Analyses”. In: *JCAP* 1610.10 (2016), p. 029. arXiv: 1607.02445 [hep-ph] (cit. on p. 78).

[299] L. Hehn et al. “Improved EDELWEISS-III sensitivity for low-mass WIMPs using a profile likelihood approach”. In: *Eur. Phys. J.* C76.10 (2016), p. 548. arXiv: 1607.03367 [astro-ph.CO] (cit. on pp. 78, 80).

[300] Malcolm Fairbairn and Thomas Schwetz. “Spin-independent elastic WIMP scattering and the DAMA annual modulation signal”. In: *J. Cosmol. Astropart. Phys.* 2009.01 (Jan. 2009), p. 037. arXiv: 0808.0704 (cit. on p. 78).

[301] Juan Herrero-Garcia, Thomas Schwetz, and Jure Zupan. “Astrophysics independent bounds on the annual modulation of dark matter signals”. In: *Phys. Rev. Lett.* 109.14 (May 2012). arXiv: 1205.0134 (cit. on p. 78).

[302] Patrick J. Fox, Jia Liu, and Neal Weiner. “Integrating Out Astrophysical Uncertainties”. In: *Phys. Rev. D* 83.10 (Nov. 2011), p. 103514. arXiv: 1011.1915 (cit. on p. 78).

[303] Mads T. Frandsen, Felix Kahlhoefer, Christopher McCabe, Subir Sarkar, and Kai Schmidt-Hoberg. “Resolving astrophysical uncertainties in dark matter direct detection”. In: *J. Cosmol. Astropart. Phys.* 2012.01 (Jan. 2012), p. 024. arXiv: 1111.0292 (cit. on p. 78).

[304] Matthew R. Buckley and W. Hugh Lippincott. “A Spin-Dependent Interpretation for Possible Signals of Light Dark Matter”. In: *Phys. Rev. D* 88.5 (June 2013), p. 056003. arXiv: 1306.2349 (cit. on p. 78).

[305] David Smith and Neal Weiner. “Inelastic Dark Matter”. In: *Phys. Rev. D* 64.4 (Jan. 2001), p. 043502. eprint: hep-ph/0101138 (cit. on p. 78).

[306] R. Foot. “Direct detection experiments explained with mirror dark matter”. In: *Phys. Lett. B* 728 (Jan. 2014), pp. 45–50. arXiv: 1305.4316 (cit. on p. 78).

[307] Thomas Schwetz and Jure Zupan. “Dark Matter attempts for CoGeNT and DAMA”. In: *J. Cosmol. Astropart. Phys.* 2011.08 (June 2011), p. 008. arXiv: 1106.6241 (cit. on p. 78).

[308] E. Aprile et al. “XENON100 Dark Matter Results from a Combination of 477 Live Days”. In: *Phys. Rev.* D94.12 (2016), p. 122001. arXiv: 1609.06154 [astro-ph.CO] (cit. on pp. 79, 81).

[309] E. A. Bagnaschi et al. “Supersymmetric Dark Matter after LHC Run 1”. In: *Eur. Phys. J.* C75 (2015), p. 500. arXiv: 1508.01173 [hep-ph] (cit. on pp. 79, 80).

[310] P. A. Amaudruz et al. “First results from the DEAP-3600 dark matter search with argon at SNOLAB”. In: (2017). arXiv: 1707.08042 [astro-ph.CO] (cit. on p. 80).

[311] G. Angloher et al. “Results on light dark matter particles with a low-threshold CRESST-II detector”. In: *Eur. Phys. J.* C76.1 (2016), p. 25. arXiv: 1509.01515 [astro-ph.CO] (cit. on p. 80).

[312] E. Aprile et al. “Physics reach of the XENON1T dark matter experiment”. In: *JCAP* 1604.04 (2016), p. 027. arXiv: 1512.07501 [physics.ins-det] (cit. on pp. 80, 82, 88, 158).

[313] B. J. Mount et al. “LUX-ZEPLIN (LZ) Technical Design Report”. In: (2017). arXiv: 1703.09144 [physics.ins-det] (cit. on pp. 80, 82, 88, 158).

[314] C. Amole et al. “Dark matter search results from the PICO-60 CF_3I bubble chamber”. In: *Phys. Rev.* D93.5 (2016), p. 052014. arXiv: 1510.07754 [hep-ex] (cit. on p. 79).

[315] C. Amole et al. “Improved dark matter search results from PICO-2L Run 2”. In: *Phys. Rev.* D93.6 (2016), p. 061101. arXiv: 1601.03729 [astro-ph.CO] (cit. on p. 79).

[316] D. S. Akerib et al. “Results on the Spin-Dependent Scattering of Weakly Interacting Massive Particles on Nucleons from the Run 3 Data of the LUX Experiment”. In: *Phys. Rev. Lett.* 116.16 (2016), p. 161302. arXiv: 1602.03489 [hep-ex] (cit. on p. 79).

[317] Z. Ahmed et al. “Search for Weakly Interacting Massive Particles with the First Five-Tower Data from the Cryogenic Dark Matter Search at the Soudan Underground Laboratory”. In: *Phys. Rev. Lett.* 102 (2009), p. 011301. arXiv: 0802.3530 [astro-ph] (cit. on p. 81).

[318] S. Desai et al. “Search for dark matter WIMPs using upward through-going muons in Super-Kamiokande”. In: *Phys. Rev.* D70 (2004). [Erratum: Phys. Rev.D70,109901(2004)], p. 083523. arXiv: hep-ex/0404025 [hep-ex] (cit. on p. 81).

[319] E. Behnke et al. “Final Results of the PICASSO Dark Matter Search Experiment”. In: *Astropart. Phys.* 90 (2017), pp. 85–92. arXiv: 1611.01499 [hep-ex] (cit. on p. 81).

[320] Changbo Fu et al. “Spin-Dependent Weakly-Interacting-Massive-Particle–Nucleon Cross Section Limits from First Data of PandaX-II Experiment”. In: *Phys. Rev. Lett.* 118.7 (2017), p. 071301. arXiv: 1611.06553 [hep-ex] (cit. on p. 81).

[321] D. S. Akerib et al. “Limits on spin-dependent WIMP-nucleon cross section obtained from the complete LUX exposure”. In: *Phys. Rev. Lett.* 118.25 (2017), p. 251302. arXiv: 1705.03380 [astro-ph.CO] (cit. on p. 81).

[322] C. Amole et al. “Dark Matter Search Results from the PICO-60 C_3F_8 Bubble Chamber”. In: *Phys. Rev. Lett.* 118.25 (2017), p. 251301. arXiv: 1702.07666 [astro-ph.CO] (cit. on p. 81).

[323] M. G. Aartsen et al. “Search for annihilating dark matter in the Sun with 3 years of IceCube data”. In: *Eur. Phys. J.* C77.3 (2017), p. 146. arXiv: 1612.05949 [astro-ph.HE] (cit. on p. 81).

[324] “Toward a next-generation dark matter search with the PICO-40L bubble chamber”. In: () (cit. on p. 81).

[325] Z. Ahmed et al. “Results from a Low-Energy Analysis of the CDMS II Germanium Data”. In: *Phys. Rev. Lett.* 106 (2011), p. 131302. arXiv: 1011.2482 [astro-ph.CO] (cit. on p. 81).

[326] W. Zhao et al. “Search of low-mass WIMPs with a p-type point contact germanium detector in the CDEX-1 experiment”. In: *Phys. Rev.* D93.9 (2016), p. 092003. arXiv: 1601.04581 [hep-ex] (cit. on p. 81).

[327] Marc Kamionkowski and Ali Kinkhabwala. “Galactic halo models and particle dark matter detection”. In: *Phys. Rev.* D57 (1998), pp. 3256–3263. arXiv: hep-ph/9710337 [hep-ph] (cit. on p. 79).

[328] Manuel Drees and Chung-Lin Shan. “Model-Independent Determination of the WIMP Mass from Direct Dark Matter Detection Data”. In: *JCAP* 0806 (2008), p. 012. arXiv: 0803.4477 [hep-ph] (cit. on p. 79).

[329] Eugenio Del Nobile, Graciela B. Gelmini, Paolo Gondolo, and Ji-Haeng Huh. “Update on the Halo-Independent Comparison of Direct Dark Matter Detection Data”. In: *Phys. Procedia* 61 (2015), pp. 45–54. arXiv: 1405.5582 [hep-ph] (cit. on p. 79).

[330] M. Beck et al. “Searching for dark matter with the enriched detectors of the Heidelberg - Moscow Double Beta Decay Experiment”. In: *Phys. Lett.* B336 (1994), pp. 141–146 (cit. on p. 80).

[331] Toby Falk, Keith A. Olive, and Mark Srednicki. “Heavy sneutrinos as dark matter”. In: *Phys. Lett.* B339 (1994), pp. 248–251. arXiv: hep-ph/9409270 [hep-ph] (cit. on p. 80).

[332] JiJi Fan, Matthew Reece, and Lian-Tao Wang. “Non-relativistic effective theory of dark matter direct detection”. In: *JCAP* 1011 (2010), p. 042. arXiv: 1008.1591 [hep-ph] (cit. on p. 80).

[333] A. Liam Fitzpatrick, Wick Haxton, Emanuel Katz, Nicholas Lubbers, and Yiming Xu. “The Effective Field Theory of Dark Matter Direct Detection”. In: *JCAP* 1302 (2013), p. 004. arXiv: 1203.3542 [hep-ph] (cit. on p. 80).

[334] Sebastian Liem, Gianfranco Bertone, Francesca Calore, et al. “Effective field theory of dark matter: a global analysis”. In: *JHEP* 09 (2016), p. 077. arXiv: 1603.05994 [hep-ph] (cit. on p. 82).

[335] Anthony DiFranzo, Keiko I. Nagao, Arvind Rajaraman, and Tim M. P. Tait. “Simplified Models for Dark Matter Interacting with Quarks”. In: *JHEP* 11 (2013). [Erratum: JHEP01,162(2014)], p. 014. arXiv: 1308.2679 [hep-ph] (cit. on p. 82).

[336] Alexandre Alves, Stefano Profumo, and Farinaldo S. Queiroz. “The dark $Z^{'}$ portal: direct, indirect and collider searches”. In: *JHEP* 04 (2014), p. 063. arXiv: 1312.5281 [hep-ph] (cit. on p. 82).

[337] Matthew R. Buckley, David Feld, and Dorival Goncalves. “Scalar Simplified Models for Dark Matter”. In: *Phys. Rev.* D91 (2015), p. 015017. arXiv: 1410.6497 [hep-ph] (cit. on p. 82).

[338] Arghya Choudhury, Kamila Kowalska, Leszek Roszkowski, Enrico Maria Sessolo, and Andrew J. Williams. "Less-simplified models of dark matter for direct detection and the LHC". In: *JHEP* 04 (2016), p. 182. arXiv: 1509.05771 [hep-ph] (cit. on p. 82).

[339] Shigeki Matsumoto, Satyanarayan Mukhopadhyay, and Yue-Lin Sming Tsai. "Effective Theory of WIMP Dark Matter supplemented by Simplified Models: Singlet-like Majorana fermion case". In: *Phys. Rev.* D94.6 (2016), p. 065034. arXiv: 1604.02230 [hep-ph] (cit. on p. 82).

[340] Nicole F. Bell, Yi Cai, James B. Dent, Rebecca K. Leane, and Thomas J. Weiler. "Dark matter at the LHC: Effective field theories and gauge invariance". In: *Phys. Rev.* D92.5 (2015), p. 053008. arXiv: 1503.07874 [hep-ph] (cit. on p. 82).

[341] Felix Kahlhoefer, Kai Schmidt-Hoberg, Thomas Schwetz, and Stefan Vogl. "Implications of unitarity and gauge invariance for simplified dark matter models". In: *JHEP* 02 (2016), p. 016. arXiv: 1510.02110 [hep-ph] (cit. on p. 82).

[342] Andrea De Simone and Thomas Jacques. "Simplified models vs. effective field theory approaches in dark matter searches". In: *Eur. Phys. J.* C76.7 (2016), p. 367. arXiv: 1603.08002 [hep-ph] (cit. on p. 82).

[343] R. Agnese et al. "Projected Sensitivity of the SuperCDMS SNOLAB experiment". In: *Phys. Rev.* D95.8 (2017), p. 082002. arXiv: 1610.00006 [physics.ins-det] (cit. on p. 82).

[344] J. Aalbers et al. "DARWIN: towards the ultimate dark matter detector". In: *JCAP* 1611 (2016), p. 017. arXiv: 1606.07001 [astro-ph.IM] (cit. on p. 82).

[345] P. A. Amaudruz et al. "DEAP-3600 Dark Matter Search". In: *Nucl. Part. Phys. Proc.* 273-275 (2016), pp. 340–346. arXiv: 1410.7673 [physics.ins-det] (cit. on p. 82).

[346] J. Calvo et al. "Status of ArDM-1t: First observations from operation with a full ton-scale liquid argon target". In: (2015). arXiv: 1505.02443 [physics.ins-det] (cit. on p. 82).

[347] J Billard, Enectali Figueroa-Feliciano, and L Strigari. *Implication of neutrino backgrounds on the reach of next generation dark matter direct detection experiments*. Vol. 89. 2. 2014, p. 023524 (cit. on pp. 82, 141).

[348] Andrzej Drukier, Katherine Freese, David Spergel, et al. "New Dark Matter Detectors using DNA for Nanometer Tracking". In: (June 2012). arXiv: 1206.6809 (cit. on p. 83).

[349] Alejandro Lopez, Andrzej Drukier, Katherine Freese, Cagliyan Kurdak, and Gregory Tarle. "New Dark Matter Detector using Nanoscale Explosives". In: (Apr. 2014). arXiv: 1403.8115 (cit. on p. 83).

[350] Alexis A. Aguilar-Arevalo, Xavier Bertou, Melissa J. Butner, et al. "DAMIC: a novel dark matter experiment". In: (Oct. 2013). arXiv: 1310.6688 (cit. on p. 83).

[351] Patrick deNiverville, David McKeen, and Adam Ritz. “Signatures of sub-GeV dark matter beams at neutrino experiments”. In: *Phys. Rev. D* 86.3 (May 2012), p. 035022. arXiv: 1205.3499 (cit. on p. 83).

[352] Rouven Essig, Marivi Fernandez-Serra, Jeremy Mardon, et al. “Direct Detection of sub-GeV Dark Matter with Semiconductor Targets”. In: *JHEP* 05 (2016), p. 046. arXiv: 1509.01598 [hep-ph] (cit. on p. 83).

[353] Rouven Essig, Jeremy Mardon, and Tomer Volansky. “Direct Detection of Sub-GeV Dark Matter”. In: *Phys. Rev.* D85 (2012), p. 076007. arXiv: 1108.5383 [hep-ph] (cit. on p. 83).

[354] Eric Kuflik, Aaron Pierce, and Kathryn M. Zurek. “Light Neutralinos with Large Scattering Cross Sections in the Minimal Supersymmetric Standard Model”. In: *Phys. Rev.* D81 (2010), p. 111701. arXiv: 1003.0682 [hep-ph] (cit. on p. 85).

[355] T. Alexander et al. “Light Yield in DarkSide-10: A Prototype Two-Phase Argon TPC for Dark Matter Searches”. In: *Astropart. Phys.* 49 (2013), pp. 44–51. arXiv: 1204.6218 [astro-ph.IM] (cit. on p. 86).

[356] Paolo Agnes, Thomas Alexander, Andrew K Alton, et al. *First results from the DarkSide-50dark matter experiment at Laboratori Nazionali del Gran Sasso*. Vol. 743. 2015, pp. 456–466 (cit. on pp. 86, 87, 90, 91, 96, 97, 106).

[357] P. Benetti et al. “First results from a Dark Matter search with liquid Argon at 87 K in the Gran Sasso Underground Laboratory”. In: *Astropart. Phys.* 28 (2008), pp. 495–507. arXiv: astro-ph/0701286 [astro-ph] (cit. on p. 86).

[358] Paolo Agnes, Luca Agostino, Ivone F M Albuquerque, et al. “Results from the first use of low radioactivity argon in a dark matter search”. In: *Phys. Rev. D* 93.8 (2016), p. 081101 (cit. on pp. 86–88, 96–98, 102).

[359] Huajie Cao, Thomas Alexander, Ani Aprahamian, et al. *Measurement of scintillation and ionization yield and scintillation pulse shape from nuclear recoils in liquid argon*. Vol. 91. 9. 2015, p. 092007 (cit. on pp. 86, 110, 165, 166, 170).

[360] E. Aprile et al. “Dark Matter Results from 225 Live Days of XENON100 Data”. In: *Phys. Rev. Lett.* 109 (2012), p. 181301. arXiv: 1207.5988 [astro-ph.CO] (cit. on p. 88).

[361] Daniel S Akerib, S Alsum, H M Araújo, et al. *Results from a Search for Dark Matter in the Complete LUX Exposure*. Vol. 118. 2. American Physical Society, 2017, p. 021303 (cit. on pp. 88, 165, 170).

[362] J. Calvo et al. “Status of ArDM-1t: First observations from operation with a full ton-scale liquid argon target”. In: (2015). arXiv: 1505.02443 [physics.ins-det] (cit. on p. 88).

[363] M. G. Boulay. “DEAP-3600 Dark Matter Search at SNOLAB”. In: *J. Phys. Conf. Ser.* 375 (2012), p. 012027. arXiv: 1203.0604 [astro-ph.IM] (cit. on p. 88).

[364] G. Bellini et al. “Cosmogenic Backgrounds in Borexino at 3800 m water-equivalent depth”. In: *JCAP* 1308 (2013), p. 049. arXiv: 1304.7381 [physics.ins-det] (cit. on pp. 89, 108).

[365] A Empl, E. V. Hungerford, R. Jasem, and P. Mosteiro. “A. Fluka Study of Underground Cosmogenic Neutron Production”. In: *JCAP* 1408 (2014), p. 064. arXiv: 1406.6081 [astro-ph.IM] (cit. on pp. 89, 108, 109).

[366] P. A. Amaudruz et al. “Measurement of the scintillation time spectra and pulse-shape discrimination of low-energy β and nuclear recoils in liquid argon with DEAP-1”. In: *Astropart. Phys.* 85 (2016), pp. 1–23. arXiv: 0904.2930 [astro-ph.IM] (cit. on p. 92).

[367] Zhou Wang, Lei Bao, Xihuan Hao, and Yonglin Ju. “Design and construction of a cryogenic distillation device for removal of krypton for liquid xenon dark matter detectors”. In: *Rev. Sci. Instrum.* 85 (2014), p. 015116 (cit. on p. 92).

[368] Alex Wright, Pablo Mosteiro, Ben Loer, and Frank Calaprice. “A Highly Efficient Neutron Veto for Dark Matter Experiments”. In: *Nucl. Instrum. Meth.* A644 (2011), pp. 18–26. arXiv: 1010.3609 [nucl-ex] (cit. on p. 96).

[369] P. Agnes et al. “The veto system of the DarkSide-50 experiment”. In: *JINST* 11.03 (2016), P03016. arXiv: 1512.07896 [physics.ins-det] (cit. on pp. 96, 97).

[370] F.A. Lindemann Ph.D. “XII. Note on the vapour pressure and affinity of isotopes”. In: *The London, Edinburgh, and Dublin Philosophical Magazine and Journal of Science* 38.223 (1919), pp. 173–181. eprint: http://dx.doi.org/10.1080/14786440708635937 (cit. on p. 99).

[371] J. De Boer. “Quantum theory of condensed permanent gases I the law of corresponding states”. In: *Physica* 14 (Apr. 1948), pp. 139–148 (cit. on p. 99).

[372] Jacob Bigeleisen. “Statistical Mechanics of Isotope Effects on the Thermodynamic Properties of Condensed Systems”. In: *The Journal of Chemical Physics* 34.5 (1961), pp. 1485–1493. eprint: https://doi.org/10.1063/1.1701033 (cit. on p. 99).

[373] G. Boato, G. Scoles, and M. E. Vallauri. “Vapour pressure of isotopic solids by a steady flow method: Argon between 72 °K and triple point", journal="Il Nuovo Cimento (1955-1965)”. In: 23.6 (1962), pp. 1041–1053 (cit. on p. 99).

[374] J. N. Canongia Lopes, A. A. H. Pádua, L. P. N. Rebelo, and J. Bigeleisen. “Calculation of vapor pressure isotope effects in the rare gases and their mixtures using an integral equation theory”. In: 118 (2003), pp. 5028–5037 (cit. on p. 99).

[375] J. C. G. Calado, F. A. Dias, J. N. C. Lopes, and L. P. N. Rebelo. “Vapor Pressure and Related Thermodynamic Properties of 36Ar”. In: *The Journal of Physical Chemistry B* 104.36 (2000), pp. 8735–8742. eprint: http://dx.doi.org/10.1021/jp0006936 (cit. on p. 99).

[376] G. Casanova, A. Levi, and N. Terzi. “Mean square force in liquid argon and separation factor of isotopes”. In: *Physica* 30.5 (1964), pp. 937 –947 (cit. on p. 99).

[377] R. Fieschi and N. Terzi. “Quantum effects in the liquid state by means of a phenomenological cell model: The vapour pressure ratio of Ne and Ar isotopes”. In: *Physica* 27 (1961), pp. 453–464 (cit. on p. 99).

[378] C. J. Martoff and P. D. Lewin. “COSMO - a program to estimate spallation radioactivity produced in a pure substance by exposure to cosmic radiation on the earth”. In: *Comput. Phys. Commun.* 72.1 (1992), pp. 96–103 (cit. on p. 105).

[379] J. J. Back and Yorck Alexander Ramachers. “ACTIVIA: Calculation of Isotope Production Cross-sections and Yields”. In: *Nucl. Instrum. Meth.* A586 (2008), pp. 286–294. arXiv: 0709.3472 [nucl-ex] (cit. on p. 105).

[380] Glen Cowan, Kyle Cranmer, Eilam Gross, and Ofer Vitells. “Asymptotic formulae for likelihood-based tests of new physics”. In: *Eur. Phys. J.* C71 (2011). [Erratum: Eur. Phys. J.C73,2501(2013)], p. 1554. arXiv: 1007.1727 [physics.data-an] (cit. on p. 120).

[381] Scott Dodelson. “Backgrounds and Projected Limits from Dark Matter Direct Detection Experiments”. In: *Phys. Rev.* D79 (2009), p. 043508. arXiv: 0812.0787 [astro-ph] (cit. on p. 120).

[382] A. Drukier and Leo Stodolsky. “Principles and Applications of a Neutral Current Detector for Neutrino Physics and Astronomy”. In: *Phys. Rev.* D30 (1984). [,395(1984)], p. 2295 (cit. on p. 122).

[383] D. Akimov et al. “Coherent Scattering Investigations at the Spallation Neutron Source: a Snowmass White Paper”. In: *Proceedings, 2013 Community Summer Study on the Future of U.S. Particle Physics: Snowmass on the Mississippi (CSS2013): Minneapolis, MN, USA, July 29-August 6, 2013*. 2013. arXiv: 1310.0125 [hep-ex] (cit. on p. 123).

[384] K. Scholberg, T. Wongjirad, E. Hungerford, et al. “The CLEAR Experiment”. In: *Particles and fields. Proceedings, Meeting of the Division of the American Physical Society, DPF 2009, Detroit, USA, July 26-31, 2009*. 2009. arXiv: 0910.1989 [hep-ex] (cit. on p. 123).

[385] S. J. Brice et al. “A method for measuring coherent elastic neutrino-nucleus scattering at a far off-axis high-energy neutrino beam target”. In: *Phys. Rev.* D89.7 (2014), p. 072004. arXiv: 1311.5958 [physics.ins-det] (cit. on p. 123).

[386] J. I. Collar, N. E. Fields, M. Hai, et al. “Coherent neutrino-nucleus scattering detection with a CsI[Na] scintillator at the SNS spallation source”. In: *Nucl. Instrum. Meth.* A773 (2015), pp. 56–65. arXiv: 1407.7524 [physics.ins-det] (cit. on p. 123).

[387] Q. R. Ahmad et al. “Direct evidence for neutrino flavor transformation from neutral current interactions in the Sudbury Neutrino Observatory”. In: *Phys. Rev. Lett.* 89 (2002), p. 011301. arXiv: nucl-ex/0204008 [nucl-ex] (cit. on p. 127).

[388] John N. Bahcall, Aldo M. Serenelli, and Sarbani Basu. “New solar opacities, abundances, helioseismology, and neutrino fluxes”. In: *Astrophys. J.* 621 (2005), pp. L85–L88. arXiv: astro-ph/0412440 [astro-ph] (cit. on pp. 127, 128).

[389] Ilídio Lopes and Sylvaine Turck-Chièze. “Solar neutrino physics oscillations: Sensitivity to the electronic density in the Sun’s core”. In: *Astrophys. J.* 765 (2013), p. 14. arXiv: 1302.2791 [astro-ph.SR] (cit. on pp. 128, 157).

[390] Louis E. Strigari. “Neutrino Coherent Scattering Rates at Direct Dark Matter Detectors”. In: *New J. Phys.* 11 (2009), p. 105011. arXiv: 0903.3630 [astro-ph.CO] (cit. on p. 128).

[391] Y. Fukuda et al. “Study of the atmospheric neutrino flux in the multi-GeV energy range”. In: *Phys. Lett.* B436 (1998), pp. 33–41. arXiv: hep-ex/9805006 [hep-ex] (cit. on p. 128).

[392] B. Aharmim et al. “Measurement of the Cosmic Ray and Neutrino-Induced Muon Flux at the Sudbury Neutrino Observatory”. In: *Phys. Rev.* D80 (2009), p. 012001. arXiv: 0902.2776 [hep-ex] (cit. on p. 128).

[393] P. Adamson et al. “Measurements of atmospheric neutrinos and antineutrinos in the MINOS Far Detector”. In: *Phys. Rev.* D86 (2012), p. 052007. arXiv: 1208.2915 [hep-ex] (cit. on p. 128).

[394] R. Abbasi et al. “Measurement of the atmospheric neutrino energy spectrum from 100 GeV to 400 TeV with IceCube”. In: *Phys. Rev.* D83 (2011), p. 012001. arXiv: 1010.3980 [astro-ph.HE] (cit. on p. 128).

[395] M. Honda, T. Kajita, K. Kasahara, and S. Midorikawa. “Improvement of low energy atmospheric neutrino flux calculation using the JAM nuclear interaction model”. In: *Phys. Rev.* D83 (2011), p. 123001. arXiv: 1102.2688 [astro-ph.HE] (cit. on pp. 128, 129).

[396] John F. Beacom. “The Diffuse Supernova Neutrino Background”. In: *Ann. Rev. Nucl. Part. Sci.* 60 (2010), pp. 439–462. arXiv: 1004.3311 [astro-ph.HE] (cit. on p. 129).

[397] Jocelyn Monroe and Peter Fisher. “Neutrino Backgrounds to Dark Matter Searches”. In: *Phys. Rev.* D76 (2007), p. 033007. arXiv: 0706.3019 [astro-ph] (cit. on p. 129).

[398] Glen Cowan, Kyle Cranmer, Eilam Gross, and Ofer Vitells. “Asymptotic formulae for likelihood-based tests of new physics”. In: *Eur. Phys. J. C* 71.2 (June 2013), pp. 1–19. arXiv: 1007.1727 (cit. on p. 141).

[399] F. Ruppin, J. Billard, E. Figueroa-Feliciano, and L. Strigari. “Complementarity of dark matter detectors in light of the neutrino background”. In: *Phys. Rev.* D90.8 (2014), p. 083510. arXiv: 1408.3581 [hep-ph] (cit. on p. 146).

[400] Justin Evans, Diego Garcia Gamez, Salvatore Davide Porzio, Stefan Söldner-Rembold, and Steven Wren. “Uncertainties in Atmospheric Muon-Neutrino Fluxes Arising from Cosmic-Ray Primaries”. In: *Phys. Rev.* D95.2 (2017), p. 023012. arXiv: 1612.03219 [astro-ph.HE] (cit. on p. 152).

[401] William J. Marciano and Zohreh Parsa. “Neutrino electron scattering theory”. In: *J. Phys.* G29 (2003), pp. 2629–2645. arXiv: hep-ph/0403168 [hep-ph] (cit. on pp. 156, 157).

[402] Henry T. Wong, Hau-Bin Li, and Shin-Ted Lin. “Derivations of Atomic Ionization Effects Induced by Neutrino Magnetic Moments”. In: *Phys. Rev. Lett.* 105 (2010), p. 061801. arXiv: 1001.2074 [hep-ph] (cit. on p. 156).

[403] J. A. Formaggio and G. P. Zeller. “From eV to EeV: Neutrino Cross Sections Across Energy Scales”. In: *Rev. Mod. Phys.* 84 (2012), pp. 1307–1341. arXiv: 1305.7513 [hep-ex] (cit. on p. 157).

[404] Andrzej K Drukier, Katherine Freese, and David N Spergel. *Detecting cold dark-matter candidates*. Vol. 33. 12. American Physical Society, 1986, pp. 3495–3508 (cit. on p. 164).

[405] R Bernabei, P Belli, F Cappella, et al. *First results from DAMA/LIBRA and the combined results with DAMA/NaI*. Vol. 56. 3. Springer-Verlag, 2008, pp. 333–355 (cit. on p. 164).

[406] Steve Ahlen, N Afshordi, James B R Battat, et al. *THE CASE FOR A DIRECTIONAL DARK MATTER DETECTOR AND THE STATUS OF CURRENT EXPERIMENTAL EFFORTS*. Vol. 25. 01. World Scientific Publishing Company, 2010, pp. 1–51 (cit. on p. 165).

[407] J. B. R. Battat, I. G. Irastorza, A. Aleksandrov, et al. *Readout technologies for directional WIMP Dark Matter detection*. Vol. 662. 2016, pp. 1–46. arXiv: 1610.02396 [physics.ins-det] (cit. on p. 165).

[408] AnDi Tan, MengJiao Xiao, XiangYi Cui, et al. *Dark Matter Results from First 98.7 Days of Data from the PandaX-II Experiment*. Vol. 117. 12. American Physical Society, 2016, p. 121303 (cit. on p. 165).

[409] D. R. Nygren. “Columnar recombination: a tool for nuclear recoil directional sensitivity in a xenon-based direct detection WIMP search”. In: *J. Phys. Conf. Ser.* 460 (2013), p. 012006 (cit. on p. 165).

[410] R. Acciarri et al. “Effects of Nitrogen contamination in liquid Argon”. In: *JINST* 5 (2010), P06003. arXiv: 0804.1217 [nucl-ex] (cit. on p. 165).

[411] D W Swan. *Ionization of liquid argon by particles*. Vol. 85. 6. IOP Publishing, 1965, pp. 1297–1302 (cit. on p. 165).

[412] T. Alexander, H. O. Back, H. Cao, et al. *Observation of the dependence on drift field of scintillation from nuclear recoils in liquid argon*. Vol. 88. American Physical Society, 2013, p. 092006 (cit. on p. 165).

[413] J. Thomas and D. A. Imel. “Recombination of electron-ion pairs in liquid argon and liquid xenon”. In: *Phys. Rev.* A36 (1987), pp. 614–616 (cit. on p. 166).

[414] R. Acciarri et al. “A study of electron recombination using highly ionizing particles in the ArgoNeuT Liquid Argon TPC”. In: *JINST* 8 (2013), P08005. arXiv: 1306.1712 [physics.ins-det] (cit. on pp. 166, 167).

[415] J Billard, F Mayet, and D Santos. *Exclusion, Discovery and Identification of Dark Matter with Directional Detection*. Vol. 53. EDP Sciences, 2012, pp. 67–75 (cit. on p. 167).

[416] Nassim Bozorgnia, Graciela B Gelmini, and Paolo Gondolo. *Aberration features in directional dark matter detection*. Vol. 2012. 08. IOP Publishing, 2012, pp. 011–011 (cit. on pp. 167, 172).

[417] Craig J Copi and Lawrence M Krauss. *Angular signatures for galactic halo weakly interacting massive particle scattering in direct detectors: Prospects and challenges*. Vol. 63. 4. American Physical Society, 2001, p. 043507 (cit. on p. 167).

[418] F. Mayet et al. *A review of the discovery reach of directional Dark Matter detection*. Vol. 627. 2016, pp. 1–49. arXiv: 1602.03781 [astro-ph.CO] (cit. on p. 167).

[419] Ciaran A. J. O’Hare. “Detecting WIMPs, neutrinos and axions in the next generation of dark matter experiment”. In: *PhD Thesis* University of Nottingham (2017) (cit. on p. 167).

[420] Paolo Gondolo. *Recoil momentum spectrum in directional dark matter detectors*. Vol. 66. 10. American Physical Society, 2002, p. 103513 (cit. on p. 168).

[421] A Blaauw, C S Gum, J L Pawsey, and G Westerhout. *The New I.A.U. System of Galactic Coordinates (1958 Revision)*. Vol. 121. 2. Oxford University Press, 1960, pp. 123–131 (cit. on p. 169).

[422] Moqbil S. Alenazi and Paolo Gondolo. *Directional recoil rates for WIMP direct detection*. Vol. 77. American Physical Society, 2008, p. 043532 (cit. on p. 170).

[423] Matthew J. Lewis and Katherine Freese. *The Phase of the annual modulation: Constraining the WIMP mass*. Vol. 70. 2004, p. 043501. arXiv: astro-ph/0307190 [astro-ph] (cit. on p. 178).

[424] Katherine Freese, Mariangela Lisanti, and Christopher Savage. *Colloquium: Annual modulation of dark matter*. Vol. 85. 4. American Physical Society, 2013, pp. 1561–1581 (cit. on p. 178).

[425] John Tatarowicz and C Jeff Martoff. *Optimized running conditions and sensitivity for direction sensitive detectors of WIMP dark matter*. Vol. 35. 5. 2011, pp. 235–241 (cit. on p. 178).

[426] Vassily Plyaskin. “Calculation of atmospheric neutrino flux”. In: *Phys. Lett.* B516 (2001), pp. 213–235. arXiv: hep-ph/0103286 [hep-ph] (cit. on p. 183).

[427] Glen Cowan, Kyle Cranmer, Eilam Gross, and Ofer Vitells. *Asymptotic formulae for likelihood-based tests of new physics*. Vol. 71. 2. 2011, pp. 1–19 (cit. on p. 184).

[428] G. Fricke, C. Bernhardt, K. Heilig, et al. “Nuclear Ground State Charge Radii from Electromagnetic Interactions”. In: *At. Data. Nucl. Data Tables* 60.2 (July 1995), pp. 177–285 (cit. on p. 191).

[429] Daniel Z. Freedman, David N. Schramm, and David L. Tubbs. “The Weak Neutral Current and Its Effects in Stellar Collapse”. In: *Ann. Rev. Nucl. Part. Sci.* 27 (1977), pp. 167–207 (cit. on p. 192).

[430] Jiajun Liao and Danny Marfatia. “COHERENT constraints on nonstandard neutrino interactions”. In: *Phys. Lett.* B775 (2017), pp. 54–57. arXiv: 1708.04255 [hep-ph] (cit. on p. 192).

[431] Pilar Coloma, M. C. Gonzalez-Garcia, Michele Maltoni, and Thomas Schwetz. “A COHERENT enlightenment of the neutrino Dark Side”. In: (2017). arXiv: 1708.02899 [hep-ph] (cit. on p. 192).

[432] A. C. Dodd, E. Papageorgiu, and S. Ranfone. “The Effect of a neutrino magnetic moment on nuclear excitation processes”. In: *Phys. Lett.* B266 (1991), pp. 434–438 (cit. on p. 192).

[433] T. S. Kosmas, O. G. Miranda, D. K. Papoulias, M. Tortola, and J. W. F. Valle. “Probing neutrino magnetic moments at the Spallation Neutron Source facility”. In: *Phys. Rev.* D92.1 (2015), p. 013011. arXiv: 1505.03202 [hep-ph] (cit. on p. 192).

[434] Bhaskar Dutta, Rupak Mahapatra, Louis E. Strigari, and Joel W. Walker. “Sensitivity to Z-prime and nonstandard neutrino interactions from ultralow threshold neutrino-nucleus coherent scattering”. In: *Phys. Rev.* D93.1 (2016), p. 013015. arXiv: 1508.07981 [hep-ph] (cit. on p. 192).

[435] J. Barranco, O. G. Miranda, and T. I. Rashba. “Low energy neutrino experiments sensitivity to physics beyond the Standard Model”. In: *Phys. Rev.* D76 (2007), p. 073008. arXiv: hep-ph/0702175 [hep-ph] (cit. on p. 192).

[436] Patrick deNiverville, Maxim Pospelov, and Adam Ritz. “Light new physics in coherent neutrino-nucleus scattering experiments”. In: *Phys. Rev.* D92.9 (2015), p. 095005. arXiv: 1505.07805 [hep-ph] (cit. on p. 192).

[437] Lawrence M. Krauss. “Low-energy neutrino detection and precision tests of the standard model”. In: *Phys. Lett.* B269 (1991), pp. 407–411 (cit. on p. 192).

[438] James R. Wilson. “Coherent Neutrino Scattering and Stellar Collapse”. In: *Phys. Rev. Lett.* 32 (1974), pp. 849–852 (cit. on p. 192).

[439] D. N. Schramm and W. D. Arnett. “Neutral currents and supernova”. In: *Phys. Rev. Lett.* 34 (1975), pp. 113–116 (cit. on p. 192).

[440] T. S. Kosmas, D. K. Papoulias, M. Tortola, and J. W. F. Valle. “Probing light sterile neutrino signatures at reactor and Spallation Neutron Source neutrino experiments”. In: *Phys. Rev.* D96.6 (2017), p. 063013. arXiv: 1703.00054 [hep-ph] (cit. on p. 192).

[441] F. T. Avignone and Yu. V. Efremenko. “Neutrino nucleus cross-section measurements at intense, pulsed spallation sources”. In: *J. Phys.* G29 (2003), pp. 2615–2628 (cit. on p. 193).

[442] J. Barranco, O. G. Miranda, and T. I. Rashba. “Probing new physics with coherent neutrino scattering off nuclei”. In: *JHEP* 12 (2005), p. 021. arXiv: hep-ph/0508299 [hep-ph] (cit. on pp. 195, 200).

[443] Spencer Klein and Joakim Nystrand. “Exclusive vector meson production in relativistic heavy ion collisions”. In: *Phys. Rev.* C60 (1999), p. 014903. arXiv: hep-ph/9902259 [hep-ph] (cit. on pp. 195, 205).

[444] Kelly Patton, Jonathan Engel, Gail C. McLaughlin, and Nicolas Schunck. “Neutrino-nucleus coherent scattering as a probe of neutron density distributions”. In: *Phys. Rev.* C86 (2012), p. 024612. arXiv: 1207.0693 [nucl-th] (cit. on p. 197).

[445] D. K. Papoulias and T. S. Kosmas. “Standard and Nonstandard Neutrino-Nucleus Reactions Cross Sections and Event Rates to Neutrino Detection Experiments”. In: *Adv. High Energy Phys.* 2015 (2015), p. 763648. arXiv: 1502.02928 [nucl-th] (cit. on pp. 197, 217).

[446] C. Patrignani et al. “Review of Particle Physics”. In: *Chin. Phys.* C40.10 (2016), p. 100001 (cit. on p. 198).

[447] I. Angeli and K. P. Marinova. “Table of experimental nuclear ground state charge radii: An update”. In: *Atom. Data Nucl. Data Tabl.* 99.1 (2013), pp. 69–95 (cit. on p. 198).

[448] C. Garcia-Recio, J. Nieves, and E. Oset. “Neutron distributions from pionic atoms”. In: *Nucl. Phys.* A547 (1992), pp. 473–487 (cit. on p. 198).

[449] V. E. Starodubsky and N. M. Hintz. “Extraction of neutron densities from elastic proton scattering by Pb-206, Pb-207, Pb-208 at 650-MeV”. In: *Phys. Rev.* C49 (1994), pp. 2118–2135 (cit. on p. 198).

[450] A. Trzcinska, J. Jastrzebski, P. Lubinski, et al. “Neutron density distributions deduced from anti-protonic atoms”. In: *Phys. Rev. Lett.* 87 (2001), p. 082501 (cit. on p. 198).

[451] B. C. Clark, L. J. Kerr, and S. Hama. “Neutron densities from a global analysis of medium-energy proton nucleus elastic scattering”. In: *Phys. Rev.* C67 (2003), p. 054605. arXiv: nucl-th/0209052 [nucl-th] (cit. on p. 198).

[452] T. W. Donnelly, J. Dubach, and Ingo Sick. “Isospin Dependences in Parity Violating Electron Scattering”. In: *Nucl. Phys.* A503 (1989), pp. 589–631 (cit. on p. 199).

[453] G. A. Lalazissis, J. Konig, and P. Ring. “A New parametrization for the Lagrangian density of relativistic mean field theory”. In: *Phys. Rev.* C55 (1997), pp. 540–543. arXiv: nucl-th/9607039 [nucl-th] (cit. on pp. 199, 207).

[454] B. G. Todd-Rutel and J. Piekarewicz. “Neutron-Rich Nuclei and Neutron Stars: A New Accurately Calibrated Interaction for the Study of Neutron-Rich Matter”. In: *Phys. Rev. Lett.* 95 (2005), p. 122501. arXiv: nucl-th/0504034 [nucl-th] (cit. on p. 199).

[455] M. Beiner, H. Flocard, Nyguyen van Giai, and P. Quentin. “Nuclear ground state properties and selfconsistent calculations with the Skyrme interactions: 1. Spherical description”. In: *Nucl. Phys.* A238 (1975), pp. 29–69 (cit. on p. 199).

[456] E. Chabanat, P. Bonche, P. Haensel, J. Meyer, and R. Schaeffer. “A Skyrme parametrization from subnuclear to neutron star densities. 2. Nuclei far from stablities”. In: *Nucl. Phys.* A635 (1998). [Erratum: Nucl. Phys.A643,441(1998)], pp. 231–256 (cit. on pp. 199, 207).

[457] D. Vautherin and D. M. Brink. “Hartree-Fock calculations with Skyrme’s interaction. 1. Spherical nuclei”. In: *Phys. Rev.* C5 (1972), pp. 626–647 (cit. on p. 199).

[458] Charles J. Horowitz and Jorge Piekarewicz. “The Neutron radii of Pb-208 and neutron stars”. In: *Phys. Rev.* C64 (2001), p. 062802. arXiv: nucl-th/0108036 [nucl-th] (cit. on p. 199).

[459] F. J. Fattoyev, J. Piekarewicz, and C. J. Horowitz. “Neutron skins and neutron stars in the multi-messenger era”. In: (2017). arXiv: 1711.06615 [nucl-th] (cit. on pp. 199, 209).

[460] J. Piekarewicz, A. R. Linero, P. Giuliani, and E. Chicken. “Power of two: Assessing the impact of a second measurement of the weak-charge form factor of ^{208}Pb”. In: *Phys. Rev.* C94.3 (2016), p. 034316. arXiv: 1604.07799 [nucl-th] (cit. on pp. 201, 207).

[461] J. Friedrich and N. Voegler. “The salient features of charge density distributions of medium and heavy even-even nuclei determined from a systematic analysis of elastic electron scattering form factors”. In: *Nucl. Phys.* A373 (1982), pp. 192–224 (cit. on p. 201).

[462] C. J. Horowitz et al. “Weak charge form factor and radius of 208Pb through parity violation in electron scattering”. In: *Phys. Rev.* C85 (2012), p. 032501. arXiv: 1202.1468 [nucl-ex] (cit. on p. 206).

[463] J. Bartel, P. Quentin, M. Brack, C. Guet, and H. B. Hakansson. “Towards a better parametrisation of Skyrme-like effective forces: A Critical study of the SkM force”. In: *Nucl. Phys.* A386 (1982), pp. 79–100 (cit. on p. 207).

[464] J. Dobaczewski, H. Flocard, and J. Treiner. “Hartree-Fock-Bogolyubov descriptions of nuclei near the neutrino dripline”. In: *Nucl. Phys.* A422 (1984), pp. 103–139 (cit. on p. 207).

[465] P. G. Reinhard and H. Flocard. “Nuclear effective forces and isotope shifts”. In: *Nucl. Phys.* A584 (1995), pp. 467–488 (cit. on p. 207).

[466] M. Kortelainen, J. McDonnell, W. Nazarewicz, et al. “Nuclear energy density optimization: Large deformations”. In: *Phys. Rev.* C85 (2012), p. 024304. arXiv: 1111.4344 [nucl-th] (cit. on p. 207).

[467] M. M. Sharma, M. A. Nagarajan, and P. Ring. “rho meson coupling in the relativistic mean field theory and description of exotic nuclei”. In: *Phys. Lett.* B312 (1993), pp. 377–381 (cit. on p. 207).

[468] M. Bender, K. Rutz, P. G. Reinhard, J. A. Maruhn, and W. Greiner. “Shell structure of superheavy nuclei in selfconsistent mean field models”. In: *Phys. Rev.* C60 (1999), p. 034304. arXiv: nucl-th/9906030 [nucl-th] (cit. on p. 207).

[469] C. J. Horowitz, S. J. Pollock, P. A. Souder, and R. Michaels. “Parity violating measurements of neutron densities”. In: *Phys. Rev.* C63 (2001), p. 025501. arXiv: nucl-th/9912038 [nucl-th] (cit. on p. 207).

[470] B. Alex Brown, A. Derevianko, and V. V. Flambaum. “Calculations of the neutron skin and its effect in atomic parity violation”. In: *Phys. Rev.* C79 (2009), p. 035501. arXiv: 0804.4315 [hep-ph] (cit. on p. 207).

[471] D. Vretenar, G. A. Lalazissis, and P. Ring. “Neutron density distributions for atomic parity nonconservation experiments”. In: *Phys. Rev.* C62 (2000), p. 045502. arXiv: nucl-th/0004018 [nucl-th] (cit. on p. 207).

[472] Tapas Sil, M. Centelles, X. Vinas, and J. Piekarewicz. “Atomic parity non-conservation, neutron radii, and effective field theories of nuclei”. In: *Phys. Rev.* C71 (2005), p. 045502. arXiv: nucl-th/0501014 [nucl-th] (cit. on pp. 207, 208).

[473] B. Alex Brown. “Neutron radii in nuclei and the neutron equation of state”. In: *Phys. Rev. Lett.* 85 (2000), pp. 5296–5299 (cit. on p. 209).

[474] C. J. Horowitz and J. Piekarewicz. “Neutron star structure and the neutron radius of Pb-208”. In: *Phys. Rev. Lett.* 86 (2001), p. 5647. arXiv: astro-ph/0010227 [astro-ph] (cit. on p. 209).

[475] P. G. Reinhard and W. Nazarewicz. “Information content of a new observable: The case of the nuclear neutron skin”. In: *Phys. Rev.* C81 (2010), p. 051303. arXiv: 1002.4140 [nucl-th] (cit. on p. 209).

[476] M. B. Tsang et al. “Constraints on the symmetry energy and neutron skins from experiments and theory”. In: *Phys. Rev.* C86 (2012), p. 015803. arXiv: 1204.0466 [nucl-ex] (cit. on p. 209).

[477] G. Hagen et al. “Neutron and weak-charge distributions of the ^{48}Ca nucleus”. In: *Nature Phys.* 12.2 (2015), pp. 186–190. arXiv: 1509.07169 [nucl-th] (cit. on p. 209).

[478] M. Baldo and G. F. Burgio. “The nuclear symmetry energy”. In: *Prog. Part. Nucl. Phys.* 91 (2016), pp. 203–258. arXiv: 1606.08838 [nucl-th] (cit. on p. 209).

[479] Bharat Kumar, B. K. Agrawal, and S. K. Patra. “New relativistic effective interaction for finite nuclei, infinite nuclear matter and neutron stars”. In: (2017). arXiv: 1711.04940 [nucl-th] (cit. on p. 209).

[480] T. W. Donnelly and J. D. Walecka. “Semileptonic Weak and Electromagnetic Interactions with Nuclei: Isoelastic Processes”. In: *Nucl. Phys.* A274 (1976), pp. 368–412 (cit. on p. 217).

[481] V. C. Chasioti and T. S. Kosmas. “A unified formalism for the basic nuclear matrix elements in semi-leptonic processes”. In: *Nucl. Phys.* A829 (2009), pp. 234–252 (cit. on p. 217).

[482] T. S. Kosmas, J. D. Vergados, O. Civitarese, and A. Faessler. “Study of the muon number violating (mu-, e-) conversion in a nucleus by using quasiparticle RPA”. In: *Nucl. Phys.* A570 (1994), pp. 637–656 (cit. on p. 217).